

## Abstract

# Flying Qubit Operations in Superconducting Circuits

Anirudh Narla

2017

The quantum non-demolition (QND) measurement process begins by entangling the system to be measured, a qubit for example, with an ancillary degree of freedom, usually a system with an infinite-dimensional Hilbert space. The ancilla is amplified to convert the quantum signal into a measurable classical signal. The continuous classical signal is recorded by a measurement apparatus; a discrete measurement outcome is recovered by thresholding the integrated signal record. Measurements play a central role in technologies based on quantum theory, like quantum computation and communication. They form the basis for a wide range of operations, ranging from state initialization to quantum error correction. Quantum measurements used for quantum computation must satisfy three essential requirements of being high fidelity, quantum non-demolition and efficient. Satisfying these criteria necessitates control over all the parts of the quantum measurement process, especially generating the ancilla, entangling it with the qubit and amplifying it to complete the measurement.

For superconducting quantum circuits, a promising platform for realizing quantum computation, a natural choice for the ancillae are modes of microwave-frequency electromagnetic radiation. In the paradigm of circuit quantum electrodynamics (cQED) with three-dimensional circuits, the most commonly used ancillae are coherent states, since they are easy to generate, process and amplify. Using these flying coherent states, we present results for achieving QND measurements of transmon qubits with fidelities of  $\mathcal{F} > 0.99$  and efficiencies of  $\eta = 0.56 \pm 0.01$ . By also treating the measurement as a more general quantum operation, we use the ancillae as carriers of quantum information to generate remote entanglement between two transmon qubits in separate cavities. By using microwave single photons as the flying qubits, it is possible to generate remote entanglement that is robust to loss since the generation of entanglement is uniquely linked to a particular measurement outcome. We demonstrate, in a single experiment,

the ability to efficiently generate and detect single microwave photons and use them to generate robust remote entanglement between two transmon qubits. This operation forms a crucial primitive in modular architectures for quantum computation. The results of this thesis extend the experimental toolbox at the disposal to superconducting circuits. Building on these results, we outline proposals for remote entanglement distillation as well as strategies to further improve the performance of the various tools.

# Flying Qubit Operations in Superconducting Circuits

A Dissertation  
Presented to the Faculty of the Graduate School  
of  
Yale University  
in Candidacy for the Degree of  
Doctor of Philosophy

by  
Anirudh Narla

Dissertation Director: Michel H. Devoret

December 2017

ProQuest Number: 10783459

All rights reserved

INFORMATION TO ALL USERS

The quality of this reproduction is dependent upon the quality of the copy submitted.

In the unlikely event that the author did not send a complete manuscript and there are missing pages, these will be noted. Also, if material had to be removed, a note will indicate the deletion.



ProQuest 10783459

Published by ProQuest LLC (2018). Copyright of the Dissertation is held by the Author.

All rights reserved.

This work is protected against unauthorized copying under Title 17, United States Code  
Microform Edition © ProQuest LLC.

ProQuest LLC.  
789 East Eisenhower Parkway  
P.O. Box 1346  
Ann Arbor, MI 48106 – 1346

© 2017 by Anirudh Narla  
All rights reserved.

# Contents

<b>Contents</b>	<b>iii</b>
<b>List of Figures</b>	<b>v</b>
<b>List of Tables</b>	<b>vii</b>
<b>Nomenclature</b>	<b>viii</b>
<b>Acknowledgments</b>	<b>xvii</b>
<b>1 Introduction and Overview</b>	<b>1</b>
1.1 Introduction . . . . .	1
1.2 Unpacking Quantum Measurements . . . . .	3
1.3 Quantum Measurements in Quantum Information . . . . .	8
1.4 Superconducting Qubits and circuit-QED - A Platform for Quantum Information .	16
1.5 Efficient Single Qubit Measurements . . . . .	20
1.6 Coherent State Based Remote Entanglement Mediated by a JPC . . . . .	27
1.7 Single Photon Based Remote Entanglement . . . . .	34
1.8 Towards Modular Entanglement Distillation - Perspectives and Future Directions .	44
<b>2 Qubits, Amplifiers, and Measurements in Superconducting Quantum Circuits</b>	<b>49</b>
2.1 Overview . . . . .	49
2.2 Transmon Qubits and 3D Superconducting Cavities . . . . .	50
2.3 The Josephson Parametric Converter . . . . .	56
2.4 Dispersive Readout of a Qubit in Circuit QED . . . . .	63
2.4.1 Finite Efficiency - The cost of information loss . . . . .	70
2.4.2 Higher Qubit Levels . . . . .	73
<b>3 Efficient Single Qubit Measurements</b>	<b>75</b>
3.1 Overview . . . . .	75
3.2 Optimizing Qubit-Cavity Systems for Readout . . . . .	76
3.3 Engineering Experimental Systems - Cryogenic, Microwave and Quantum Hygiene	78
3.3.1 Thermalization . . . . .	79
3.3.2 Magnetic Shielding . . . . .	80
3.3.3 Filtering against Radiation . . . . .	81

3.3.4	Fabrication and Sample Design . . . . .	82
3.3.5	Input Lines . . . . .	82
3.3.6	Output Lines . . . . .	84
3.4	System Parameters . . . . .	87
3.5	Purcell Filters - Long Lived Qubits in Fast Cavities . . . . .	87
3.6	Overdrive Pulses . . . . .	91
3.7	Shaped Demodulation . . . . .	95
3.8	Single Qubit Measurement Fidelity . . . . .	98
3.9	Measurement as a Quantum Operation . . . . .	105
3.10	Extracting Measurement Efficiency from Observation of the Quantum Zeno Effect	110
3.10.1	Theory . . . . .	111
3.10.2	Experimental Results . . . . .	114
<b>4</b>	<b>Coherent State Based Remote Entanglement Mediated by a JPC</b>	<b>118</b>
4.1	Overview . . . . .	118
4.2	Experimental Setup . . . . .	119
4.3	Joint and Entangling Measurements . . . . .	124
4.3.1	Which-Path Erasing Measurements for Entanglement Generation . . . . .	125
4.3.2	Joint Measurements for Two-Qubit Tomography . . . . .	130
4.4	Experimental Results and Analysis . . . . .	131
4.5	Perspectives and Future Directions . . . . .	138
<b>5</b>	<b>Remote Entanglement with Single Flying Microwave Photons</b>	<b>140</b>
5.1	Overview . . . . .	140
5.2	Experimental Implementation . . . . .	142
5.2.1	Joint Alice and Bob measurement . . . . .	145
5.2.2	Detector qubit measurement . . . . .	145
5.3	Generating Single Photons . . . . .	147
5.4	Detecting Single Photons . . . . .	155
5.4.1	Simulations . . . . .	156
5.4.2	Detector Characterization . . . . .	158
5.4.3	Detector Optimization . . . . .	160
5.5	Qubit-Photon Entanglement . . . . .	161
5.5.1	Generating and Detecting Single Photons . . . . .	162
5.5.2	Demonstrating Qubit-Photon Entanglement . . . . .	163
5.6	Joint Tomography and Calibration . . . . .	167
5.7	Experimental Results . . . . .	168
5.7.1	Pulse Sequence . . . . .	169
5.7.2	Control Experiments . . . . .	170
5.8	Entanglement Fidelity . . . . .	171
5.8.1	Qubit Decoherence . . . . .	172
5.8.2	Dark Counts . . . . .	172
5.8.3	Tomography . . . . .	174
5.8.4	Error Analysis . . . . .	175
5.9	Future Directions . . . . .	175

5.9.1	Improving the Single Photon Detector . . . . .	176
5.9.2	Single Round Protocols for Increased Generation Rate . . . . .	178
<b>6</b>	<b>Perspectives of this Work Towards Entanglement Distillation, and Beyond</b>	<b>180</b>
6.1	Overview of Entanglement Distillation . . . . .	180
6.2	Modules for Remote Entanglement Distillation . . . . .	186
6.3	Future Challenges and Prospects . . . . .	192
6.3.1	Increased Coherence . . . . .	193
6.3.2	Small Modules . . . . .	194
6.3.3	Routers and Integrated Directional Components . . . . .	195
6.3.4	Channel Cost and Hardware Complexity . . . . .	195
	<b>Bibliography</b>	<b>198</b>

# List of Figures

<b>Introduction and Overview</b>	<b>1</b>
1.1 Unpacking A Quantum Measurement . . . . .	4
1.2 Protocol Schematic for Concurrent Remote Entanglement Generation . . . . .	10
1.3 A Modular Architecture for Quantum Computing . . . . .	13
1.4 Quantum Circuit for a Remote CNOT Gate between Modules . . . . .	15
1.5 Schematic for Readout of a 3D Transmon Qubit . . . . .	18
1.6 Single Qubit Measurement . . . . .	21
1.7 Single Qubit Measurement Tomograms . . . . .	23
1.8 Single Qubit Measurement Efficiency . . . . .	25
1.9 Coherent State based Remote Entanglement Protocol Schematic . . . . .	28
1.10 Coherent State based Remote Entanglement Tomography . . . . .	31
1.11 Single Photon Based Remote Entanglement Experiment and Protocol Schematic .	36
1.12 Two-Qubit Remote Entanglement . . . . .	40
1.13 Remote Entanglement Characterization . . . . .	41
1.14 Remote Entanglement Distillation Protocol . . . . .	45
<b>Qubits, Amplifiers, and Measurements in Superconducting Quantum Circuits</b>	<b>49</b>
2.1 A Summary of the 3D Transmon-Cavity System in cQED . . . . .	53
2.2 A Summary of the Josephson Parametric Converter . . . . .	59
2.3 Effective Block Diagram for the JPC . . . . .	61
2.4 Single Qubit Measurement Schematic in circuit-QED . . . . .	64
2.5 Transmission Measurement in circuit-QED . . . . .	67
2.6 Reflection Measurement in circuit-QED . . . . .	68
2.7 Contrasting Efficient and Inefficient Measurements . . . . .	72
<b>Efficient Single Qubit Measurements</b>	<b>75</b>
3.1 Waveguide Based Purcell Filters for 3D Transmon Qubits . . . . .	89
3.2 Overdrive Pulses for Qubit Readout . . . . .	92
3.3 Cavity Response and Demodulation Waveforms . . . . .	97
3.4 Single Qubit State Preparation and Measurement . . . . .	102
3.5 Variable Strength Measurement Back-action Histograms and Tomograms . . . . .	107
3.6 Theoretical Quantum Zeno Behavior of a Driven Monitored Qubit . . . . .	113

3.7	Extracting Quantum Measurement Efficiency from the Quantum Zeno Effect . . .	116
<b>Coherent State Based Remote Entanglement Mediated by a JPC</b>		<b>118</b>
4.1	Detailed Experimental Setup . . . . .	120
4.2	Signal and Idler Quantum Measurement Efficiencies . . . . .	122
4.3	Two Qubit Joint and Entangling Readout with a JPC . . . . .	126
4.4	Erasing Which-Path Information by Tuning Cavity Output Fields . . . . .	129
4.5	Histograms and Tomograms of Select Pauli Components . . . . .	133
4.6	Changing the Generated Odd Bell State Phase with Measurement Outcome . . .	135
4.7	Mutual Information from an Entangling Measurement . . . . .	136
<b>Remote Entanglement with Single Flying Microwave Photons</b>		<b>140</b>
5.1	Detailed Experimental Setup . . . . .	143
5.2	Alice, Bob and Detector Qubit Readout Spectra and Histograms . . . . .	146
5.3	Single Photon Generation with Sideband Pumps . . . . .	150
5.4	Spectroscopy and Damped Rabi Oscillations for Two-Photon Sideband Transitions on Alice . . . . .	152
5.5	Calibrating the Two-Photon Coupling Rate . . . . .	154
5.6	Single Photon Detector - Simulations . . . . .	157
5.7	Single Photon Detector - Characterization . . . . .	159
5.8	Single Photon Detector - Optimization . . . . .	160
5.9	Single Photon Generation and Detection . . . . .	162
5.10	Signatures of Alice Qubit/Flying Photon Entanglement . . . . .	164
5.11	Signatures of Qubit-Photon Entanglement: Data vs. Theory . . . . .	165
5.12	Detailed Pulse Sequence . . . . .	169
5.13	Control Sequence Data . . . . .	171
5.14	Schematic for Emitting and Capturing Single Photons . . . . .	177
<b>Perspectives of this Work Towards Entanglement Distillation, and Beyond</b>		<b>180</b>
6.1	Quantum Circuit for a Remote Unitary Gate between Modules . . . . .	181
6.2	Schematics for Modules to Implement Remote Entanglement Distillation . . . .	188
6.3	Schematics for Modules to Implement Remote Entanglement Distillation . . . .	190

# List of Tables

3.1	High-fidelity measurements - qubit and cavity parameters . . . . .	87
3.2	High-fidelity measurements - measured $\langle Z \rangle$ . . . . .	103
4.1	Coherent state based remote entanglement - Alice and Bob qubit and cavity parameters . . . . .	119
5.1	Single photon based remote entanglement - Alice, Bob, and Detector qubit and cavity parameters . . . . .	142

# Nomenclature

## Acronyms

CNOT	Controlled NOT Gate
SWAP	SWAP Gate
ADC	Analog to Digital Converter
AWG	Arbitrary Waveform Generator
cQED	Circuit Quantum Electrodynamics
CSB	Cavity Sideband
DP-JBA	Double-Pumped Josephson Bifurcation Amplifier
HEMT	High Electron Mobility Transistor
JBA	Josephson Bifurcation Amplifier
JPC	Josephson Parametric Converter
JRM	Josephson Ring Modulator
NVR	Noise Visibility Ratio
QEC	Quantum Error Correction
QND	Quantum Non-Demolition

QSB	Qubit Sideband
RWA	Rotating Wave Approximation
SB	Sideband
SEM	Scanning Electron Microscope
SNAIL	Superconducting Non-linear Asymmetric Inductive eLement
SNR	Signal-to-Noise Ratio
SQUID	Superconducting Quantum Interference Device

### Constants

$\hbar$	Reduced Planck Constant
$\phi_0 = \frac{\Phi_0}{2\pi} = \frac{\hbar}{2e}$	Reduced magnetic flux quantum
$\Phi_0 = \frac{h}{2e}$	Magnetic flux quantum
$e$	Electron charge
$k_B$	Boltzmann constant

### Symbols

$ 0\rangle$	Vacuum state or Fock state with zero photon number
$ \bar{G}\rangle$ ( $ \bar{E}\rangle$ )	Measurement outcome for finding the qubit in the state not $ g\rangle$ ( $ e\rangle$ )
$\bar{I}_m/\sigma$	Strength of a general measurement in the dispersive cQED readout regime
$\mathbf{a}, \mathbf{a}^\dagger$	Annihilation and creation operators for cavity mode
$\mathbf{b}, \mathbf{b}^\dagger$	Annihilation and creation operators for qubit mode
$H_{\text{cQED}}$	cQED Hamiltonian

$H_{\text{drive}}$	Drive Hamiltonian
$H_{\text{int}}$	Interaction Hamiltonian
$H_{\text{JPC}}$	JPC Interaction Hamiltonian
$H$	Hamiltonian
$M_\nu$	Measurement operator associated with the measurement outcome $\nu$
$O$	Observable
$U_{\text{BS}}$	Unitary performed by a beam-splitter
$U_{\text{cQED}}$	Unitary performed during the dispersive readout of a superconducting qubit in cQED
$U_{\text{JPC}}$	Unitary performed by a JPC
$U$	Unitary operation
$X, Y, Z$	Pauli operators or matrices for a single qubit
$\chi$	Dispersive shift between a qubit and readout cavity
$\chi_{ij}$	Generalized dispersive shift between the modes $i$ and $j$
$\chi_{qq}$	Transmon qubit anharmonicity
$\Delta_i$	Detuning from mode $i$
$\eta$	Quantum measurement efficiency
$ G\rangle ( E\rangle)$	Measurement outcome for finding the qubit in $ g\rangle ( e\rangle)$
$\Gamma$	Decay rate
$\Gamma_m$	Measurement induced dephasing rate

$\bar{I}_m, \bar{Q}_m$	Average values of $I_m$ and $Q_m$ for a distribution of measurement outcomes
$\kappa$	Cavity/Resonator bandwidth
$ E^\pm\rangle = \frac{1}{\sqrt{2}}( gg\rangle \pm  ee\rangle)$	Even Bell state of two stationary qubits
$ e^\pm\rangle = \frac{1}{\sqrt{2}}( gg\rangle \pm  ee\rangle)$	Even Bell state of two flying qubits
$ i\rangle$	Fock state of photon number $i$
$ O^\pm\rangle = \frac{1}{\sqrt{2}}( ge\rangle \pm  eg\rangle)$	Odd Bell state of two stationary qubits
$ o^\pm\rangle = \frac{1}{\sqrt{2}}( ge\rangle \pm  eg\rangle)$	Odd Bell state of two flying qubits
$\langle i \rangle$	Average value of $i$
$\langle i \rangle_c$	Conditional average value of $i$
$\mathcal{E}(\rho)$	Quantum operation
$\mathcal{C}$	Concurrence
$\mathcal{F}$	Fidelity
$\mathcal{F}_{\text{det}}$	Single photon detector readout fidelity
$\mathcal{F}_d$	Remote entanglement fidelity limited by dark counts
$\mathcal{F}_{\text{joint}}$	Joint readout fidelity of two qubits
$\mathcal{N}$	Normalization constant for a density matrix or wave function
$\bar{n}$	Average photon number, typically in a microwave pulse or a cavity
$\nu$	Measurement outcome
$\omega$	Angular frequency
$\omega_c$	Cavity resonance frequency

$\omega_q$	Qubit frequency
$\omega_{ef}$	Qubit excited to second excited state transition frequency
$\omega_{ge}$	Qubit ground to excited state transition frequency
$\omega_{ij}$	Transition frequency between the $i$ and $j$ states of a qubit-cavity system
$\Omega_R$	Rabi oscillation frequency
$\Phi$	Magnetic flux
$\Pi_{\nu_i}$	Projector onto the outcome $\nu_i$
$\psi$	Wave function
$\rho$	Density matrix
$\sigma$	Standard deviation of a Gaussian distribution or a Gaussian pulse
$\sigma_I, \sigma_Q$	Variance of a coherent state along the I and Q axis
$\sigma_m$	Variance of a coherent state when efficiently measured by a phase-preserving amplifier
Tr	Trace of a matrix
Tr <sub><math>i</math></sub>	Partial trace of a matrix over the subsystem $i$
$\tilde{a}, \tilde{a}^\dagger$	Displaced mode operators
$\varphi$	Phase across a circuit element or mode
$\xi$	Pump amplitude
$A$	Attenuation (in dB)
$a_{out}^{(g)}(t), a_{out}^{(e)}(t)$	Cavity output field for qubit in the ground, excited state

$a_{I,out}(t), a_{Q,out}(t)$	I and Q components of the cavity output field
$A_{ji}$	Probability matrix that the state $i$ is recorded as outcome $j$
$B$	Bandwidth
$E_0, E_1$	Operation elements of a quantum operation
$E_C$	Charging energy
$E_J$	Josephson energy
$f = \frac{\omega}{2\pi}$	Frequency
$G$	Power gain (typically in dB)
$g_3$	Three-wave mixing coupling strength
$g_{2ph}$	Two-photon coupling strength
$I$	Current
$I(\rho_{AB})$	Mutual information of a two-qubit density matrix $\rho_{AB}$
$I_0$	Critical current of a Josephson junction
$I_m, Q_m$	I and Q components of a measurement outcome for a demodulated microwave signal
$n$	Photon number
$n_{th}$	Thermal photon number
$P$	Power
$p$	Participation ratio
$P_{click}$	Probability of getting a click on a single photon detector
$P_d$	Probability of a dark count event on a single photon detector

$Q$	Quality factor
$R_i^j(\theta)$	Single qubit rotation around the $i$ -axis on the $j^{\text{th}}$ transition by an angle $\theta$
$S(\rho)$	von Neumann entropy of the density matrix $\rho$
$T$	Temperature
$T_N$	Amplifier noise temperature
$T_Q = \hbar\omega/2k_B$	Quantum noise temperature
$T_\phi$	Qubit dephasing time
$T_1$	Qubit relaxation time
$T_{2\text{Bell}}$	Bell state Hahn-echo decoherence time
$T_{2\text{E}}$	Qubit Hahn-echo decoherence time
$T_{2\text{R}}$	Qubit Ramsey decoherence time
$T_m$	Measurement time
$T_{\text{rep}}$	Protocol or sequence repetition time
$T_{\text{SB}}$	Sideband pulse length
$T_{\text{seq}}$	Protocol or sequence time
$V$	Voltage
$W(t)$	Demodulation envelope
$W_I(t)$	I-component of demodulation envelope
$W_Q(t)$	Q-component of demodulation envelope
$X, Y, Z$	Bloch vector components for a single qubit

I, Q

In-phase and quadrature components of a microwave signal

# Acknowledgments

This journey to a Ph.D has sometimes been described as a solitary one. My experience has been anything but. I have had the pleasure of working with and learning from amazing people and the love and camaraderie of great friends and family.

First and foremost, to my advisor Michel Devoret, thank you for the opportunity to work with you. I could not have asked for a better advisor to guide me through the past few years or a better lab environment in which to work. Your insight and passion for physics has been nothing short of inspiring and infectious. Through the many discussions with you, I have learned so much about how to not only analyze problems and perform experiments but also how to communicate and practice science (and so much beyond).

I would like to thank the other members of my thesis committee, Rob Schoelkopf and Liang Jiang, who have also been instrumental in my getting here. Your questions and comments especially during presentations were invaluable in guiding the direction of this research. More, your ideas for new experiments and contagious excitement have again and again stoked my interest in the field.

I am very grateful to all the support and advice from Dan Prober over the last six years. I would also like to thank you, Larry Wilen, and Konrad Kaczmarek for the opportunities you gave me to help teach your classes; they were an excellent experience that made me a better teacher.

I am indebted to Luigi Frunzio for teaching me the dark arts of fabrication and for all the help with the various administrative, logistics and scientific tasks throughout the PhD. Conversations with you were always fun and I really do hate to disappoint you by graduating so far ahead of schedule.

For most of my PhD, I had the propitious opportunity to closely work with three people, Michael Hatridge, Shyam Shankar, and Katrina Sliwa. I am very grateful to all three of them for being so patient with my endless stream of questions and teaching me to be a more independent researcher. Thank you Michael for first taking me under your wing and teaching me so much of what I know about experimental physics and research, especially how to not do it wrong. I owe a lot of my research work ethic to your tutelage, which is best captured by your many memorable catchphrases. Shyam, I have learned so much from your methodical and patient approach to problem solving; no problem feels intractable when working with you.

To Chris Axline and Kevin Chou, my fellow members of the applied plumbing team, this endeavor, consecrated in the waters of Becton, would have been unbearably harder without you. Thank you for all your help, both on the good days where we got to plumb microwaves and even some quantum information, but even more on those hellish weekend mornings and late nights where we dealt with whatever the building, facilities, and fridges threw at us. To the next generation of people taking over the reins, I only hope that we left everything in better shape than we found it.

I am also deeply grateful to Nick Dent who taught me a lot about cryogenics and without whom troubleshooting the myriad problems we faced on that front would have been impossible. I am furthermore grateful to Vinnie Bernardo who was crucial to the success of the many design and machining projects that we embarked on. Navigating Yale would not have been possible without the always reassuring and smiling help of Giselle DeVito, Maria Rao, Terri Evangeliste, and Nuch Graves.

To all the graduate students and postdocs that I have had the pleasure to work with and become friends with over the years, especially Alex Grimm, Andrei Petrenko, Brian Lester, Brian Vlastakis, Evan Zalys-Geller, Faustin Carter, Flavius Schackhert, Gail, Gerhard Kirchmair, Gijs de Lange, Ioan Pop, Jacob Blumoff, Kurtis Geerlings, Kyle Serniak, Luke Burkhart, Nick Frattini, Phil Reinhold, Shantanu Mundadha, Steven Touzard, Teresa Brecht, Uri Vool, Wolfgang Pfaff, Yiwen Chu, Yvonne Gao, and Zaki Leghtas, thank you for making the 4<sup>th</sup> floor of Becton the special place it is. Your amazing ideas, intelligence, dedication, friendship, and snark made the

last six years the most productive, educational and fun of my life.

I am also very thankful to my friends outside of lab, some of whom I have known for many years and others whom I met at Yale - Angela Steinauer, Andrew Sinclair, Brian Tennyson, Eric Jin, Greg Hutchings, Julie Sinclair, Marcus Wong, Michael Chang, Michelle Hutchings, Min Kim, Thoe Michaelos, and Val Morley. All of you helped make the last few years a lot more fun and exciting, especially during the many rough patches, and I am very happy for all the adventures we have had together. I only hope that there are many more in store.

Finally, to Amma, Nanna and Aashray, who have always believed in me and supported me, all I can say is that I would not be here without you.



# Introduction and Overview

The only 'failure' of quantum theory is its inability to provide a natural framework for our prejudices about the workings of the Universe

---

Wojciech Zurek

## 1.1 Introduction

The phenomenal impact that quantum mechanics has had on science and technology is perhaps best exemplified by its almost commonplace use in the day-to-day lexicon (abstruse phrases like 'quantum leap' aside). This in spite of, or maybe due to, that, when first encountered in introductory classes or textbooks, the ideas of quantum mechanics can be fairly peculiar because they lie in stark contrast to how we think about the classical systems that have shaped our intuitions of the world. Unlike classical systems, when quantum systems are measured, not all the observables can have deterministic outcomes [26, 49]. This is because the measurement of some observable of the system is not a passive process that reveals to an observer some already determined information about the system like in classical mechanics; instead the act of measurement causes the system to be steered into the state associated with the outcome of the measurement. In other words, it is not "what you see is what you get" but "what you get *is* what

you see". What is more, quantum objects can exhibit properties completely alien to the classical world like entanglement where even distant objects can exhibit correlated behavior. It seems hardly surprising that quantum theory has inspired everything from confusion to amazement to disbelief. Debates of the nature of reality notwithstanding, quantum mechanics is one of the most successful theories in physics, accurately describing nature at a microscopic level with astounding accuracy for the last century.

Beyond providing the framework for a number of physical theories and playing an integral role in a wide range of current technologies, quantum physics is also a driver of many future technologies. Exploiting the properties of superposition and entanglement, potential applications envisioned and at the focus of active research range from long-distance secure communication to entanglement enhanced sensing to quantum computation. It is the last of these that is the primary motivator for the work in this thesis. Since Richard Feynman originally proposed the idea in 1982 [41], the field of quantum computing has progressed steadily until over the last decade or two where progress seems to have accelerated to the present where industry is now getting invested in the realization of a quantum computer. These advances signify the increasing adeptness with which we can control, manipulate and measure quantum systems in laboratory settings, ideas that even years ago seemed entirely in the realm of theory. Thus, leaving a more general history of quantum physics and quantum computations as well as perspectives on its future to more accomplished experts capable of more illuminating writing, here we cite only one quote that conveys the excitement that technologies based on quantum mechanics inspire: "It's a magical world, Hobbes ol' biddy. Let's go exploring!" - Calvin, *Calvin and Hobbes*.

In this thesis, we will begin by exploring the importance of quantum measurements especially in the context of quantum information in Ch. 1. After a brief introduction to the experimental systems used in this thesis in Ch. 2, we proceed to discuss how to implement and optimize single-qubit measurements in Ch. 3, highlighting the benchmarks for measurements that are important in quantum information applications. Increasing the complexity of the experiments, we then use these single-qubit measurements as a building block for generating entanglement between remote qubits in two different ways in Ch. 4 and Ch. 5. Finally, based on the experimental results in this

thesis, we discuss interesting and critical next steps and future prospects for quantum information with superconducting in Ch. 6. The first chapter, Ch. 1, summarizes all the important results in the same order of the chapters with more details about the experiments, theory and analyses provided in the corresponding chapters.

## 1.2 Unpacking Quantum Measurements

The seemingly simple postulates of quantum mechanics that are encountered during an introduction to the subject belie its amazing complexity and subtlety, an exemplar of which is the process of quantum measurement. While only one of many postulates that describe the behavior of quantum systems, we specifically consider the postulate about quantum measurement, since measurement is a central focus of this thesis. Physically measurable properties about the system as associated with observables  $\mathcal{O}$ , a Hermitian operator acting on the Hilbert space of the system. The possible outcomes of this measurement are the eigenvalues  $\nu_i$  of the operator  $\mathcal{O}$ . Thus, the observable can be spectrally decomposed into  $\mathcal{O} = \sum_i \nu_i \Pi_{\nu_i}$  where  $\Pi_{\nu_i}$  is the projector onto the eigenvector of  $\mathcal{O}$  associated with the eigenvalue  $\nu_i$ . The probability of any outcome is given by  $P_{\nu_i} = \langle \psi | \Pi_{\nu_i} | \psi \rangle$  and the result of measuring the outcome  $\nu_i$  is to project the quantum system to the (eigen)state  $\Pi_{\nu_i} | \psi \rangle / \sqrt{P_{\nu_i}}$  [26, 99]. Thus, this process is appropriately referred to as a projective measurement.

Consider, for a concrete and relevant example, a qubit in the state  $\psi = \alpha |g\rangle + \beta |e\rangle$  where  $|\alpha|^2 + |\beta|^2 = 1$ . One commonly measured observable of such a qubit is  $Z$  which has the measurement outcomes  $-1$  and  $+1$  associated with the eigenvectors  $|g\rangle$  and  $|e\rangle$  respectively. Thus, measuring  $Z$  for this qubit results in the outcome  $-1$  with probability  $|\alpha|^2$  and the outcome  $+1$  with probability  $|\beta|^2$  [99]. This process of measuring any observable of a qubit is usually depicted by the symbol for a meter when discussed in the context of quantum information circuits (see Fig. 1.1A). However, this description only provides a mathematical prescription for understanding the results of a measurement and does not elucidate how the physical process of measuring a quantum system actually occurs.

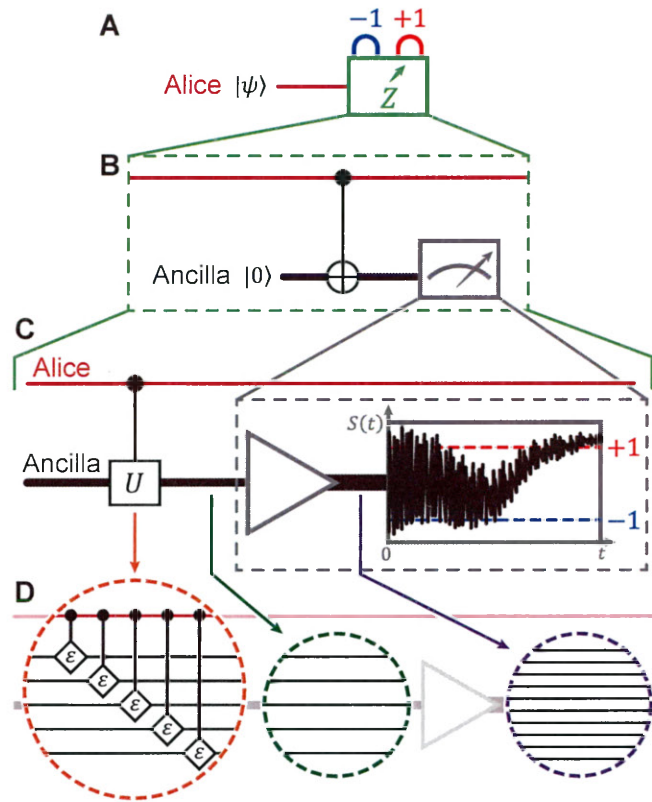


**Figure 1.1 | Unpacking A Quantum Measurement.** A) Quantum circuit symbol for the measurement of a qubit. The measurement of a qubit is often depicted using the symbol for a meter. Here, the observable  $Z$  of the Alice qubit is measured resulting in a measurement outcome  $\nu$  of either  $+1$  or  $-1$ . B) Quantum circuit for a non-demolition measurement. The non-destructive measurement of a quantum system usually consists of two steps: first, the system to be measured, Alice (red), is entangled (for example with a CNOT gate as shown) with an ancilla (black) that can be used as a pointer variable. The measurement is then completed by measuring the state of the ancilla. Common pointer variables are systems with Hilbert spaces larger than a qubit (indicated by the relative thickness of the red and black lines). C) Quantum circuit for the measurement of the ancilla. However, even this more refined picture of a quantum measurement still does not capture the usual case of the measurement producing a continuous classical signal that is recorded by the experimental apparatus. The measurement of the ancilla after it is entangled with the qubit crucially relies on amplification. When amplified, the ancilla is converted from a discrete signal into a continuous signal that can be recorded by a classical measurement apparatus. By integrating this signal over time, an observer can recover a discrete measurement outcome of the measurement by thresholding the acquired signal. D) The larger Hilbert space ancilla can be equivalently understood as a train of two-level systems weakly interacting with the qubit, each accumulating a small phase shift  $\epsilon$  (orange inset). Under amplification, the size of the ancilla Hilbert space increases (green to purple inset), as the distance in phase-space between the pointer variable states associated with the measurement outcome increases, converting the quantum signal to a classical one.

In practice, it is often not possible to directly measure an observable of a quantum system without destroying the quantum system of interest. Instead as shown in Fig. 1.1B, to perform a non-demolition measurement, i.e QND, the quantum system, called Alice, is typically probed with some other system, referred to as an ancilla. The ancilla, also known as a pointer variable or degree of freedom, is some quantum system, that will not only interact with Alice at some time, but also has some property that can be measured by a laboratory measurement apparatus. While this ancilla, or pointer variable, can be another qubit, it is typically a system with a larger Hilbert space (indicated by the thicker line in Fig. 1.1), thus having the possibility to undergo amplification. Additionally, since the ancilla must be able to interact with both Alice and a measurement apparatus, it is usually a traveling, or flying, degree of freedom (which is why it is also sometimes referred to as a flying qubit). The interaction between the quantum system of interest and the ancilla is engineered so that the observable to be measured,  $O$ , is mapped onto some property of the ancilla. As a result of this interaction, Alice and the ancilla become entangled; in the language of quantum circuits, this is often represented, for example, by a CNOT gate between the two objects. To complete the measurement, the property of the ancilla entangled with Alice is measured, thus projecting Alice to the eigenstate associated with the measured eigenvalue of  $O$ .

Considering specifically the experimental systems used for quantum information, these measurements rely on the interactions between matter and light. In many systems, qubits are typically encoded in matter, like the state of an atom, ion or spin, and are measured using ancillae encoded in states of electromagnetic radiation, ranging from microwave to optical frequencies. For example, the state of a ancilla may be encoded in orthogonal states such as the absence or presence of photons, like the fluorescence based readout of trapped ion qubits [95] and nitrogen-vacancy center qubits [119], or encoded in the amplitude and phase of an electromagnetic field, like the dispersive readout of a superconducting transmon qubit [140]. On the other hand, qubits that are encoded in a state of light and ancillae based on matter are also used, for example in the field of linear optics [72] or Rydberg atoms [85].

However, even this more physical description of a QND projective measurement does not

address how a quantum signal encoded in the ancilla, which is by definition discrete, is actually measured by a measurement apparatus that can only detect classical signals, which are continuous. The key to this transition between the quantum and classical domains is amplification. As the ancilla degree of freedom undergoes amplification, the distance in phase-space between the orthogonal states of the ancilla increases. Thus, where the state of the qubit was encoded, for example, in ancilla states differing by a single photon or by a phase shift of  $\pi$  between small coherent state (containing a few photons), after amplification, the orthogonal states of the ancilla become classically distinguishable as the orthogonal states, for example, now differ by a very large number of photons or a phase shift of  $\pi$  between large coherent states. As this distance between the orthogonal states increases, the signal becomes insensitive to small perturbations and also continuous.

Shown as a quantum circuit in in Fig. 1.1C, the measurement process begins as in Fig. 1.1B, with an operation between Alice and the ancilla, represented here as a general unitary gate  $U$ . This gate maps the observable of Alice of interest onto some property of the ancilla by entangling the two systems. At this stage, the ancilla is still a quantum state even though it is a system with a larger, and often infinite, Hilbert space as shown in Fig. 1.1C. The gate between Alice and the ancilla is effectively a transduction of information from one quantum system to another to enable a QND measurement of the former.

In fact, the large Hilbert space ancilla can be equivalently thought of as a chain of two-level systems (or spins), each weakly interacting with Alice as illustrated in the orange inset in Fig. 1.1D. This interaction maps the observable of Alice being measured  $O$  onto the polarization of the spins. Formally, the pointer variable in this picture is sum of the polarizations, along the  $Z$ -axis for example, of each of the individual two-level systems and is scaled by the number of spins that interacted with Alice,  $N(t)$ , over the measurement time  $t$ :  $\langle \sum_{n=1}^{N(t)} S_Z^n \rangle / N(t)$ . Here,  $n$  is the index for the spins, and  $S_Z^n$  is the polarization of each spin. As the measurement time  $t$  increases, so too does the number of spins that interact with Alice, thus increasing the strength of the measurement. As a result, the noise in the measurement record,  $S'(t)$ , decreases and the signal-to-noise ratio (SNR) grows.

Next, the ancilla is amplified, indicated by the increasing thickness of the line after the amplifier in Fig. 1.1C. In the interacting spin picture, amplification results in the number of spins entangled with Alice increasing as shown by the green and purple insets in Fig. 1.1D; since the number of spins increases, so too does the size of the pointer variable in phase-space. As a result of this amplification, the small quantum signal is mapped onto a large classical signal that is eventually recorded by the experimenter's apparatus. However, when measured, this large classical signal is now continuous and no longer discrete. To recover the discrete bit of quantum information that it encodes, the classical signal is integrated as function of time until the accumulated signal crosses some experimentally determined threshold which informs the observer about the result of the measurement. Therefore, it is this thresholding process that retrieves a discrete, i.e. quantized result, from an otherwise continuous classical signal. Furthermore, the overall gain of the amplification chain determines the distinguishability of the measurement outcomes and actually sets the strength of the measurement. Indeed, as we discuss below and later in Ch. 2.4 and Ch. 3.9, the projective measurements discussed above are only a limit of the variable-strength, or weak, measurements actually performed in experiments.

To illustrate this more concretely, we consider two examples. The first is the fluorescence based measurement of a matter qubit, like a trapped ion; here, the state of Alice, the trapped ion qubit, is mapped onto the presence or absence of a photon, the ancilla. This photon is typically measured using a photomultiplier which converts that single excitation into an electrical current that can be monitored to infer a photon detection event (called a "click"). The emitted photon is first converted to an electron, effectively a second transduction process changing the ancilla from a photon to an electron. Then, this quantum signal is amplified, mapping the single electron onto many many electrons that result in an effectively classical current. Thus, (ideally) when no current is measured, it corresponds to no photon being detected, whereas when a current is measured, it indicated the detection of a photon. As a second example focusing on the experimental systems of this thesis, consider the case of a superconducting qubit, Alice, measured by microwave frequency coherent states, the ancilla. The state of the qubit is mapped onto the amplitude and phase of the coherent state; since the coherent state has a larger Hilbert space

than the qubit, this already represents a first stage of amplification. The coherent state is then further amplified through many stages of amplification (see Ch. 2.3) mapping the qubit state onto increasingly larger coherent states. Finally, the amplitude and phase of this now classical coherent state are measured and thresholded to discretize the information and determine the measurement outcome (see Ch. 2.4).

Thus amplification is a central part of a quantum measurement chain, and the details of this amplification process crucially determines the properties of the measurement process. Consequently, the understanding and careful engineering of these measurements are imperative to successful experiments with quantum systems, and are one of the focuses of this thesis. In fact, a more general, and useful, description of quantum measurements is to think of a quantum measurement as a particular type of general quantum operation [99], as discussed in more detail in Ch. 3. In this paradigm, measurements are but another way of manipulating quantum systems that also provide an observer some information about the system. Indeed, by engineering quantum measurements to gain information about carefully chosen observables of a quantum system, it is possible to employ measurements to implement a wider range of operations than just learning about the state of a qubit. This is of especially great utility in the domain of quantum information. As a particularly relevant example for this thesis, a quantum operation engineered to measure only the parity and phase of a two-qubit system can be used to generate entanglement, a crucial quantum resource.

### 1.3 Quantum Measurements in Quantum Information

It is not surprising then that quantum measurements are an invaluable part of the quantum operation toolbox used in any quantum information or communication system. Perhaps their most direct use is at the end of any quantum information algorithm to determine the result of the computation, as outlined in DiVincenzo's requirements for a quantum computer [34]. This involves measuring the state of some subset of the qubits involved in the algorithm to determine the outcome of the computation. However, since quantum measurements are actually

a type of general quantum operations that reveal to an observer information about a specific observable of the system, they have immense utility beyond informing an observer about the outcome of a computation. For example, they can be used to satisfy another of the DiVincenzo requirements for a quantum computer, qubit state initialization [82, 118]. They also form the basis for quantum error correction (QEC), where by qubits can be logically encoded in a system and protected against certain forms of errors [4, 43, 88, 127, 134]. Here, quantum measurements are engineered to monitor only the errors associated with a quantum system instead of learning any information about the computational state [28, 29, 30, 68, 101, 113, 117]. Finally, since they depend on traveling ancillae, quantum measurements can also be used to mediate interactions and information transfer between distant quantum systems; in particular, they can be used to generate remote entanglement, an essential primitive for quantum communication [7, 38, 70] and modular architectures for quantum computing [65, 93].

To these ends, there are three crucial properties that these measurements should satisfy; the first two are a direct consequence of their use at the end of a quantum computation [34] while the last is an addition, resulting of their use in operations like feedback and QEC [33]: one, they should have high fidelity; second they should be quantum non-demolition (QND) measurements; third, they should be efficient.

Requiring that the measurements have fidelity ensures that the measurement is accurate, faithfully reporting the state of a qubit, for example, to the observer without errors, i.e the probability of reporting the outcome  $|g\rangle$  when the qubit was actually in  $|e\rangle$  and vice-versa. The second requirement ensures that the measurement process leaves the qubit in the state associated with the measurement outcome, i.e measuring the qubit in  $|g\rangle$  results in the qubit ending up in  $|g\rangle$  after the measurement is completed. This can be otherwise understood as the probability that a second measurement of the qubit state will result in an identical outcome to the first, i.e the probability that the outcome  $|g\rangle$  is measured again in this case. Finally, the efficiency of a quantum measurement is a measure of the fraction of information about the system being measured that is gained by the observer to that lost to other uncontrolled or unmonitored channels. The efficiency crucially determines the speed of the measurement making it essential in

protocols where controls need to be applied on the system based on the measurement outcome. Moreover, when such measurements are used to mediate non-local interactions, any loss of information suffered by the ancillae is detrimental to the overall operation.

Therefore, engineering single qubit measurements for high-fidelity, QND-ness, and efficiency is a crucial and an important first step towards quantum computation. Results for implementing these measurements with the dispersive readout for transmon qubits are further discussed in Ch. 3 and summarized below in Sec. 1.5.

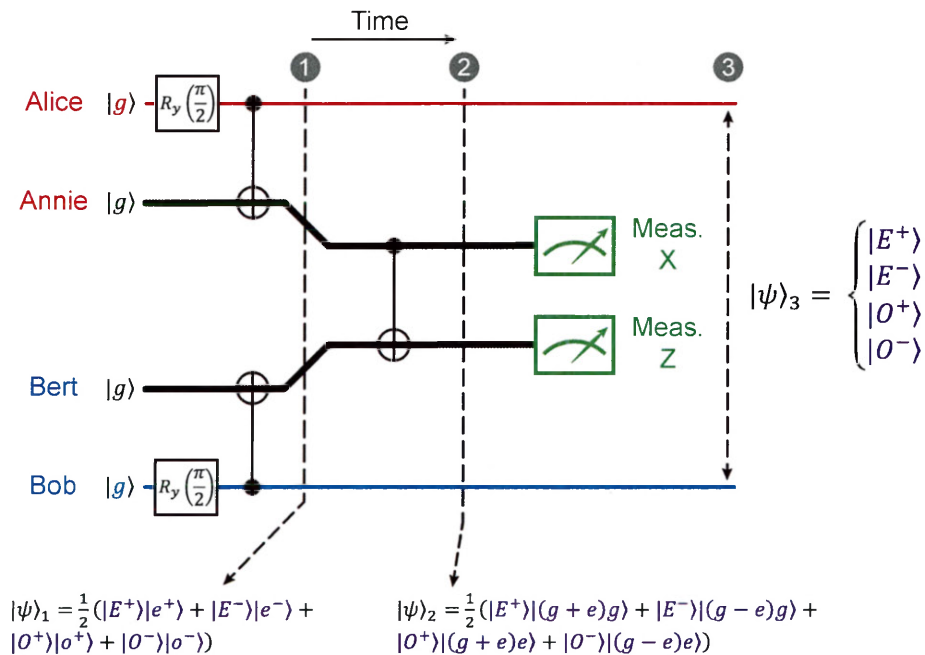


Figure 1.2 | **Protocol Schematic for Concurrent Remote Entanglement Generation.** Remote entanglement between two isolated, stationary qubits, Alice and Bob, can be generated by first entangling them with two flying ancillary qubits, Annie and Bert. A CNOT operation is performed with the stationary qubits as the controls and the traveling qubits as the targets, resulting in the state  $|\psi\rangle_1 = \frac{1}{2}(|E^+\rangle|e^+\rangle + |E^-\rangle|e^-\rangle + |O^+\rangle|o^+\rangle + |O^-\rangle|o^-\rangle)$ . Next, a CNOT between the two flying qubits is performed before finally measuring the state of the two flying qubits, one in the  $X$  basis and the other in the  $Z$  basis. The outcomes of these two measurements inform the observer of the phase and parity respectively of the generated two-qubit Bell state. Since no information directly travels from Alice to Bob and instead only to detectors in a third location, this protocol is a concurrent one.

An operation of particular interest is the generation of remote entanglement, for example a two-qubit Bell state. This is a precious operation because it is a primitive for many applications.

Fundamentally, the remote two-qubit entangled states are invaluable for Bell tests of quantum mechanics [47, 54, 126]. Such Bell states can be used for quantum teleportation and thus for the basis for long-distance quantum communication [70] and quantum repeaters [64]. Using them as a resource in non-local gates [65] makes them essential for modular architectures of quantum computing [33, 93], a promising approach towards realizing a universal quantum computer. It is this last application that makes remote entanglement generation a focus of this thesis.

Considering the specific case of two qubits, remote entanglement can be generated by implementing measurements that measure only the joint parity and phase, a general schematic of which is shown in Fig. 1.2<sup>1</sup>. Here, Alice and Bob are two distant stationary qubits that cannot directly interact with each other. Entanglement between Alice and Bob is instead generated by the measurement of two flying ancilla qubits, Annie and Bert, that first interact with the stationary qubits. Starting with all four qubits in  $|g\rangle$ , Alice and Bob are first rotated to the state  $\frac{1}{\sqrt{2}}(|g\rangle + |e\rangle)$  with a  $R_y(\pi/2)$  pulse on each qubit. Then, Alice and Annie and Bob and Bert are entangled with each other using CNOT gates, with the stationary qubits as the controls and the flying qubits as the targets. The joint state of the four qubits at this stage can be expressed in the Bell state basis as  $|\psi\rangle_1 = \frac{1}{2}(|E^+\rangle|(g+e)g\rangle + |E^-\rangle|(g-e)g\rangle + |O^+\rangle|(g+e)e\rangle + |O^-\rangle|(g-e)e\rangle)$ . All four possible Bell states of Alice and Bob are mapped onto the corresponding Bell state of the flying qubits, Annie and Bert. Next, a CNOT gate is performed between Annie and Bert resulting in the state  $|\psi\rangle_2 = \frac{1}{2}(|E^+\rangle|e^+\rangle + |E^-\rangle|e^-\rangle + |O^+\rangle|o^+\rangle + |O^-\rangle|o^-\rangle)$ . Thus, the parity along  $Z$  (i.e.  $ZZ$ ) of Alice and Bob has been mapped onto the state of Bert in the  $Z$  basis, and the parity along  $X$  (i.e.  $XX$ ) of the two has been mapped onto the state of Annie in the  $X$  basis. Consequently, the entanglement generation is completed by measuring Annie in the  $X$  basis and Bert in the  $Z$  basis; the outcomes  $Z = +1$  ( $Z = -1$ ) indicate a state of odd (even) parity and  $X = +1$  ( $X = -1$ ) indicate a state of positive (negative) phase.

An equivalent but alternative way to understand this process is to cast it in terms of the effective measurement of Alice and Bob that is being performed. Since the measurements of Annie and Bert reveal the phase and parity of the two stationary qubits, this protocol realizes a

<sup>1</sup>While particular implementations of the outlined protocol can vary, the figure provides a general prescription for how to construct a measurement that generates remote entanglement

measurement of  $XX$  and  $ZZ$  for the two qubits. Since the measurements only ever interrogate joint properties of the two qubit, no single qubit information is learned resulting in the outcome being an entangled state with no single qubit information. Even though Annie and Bert are initially only entangled with Alice and Bob respectively, the CNOT gate between the flying qubits and subsequent measurement erase the observer's ability to determine single qubit information from Annie or Bert, instead allowing only joint properties to be measured. Consequently, such measurements are also described as performing which-path information erasure.

This measurement picture is particularly elucidating because it highlights that as long as these joint measurements of a two-qubit system can be implemented, remote entanglement can be generated regardless of the physical realizations of the stationary and flying qubits. Indeed, as discussed later in this chapter and this thesis, possible choices for the flying qubits include coherent states of microwave radiation (see Sec. 1.6 and Ch. 4) or Fock states of microwave radiation (see Sec. 1.7 and Ch. 5). While the choices of flying qubits have their advantages and disadvantages (ease of implementation for coherent states versus robustness to loss for Fock states), they also determine how the CNOT gates and measurements of the flying qubits are implemented.

It is important to mention at this stage that measurement based remote entanglement between two qubits can be generated in ways other than the concurrent protocol shown in Fig. 1.2. These protocols involve either directly sending a quantum state between Alice and Bob to generate entanglement [25], or using a common pointer variable that sequentially visits both systems before being measured [121]. Unlike concurrent protocols, these sequential or direct protocols rely on a direct communication channel for information transfer between the systems being entangled. As a result, these protocols need to be carefully designed to minimize any undesirable residual interactions between the systems that may arise from the presence of a direct channel; concurrent protocols, on the other hand, achieve this by virtue of their construction.

The use of this concurrent remote entanglement as a resource in operations that process information between distant quantum objects, for example quantum state teleportation for quantum repeaters [7] or non-local gates between modules of a modular architecture for quantum comput-

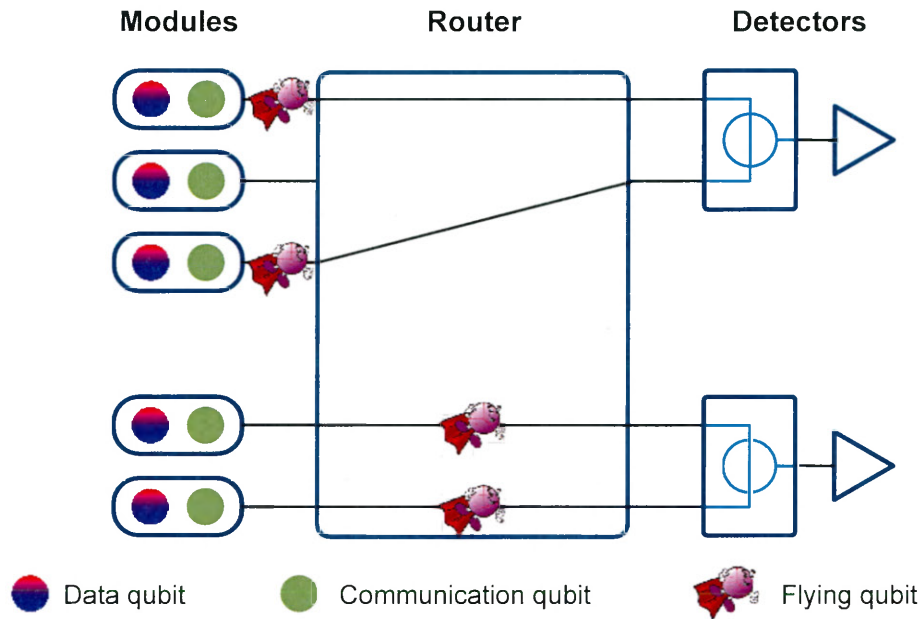


Figure 1.3 | **A Modular Architecture for Quantum Computing.** The three primary components required for a modular architecture for a quantum computer are: modules; a switchable, programmable router; and a measurement apparatus. Each module consists of at least a data qubit and a communication qubit. The data qubit is a high-coherence, likely error-corrected, quantum system that stores the quantum state of interest and is the object on which operations need to be performed to execute the desired algorithm. These data qubits are placed in separate modules to prevent undesired parasitic interactions that can limit coherence. To enable operations between these otherwise isolated data qubits, communication qubits that can interact with the environment outside the module are also used. Remote operations between data qubits are performed by using remote entanglement between communication qubits as a resource. This remote entanglement is generated by entangling the communication qubits with flying qubits which are then routed through the programmable router and jointly measured to generate heralded entanglement.

ing [24, 36, 65], necessitates that the entanglement generation algorithm of Fig. 1.2 must satisfy a number of requirements. To better understand these requirements, let us take the specific case of using remote entanglement in modular quantum computation systems which is of particular interest for the field of superconducting qubits [33].

A schematic for a modular architecture for quantum computation, shown in Fig. 1.3, illustrates the primary components that are required: isolated modules that contain a high-coherence qubit (the data qubit) used in the quantum algorithm and that interact with the environment only

through a communication qubit (green) that can be entangled with flying qubits (in purple with capes); a switchable router that enables arbitrary modules to be connected; a measurement apparatus for state initialization, remote entanglement generation, error correction etc. The, likely error-corrected, data qubits are placed in individual modules to ensure that they can be well controlled and also isolated from undesirable decoherence channels. Moreover, borrowing from the modular approaches used to build some of the first classical computers when modern computers were still in their nascency, this architecture has a number of attractive features. Its design allows for the individual testing and optimization of the various components by remaining somewhat agnostic to the physical form of its constituent elements. This is especially powerful for the current stage of quantum information systems which are still error prone and cannot be manufactured with the levels of reliability possible for the billions of transistors on modern computer chips.

Thus, while isolating the qubits in individual modules prevents spurious interactions, it comes with the disadvantage of introducing more potentially lossy elements and interconnects between objects on which operations need to be performed. To perform operations between these otherwise isolated data qubits, remote entangled states of the communication bits, generated using the protocol outlined in Fig. 1.2, in two modules are used as a resource to implement non-local gates. Because data qubits in individual modules can only interact through this resource, this enables a very high on-off ratio in this architecture that ensures that data qubits only interact by design while minimizing spurious unwanted interactions. As a concrete example for a remote operation in this architecture, the quantum circuit for a CNOT gate between two data qubits in two modules (red and blue) is shown in Fig. 1.4. Together with the single qubit operations that can be performed on the data qubits in each module, the remote CNOT gates and the ability to transmit classical information between modules in the form of conditional rotations (see Fig. 1.4) form a universal operation set required for quantum computation [99].

As a resource consumed to perform non-local gates, the quality of the entangled state, characterized by its fidelity  $\mathcal{F}$ , is crucial since it determines the ultimate fidelity of the two-qubit gate that is performed. Thus, this forms the first of the requirements that we require of the

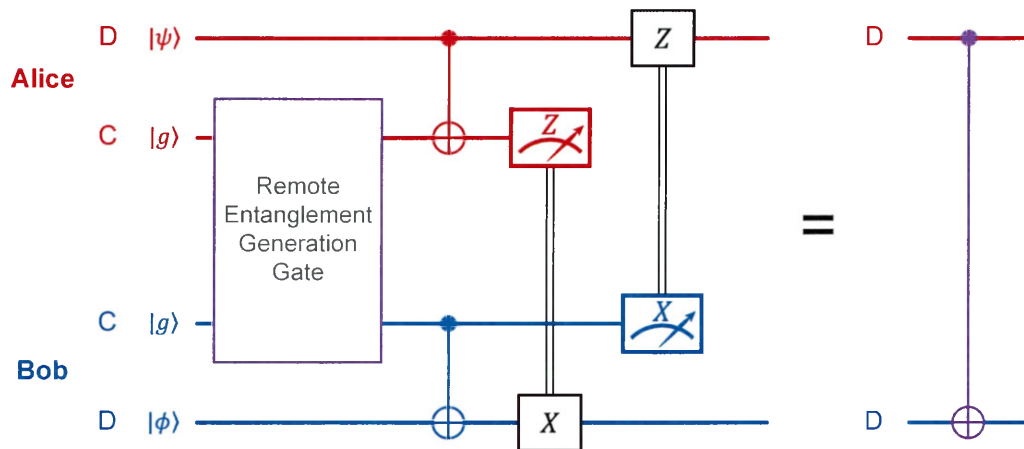


Figure 1.4 | **Quantum Circuit for a Remote CNOT Gate between Modules.** A) Circuit for a remote CNOT gate between modules. Using an entangled state between the communication qubits of two modules as a resource, a CNOT between the two data qubits in the modules can be implemented using only local operations and classical communication between the modules. First, two local CNOT gates are performed as shown between the data and communication qubits in each module. This is followed by a measurement of the communication bit in the first module (red) in the  $Z$  basis. An  $X$  gate, conditioned on the measurement outcome, is performed on the data qubit of the second module (blue). Then, the operation is completed with a measurement of the communication bit in the second module in the  $X$  basis and performing a conditional  $Z$  gate on the data qubit in the first module.

remote entanglement operation: the generated entangled state should be a high-fidelity state [7, 65, 93, 97]. Moreover, since the flying qubits used in the entanglement generation have to traverse inevitably lossy components and interconnects like the router, it is preferable to make the entanglement generation protocol robust to these losses (as demonstrated by the single-photon based remote entanglement protocol described in Fig. 1.11).

Another important requirement is the entanglement generation rate. Like the requirement that data qubit coherence times must greatly exceed the single-qubit gate times for high-fidelity gates [34], the generation rate must greatly exceed the decoherence and relaxation times of the data qubits to enable multiple gates to be performed before the information stored in these qubits is lost. Furthermore, since the entanglement resource is consumed and needs to be constantly regenerated for each operation, it is also essential to make the generation rate as high as possible to prevent undesirable latency for performing other gates. This speed requirement is further

exacerbated when entanglement distillation, the process of generating a high-fidelity entangled state probabilistically from many copies of lower-fidelity entangled states [7], is used (see Sec. 1.8 and Ch. 6).

## 1.4 Superconducting Qubits and circuit-QED - A Platform for Quantum Information

A number of different physical platforms exist for experimental realizations of quantum computing and communication, ranging from systems based on ions, neutral atoms, defects in solid state systems, quantum dots or electrical circuits to name but a few. In this thesis, the platform of concern is based on quantum electrical circuits fabricated from superconductors. Otherwise called superconducting quantum circuits, or superconducting qubits, they offer a promising approach to realizing a quantum computer since they offer the advantages (and disadvantages) of being highly-engineerable systems that can be constructed from very low-dissipation materials using the micro-fabrication techniques developed by the semiconductor industry [33]. In these circuits, quantum information is usually encoded in a degree of freedom of the electrical circuit like the charge, flux or phase to realize a qubit. Measurements are performed by using microwave radiation as ancillae with the state of the qubit mapped onto the amplitude or phase of the ancillary microwave state. Developed over the last decade or two, the building blocks for superconducting quantum circuits have improved in almost every performance metric by orders of magnitude. While research to build even better qubits and further improve readout techniques continues, the current building blocks are of sufficient robustness to form an almost common toolbox for quantum information based on superconducting quantum circuits. Complex systems consisting of many connected quantum objects have been built that are exploring new frontiers in quantum information like quantum error correction, fault tolerant quantum computing, and scaling to larger systems.

In this vein, the focus of this thesis will be on how to realize efficient measurements and remote entanglement generation using some of the standard toolbox of superconducting quantum

circuits, without describing the tools themselves in detail (for which many excellent references already exist). The key components used in the systems we describe in the following sections and chapters are the stationary qubit, the flying qubit and our meter, or measurement apparatus.

The stationary qubit of choice in this work is the transmon qubit. Further described in Fig. 2.1 and Ch. 2.2, the transmon qubit is an anharmonic LC-oscillator built by shunting a Josephson junction, effectively a non-linear inductor, by a capacitor [74]. Unlike a harmonic oscillator which has equally spaced energy levels, an anharmonic oscillator has incommensurately spaced energy levels. The lowest two energy levels, called the ground state  $|g\rangle$  and excited state  $|e\rangle$ , can be selectively driven to form an effective two-level qubit system. The frequency of this transition is typically engineered to be between  $\omega_{ge}/2\pi = 4$  to 10 GHz with the frequency of transitions to successively higher excitation states,  $|f\rangle$  and beyond, changing by the anharmonicity  $\chi_{qq}/2\pi \sim -200$  MHz.

To both enable control and readout of the qubit as well as control over its environment, the qubit is capacitively coupled to a microwave resonator in the circuit-QED paradigm [142], an analog to Cavity Quantum Electrodynamics (QED) where microwave circuits replace both the cavities (microwave or optical) and atoms [50]. In particular, for the work in this thesis, the microwave resonator is a three-dimensional microwave cavity, thus realizing what is called a 3D transmon qubit-cavity system (represented schematically in red in Fig. 1.5) [103]. In our experiments, the qubit is coupled to the  $\text{TE}_{101}$  mode of a rectangular cavity, typically chosen to be around  $\omega_c/2\pi = 7$  to 10 GHz. As a result of the coupling between the two, the cavity inherits a qubit-state dependent frequency shift (and vice versa), otherwise known as the dispersive shift  $\chi/2\pi = 0.1$  to 10 MHz. Thus, measurement of the qubit state, i.e readout, can be performed by interrogating the state of the cavity which is most commonly done using coherent state of microwave radiation. As shown in Fig. 1.5, pulses of microwave interacting with the qubit-cavity system are the ancilla (or pointer variable or flying qubit). The traveling microwave pulse acquires a qubit-state dependent amplitude and phase shift, thus entangling it with the state of the qubit. Amplifying and measuring the phase and amplitude of the microwave pulse informs the observer about the state of the qubit.

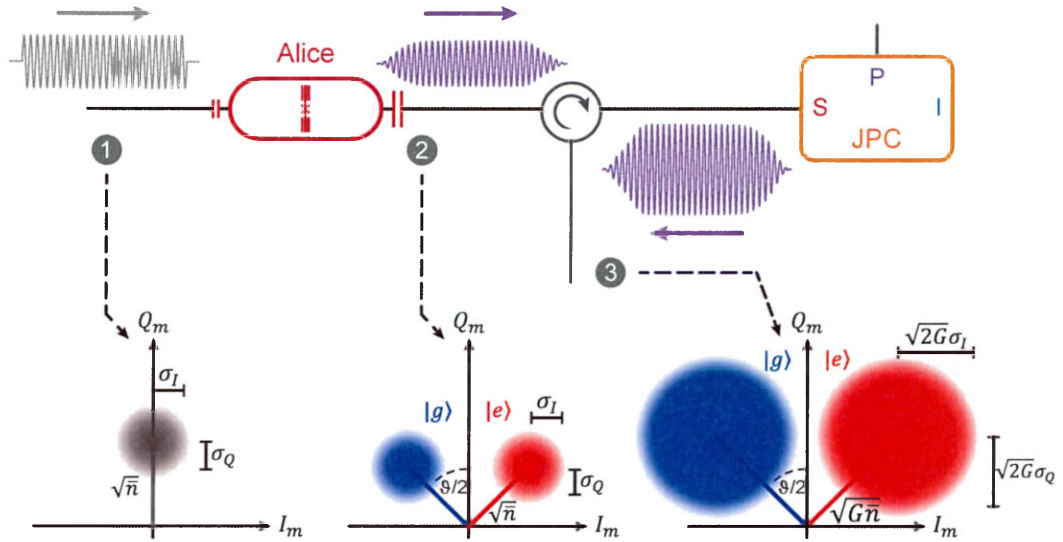


Figure 1.5 | **Schematic for Readout of a 3D Transmon Qubit.** Top: A schematic depiction of the readout of a superconducting qubit in the 3D circuit-QED architecture. The 3D qubit-cavity system is connected to one of the modes (here the signal) of a JPC via microwave circulators to enforce directionality and separate incoming and outgoing signals. A coherent state  $|\alpha\rangle$ , the traveling pointer variable of choice in this paradigm, incident on the cavity acquires a phase and amplitude response that is dependent on the state of the qubit. At the output of the cavity, the state of the qubit-flying coherent state system is represented by  $|\psi\rangle = \frac{1}{\sqrt{2}}(|g\rangle|\alpha_g\rangle + |e\rangle|\alpha_e\rangle)$ . The pointer state is then amplified by the JPC, before further amplification and demodulation by room-temperature electronics. Bottom: A representation of the pointer state in  $IQ$ -space. The initial coherent state  $|\alpha\rangle$ , shown as a Gaussian state with standard deviation  $\sigma_I = \sigma_Q = 1/2$  displaced from the origin by the average photon number  $\bar{n}$  in the state, acquires a qubit-state dependent amplitude and phase shift. Here, the state of the qubit,  $|g\rangle$  or  $|e\rangle$ , is encoded in the phase of the output coherent state,  $-\vartheta/2$  or  $+\vartheta/2$  respectively. Upon amplification by the JPC for  $G \gg 1$ , the size of the pointer variable coherent state increases to an average photon number of  $G\bar{n}$  with standard deviations  $\sqrt{G}\sqrt{2}\sigma_I$  and  $\sqrt{G}\sqrt{2}\sigma_Q$ .

A convenient representation for the coherent states used to measure the qubit is in the in-phase (I) and quadrature (Q) phase-space representation shown in the bottom of Fig. 1.5. In  $IQ$ -space, a coherent state  $|\alpha\rangle$  can be visualized as a two-dimensional Gaussian distribution where the standard deviation  $\sigma$  indicates noise in that state and the distance from the center of the distribution to the origin indicates the square root of the time-averaged photon number in the pulse  $\sqrt{\bar{n}}$  with  $\bar{n} = |\alpha|^2$ . The Gaussian distribution for these coherent states have standard deviation  $\sigma_I = \sigma_Q = 1/2$  corresponding to the half-photon of quantum noise on the states.

After interacting with the qubit-cavity system, the state of the qubit is encoded in the traveling coherent state as shown in the bottom center of Fig. 1.5. The output coherent state acquires an amplitude and  $+\vartheta/2$  ( $+\vartheta/2$ ) phase shift for the qubit being in  $|g\rangle$  ( $|e\rangle$ ). Thus, the joint stationary qubit and flying qubit state can be represented as  $|\psi\rangle = \frac{1}{\sqrt{2}}(|g\rangle|\alpha_g\rangle + |e\rangle|\alpha_e\rangle)$ . The measurement process is thus completed by using room-temperature electronics (not shown) to demodulate the microwave pulse and measure its phase and amplitude.

Since the traveling signal experiences inescapable losses and other imperfections in its journey to the measurement apparatus, something that is further exacerbated by all the experiments being housed at the base stage of a dilution refrigerator ( $T < 20$  mK), quantum-limited amplification plays a central role in enabling high-efficiency, high-fidelity measurements [131]. By amplifying the coherent state pointer variables used for readout while adding close to the minimum amount of noise allowed by quantum mechanics [20], these parametric amplifiers [8, 19, 84, 138] improve the overall signal-to-noise ratio (SNR) of the readout signal by about an order of magnitude over the conventional high-electron mobility (HEMT) based cryogenic and room-temperature amplifiers that they typically precede.

In the experiments in this thesis, the amplifier of choice is the Josephson Parametric Converter (JPC) [8, 9] operated as a phase-preserving amplifier. Further described in Ch. 2.3, the JPC is a two-mode, called signal and idler with frequencies  $\omega_S$  and  $\omega_I$  respectively, non-degenerate,  $\omega_S \neq \omega_I$ , reflection amplifier that amplifies by three-wave mixing when a pump tone at  $\omega_P = \omega_S + \omega_I$  is applied. The device is engineered with  $\omega_S/2\pi, \omega_I/2\pi = 5$  to 10 GHz with the frequency of the signal or idler mode chosen and tuned by an externally applied DC flux to match the resonance frequency of the cavity to which it is connected. The power of the applied pump is chosen to yield a power gain of  $G = 20$  dB. Thus, as shown in Fig. 1.5, the output coherent states have an increased average photon number of  $G\bar{n}$  and also a standard deviation increased by a factor  $\sqrt{G}$ .

## 1.5 Efficient Single Qubit Measurements

Having established both a road map towards a quantum computing device as well as the experimental toolbox at our disposal, we now demonstrate the ability to satisfy the requirements needed for measurements in these systems, beginning with high-fidelity and high-efficiency, QND measurements of single qubits and the underlying quantum operation performed in the 3D cQED architecture. Although the experimental system (described in detail in Fig. 4.1) consists of two superconducting 3D transmon qubits connected to the signal and idler ports of a JPC, the qubit-cavity system connected to the signal port of the JPC was not energized, and hence can be ignored. Qubit measurements were performed by applying a readout microwave pulse at the cavity frequency to encode the state of the qubit onto the phase of the output pulse, as shown in Fig. 1.5. The measurement pulse was shaped to minimize the ring-up and ring-down time (for details, see Fig. 3.2 and Ch. 3.6) of the cavity; the measured signal was demodulated using an envelope  $W(t)$  whose shape was calculated from the difference in the averaged cavity response when the qubit was prepared in  $|g\rangle$  and  $|e\rangle$  (for details, see Fig. 3.3 and Ch. 3.7).

First, we characterize the fidelity of the single-qubit measurement using a protocol outlined in Fig. 1.6A (the detailed pulse sequence is shown in Fig. 3.4A). At the beginning of the protocol, the state of the qubit is scrambled with a measurement pulse followed by a  $R_y^{ge}(\pi/2)$  to initialize the qubit in an equal superposition state of  $|g\rangle$  and  $|e\rangle$ . This has the advantage of erasing the history of the qubit and allowing the experiment to be repeated at  $T_{\text{rep}} = 20 \mu\text{s}$ , much faster than the relaxation time of the qubit  $T_1 = 70 \mu\text{s}$ . A first measurement for qubit state preparation, labeled  $M_1$  in Fig. 1.6A, is performed; a linear-scale (left in Fig. 1.6B) histogram and a logarithmic-scale (right in Fig. 1.6B) histogram of the measurement outcomes confirm that the states  $|g\rangle$  and  $|e\rangle$  are equally probable with small contamination from  $|f\rangle$  and higher states. Only trials where the qubit was measured to be in  $|g\rangle$ , determined by the circular threshold shown in blue, are retained by post-selection. The qubit is then rotated to  $|e\rangle$  with a  $R_y^{ge}(\pi)$  pulse or left in  $|g\rangle$  by applying no pulse (performing  $Id$ ). Finally, a second measurement, labeled  $M_2$  in Fig. 1.6A, is performed to confirm the state of the qubit after preparation. Histograms of the measurement outcomes

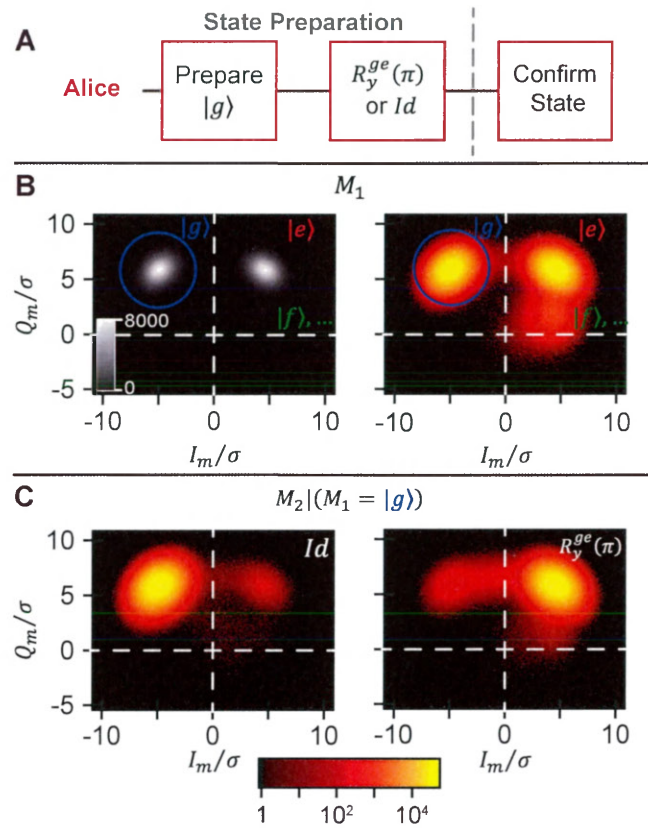


Figure 1.6 | **Single Qubit Measurement.** A) Schematic pulse sequence to prepare and confirm the state of a single qubit. B) Histograms of the first measurement on a linear (left) and logarithmic (right) scale. The measurement of the qubit state after the scrambling pulse confirms that it is in the equal superposition state  $1/\sqrt{2}(|g\rangle + |e\rangle)$  indicated by the equal brightness of the blobs associated with the measurement outcome  $|g\rangle$  or  $|e\rangle$ . The same data shown on a logarithmic scale (right) reveals some contamination of  $|f\rangle$  and other higher states in the initial qubit state. Only those experiments where the qubit was found in  $|g\rangle$  (blue circle) are retained by post-selection. C) Histograms of the second measurement conditioned on the outcome of the first measurement  $M_1 = |g\rangle$ . The outcome of the second measurement confirms that the application of the  $Id$  ( $R_y^{ge}(\pi)$ ) pulse prepares the qubit in  $|g\rangle$  ( $|e\rangle$ ) with fidelity  $\mathcal{F} = 0.993$ .

for applying the  $Id$  pulse (left) and the  $R_y^{ge}(\pi)$  pulse (right) are shown in Fig. 1.6C.

From this protocol, a blind fidelity of  $\mathcal{F} = 0.993$  was calculated; this fidelity, which also includes state preparation, errors, is the fraction of times that the measurement outcome ( $|G\rangle$  or  $|E\rangle$ ) agreed with the state that the qubit was prepared in ( $|g\rangle$  or  $|e\rangle$ ):

$$\mathcal{F}_{\text{blind}} = \frac{1}{2} [P(|G\rangle | |g\rangle) + P(|E\rangle | |e\rangle)] = 1 - \frac{1}{2} [P(|G\rangle | |e\rangle) - P(|E\rangle | |g\rangle)] \quad (1.1)$$

Moreover, we can also estimate the QND-ness of the measurement from this data. Looking at the case where the  $Id$  pulse was applied, we find that the probability that the second measurement confirms that the qubit is again found in  $|g\rangle$  is  $P(|G\rangle | |g\rangle) = 0.9985$  implying that the measurement of  $|g\rangle$  is highly QND. On the other hand, from the other case of applying a  $R_y^{ge}(\pi)$  pulse, the probability of the second measurement finding the qubit in  $|e\rangle$  was  $P(|E\rangle | |e\rangle) = 0.994$ , implying that the measurement of  $|e\rangle$  is less QND. Indeed, one of the primary limitations of both the fidelity and the QND-ness of the measurements is the reduction in the qubit  $T_1$  that occurs when the cavity is populated with photons, resulting in the observed asymmetry between  $P(|G\rangle | |g\rangle)$  and  $P(|E\rangle | |e\rangle)$ . Unfortunately, this effect, while often observed, still eludes a theoretical explanation and will need to be addressed to improvement single-qubit measurements to fidelities beyond  $\mathcal{F} > 0.999$ . A more detailed discussion of the error budget along with some prospects for improvements is presented in Ch. 3.8.

We now proceed to characterize the efficiency of the single-qubit measurement by treating it as a quantum operation and analyzing the back-action of the measurement on the qubit state. The theory behind the measurement operator formalism is outlined further in Ch. 2.4 based on the detailed theoretical analysis derived in [51]. To analyze the back-action of a measurement, we modify the pulse sequence of Fig. 1.6A by adding a variable-strength measurement and performing full single-qubit state tomography as outlined in Fig. 1.7A (for a detailed pulse sequence, see Fig. 3.5A). As before, the qubit state is first scrambled with a  $R_x^{ge}(\pi/2)$  pulse and measured to post-select on outcomes where the qubit start in  $|g\rangle$ . The qubit is then rotated to  $Y = +1$  ( $1/\sqrt{2}(|g\rangle + i|e\rangle)$ ) with a  $R_x^{ge}(\pi/2)$  pulse. Then, a variable-strength measurement is performed on the qubit by applying a measurement pulse whose amplitude is swept resulting in a measurement outcome  $(I_m/\sigma, Q_m/\sigma)$ ; the strength of the measurement  $\bar{I}_m/\sigma$  is characterized by the distance of the measurement outcome distributions from the origin  $\bar{I}_m$  scaled by the standard deviation of the distribution  $\sigma$  and is swept from  $\bar{I}_m/\sigma = 0$  to 2.35. Finally, the back-action of this variable-strength measurement on the qubit state is determined by using one of three qubit rotation pulses,  $R_y^{ge}(\pi/2)$ ,  $R_x^{ge}(-\pi/2)$  or  $Id$ , to measure the  $X$ ,  $Y$ , and  $Z$  components respectively of the qubit Bloch vector.

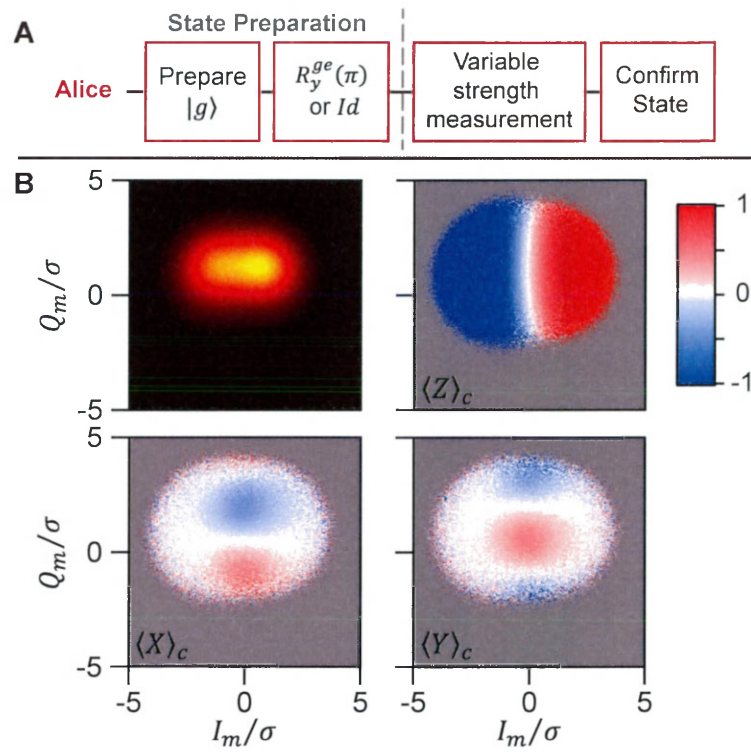


Figure 1.7 | **Single Qubit Measurement Tomograms.** A) Schematic pulse sequence to measure the measurement efficiency  $\eta$  using the back-action of a variable-strength measurement. B) Histograms and conditional tomograms of the final qubit state after a weak measurement. Outcomes are shown for a variable measurement of strength  $\bar{I}_m/\sigma = 1.0$ . The histogram shows the probability of a given outcome  $(I_m/\sigma, Q_m/\sigma)$ ; the conditional tomograms plot the average  $X$ ,  $Y$ , and  $Z$  Bloch vector components extracted from the tomography measurement on a color scale between  $+1$  (red) and  $-1$  (blue) for each outcome  $(I_m/\sigma, Q_m/\sigma)$  of the variable-strength measurement.

Shown in Fig. 1.7B are a histogram (top left) of the experimentally obtained measurement outcomes  $(I_m/\sigma, Q_m/\sigma)$  and tomograms,  $\langle Z \rangle_c$  (top right),  $\langle X \rangle_c$  (bottom left), and  $\langle Y \rangle_c$  (bottom right), of the corresponding Bloch vector components for each measurement outcome for a moderate strength measurement of  $\bar{I}_m/\sigma = 1.0$  (similar data for weaker and stronger measurement strengths are shown in Fig. 3.5; here, only the data for  $\bar{I}_m/\sigma = 1.0$  is shown for brevity since it highlights all the salient features of the measurement operation). For measurement outcomes with large non-zero values of  $I_m/\sigma$ , the back-action looks like the strong projective measurement of a qubit obtained in Fig. 1.6 with the final qubit state being  $|g\rangle$  ( $|e\rangle$ ) for  $I_m/\sigma \ll 0$  ( $I_m/\sigma \gg 0$ ) indicated by  $\langle Z \rangle_c \sim -1$  ( $\langle Z \rangle_c \sim +1$ ). However, for measurement outcomes where

$I_m/\sigma = 0$ , the back-action does not look like a projective measurement. Indeed, that  $\langle Z \rangle_c = 0$  indicates that the qubit remains on the equator of the Bloch sphere and is not driven to the  $|g\rangle$  or  $|e\rangle$  measurement eigenstates. Instead, the back-action of the measurement is to stochastically rotate the qubit around the equator of the Bloch sphere; while the measurement outcome itself is unpredictable, it is perfectly correlated to the final qubit state demonstrating that the measurement is indeed a quantum operation. The observed oscillations in  $\langle X \rangle_c$  and  $\langle Y \rangle_c$ , with  $\langle Z \rangle_c = 0$ , around  $Q_m/\sigma \sim 0$  are due to these stochastic kicks to the qubit.

Since the quantum operation associated with a measurement outcome  $Q_m/\sigma = 0$  is a stochastic rotation of the qubit around the equator, any information about the qubit state lost to unrecorded information channels will impede the observer's ability to track the final qubit state, thus decreasing the Bloch vector amplitude from measurement-induced dephasing [51] (for more details, see Ch. 2.4). Thus, the measured Bloch vector amplitude for  $I_m/\sigma = 0$  provides for determining the measurement efficiency,  $\eta$ . From the equations for the final qubit Bloch vector components as a function of the measurement outcome (see Ref. [51] and Ch. 2.4), the equatorial Bloch vector components for a measurement of outcome  $I_m = 0$  are:

$$\langle X \rangle_c (I_m = 0) = \sin \left( \frac{Q_m \bar{I}_m}{\sigma} + \theta \right) e^{-\left(\frac{\bar{I}_m}{\sigma}\right)^2 \frac{1-\eta}{\eta}} e^{-\frac{T_{\text{seq}}}{T_{2R}}} \quad (1.2)$$

$$\langle Y \rangle_c (I_m = 0) = \cos \left( \frac{Q_m \bar{I}_m}{\sigma} + \theta \right) e^{-\left(\frac{\bar{I}_m}{\sigma}\right)^2 \frac{1-\eta}{\eta}} e^{-\frac{T_{\text{seq}}}{T_{2R}}} \quad (1.3)$$

where  $\theta$  is a phase offset extracted from the fit,  $T_{\text{seq}}$  is the time between the initial  $R_x^{ge}(\pi/2)$  and tomography pulses, and  $T_{2R}$  is the Ramsey dephasing time of the qubit. Thus, the  $Q_m/\sigma$  outcome effectively encodes the phase of the back-action on the qubit state; note that the frequency of these stochastic oscillations increases with the measurement strength  $\bar{I}_m/\sigma$ . Since the fits also provides an estimate of  $\bar{I}_m/\sigma$  from the frequency of the oscillations independent of that obtained from the histograms, this method for extracting  $\eta$  is self-calibrating. Taking a vertical slice of the data from  $\langle X \rangle_c$  and  $\langle Y \rangle_c$  in Fig. 1.7 for outcomes within  $|\bar{I}_m/\sigma| < 0.26$  and averaging over the  $I_m/\sigma$  values, the data shown in Fig. 1.8A was obtained (orange and green

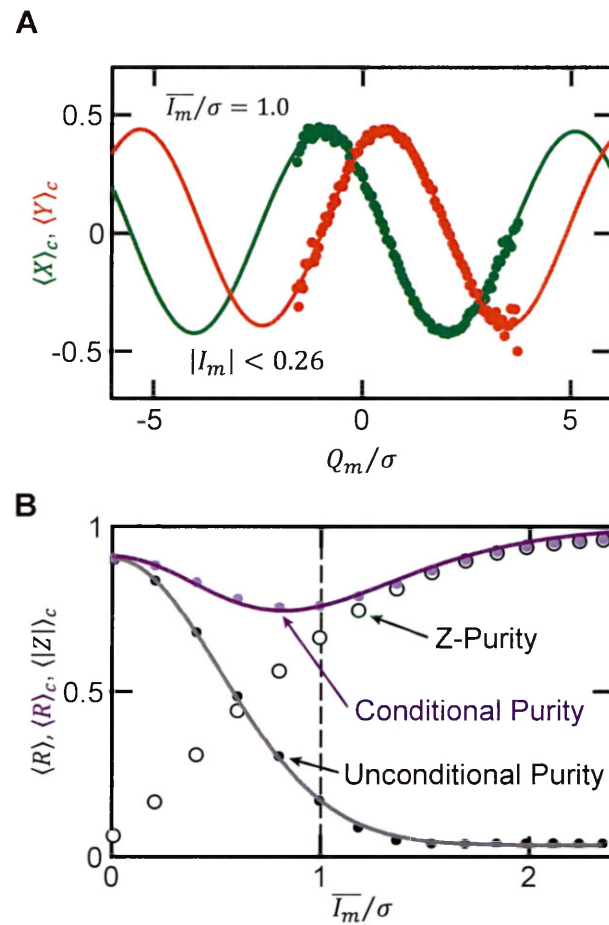


Figure 1.8 | **Single Qubit Measurement Efficiency.** A) Slices of  $\langle X \rangle_c$  and  $\langle Y \rangle_c$  along the  $Q_m/\sigma$  axis for  $\bar{I}_m/\sigma = 1.0$ . Conditional tomography results,  $\langle X \rangle_c$  and  $\langle Y \rangle_c$  within  $|I_m/\sigma| < 0.26$  are averaged and plotted versus  $Q_m/\sigma$  revealing that the final qubit state is along the equator for these measurement outcomes. The data are shown in points with fits to the data in solid lines. From the fits, a measurement efficiency of  $\eta = 0.56 \pm 0.01$  was extracted. B) Unconditional (black points), conditional (purple points) and Z-component (black circles) of the final Bloch vector after a variable-strength measurement. The Z-component of the final Bloch vector (called the Z-purity) as well as the magnitude of the final Bloch vector when the middle measurement is recorded (the conditional purity) or not recorded (the unconditional purity) are plotted as a function of  $\bar{I}_m/\sigma$ . As the strength of the measurement increases, so too does its projectiveness characterized by the Z-purity approaching unity. When the middle measurement is not recorded, the final qubit state looks completely scrambled and the Bloch vector magnitude goes to zero. On the other hand, when the middle measurement is recorded, the final Bloch vector component remains close to unity with a drop resulting from the imperfect measurement efficiency. Fits to the data, shown in solid lines, yield a value of the  $\eta = 0.54 \pm 0.01$ .

point). From fits to the data (orange and green solid lines), we extract that  $\eta = 0.56 \pm 0.01$  and confirm  $\bar{I}_m/\sigma = 1.0$ .

As yet another way of extracting the measurement efficiency from this data, beyond looking at a single measurement strength, we can look at the back-action for different  $\bar{I}_m/\sigma$ . As shown in Fig. 1.8B, for each measurement strength, we calculate the magnitude of the Bloch vector, for both the cases where the middle measurement is recorded ( $\langle R \rangle_c$  in purple points) and ignored (i.e averaged over) ( $\langle R \rangle$  in black circles), and the  $Z$ -component of the Bloch vector ( $\langle |Z| \rangle_c$  in black points). Again, we see that as we increase the measurement strength,  $\langle |Z| \rangle_c$  increases, approaching one; this demonstrates that our finite-strength measurement becomes a textbook projective measurement in the limit of large measurement strength by effectively purifying the qubit Bloch vector by projecting it to the poles of the Bloch sphere corresponding to the eigenstates of the measurement. Similarly, when we record the measurement outcome and correlated qubit state, the final qubit Bloch vector amplitude remains close to unity, corresponding to a close to pure qubit state. Loss of information about the state of the qubit results in the magnitude of the Bloch vector decreasing as the qubit state becomes less pure, shown by the dip in  $\langle R \rangle_c$  for moderate measurement strength. As a result, when we look at the final qubit state unconditioned on the outcome of the variable-strength measurement, the qubit quickly dephases as a result of the loss of qubit state information. From fits of  $\langle R \rangle$  to  $\exp[-(\bar{I}_m/\sigma)^2/\eta]$ , we extract  $\eta = 0.54 \pm 0.01$  in close agreement with the value measured from fits to  $\langle X \rangle_c$  and  $\langle Y \rangle_c$ .

While this quantum efficiency represents a significant improvement over the  $\eta \sim 0.2$  originally measured in [51], there is still room for significant improvement since only a little more than half the information about the qubit state actually makes it to the observer instead of being lost to other unrecorded information channels. The extracted overall measurement efficiency,  $\eta = \eta_{\text{base}}\eta_{\text{JPC}}\eta_{\text{out}}$ , is thus actually a result of information loss through a number of different channels: (1)  $\eta_{\text{base}}$  is the efficiency between the qubit-cavity system and the JPC; (2)  $\eta_{\text{JPC}}$  is the efficiency of the JPC amplifier itself; (3)  $\eta_{\text{out}}$  is the efficiency of the output electronics chain after the JPC. From an estimate of the insertion loss of the components between the qubit-cavity system and the JPC, we estimate  $\eta_{\text{base}} \sim 0.8$ . The internal quality factor of the JPC compared to its coupling-

determined linear bandwidth sets a limit of  $\eta_{\text{JPC}} \sim 0.9$  while a measure of the noise-visibility-ratio (NVR) also limits  $\eta_{\text{out}} \sim 0.9$ . Together, they limit us to  $\eta \sim 0.65$  in reasonable agreement to what we measure. We attribute the discrepancy between the two to other unaccounted for sources of information loss, for example, the spectral content of the pulses used to measure the qubit exceeding the bandwidth of the following JPC. An alternative experiment using a continuous-wave (CW) protocol to measure  $\eta$  is discussed in Ch. 3.10 where we also present prospects for improving the various sources of measurement efficiency.

Thus, while further improving all the aspects of the measurement, especially the measurement efficiency, is still an area of active research, the formalism of a understanding measurement as a generalized stochastic quantum operation is invaluable in quantifying the fidelity, QND-ness and efficiency of our single-qubit measurements. As we discuss further in Ch. 3, these techniques can be applied across qubit-cavity systems of very different bandwidths and dispersive shifts to implement measurements with  $\mathcal{F} > 0.99$  in every case, demonstrating that single-qubit measurements are of sufficiently quality to be a standard tool in the superconducting quantum circuit toolbox.

## 1.6 Coherent State Based Remote Entanglement Mediated by a JPC

Building on the single-qubit measurement operation, we now extend it to realize a which-path erasure joint measurement of two qubit to generate remote entanglement, another crucial step in our road-map. Implementing the protocol outlined in Fig. 1.2 requires two key elements: (1) the ability to entangle a stationary qubit with a flying qubit; (2) erasing the which-path information in the flying qubits by performing a measurement that only reveals joint information about the two qubit state, i.e parity and phase. A demonstration of the first requirement is the previously discussed quantum operation picture of a single-qubit measurement; the stationary qubit is the 3D transmon while the flying qubit is two different coherent states of microwave radiation with the entanglement between the two generated by the dispersive interaction. The second element,

performing a joint measurement on two coherent states to erase which-path information, can actually be performed with the very same JPC used for quantum-limited amplification of the flying qubits.

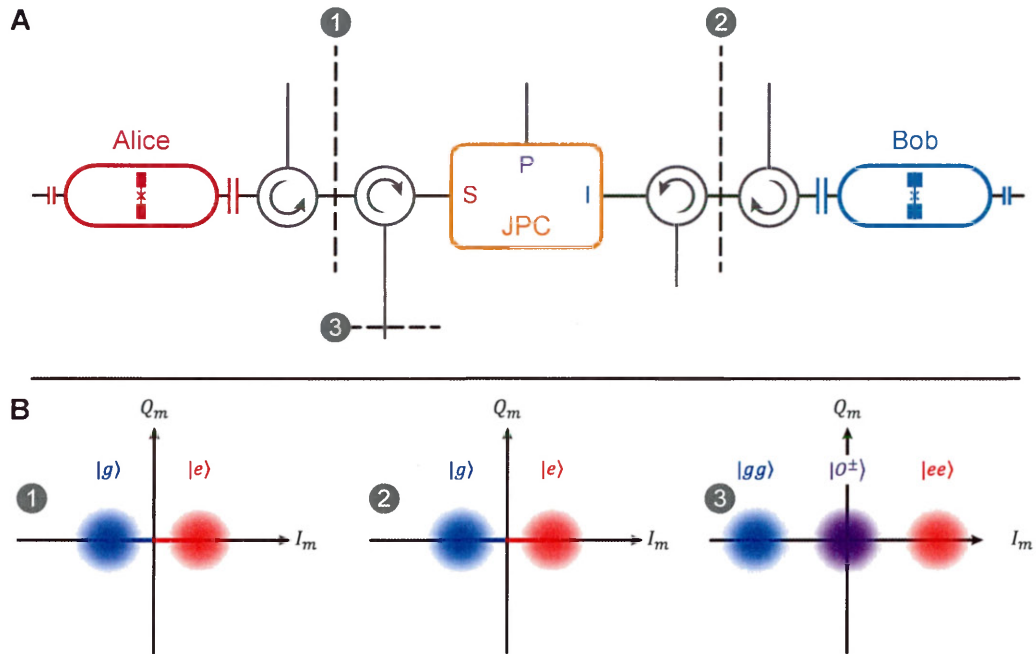


Figure 1.9 | **Coherent State based Remote Entanglement Protocol Schematic.** A) Schematic for the generation of remote entanglement by the operation of a JPC on flying coherent states. Two 3D superconducting qubit-cavity systems, Alice and Bob, are connected to the signal and idler ports of a JPC respectively. Coherent states incident on Alice and Bob are entangled with the state of a qubit by the dispersive qubit-cavity interaction in cQED. Subsequently, these states enter a JPC; the output state is a sum of the input states on the signal and idler modes. B) Representations of the flying coherent states in  $IQ$ -space. After interacting with the qubit-cavity system, the output coherent state is entangled with the state of the qubit, represented by the two states  $|\alpha_g\rangle$  or  $|\alpha_e\rangle$  for the  $|g\rangle$  and  $|e\rangle$  respectively. When incident on the JPC, the resulting output mode is the amplified sum of the input states. Consequently, if the two inputs on the signal and idler are identical, then the outcomes  $|gg\rangle$  and  $|ee\rangle$  result in large negative and positive values of  $I_m/\sigma$ . However, both the outcomes  $|ge\rangle$  and  $|eg\rangle$  are mapped onto same output state centered on the origin of the  $IQ$ -plane, and are hence indistinguishable. Thus, for measurement outcomes near the origin, the joint measurement operation performed by the JPC erases the which-path information and projects the two qubits to an odd Bell state.

As shown in Fig. 1.9A, the system consists of two 3D transmon qubit-cavity systems, Alice (red) and Bob (blue); their strongly coupled output ports are connected to the signal and idler ports respectively of a JPC through circulators that enforce directionality of incoming and

outgoing microwave signals (for a detailed experimental setup, see Fig. 4.1). The resonance frequencies and the bandwidths of the cavities were chosen so that the JPC provided gain on the signal and idler that was centered around the readout frequency. Furthermore, the JPC pump frequency was chosen to be the at the sum of the two frequencies at which readout pulses were applied to maintain phase stability between all three microwave tones (for details, see Ch. 4.3).

To generate remote entanglement, the Alice and Bob qubits, each starting in  $1/\sqrt{2}(|g\rangle + i|e\rangle)$ , are first entangled with flying qubits in the coherent state basis using the dispersive interaction of circuit-QED described in Ch. 1.5. Two microwave pulses, one each on the Alice and Bob system at their respective readout frequencies  $\omega_{A/B}^g - \chi/2$ , are applied to the weakly-coupled ports of the cavities to drive the systems in transmission (for more details, see Ch. 2.4). Each coherent state flying qubit acquires a qubit-state dependent phase shift resulting in the stationary-qubit flying-qubit entangled state  $1/\sqrt{2}(|g\rangle|\alpha_g\rangle + i|e\rangle|\alpha_e\rangle)$ . This entanglement between the stationary and flying qubits is represented in  $IQ$ -space in Fig. 1.9B (labeled 1 and 2 for Alice and Bob respectively). Here, the color of the Gaussian distribution represents the state of the stationary qubit (blue for  $|g\rangle$  and red for  $|e\rangle$ ) while the location of the distribution in  $IQ$ -space represents the state of the flying qubit ( $|\alpha_g\rangle$  on left and  $|\alpha_e\rangle$  on right in 1 and 2).

Subsequently, the flying coherent-state qubits enter the signal and idler ports of the JPC, which performs a joint which-path erasing measurement of the flying qubits [130]. As described further in Ch. 2.3, when operated as a phase-preserving amplifier in the high-gain limit, the output of the JPC (on both the signal and idler ports) is the amplified sum of the inputs on the signal and idler ports. To understand how this summation operation results in a joint which-path erasing measurement, it is convenient to look at the  $IQ$ -space representation of the stationary and flying qubits in Fig. 1.9B. The output of the JPC (labeled 3 in Fig. 1.9B) is just the vector sum of the two inputs (labeled 1 and 2). Thus, when both Alice and Bob are in  $|g\rangle$  ( $|e\rangle$ ) corresponding to a flying coherent state of negative (positive) displacement along the  $I_m$ -axis, the output is a coherent state of even larger negative (positive) displacement corresponding to the state  $|gg\rangle$  ( $|ee\rangle$ ) shown in blue (red). On the other hand, when one qubit is in  $|g\rangle$  and one is in  $|e\rangle$ , this summation produces an output coherent state centered at the origin (purple) regardless

of which qubit, Alice or Bob, is  $|g\rangle$  or  $|e\rangle$ . Thus, the measurement only informs the observer that the output state is one of odd parity; since the two even parity states  $|gg\rangle$  and  $|ee\rangle$  are not mapped to the same output, we call this operation a half-parity measurement. The measurement outcome  $I_m$  thus measures the observable  $ZI + IZ$  of the two qubits, projecting between an odd-parity manifolds or two even-parity computational states, hence realizing the operation of the  $Z$  measurement of the flying qubits in Fig. 1.2. Paralleling the quantum operation of a single-qubit measurement described in Ch. 1.5, the measurement outcome  $Q_m$  in this joint measurement scheme encodes the phase of the output state, analogous to the  $X$  measurement of the flying qubits in Fig. 1.2. From this  $Q_m$  measurement outcome, the observer learns about the phase of the generated odd-Bell state; since the Bell-state phase oscillates with  $Q_m$  (just like  $\langle X \rangle_c$  and  $\langle Y \rangle_c$  for a single-qubit oscillate with  $Q_m$ ), this phase measurement unfortunately also suffers from the same sensitivity to measurement efficiency that its single-qubit analog does where the frequency of the oscillations in the phase increases with the measurement strength. Consequently, while one would ideally (i.e. in the case of perfect efficiency) use a large measurement strength to separate the desired odd-state manifold from the even states, in practice (i.e. in the case of finite efficiency), the measurement strength needs to be chosen to balance the two requirements of projecting between parity states without destroying the phase information (for a more detailed discussion, see Ch. 4).

Therefore, this protocol uses the same tools already demonstrated with efficient single-qubit measurements to realize remote entanglement generation. However, the success of this protocol crucially depends on two elements: (1) the output coherent state of two inputs (Alice in  $|g\rangle$  and Bob in  $|e\rangle$  or vice versa) being indistinguishable from each other; (2) high efficiency on the Alice and Bob chains to minimize information loss. Successfully realizing the first requirement depends on making the signal and idler inputs to the JPC indistinguishable by matching the Alice and Bob side flying coherent-state qubits. Further discussed in Fig. 4.4 and Ch. 4.3, this was experimentally accomplished by tuning the relative phase and amplitudes of the pulses applied to Alice and Bob to make the amplitude displacement along  $I_m$  and the phase between  $|\alpha_g\rangle$  and  $|\alpha_e\rangle$  as similar as possible. We estimate that the distinguishability of the flying qubits is not a

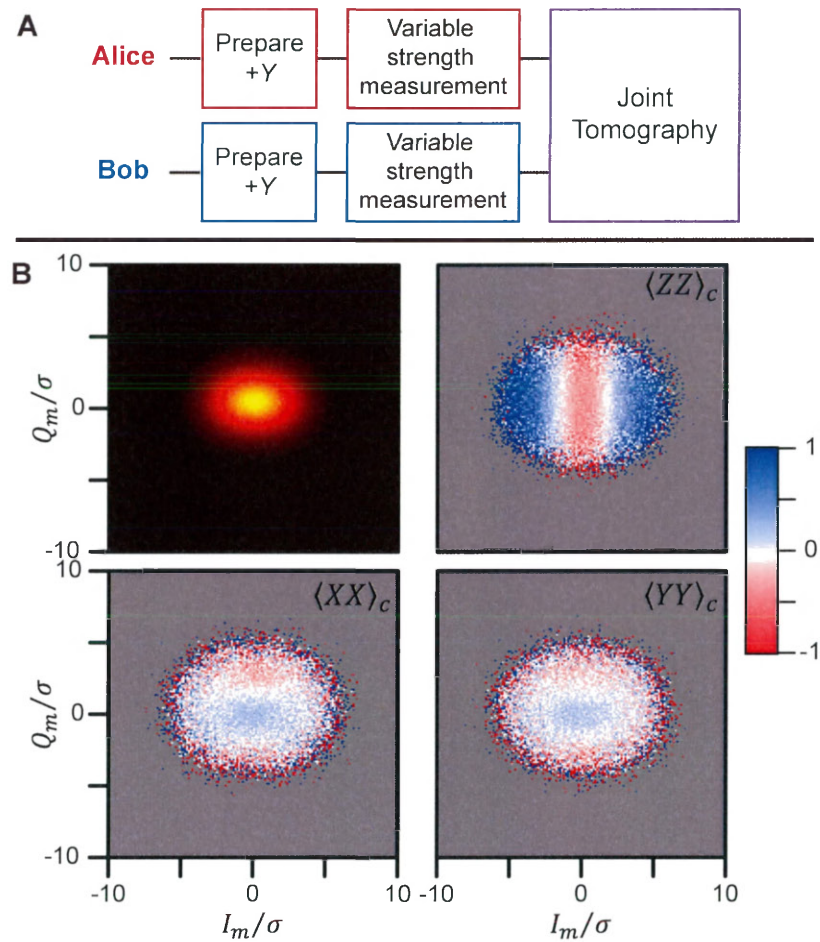


Figure 1.10 | **Coherent State based Remote Entanglement Tomography.** A) Schematic pulse sequence for generating remote entanglement by measurement with a JPC. B) Histogram and select conditional two-qubit density matrix components in the Pauli basis for an entangling measurement. The probability of measuring a particular outcome  $(I_m/\sigma, Q_m/\sigma)$  of the entangling measurement is shown by the histogram (top left). For each measurement outcome, the measured values of  $\langle XX \rangle_c$ ,  $\langle YY \rangle_c$ , and  $\langle ZZ \rangle_c$  extracted from full two-qubit tomography performed after the entangling measurement are shown in the three conditional tomograms.

major source of infidelity, only limiting the measured Bell-state fidelity to  $\mathcal{F} = 0.9$ . The second requirement is more challenging and, as we discuss later (and also in Ch. 4), is the most significant limitation to the fidelity achieved in the experiment. To exceed the entanglement threshold of  $\mathcal{F} > 0.5$ , the measurement efficiencies of the Alice and Bob systems must individually at least exceed  $\eta > 0.5$  for the case of qubits with infinite relaxation and coherence times [130]. In this experiment, the setup was carefully constructed to minimize losses between the qubit-cavity

systems and the JPC and maximize the NVR of the JPC (for more details, see Ch. 4.2), thus achieving  $\eta_{\text{Alice}} = 0.53 \pm 0.01$  and  $\eta_{\text{Bob}} = 0.60 \pm 0.01$  (data shown in Fig. 4.2).

The pulse sequence to implement this protocol is very similar to that used to analyze the operation of a single qubit measurement; outlined in Fig. 1.10A (for a detailed pulse sequence, see Fig. 4.5A), the Alice and Bob qubits are first scrambled and measured to initialize them to  $|gg\rangle$  by post-selection, in a manner similar to that outlined in Ch. 1.5. Then a  $R_y^{ge}(\pi/2)$  pulse was applied to both qubits to prepare them in the state  $1/\sqrt{2}(|g\rangle + i|e\rangle)$ . Next, an entangling measurement of variable-strength was performed, where the relative amplitude and phase of the microwave pulses applied to Alice and Bob were tuned to minimize the JPC's ability to distinguish single-qubit information. The outcome of this measurement ( $I_m/\sigma, Q_m/\sigma$ ) was recorded and binned in  $201 \times 201$  histogram for each measurement strength,  $\bar{I}_m/\sigma$ . Finally, the back-action of this entangling measurement was determined by performing full two-qubit state tomography on the Alice and Bob qubits. A combination of 15 qubit rotations was followed by a joint two-qubit measurement in the computation state basis (for more information about this type of measurement and how it differs from the entangling measurement, see Fig. 4.3). From these 15 measurements, the final two-qubit density matrix was calculated in the Pauli basis for each of the  $201 \times 201$  measurement outcomes for each measurement strength.

Here, we only focus on the data for a moderate strength measurement of  $\bar{I}_m/\sigma \sim 1$ , chosen to balance between projective between the odd and even states while resolving the oscillations between odd Bell states of different phase; for measurement outcomes and tomography results at different measurement strengths, see Fig. 4.5. The probability of obtaining any particular outcome is shown in the histogram in Fig. 1.10B (top left), illustrating that at this measurement strength, the odd Bell-state manifold is not completely separated from the outcomes corresponding to  $|gg\rangle$  and  $|ee\rangle$ . Nevertheless, as we can see from the  $\langle ZZ \rangle_c$  tomogram (top right), the operation still project between the odd manifold and the even states; measurement outcomes with  $I_m/\sigma \sim 0$  result in a final two-qubit state of odd parity  $\langle ZZ \rangle_c \sim -0.4$  (red) whereas outcomes with  $|I_m/\sigma| \gg 0$  result in an even parity state (blue). Furthermore, for measurement outcomes along  $I_m/\sigma = 0$ , the odd Bell-state phase oscillates with  $Q_m/\sigma$  as expected, demonstrated by

the oscillations in  $\langle XX \rangle_c$  and  $\langle YY \rangle_c$  (similar oscillations can also be seen in  $\langle XY \rangle_c$  and  $\langle YX \rangle_c$  as shown in Fig. 4.6). Close paralleling the single-qubit case, as the parity-projectivity of the two-qubit measurement increases, i.e. outcomes with  $|I_m/\sigma| \gg 0$ , the  $\langle XX \rangle_c$  and  $\langle YY \rangle_c$  components of the resulting density matrix vanish.

From the reconstructed density matrices calculated along  $I_m/\sigma \sim 0$ , we calculate the fidelity to an odd Bell-state of arbitrary phase,  $\mathcal{F} = \text{Tr}(\rho_{\text{meas}} |O^{arb}\rangle \langle O^{arb}|) = 0.45 \pm 0.02$ , below the entanglement threshold of  $\mathcal{F} = 0.5$ .

This fidelity is a result of various imperfections in the experimental system: (1) decoherence of the two qubits which limits the fidelity to  $\mathcal{F}_{T_{2\text{Bell}}}$ ; (2) the finite distinguishability of the two inputs to the JPC characterized by  $\mathcal{F}_{\text{dist}}$ ; (3) the finite measurement efficiency of the Alice and Bob systems characterized by  $\mathcal{F}_\eta$ . From the measured value of  $T_{2\text{Bell}} = 15 \mu\text{s}$  and the protocol time,  $T_{\text{seq}} = 1.65 \mu\text{s}$ , we expect  $\mathcal{F}_{T_{2\text{Bell}}} \cong 0.95$ . As outlined previously (and discussed in further detail in Ch. 4), the fidelity is limited to  $\mathcal{F}_{\text{dist}} \cong 0.9$  due to the finite distinguishability of the inputs to the JPC. Consequently, the dominant source of infidelity is the finite measurement efficiency of Alice and Bob which we estimate limits the experiment to  $\mathcal{F}_\eta \cong 0.5$ . The measurements efficiencies in this experiment are limited by the same factors discussed above in Ch. 1.5.

Consequently, without significant improvements to the measurement efficiency, ideally to  $\eta > 0.8$ , using coherent states as flying qubits remains a non-starter in this method of generating remote entanglement. However, if it were possible to arrange the  $IQ$ -space measurement outcomes such that the phase of the generated Bell state didn't oscillate with  $Q_m$ , but instead, for example, so that four outcome distributions were obtained, one each for the odd or even Bell state of positive or negative phase, then it would be possible to make the coherent-state based protocol tolerant to losses. Unfortunately, despite some theoretical effort into the subject [122], realizing such an operation still remains elusive.

## 1.7 Single Photon Based Remote Entanglement

In the absence of a coherent-state protocol that can generate remote entanglement at the currently experimentally realizable measurement efficiencies, we are confronted with the challenge of either re-engineering our experimental systems to significantly reduce sources of loss or, as we now proceed to discuss, re-engineering the protocol to be tolerant to loss. The latter approach is especially promising since losses are an inevitable part of any system and making a protocol robust to loss is a desirable feature for any system, regardless of how low the losses may be. To embark on this path, we begin by borrowing a tool from the field of quantum optics where the transmission of quantum information over distance with large losses is routine: single photon (i.e. Fock) states.

The concept of a photon, the quantum of excitation of the electromagnetic field, was introduced by Planck and Einstein to explain the black-body radiation spectrum[107] and the photoelectric effect[39]. However, experiments that would definitively prove the existence of traveling optical photons as independent entities were only understood[27, 48] and realized[56] much later in the 20<sup>th</sup> century. Although there is no reason to suppose that microwave photons would behave differently than their optical counterparts, revealing and manipulating them is challenging because their energies are 4 to 5 orders of magnitude lower. Cavity-QED, and later on circuit-QED, have established the reality of stationary quantum microwave excitations of a superconducting resonator by strongly coupling them to Rydberg[50] and superconducting artificial atoms[124]. The production of traveling microwave photons was then indirectly demonstrated using linear amplifiers to measure the state of the radiation[15, 58, 77]. However, while there have been proposals and implementations of single flying microwave photon detectors[22, 40, 61], controlling and employing the single-photon nature of microwave radiation is still an open challenge. Here, we carry over to the microwave domain the remote entanglement experiment performed in quantum optics by realizing and operating a single photon detector based on a superconducting 3D transmon qubit[103].

With single microwave photon detectors still not commonly used, the only form of remote

entanglement realized so far with superconducting qubits has been through the use of continuous variable coherent states as the flying information carriers[121]. While such states can be efficiently synthesized by standard microwave equipment and processed by quantum-limited linear parametric amplifiers[8, 19] readily available at microwave frequencies, the disadvantage is this route is its sensitivity to losses in the paths of the flying states. In contrast, remote entanglement using flying single photons is robust to these losses, as demonstrated in the optical domain[10, 31, 54, 55, 91, 135]. This protocol offers the advantage that only the successful detection of photons is linked to the production of a pure entangled state[6, 16]. This feature is particularly important for generating entanglement between two distant stationary qubits, a crucial element of the modular architecture of quantum computation[93] and the proposed quantum internet[70]. Furthermore, scaling up the modular architecture requires no direct connections between modules, unlike previously demonstrated sequential methods[121], maintain a strong on/off ratio. Thus, demonstrating robust remote entanglement which satisfies this requirement, i.e. a *concurrent* protocol, is a vital step in the implementation of the modular architecture with superconducting qubits.

The experiment, housed in a dilution refrigerator below 20 mK, consists of two different superconducting transmon qubits (see Fig. 1.11A), referred to as Alice and Bob, in separate 3D cavities[103]. The cavities have nearly identical resonance frequencies in order to make the flying photons generated in each system indistinguishable (see Ch. 5.3). Their strongly coupled output ports are connected by microwave coaxial cables to the two input ports of a  $180^\circ$  hybrid, the microwave equivalent of a 50/50 beam-splitter. One of the output ports of the hybrid is connected to a microwave single photon detector which is realized by a third 3D cavity also containing a transmon. The other output port of the hybrid is terminated in a  $50 \Omega$  load. To ensure signal flow as shown by the arrows in Fig. 1.11A, microwave isolators/circulators (not shown; for a detailed experimental schematic, see Fig. 5.1) are inserted into the lines connecting each qubit to the hybrid. These provide robust isolation between modules and connect the system output to readout electronics.

To entangle the remote qubits, flying microwave single photon states are used as carriers of

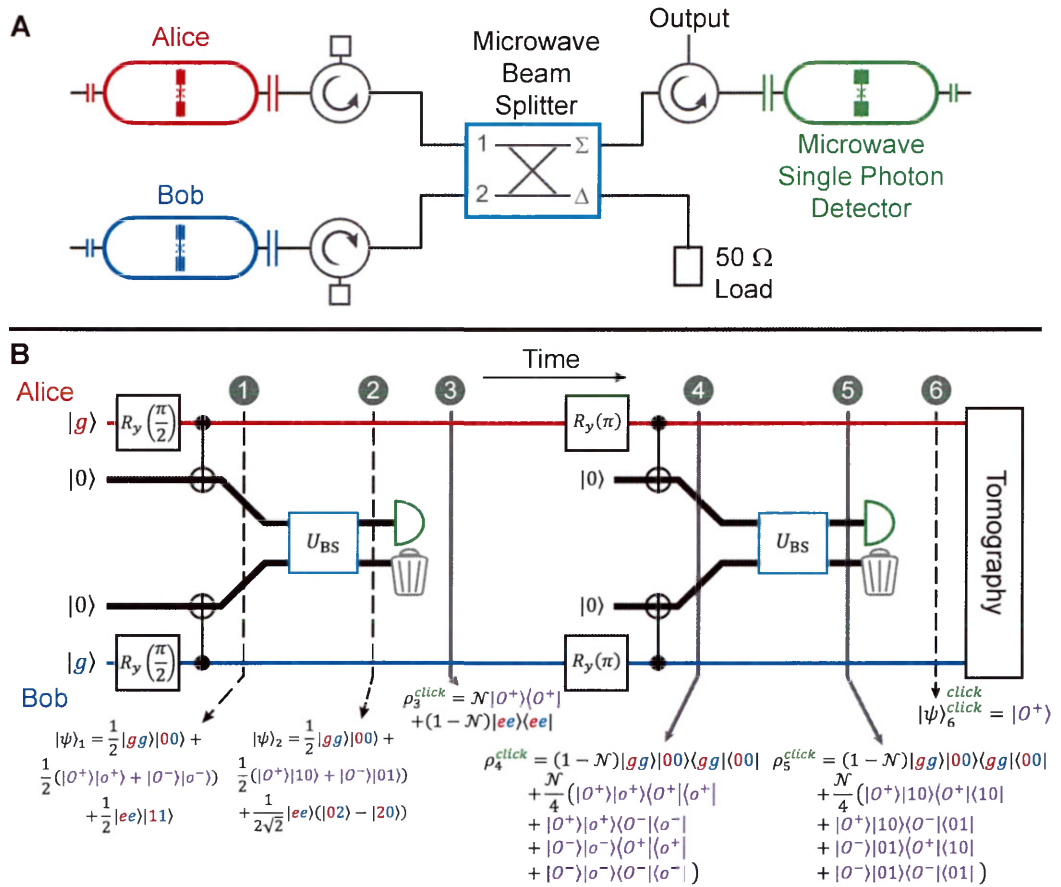


Figure 1.11 | **Single Photon Based Remote Entanglement Experiment and Protocol Schematic.** A) Two superconducting 3D transmon qubits, Alice and Bob, are connected by coaxial cables to the two input ports of the microwave equivalent of a 50/50 beam-splitter. One of the output ports of the splitter is connected to a microwave single photon detector also realized by a 3D transmon qubit. The other port of the splitter is terminated in a cold 50  $\Omega$  load. B) Quantum circuit diagram of the remote entanglement protocol, with the states of the quantum system at various steps. The Alice and Bob (red and blue) qubits are each prepared in the state  $\frac{1}{\sqrt{2}}(|g\rangle + |e\rangle)$  by a single qubit gate  $R_y(\frac{\pi}{2})$ . They are then entangled with flying single photons (black) via a CNOT-like operation. The states  $|O^\pm\rangle = \frac{1}{\sqrt{2}}(|ge\rangle \pm |eg\rangle)$  represent odd Bell states of the Alice and Bob qubits while  $|o^\pm\rangle = \frac{1}{\sqrt{2}}(|10\rangle \pm |01\rangle)$  represent odd Bell states of flying single photons in the Alice and Bob channels respectively. The flying photons interfere on the beam-splitter whose unitary action  $U_{BS}$  erases their which-path information. Following a  $\pi$ -pulse on Alice and Bob, the CNOT-like operation and beam-splitter steps are repeated to remove contributions of the unwanted  $|ee\rangle$  state. Detecting two photon clicks in a pair of consecutive rounds heralds the  $|O^+\rangle = \frac{1}{\sqrt{2}}(|ge\rangle + |eg\rangle)$  Bell state of Alice and Bob.

quantum information according to the protocol proposed in [6]. As outlined in Fig. 1.11B, the remote entanglement protocol begins by initializing both qubit-cavity systems in  $\frac{1}{\sqrt{2}}(|g\rangle + |e\rangle) \otimes |0\rangle$ , the state on the equator of the Bloch sphere with no photons in their respective cavities. Through a controlled-NOT (CNOT)-like operation, whose implementation is detailed later in the text, the qubits are now entangled with flying single photons where the state of each qubit-photon pair becomes  $\frac{1}{\sqrt{2}}(|g0\rangle + |e1\rangle)$ . The joint state of all stationary and flying qubits can be expressed as  $|\psi\rangle_1 = \frac{1}{2}(|gg\rangle|00\rangle + |O^+\rangle|o^+\rangle + |O^-\rangle|o^-\rangle + |ee\rangle|11\rangle)$  where  $|O^\pm\rangle = \frac{1}{\sqrt{2}}(|ge\rangle \pm |eg\rangle)$  represent the odd Bell states of the Alice and Bob qubits and  $|o^\pm\rangle = \frac{1}{\sqrt{2}}(|10\rangle \pm |01\rangle)$  represent the odd Bell states of flying single photons in Alice's and Bob's channels, respectively. The photons interfere on the  $180^\circ$  hybrid whose action, analogous to that of a beam-splitter, is described by the unitary  $U_{BS} = e^{-3\pi(\mathbf{a}^\dagger\mathbf{b} - \mathbf{a}\mathbf{b}^\dagger)/4}$ . This maps  $|o^+\rangle \rightarrow |10\rangle$  ( $|o^-\rangle \rightarrow |01\rangle$ ), taking the two flying odd Bell states to a single photon state in the Alice or Bob branch of the detector part of the system. This operation erases the which-path information of the photons and produces Hong-Ou-Mandel interference[56]. After the hybrid, the total system state is  $|\psi\rangle_2 = \frac{1}{2}(|gg\rangle|00\rangle + |O^+\rangle|10\rangle + |O^-\rangle|01\rangle + \frac{1}{\sqrt{2}}|ee\rangle(|02\rangle - |20\rangle))$ . At this point, the photons in the Alice channel enter the detector which distinguishes between detecting a photon, a 'click', or detecting nothing, called 'no click'. Ideally, by heralding on only single photon detection events, the  $|O^+\rangle$  is selected out from all the other states. However, losses in the system between the qubits and the detector and the inability of the detector to distinguish between the Fock states  $|1\rangle$  and  $|2\rangle$  instead result in the mixed density matrix  $\rho_3^{click} = \mathcal{N}|O^+\rangle\langle O^+| + (1 - \mathcal{N})|ee\rangle\langle ee|$  when the detector clicks. Here, the normalization constant  $\mathcal{N}$  depends on loss in the system and the characteristics of the detector (see Ch. 5.8). In particular, it depends on the probabilities with which it maps the input flying photon states,  $|1\rangle$  and  $|2\rangle$ , to an outcome of click. Another crucial assumption in  $\rho_3^{click}$  is that the detector has no dark counts, i.e. it never clicks when it receives  $|0\rangle$ . A fuller version of  $\rho_3^{click}$  including dark counts is given in the Ch. 5.8. Thus, at this stage, the qubits are in the state  $|O^+\rangle$  with probability  $\mathcal{N}$  and we would like to remove the undesired  $|ee\rangle$  state.

To achieve this, a  $R_y(\pi)$  pulse is applied on both Alice and Bob followed by a second round

of entangling the qubits with flying photons, interfering them on the hybrid and detecting them. The  $\pi$ -pulse takes  $|ee\rangle \rightarrow |gg\rangle$ ; consequently, in the second round, the unwanted state is mapped onto  $|gg\rangle|00\rangle$ , and thus it can be selected out by detecting a photon. On the other hand,  $|O^+\rangle$  is mapped onto a superposition of  $|O^+\rangle|10\rangle$  and  $|O^-\rangle|01\rangle$ . Conditioning on measuring clicks in two consecutive rounds of the protocol results in the odd Bell state  $|\psi\rangle_6^{click, click} = |O^+\rangle$ . A result of this dual conditioning is that losses in the system only reduces the success probability of the protocol and not the fidelity of the generated entangled state. Replacing the cold  $50\ \Omega$  load with a second detector would increase the success probability by a factor of 4 and allows for the generation of both the  $|O^+\rangle$  and  $|O^-\rangle$  states depending on whether the same or different detectors go click on each round, respectively. Since it does not improve the fidelity of entanglement, we omitted the second detector to simplify the microwave control electronics and cold hardware.

Successfully realizing this protocol required simultaneously: (1) implementing the generation of single photon Fock states which are entangled with the stationary qubits and (2) detecting the subsequent single photon states. Furthermore, the frequencies and temporal envelopes of the photons arising from each cavity had to be controlled to ensure that the detector cannot distinguish between them.

The first ingredient, previously termed a CNOT-like operation, actually maps an arbitrary qubit state  $\alpha|g0\rangle + \beta|e0\rangle$ , where  $\alpha$  and  $\beta$  are arbitrary complex coefficients, onto the joint qubit-flying photon state  $\alpha|g0\rangle + \beta|e1\rangle$  (this operation is not a unitary in the manifold  $\{|g0\rangle, |g1\rangle, |e0\rangle, |e1\rangle\}$  because it takes  $|e1\rangle$  to  $|f1\rangle$ ; however, this has no effects on the protocol since the cavity always starts in  $|0\rangle$ ). This is done by exploiting  $|f\rangle$ , the second excited state of the transmon qubit[74], as well as the two-photon transition  $|f0\rangle \leftrightarrow |e1\rangle$ [71, 105]. As described in further detail in Fig. 5.10A (and Fig. 5.3), starting with the qubit in  $\alpha|g\rangle + \beta|e\rangle$ , the operation is realized by first applying a  $\pi$ -pulse at  $\omega_{ef}^0$ , taking the qubit to  $\alpha|g\rangle + \beta|f\rangle$ , and then applying a  $\pi$ -pulse on the  $|f0\rangle \leftrightarrow |e1\rangle$  with two sideband tones  $(\omega_{QSB}, \omega_{CSB})$ . This maps the qubit state onto the joint qubit-intra-cavity state,  $\alpha|g0\rangle + \beta|e1\rangle$ . Finally, the photon state leaks out of the cavity, becoming a flying state that is entangled with the qubit. As a result, the traveling photon has the frequency  $\omega_A^e$  ( $\omega_B^e$ ) and a decaying exponential temporal waveform with the decay constant

$\kappa_A$  ( $\kappa_B$ ). The indistinguishability of the photons, then, was achieved in this experiment by the nearly identical frequencies and bandwidths of the Alice and Bob cavities (as given above and further discussed in Ch. 5.5). Note that although the photons need to overlap in frequency, there is no requirement here for the qubits to be identical.

The second ingredient of the experiment, microwave single photon detection, is the novel technical component of our demonstration. Put simply, this detector is just another transmon-3D cavity system like Alice and Bob. The strongly coupled port of the cavity is the detector input port. In the strong dispersive regime where the qubit is operated ( $\chi_D/2\pi = 3$  MHz,  $\kappa_D/2\pi = 1$  MHz), we can selectively  $\pi$ -pulse the qubit conditioned on the presence of one intra-cavity photon[124], mapping the flying photon onto the state of the detector qubit. To operate this system as a detector of single flying photons, we tuned the cavity frequency  $\omega_D^g/2\pi = 7.6222$  GHz close to  $\omega_A^e$  and  $\omega_B^e$  and matched the linewidths of all three cavities. This condition ensured that the detector efficiency is maximized. The incident single photons from Alice and Bob will excite the detector cavity  $\sim 50\%$  of the time (see Ch. 5.4) since their decaying exponential temporal waveforms are not mode-matched to the cavity. Thus, the selective  $\pi$ -pulse excites the qubit only if a photon was received, with the length and timing of this pulse determining the detector efficiency (see Ch. 5.4). Once the photon leaks back out, a conventional cQED dispersive readout of the qubit state[11] completes the quantum non-demolition (QND) photon detection process. Measuring the qubit in the excited state corresponds to a photon detection event (click). Finally, the detector is reset by returning the qubit to  $|g\rangle$  with an un-selective  $\pi$ -pulse.

This microwave photon detector satisfies three important criteria in an architecture that is easily integrated with current state-of-the art cQED experiments. First, the detector has a reasonable efficiency,  $\eta \approx 0.5$ , since about half of all incident photons enter the detector. Second, this detector has low dark counts (the probability of the detector reporting a click even when no photon entered the detector)  $P_d < 0.01$ , limited by the frequency selectivity of the  $\pi$ -pulse. Finally, it has a short re-arm time of 450 ns determined by how long it takes to empty the cavity and reset the qubit. We discuss avenues to further improving this detector in Ch. 5.4. Nevertheless, as we show below, the detector performance is sufficient for generating remote

entanglement.

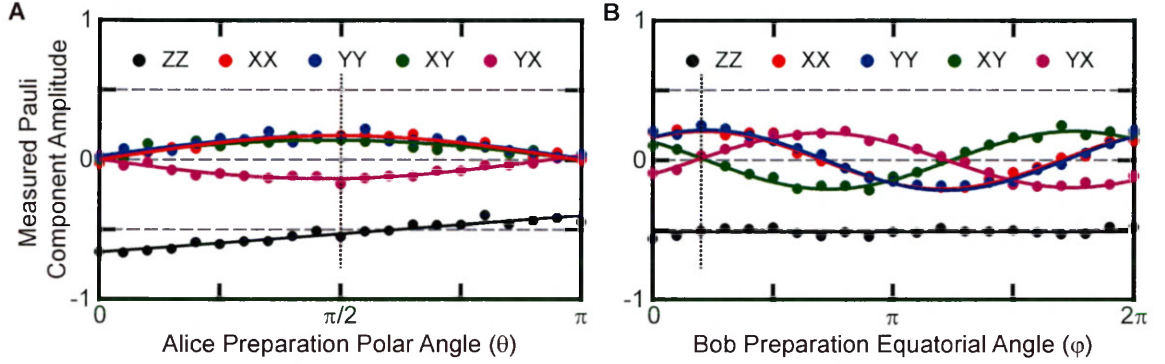


Figure 1.12 | **Two-Qubit Remote Entanglement.** Measured amplitudes of the relevant two-qubit Pauli vector components as a function of qubit preparation. After the remote entanglement protocol described in Fig. 1.11B, joint tomography was performed on the qubits conditioned on the detector reporting a click for each round. A) With Bob always initialized in  $\frac{1}{\sqrt{2}}(|g\rangle + |e\rangle)$ , Alice was prepared in the variable state  $\cos(\theta/2)|g\rangle + \sin(\theta/2)|e\rangle$ . Data (points) and fits (lines) confirm that entanglement is maximized when  $\theta = \pi/2$  (dotted line). B) With Alice always initialized in  $\frac{1}{\sqrt{2}}(|g\rangle + |e\rangle)$ , Bob was prepared in the variable state  $\frac{1}{\sqrt{2}}(|g\rangle + e^{i\phi}|e\rangle)$ . The components of the Pauli vector oscillate with  $\phi$  sinusoidally as expected. The complete density matrix for  $\phi$  given by the dotted line is shown in Fig. 1.13 (left) in the Pauli basis.

Having detailed the experimental realization of the necessary tools, we next perform the full remote entanglement protocol. The final two-qubit density matrix was measured in the Pauli basis with joint tomography (see Ch. 5.6) conditioned on detecting two clicks. For an arbitrary Bell state, the only non-zero Pauli components are  $\langle ZZ \rangle$ ,  $\langle XX \rangle$ ,  $\langle YY \rangle$ ,  $\langle XY \rangle$ , and  $\langle YZ \rangle$ , which are displayed in Fig. 1.12. We first confirm that the protocol entangles the qubits only when they start in the correct state. With Bob initialized in  $\frac{1}{\sqrt{2}}(|g\rangle + |e\rangle)$ , Alice was prepared in  $\cos(\theta/2)|g\rangle + \sin(\theta/2)|e\rangle$ . Entanglement is maximized for  $\theta = \pi/2$  (see Fig. 1.12A dotted line), with extremal values for  $\langle XX \rangle$ ,  $\langle YY \rangle$ ,  $\langle XY \rangle$  and  $\langle YX \rangle$ , and with the expected negative  $\langle ZZ \rangle$  indicating a state of odd parity. On the other hand, for  $\theta = 0$  ( $\theta = \pi$ ), the final two-qubit state should be the separable state  $|eg\rangle$  ( $|ge\rangle$ ) as indicated by  $\langle XX \rangle = \langle YY \rangle = \langle XY \rangle = \langle YX \rangle = 0$  and  $\langle ZZ \rangle < 0$ . We attribute the deviation of  $\langle ZZ \rangle$  from  $-1$  to the dark counts in the detector and the finite  $T_1$ 's of the two qubits.

Next, we show that when both qubits are initialized along the equator of the Bloch sphere,



of the two qubits which limits the fidelity to  $\mathcal{F}_{T_{2\text{Bell}}}$  and (2) imperfections of the detector which are characterized by  $\mathcal{F}_{\text{det}}$ . From the measured value of  $T_{2\text{Bell}} = 6 \mu\text{s}$  and the protocol time,  $T_{\text{seq}} = 2.5 \mu\text{s}$ , we expect  $\mathcal{F}_{T_{2\text{Bell}}} \cong 0.8$ . The infidelity associated with the imperfect detector is characterized by the dark count ratio  $P_{\text{d}}/P_{\text{click}}$ , which is the fraction of detection events that are reported as clicks even though no actual photon was sent. In this experiment,  $P_{\text{d}}/P_{\text{click}} = 0.05$ , primarily limited by the finite selectivity of the detection pulse and the imperfect readout of the detector qubit, which results in  $\mathcal{F}_{\text{det}} \cong 0.9$ . A theoretical model incorporating these two imperfections was used to calculate an expected fidelity  $\mathcal{F}_{\text{thy}} = 0.76$  (see Ch. 5.8). The remaining infidelity is a result of sources that are harder to characterize and will need to be explored in further work, like, for instance, the imperfections of the CNOT-like operation and the distinguishability of the photons. Nevertheless, the current results clearly establish the viability of this protocol and, by extension, the modular architecture for superconducting qubits.

Another figure of merit for this experiment is the entanglement generation rate which is determined by the repetition rate,  $T_{\text{rep}} = 21 \mu\text{s}$ , and the success probability of the experiment. The latter is determined by the product of state initialization via post-selection (57%) and the detector click probability in the first (8%) and second (9%) rounds respectively leading to an overall success probability of 0.4%. The corresponding generation rate of about  $200 \text{ s}^{-1}$  is orders of magnitude faster than similar experiments performed with nitrogen-vacancy centers in diamond ( $2 \times 10^{-3} \text{ s}^{-1}$ )[10], neutral atoms ( $9 \times 10^{-3} \text{ s}^{-1}$ )[55] or trapped ion systems ( $4.5 \text{ s}^{-1}$ )[59]; it is however slower than rates achieved in experiments with quantum dot hole spins ( $2300 \text{ s}^{-1}$ )[31] or quantum dot based electron spin qubits ( $7300 \text{ s}^{-1}$ )[135]. We note, however, that our generation rate (200 Hz) does not exceed the decoherence rate of the two qubits (26 kHz) and thus does not yet cross the threshold for fault tolerance[59, 93] though there are many prospects for enhancement.

Improvements in generation rate and fidelity are possible with readily available upgrades to the hardware and software of our experiment. Firstly, a factor of 4 increase in success can be achieved by installing the omitted second detector. Secondly, shaping the generated photons and detection pulse to mode match the flying photons to the detector would increase the detection efficiency

by at least 50% and hence multiply the generation rate by at least a factor of 2. Moreover, this would reduce both the dark count fraction and the distinguishability of the traveling photons which would directly benefit the entanglement fidelity by bringing  $\mathcal{F}_{\text{det}}$  closer to unity. Thirdly, an order of magnitude better coherence times for the two qubits have been demonstrated in similar 3D qubit-cavity systems[3], which should readily carry over to this experiment and improve  $\mathcal{F}_{T_{2\text{Bell}}}$ . Finally, the overall throughput of the experiment can be increased by an order of magnitude by the use of real-time feedback capabilities that have been recently demonstrated for superconducting qubits[83, 118].

Combined, these upgrades could increase the entanglement generation rate by a few orders of magnitude to around 10 kHz, to beyond the decoherence rates of approximately 100 Hz experimentally demonstrated in 3D cQED-based quantum memories[111]. These 3D microwave cavity based memories can be readily integrated into the current system to store the generated remote entangled states thus allowing for the qubits to be reused to generate additional entangled pairs. Together with the ability to perform high-fidelity local operations between the qubit and the memory, this would offer the possibility of realizing remote entanglement distillation[7, 37], a crucial next step in realizing fault-tolerant modular systems that is discussed further in Ch. 1.8 and Ch. 6.

Thus, we have demonstrated, in a single experiment, the set of tools that had been previously the exclusive privilege of quantum optics experiments: the availability of flying microwave single photon sources and detectors together with the spatial and temporal control of traveling photons to make them indistinguishable. With these tools, we have realized two-photon interference of microwave photons and the generation of loss-tolerant entanglement between distant superconducting qubits with concurrent measurements. The protocol speed and prospects for improving fidelity make this a very promising implementation for remote entanglement and the distribution of quantum information with microwave flying photons. Thus, this experiment opens new prospects for the modular approach to quantum information with superconducting circuits.

## 1.8 Towards Modular Entanglement Distillation - Perspectives and Future Directions

Together with efficient single-qubit control and measurements, generating remote entanglement demonstrates all the primitive operations necessary for a modular quantum computation system. While there is of course continuing work to further improve the fidelity, efficiency and speed of all of these operations, this toolbox sets the stage for building and understanding distributed, small-scale modular systems of (a few) qubits. One of the primary initial objectives for such systems would be demonstrating two-qubit gates between data qubits in remote modules as a necessary ingredient for universal quantum computation.

Realizing this objective, of course, introduces a new set of benchmarks against which to quantify the performance of these more complex systems. Like any other operations performed in a quantum computation, the two-qubit operations too must be of very high-fidelity [34]. Since a remote-entangled qubit pair is a resource consumed in this operation, the fidelity of the entangled state is a crucial determinant of the ultimate fidelity of the gate. While a few strategies to address sources of infidelity for the single-photon based remote entanglement protocol were discussed above in Ch. 1.7 and are the topics of active research, there will always remain unavoidable sources of error like decoherence, photon loss etc. Thus, in an analog to how quantum error correction is used to extend the lifetime of a quantum system beyond that of its imperfect constituents, high-fidelity entangled states can be generated from many copies of lower-fidelity entangled states [7, 32, 37]. Otherwise known as entanglement distillation or purification, this is a protocol whereby two parties, Alice and Bob, that share many copies of entangled states, each with fidelity  $\mathcal{F}$  to a Bell state, can probabilistically generate a single entangled state of fidelity  $\mathcal{F}' > \mathcal{F}$  by performing only local operations on their qubits and communicating classically between them. Realizing entanglement distillation is essential to the success of any protocol that relies on entangled states as a resource, making it a necessary milestone towards a modular quantum architecture for quantum computation.

Experimentally realizing entanglement distillation is an active area of research [92, 93, 97]

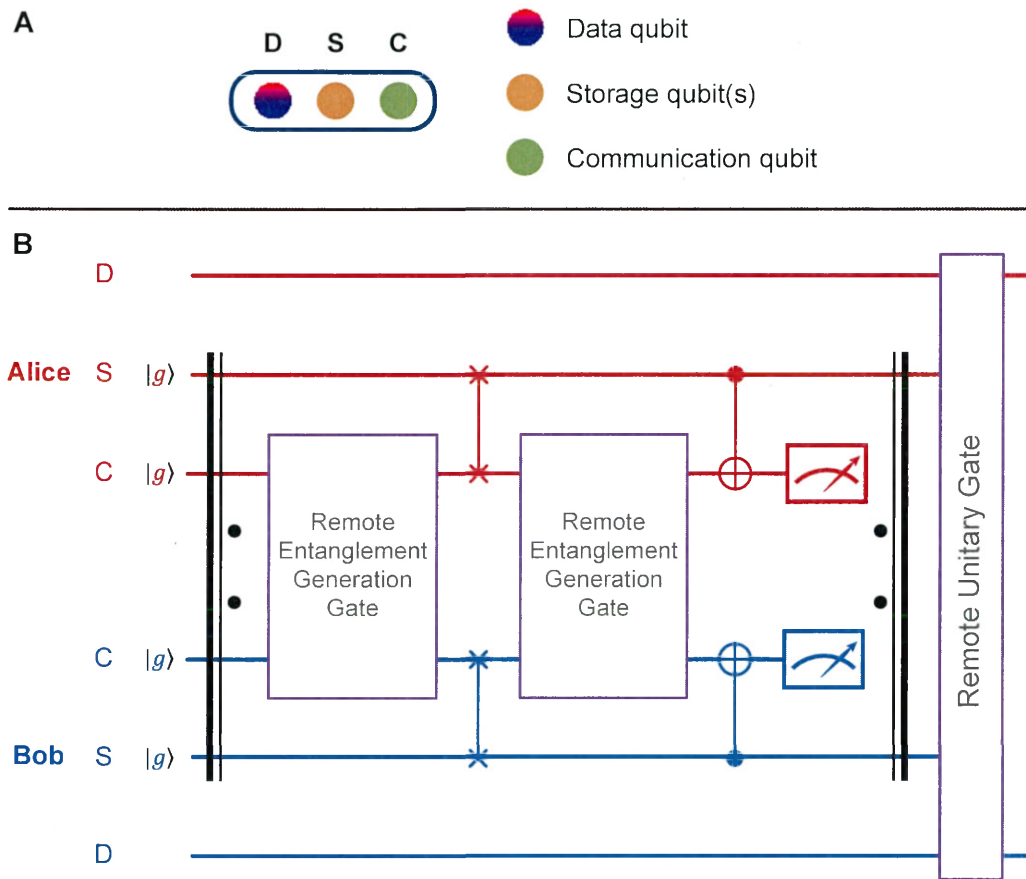


Figure 1.14 | **Remote Entanglement Distillation Protocol.** A) Schematic of a minimal module required for entanglement distillation. One, arguably necessary, avenue toward achieving higher entanglement fidelity between modules is to implement entanglement distillation where multiple copies of low-fidelity entangled states are used to probabilistically generate a single high-fidelity entangled state. This requires increasing the number of modes available in each module, adding a storage qubit to the already present data and communication qubits. B) Circuit schematic for entanglement distillation and remote unitary operations between modules. Remote entanglement distillation can be performed by first generating entanglement between the communication qubits of two modules, swapping that entanglement into the storage qubits and then repeating the entanglement generation process between the two communication qubits. To then produce an entangled state of higher fidelity, a local CNOT operation between the storage and communication qubit in each module is followed by a measurement of each communication qubit. When the two detectors measure the same outcome, a Bell state of the two storage qubits with higher fidelity is generated. This process can be repeated until a desired fidelity of the storage Bell state is achieved. Finally, this entangled state can be used as a resource to perform a non-local arbitrary unitary operation between the two data qubits in each module.

with the first results appearing in nitrogen-vacancy systems [66]. Since entanglement distillation requires multiple copies of entangled states between modules, this required extending the functionality of a module beyond what was presented in Fig. 1.3 in Ch. 1.3. As shown in Fig. 1.14A, a module is now expanded to contain a storage qubit which, as its name implies, is used to store an entangled state for distillation. In fact, this storage may actually (need to) be many physical qubits or a multi-mode system, for example a high- $Q$  harmonic oscillator, since distillation circuits that can correct arbitrary errors in the resource entangled state (with errors in the local gates) require multiple copies of the resource entangled state to produce a high fidelity pair. Some perspectives of how these storage qubits may be incorporated into the current modules is outlined in Ch. 6. Furthermore, this storage qubit must be able to interact with the communication qubit to enable entanglement to be loaded into the storage; directly allowing the storage qubit(s) to communicate with the environment would greatly increase the number and complexity of the communication network between modules. Thus, we instead consider the case where only communication qubits can be used to generate remote entanglement.

In this paradigm, a basic circuit schematic outlining entanglement distillation is shown in Fig. 1.14B, differing slightly from its original inception [7]. First, a remote entangled state is generated between the communication qubits of two modules (the only objects between which entanglement can be directly generated, using the protocol outlined in Ch. 1.7 for example). Then, using a SWAP operation between the communication and storage qubit in each module, the remote entangled state is transferred to the storage qubit, also resetting the communication qubit to  $|g\rangle$ . Subsequently, another copy of an entangled state between the two communication qubits is generated. Although this process could be repeated until all the storage qubits (or the many modes of the storage) have been populated with entangled pairs, here we limit ourselves to the case of a single storage and communication qubit. With the copies of the entangled pairs, purification is performed by doing a local CNOT between the storage (control) and communication (target) qubit in each module before measuring the state of the communication qubit. A higher-fidelity entangled state of the storage qubit is generated when the outcomes of the two measurements agree. Although this protocol could be repeated to achieve higher fidelity, with an

increasing cost in entangled pairs [7], it does not correct all the errors that the initial entangled state may suffer from. Protocols that can distill entanglement robust to multiple errors, imperfect gates and measurements require more elaborate protocols with more resource entangled pairs and storage qubits [32, 65, 97]. Moreover, the choice of the distillation protocol depends on the magnitude and types of errors that the various components of the distillation protocol suffer from making the choice of what protocol to implement strongly system dependent. Thus, in the discussion in this thesis, we instead focus on how to expand modules so that they may be used to perform distillation and other inter-module operations. For example, once an entangled state of the storage qubits of two qubits is available, it is then consumed to perform the desired two-qubit gate between the data qubits of the modules in a protocol outlined by Fig. 6.1.

Therefore, an imperative avenue of research towards the ends of both entanglement distillation and remote unitary operations is the development of a module with all the elements and functionality described above (and in Fig.1.14A). A detailed discussion of a few specific potential strategies along with their various advantages and disadvantages is presented in Ch. 6.2. Here we only present some of the necessary design requirements. The communication qubits in these modules must be engineered to enable high remote entanglement generation rates, resulting in a competition between the requirement of strong coupling to the external environment and the requirement for this qubit to also have high coherence so as not to limit the entanglement fidelity. On the other hand, the data and storage qubits need to have even longer coherence times since they need to store quantum states while entanglement is generated and distilled. Again, this needs to be realized while maintaining the ability to perform operations between these qubits and the probably lower-coherence communication qubit. Indeed, as is a ubiquitous challenge across all experimental system, balancing the need for coupling between modes of disparate coherence is one of the main engineering challenges for modules [66, 97, 137]. Using one of the very motivations for the modular architecture, one possible strategy to balancing these requirements is tunable couplings between these various objects in a module (see Fig. 6.3B and Ch. 6.2).

In addition to the milestones of modules, remote unitary operations, and entanglement distillation, there are still more aspects of a modular architecture to further investigate. Chief among

these is the switchable router, which remains but a proposal at this point with no experimental prototype beyond elements that could be used to as the building blocks for such a router [21, 69, 132]. Beyond that exist a plethora of engineering problems, specific to superconducting qubits and to quantum information in general, resulting from the scaling from a few qubit systems to the hundreds or thousands of qubits that are eventually envisioned. To say that, as far as this field has advanced in the past few decades, there remains, then, a protracted and arduous path to quantum information and communication systems risks an understatement. Yet, the formidable progress and exponential growth in every aspect of these systems may also cautiously justify the optimism that quantum computation and communication technology is an inevitability.

# 2

## Qubits, Amplifiers, and Measurements in Superconducting Quantum Circuits

... experimental physicists tend not to be the most avid or credulous readers of the quantum measurement literature

---

Sir Anthony Leggett

### 2.1 Overview

In this chapter, we introduce some of the tools of the superconducting quantum circuit trade, focusing on the devices used in the experiments in this thesis. Instead of describing the theory of operation and experimental implementation of each device in detail from first principles (which would require its own thesis for each device), we provide a general overview of their operation, highlighting how the parameters of these devices have been designed and engineered for their use in the experiments discussed here. We begin in Ch. 2.2 by talking about Josephson junction, the non-linear element underlying almost all superconducting quantum circuits, and how it is used to

build a qubit, a basic building block for quantum information, in the paradigm of dispersive circuit-QED. After a brief introduction in Ch. 2.3 to the JPC, our nearly-quantum-limited parametric amplifier of choice, we in Ch. 2.4 summarize the dispersive readout of qubits using these tools. Finally, we provide a conceptual overview of how inefficient measurements adversely affect our systems.

## 2.2 Transmon Qubits and 3D Superconducting Cavities

Superconducting quantum circuits encode quantum information in a quantum degree of freedom of an electrical circuit, like the flux, phase or charge, much like information is encoded in the energy levels of atomic or ionic qubits or the spins of electronic or nuclear qubits. Thus, just like their atomic, ionic or electronic counterparts, superconducting quantum circuits require non-linearity to realize a system that has selectively addressable energy levels. This non-linearity is provided by the Josephson junction, which also has the appealing property of being a very low dissipation element, making a fundamental building block of superconducting quantum circuits. The Josephson junction has a non-linear relationship between the phase, the difference in the superconducting order parameter,  $\varphi(t)$  and current  $I(t)$  across the junction:

$$I(t) = I_0 \sin(\varphi(t)) \quad (2.1)$$

where  $I_0$  is the critical current of the Josephson junction. As a result, the Josephson junction behaves like a non-linear inductor with the junction inductance  $L_J$  depending on the phase across the junction:

$$L_J = \frac{\phi_0}{I_0 \cos(\varphi)} \quad (2.2)$$

where  $\phi_0 = \Phi_0/2\pi = \hbar/2e$  is the reduced magnetic flux quantum. Based on this element, a veritable menagerie of superconducting qubits have been created but, in the past few years, one has emerged as the most widely used for its ease of fabrication, operation, and, especially, its coherence properties: the transmon [74, 103, 115].

The transmon qubit, shown in orange in Fig. 2.1A, consists of a Josephson junction shunted by a capacitor, forming an anharmonic oscillator. Unlike a quantum harmonic oscillator that has equally spaced energy levels, an anharmonic oscillator has incommensurately spaced energy levels, much like an atom, earning circuits based on them the moniker of superconducting artificial atoms. To enable control and readout of the transmon qubit, it is in turn capacitively coupled to a microwave frequency resonator (purple in Fig. 2.1A) realizing the paradigm that is now commonly referred to as circuit quantum electrodynamics (cQED). Specifically, the experiments in this thesis, the resonator is a mode of a 3D microwave-frequency cavity realizing what is called a three-dimensional (3D) transmon in the dispersive regime of circuit-QED [124, 142]. The 3D regime is attractive since the cavity can be made to be very low-loss with vacuum as the dielectric to store electromagnetic energy; this directly translates to improvements in qubit coherence properties as well as the simplified sample fabrication and testing by obviating components like printed-circuit boards [3, 103].

The resulting Hamiltonian of this qubit-cavity system is:

$$\mathbf{H}/\hbar = \omega_c \mathbf{a}^\dagger \mathbf{a} + \omega_q \mathbf{b}^\dagger \mathbf{b} - \frac{E_J}{\hbar} (\cos \varphi + \varphi^2/2) \quad (2.3)$$

$$\varphi = \varphi_c (\mathbf{a} + \mathbf{a}^\dagger) + \varphi_q (\mathbf{b} + \mathbf{b}^\dagger) \quad (2.4)$$

Here,  $\mathbf{a}$  is the annihilation operator for the cavity mode at frequency  $\omega_c$ ,  $\mathbf{b}$  is the annihilation operator for the qubit mode at frequency  $\omega_q$ ,  $E_J$  is the Josephson energy, and  $\varphi$  is the superconducting phase across the junction, which can be written as the linear combination of the phase across the cavity mode  $\varphi_c$  and the qubit mode  $\varphi_q$ . Expanding the cosine to fourth order and making a rotating-wave approximation to only keep non-rotating terms, we obtain the circuit-QED Hamiltonian

$$\mathbf{H}_{\text{cQED}}/\hbar = \omega_c \mathbf{a}^\dagger \mathbf{a} + \omega_q \mathbf{b}^\dagger \mathbf{b} - \frac{1}{2} \chi_{qq} \mathbf{b}^{\dagger 2} \mathbf{b}^2 - \chi \mathbf{a}^\dagger \mathbf{a} \mathbf{b}^\dagger \mathbf{b} - \frac{1}{2} \chi_{cc} \mathbf{a}^{\dagger 2} \mathbf{a}^2 \quad (2.5)$$

where  $\chi_{qq}$  is the qubit anharmonicity,  $\chi_{cc}$  is the Kerr non-linearity acquired by the cavity, and

$\chi$  is the dispersive shift between the qubit and cavity. The three non-linearities are related by  $\chi = -2\sqrt{\chi_{qq}^2\chi_{cc}^2}$  [100]. For the experiments discussed in this thesis, the Kerr term was small and thus was ignored. We operate in the dispersive regime where the qubit frequency, typically  $\omega_q/2\pi = 4$  to 10 GHz, is detuned, typically by many gigahertz, from the cavity frequency, typically  $\omega_c/2\pi = 5$  to 10 GHz. This prevents the qubit and cavity from directly exchanging energy, enabling significantly increased qubit coherence times [57]. As a result of the anharmonicity of the qubit, designed to be  $\chi_{qq}/2\pi \sim 200$  MHz, the energy levels can be selectively addressed; the lowest two levels, called the ground state  $|g\rangle$  and the excited state  $|e\rangle$  are used to realize an effective two-level qubit system (see Fig. 2.1B) with a transition frequency  $\omega_q = \omega_{ge} \sim \sqrt{8E_J E_C}$ . Crucially, the value of the anharmonicity is also carefully chosen so that the ratio of the Josephson energy  $E_J$  to the charging energy  $E_C$  (where  $E_C \sim \chi_{qq}$ ) is  $E_J/E_C \sim 100$  to make the transmon insensitive to charge noise [74].

It is important to point out at this stage that although the transmon is an anharmonic oscillator, it can be treated as an effective two-level qubit system assuming that no higher order states are ever populated. This can be done formally by limiting the Hilbert space to two states and defining effective Pauli operators based on the transmon mode operators

$$\frac{1 + \mathbf{Z}}{2} = \Pi_2 \mathbf{b}^\dagger \mathbf{b} \Pi_2 \quad (2.6)$$

$$\mathbf{X} = \Pi_2 \frac{\mathbf{b} + \mathbf{b}^\dagger}{2} \Pi_2 \quad (2.7)$$

$$\mathbf{Y} = \Pi_2 \frac{\mathbf{b} - \mathbf{b}^\dagger}{2i} \Pi_2 \quad (2.8)$$

where  $\Pi_2$  is the projector onto a Hilbert space of dimension two. With this transformation, we can use the Bloch sphere and Pauli representations of a qubit for our transmon, justifying our use of the word transmon and qubit interchangeably in this thesis. However, as we discuss at the end of this section and later in the thesis (Ch. 5), the higher order transmon states cannot be entirely ignored because they can be sources of error or useful resources.

As a result of their coupling, the cavity (qubit) acquires a qubit (cavity) state-dependent frequency shift of  $\chi$ . The dispersive shift forms not only the basis for the qubit readout, discussed in

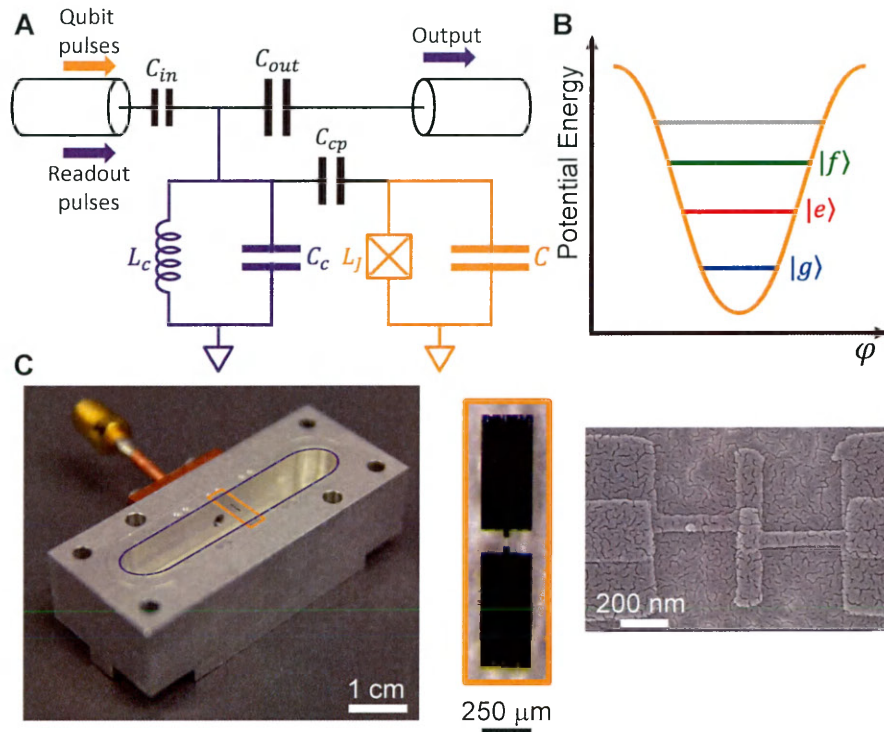


Figure 2.1 | **A Summary of the 3D Transmon-Cavity System in cQED.** A) Schematic of the effective circuit of a 3D transmon-cavity system in cQED. A transmon qubit (orange), consisting of a capacitively shunted Josephson junction, is capacitively coupled to a microwave resonator (purple). While, in practice, the resonator is a mode of a 3D cavity, it is schematically represented as an LC-oscillator. The qubit-cavity system is coupled to the external environment through two ports, a weakly-coupled input port, and a strongly-coupled output port. Microwave signals at the qubit frequency are used to rotate the state of the qubit while microwave signals at the cavity frequency are used to measure the state of the qubit. B) Energy level diagram of a transmon qubit. The 3D transmon is an anharmonic oscillator because the Josephson junction behaves like a non-linear inductor. Unlike a harmonic oscillator with equally spaced energy levels, the transmon has unequally spaced energy level where, to first order, the energy level difference decreases by the anharmonicity  $\alpha$  with each additional excitation, allowing the transitions between energy levels to be individually driven. The lowest two energy levels form the ground  $|g\rangle$  and excited  $|e\rangle$  states of the qubit, although higher states like the second excited state  $|f\rangle$  can also be used as a resource. C) Pictures of a qubit in a 3D cavity, microscope image of a 3D transmon qubit and SEM image of a Josephson junction. Left: One half of a 3D rectangular aluminum cavity with a transmon qubit fabricated on a sapphire chip placed at the center of the cavity; the transmon is coupled to the  $TE_{101}$  mode of the cavity. Center: An optical microscope image of the transmon qubit chip showing the dipole antenna that capacitively couple the qubit to the cavity and also act as the shunting capacitance across the Josephson junction. Right: A SEM image of the Josephson junction at the heart of a transmon; the junction is fabrication by a double-angle evaporation of aluminum fabrication technique.

further detail below in Ch. 2.4, but also is essential for a variety of other qubit-cavity interactions, for example, sideband transitions (see Ch. 5.4) and state-selective control pulses on the qubit (see Ch. 5.4). Crucially, the value of  $\chi$  can be engineered (independently of  $\chi_{qq}$ ) across a few orders of magnitude,  $\chi/2\pi \sim 0.1$  to 10 MHz, depending on the experimental requirements.

The cavity is capacitively coupled to two transmission lines called the input and the output, so named for the roles they serve, as shown in Fig. 2.1B. Microwave signals (at the qubit frequency) to control the qubit enter the system through the input port as do microwave signals (at the cavity frequency) for readout. After interacting with the qubit-cavity system, the readout signals exit through the output port. The values of the input and output coupling capacitors,  $C_{\text{in}}$  and  $C_{\text{out}}$ , set the coupling quality factors,  $Q_{\text{in}}$  and  $Q_{\text{out}}$ ; these couplings are designed so that  $Q_{\text{in}} \gg Q_{\text{out}}$  ( $C_{\text{in}} \ll C_{\text{out}}$ ) ensuring that signals preferentially leave on the output port, minimizing any information loss via the input port<sup>1</sup>. Specifically, we choose  $Q_{\text{in}} \sim 10^6$  and  $Q_{\text{out}} \sim 10^3$  so that the cavity is over-coupled to the output. This realizes a output coupling-limited cavity bandwidth of  $\kappa/2\pi \sim 1$  to 5 MHz enabling readout of the qubit in a time,  $T_m \sim 5/2\pi\kappa \sim 200$  to 1000 ns much shorter than the relaxation or decoherence time of the qubit. With the design choices, 3D transmons routinely achieve relaxation lifetimes of  $T_1 \sim 100 \mu\text{s}$  and decoherence times of  $T_{2R}, T_{2E} \sim 20$  to 50  $\mu\text{s}$ , like the qubits used in the experiments for this thesis.

A typical 3D transmon qubit-cavity system is shown in Fig. 2.1C. The Josephson junction and the center of the transmon qubit (right in Fig. 2.1C) is a superconductor-insulator-superconductor junction made of an Al/ $\text{AlO}_x$ /Al fabricated by the deposition of two layers of thin-film Al with an intermediate oxidation step to create the insulating barrier. The transmons used were fabricated using either the Dolan-bridge [35] or bridge-free electron-beam lithography techniques [79] on double-side-polished chips of *c*-plane sapphire (chosen over *Si* for the improved coherence properties observed [23]). The junctions are connected via leads to two rectangular pads that act as the shunting capacitance of the transmon as well as the coupling capacitance to the cavity (center in Fig. 2.1C). The qubit chip are placed in a 3D cavity, here a rectangular one (left in Fig. 2.1C). Typically, the cavity is machined from a superconducting material like Al or

<sup>1</sup>It is not necessary to engineer such asymmetric couplings, especially for cavities coupled to qubits that are not used for readout.

a normal metal like Cu, although in this thesis, some of the cavities were made of indium-plated copper. The transmon qubit and cavity parameters as well as their couplings are designed using finite-element simulations and black-box quantization [100], which enable going directly from desired Hamiltonian parameters, like  $\chi$  or  $\chi_{qq}$  for example, to fabrication parameters, like junction inductance or antenna size for example.

Although a very commonly used and well-understood system with properties that enable their use in a wide range of experiments, these systems still have some limitations that detrimentally affect the experiments they are used in. One of the primary shortcomings of the transmon is its relaxation and coherence properties, which although among the best for superconducting qubits, have not improved significantly in the past few years since the advent of the 3D architecture [103, 115]. State of the art relaxation times on the order of  $T_1 \sim 100 \mu\text{s}$ , while sufficient for readout fidelities of  $\mathcal{F} \sim 0.99$ , will need to be improved by an order of magnitude or more for higher fidelities still. What currently limits  $T_1$  and how to improve it is not clear and requires further investigation. More critically, the typical qubit coherence times of  $T_{2R} \sim 20$  to  $50 \mu\text{s}$  fall far short of the maximum value of  $2T_1$  since they are limited by their pure dephasing time  $T_\phi$ . Conjectured to be limited by the anomalously high thermal photon number in the cavity that the qubit is coupled to [115, 125], the low decoherence times of the transmon is one of the biggest sources of error in many experiments (like those of this thesis) and will need to be improved to prevent it from becoming the weak-link in future experiments. Beyond their coherence properties, transmon qubits also suffer from problems with reproducibility in fabrication and large variability in performance across fabrication and experimental runs because of inadequate control of their environments. Finally, although the dominant physics of the system is described by the cQED Hamiltonian of Eq. 2.3, there are many ignored terms in the rotating-wave approximation; these higher order terms are a suspected source of observed, but not well understood, effects like reduction of qubit  $T_1$  during readout or spurious leakages and higher order transitions when strong pump tones are applied to the system for example.

Beyond the systems described here, which have been designed with efficient qubit readout in mind, there exist many other tools in the superconducting quantum toolbox. For example, high-

coherence 3D cavities can be used as memories to store quantum information for times longer than 3D transmons[111] and will be important in our discussions about future prospects towards remote entanglement distillation in Ch. 6. Furthermore, the tools described above and their design considerations form the foundation for readout across a wide range of cQED systems and architectures [3, 86, 143] making these ideas generally applicable beyond just the experiments described in the following chapters.

## 2.3 The Josephson Parametric Converter

As amplification is crucial to converting small quantum signals into measurably large classical signals, the properties of that amplification process, like the amount of gain and added noise for example, determine characteristics of measurement process like fidelity, QND-ness and efficiency. For the readout of superconducting qubits, Josephson junction based parametric amplifiers operating near the quantum limit [20] are an essential component as a first-stage pre-amplifier in an efficient output amplification chain (for example, see Fig. 4.1 or Fig. 5.1). Maximizing the measurement efficiency demands minimizing the losses in the output signal chain while simultaneously maximizing the gain with the least possible added noise in the amplification chain. Crucially, the noise temperature of an output chain, and hence its efficiency, is dominantly determined by the losses before the first amplifier in the output chain as well as that amplifier's gain and noise temperature [109, 131]. Josephson junction parametric amplifiers can routinely achieve gains of 20 dB with nearly quantum-limited noise performance. Thus, by using these parametric amplifiers as a first-stage pre-amplifier at base (20 mK) before following amplifiers like high electron mobility (HEMT) amplifiers (at 3 K), the amplified quantum signals from the qubit-cavity system being measured can exceed the added noise of the following amplifiers, in turn greatly improving the efficiency over output chains based on HEMT amplifiers alone. This has made them instrumental in the observation of quantum jumps [140], the detailed study of the quantum back-action of measurement [51, 94] and feedback [78, 139], and quantum error correction [101] and will continue to remain essential in future experiments.

Unsurprisingly, quantum-limited Josephson junction based parametric amplifiers are an area of active research resulting in the development of a wide variety of amplifiers over the years, each with their own advantages and disadvantages. Of this pantheon of devices, the experiments in this thesis use one in particular, the Josephson Parametric Converter (JPC). Leaving a more detailed discussion of the theory, design, operation and optimization of JPCs to the comprehensive Refs. [123, 131], here we present only a brief summary, beginning with some of the JPC's advantages compared to other amplifiers:

- **Linearity** - Unlike latching or bifurcating amplifiers, like the Josephson Bifurcation Amplifier, [128, 129, 138], linear amplifiers, like the JPC, do not need to be reset, making them fast, a necessary quality for efficient readout and applications like quantum error correction.
- **Phase-preserving amplification** - The JPC, when operated as described below, amplifies both the I and Q quadratures of input microwave radiation unlike phase-sensitive amplifiers that amplify one quadrature and de-amplify the other [18, 19]. They do not require good phase stability between the microwave tones that pump the amplifiers and generate the readout signals, simplifying experimental complexity.
- **Frequency and spatial non-degeneracy** - Compared to frequency and spatial degenerate four-wave mixing amplifiers [52], the JPC operates based on three-wave mixing with spatially different ports for each mode of the device. It therefore avoids the disadvantage of a large pump tone at the same frequency and on the same port as the much weaker signal tone<sup>2</sup>.
- **Ease of fabrication and operation** - Compared to non-resonant devices like traveling wave amplifiers that consist of thousands of Josephson junctions [84], the JPC is simpler to fabricate with many fewer junctions. In addition, the JPC is also flexible to operate, with the center frequency, gain, bandwidth and compression power being tunable in-situ.

---

<sup>2</sup>Although strategies like using two detuned pumps [131] or flux-pumping [147] can remove the resonant pump tone problem, they introduce new engineering and design challenges of their own.

The JPC is a robust and versatile amplifier, making it a compelling choice as a characterized and easy-to-use module in more complex experiments with superconducting qubit. Of course, the JPC is not without its own disadvantages which we briefly address at the end of this section.

At its heart, the JPC consists of a ring of four identical Josephson junctions, called a Josephson Ring Modulator (JRM); as shown in Fig. 2.2, the JRM has four orthogonal electrical modes, two differential modes called  $X$  and  $Y$ , a common mode called  $Z$  (pump), and a zero-frequency offset mode called  $W$  (not shown) that is not coupled to and hence not used [9]. The JRM is placed at the center of a pair of transmission-line resonators. placing it at the current anti-nodes of fundamental  $\lambda/2$  modes of the resonators. Thus, the differential  $X$  and  $Y$  modes of the JRM couple to the horizontal idler (blue) resonator of frequency  $\omega_I$  and the vertical signal (red) resonator of frequency  $\omega_S$  respectively. These resonators are connected to transmission lines by coupling capacitors designed to over-couple the signal and idler resonators, i.e  $Q_c \ll Q_{\text{int}}$ . This ensures that microwave signals enter and leave the device faster than any internal loss rates of the device.

The idler and signal modes are driven resonantly on the  $\Delta$  ports of a pair of  $180^\circ$ -hybrids to match the current patterns of the  $X$  and  $Y$  modes respectively of the JRM. The pump mode is driven non-resonantly at  $\omega_P = \omega_S + \omega_I$  on the  $\Sigma$  of one of the two  $180^\circ$ -hybrids. Although driving the exact  $Z$ -mode pattern shown in the bottom right of Fig. 2.2 requires a third cascaded  $180^\circ$ -hybrid, in experiments, this third hybrid is often omitted to reduce hardware while still providing sufficient coupling to the  $Z$  mode. When the JPC is biased to a magnetic flux of  $\Phi/2$  by an external coil, the device behaves as a three-wave mixing phase-preserving amplifier with the following interaction term under the rotating wave approximation [123]:

$$\mathbf{H}_{\text{JPC}}/\hbar = g_3 \left( \mathbf{a}^\dagger \mathbf{b}^\dagger \mathbf{c} + \mathbf{a} \mathbf{b} \mathbf{c}^\dagger \right) \quad (2.9)$$

Here,  $\mathbf{a}$ ,  $\mathbf{b}$ , and  $\mathbf{c}$  are the mode operators for the idler, signal and pump modes respectively and  $g_3$  is the strength of the three-wave mixing coupling.

In this mode of operation, the JPC can be effectively treated as a two-port device, where

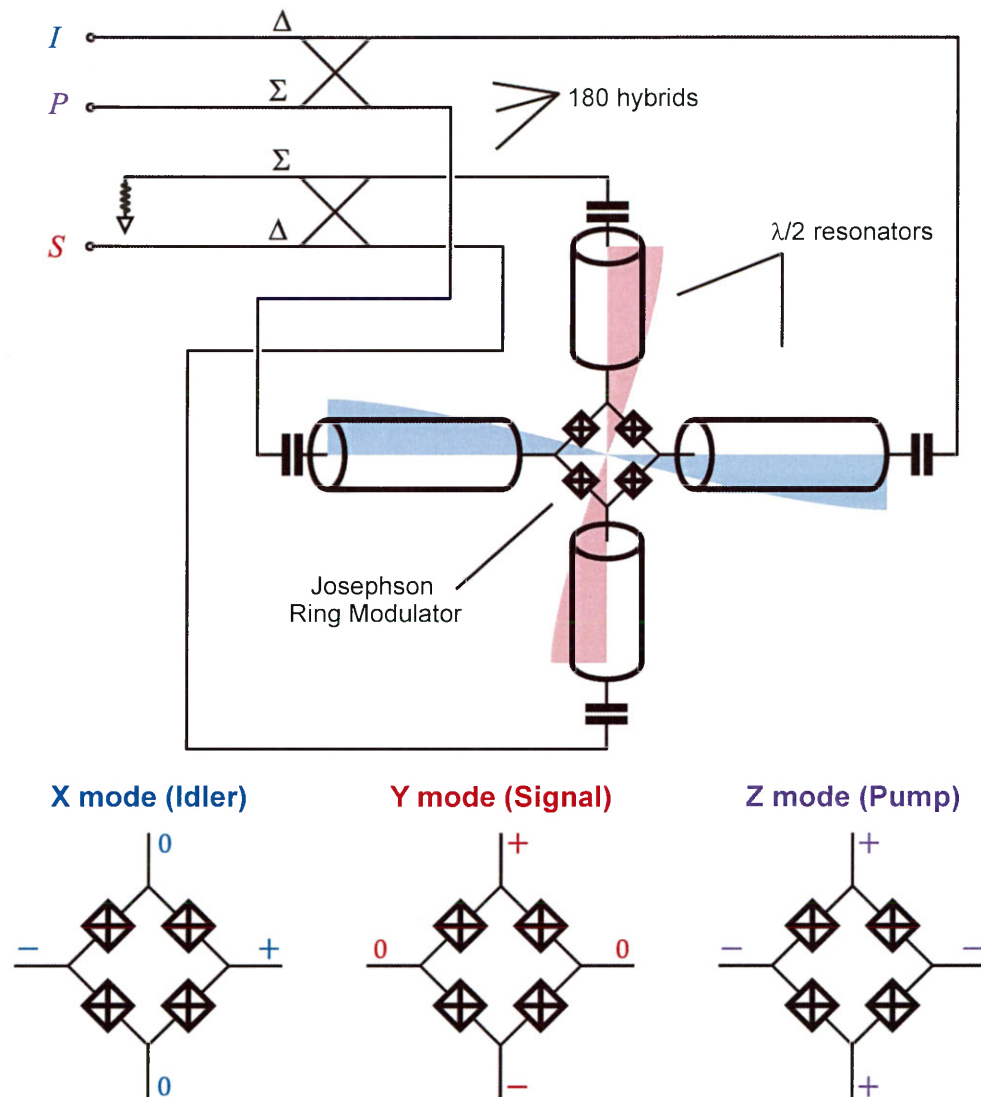


Figure 2.2 | **A Summary of the Josephson Parametric Converter.** The Josephson Parametric Converter (JPC) consists of a ring of four Josephson junctions (called the Josephson Ring Modulator or JRM) placed in the middle of two  $\lambda/2$  microstrip resonators. These form the resonant signal ( $\omega_S$ ) and idler ( $\omega_I$ ) modes of the device. Driven by hybrids, the idler couples to the X-mode of the ring and the signal to the Y-mode. Driving with a non-resonant pump tone coupled to the Z-mode at the sum of the signal and idler frequencies ( $\omega_P = \omega_S + \omega_I$ ) results in three-wave mixing in the JRM. Consequently, a pump photon is coherently converted into a signal and a idler photon. As a result, small signals incident on the signal and idler modes are reflected with gain.

incoming microwave signals are typically from a qubit-cavity system, and outgoing signals go to further amplification. Shown in Fig. 2.3A is a schematic of how the JPC is typically connected

in an experiment; the separation of these incoming and outgoing signals is achieved using non-reciprocal elements like the circulators in Fig. 2.3A. The two-port scattering matrix of this device on resonance, shown visually in Fig. 2.3B, relates the JPC output signals  $a^{out}$  to those incident  $a^{in}$ :

$$\begin{pmatrix} a_I^{out} \\ a_S^{\dagger out} \end{pmatrix} = \begin{pmatrix} \sqrt{G} & -ie^{-i\phi_p}\sqrt{G-1} \\ ie^{i\phi_p}\sqrt{G-1} & \sqrt{G} \end{pmatrix} \begin{pmatrix} a_I^{in} \\ a_S^{\dagger in} \end{pmatrix} \quad (2.10)$$

where  $G$  is the power gain and  $\phi_p$  is the phase of the pump drive. The power gain is determined by the power of the pump tone. Thus, the JPC provides amplification in two ways: (1) reflection gain where incident signals are reflected with gain but without frequency conversion; (2) transmission gain where incident signals are amplified with frequency and port conversion between the signal and idler frequencies.

Although the JPC can be operated in a number of different ways, for example a gain-less frequency converter (from which its name is derived) [123], a circulator or even a directional amplifier [131, 132], here, we limit our discussion to how it is used in the experiments in this thesis as a phase-preserving amplifier. Although the frequency of the signal and idler resonators can be engineered to be almost anywhere between 5 to 11 GHz, for the experiments in this thesis, they were chosen to be near the frequencies of the cavities they were connected to, putting them around 7.5 GHz or 9.0 GHz. The devices were designed and fabricated with quality factors of about  $Q_c = 100$  to maximize the instantaneous bandwidth (typically between 50 to 100 MHz) while keeping the device stable by satisfying  $Q_c p \sim 10$ , where  $p$ , the participation ratio, is the ratio of the Josephson inductance to the total inductance [123]. One important difference of the JPCs used in the experiments of this thesis from their description presented above is that the devices had JRMs which were shunted by 4 additional Josephson junction to significantly increase their tunable bandwidth to around 200 MHz [120]. The JPCs were operated at a power gain of 20 dB so that amplified signals from the JPC exceeded the added noise of the following HEMT amplifier. At this gain, they typically had an instantaneous bandwidth of about 5 to 10 MHz with an NVR ranging between 7 to 10 dB. The operating gain was chosen to balance between having sufficiently large NVR to enable single-shot readout while keeping the instantaneous bandwidth

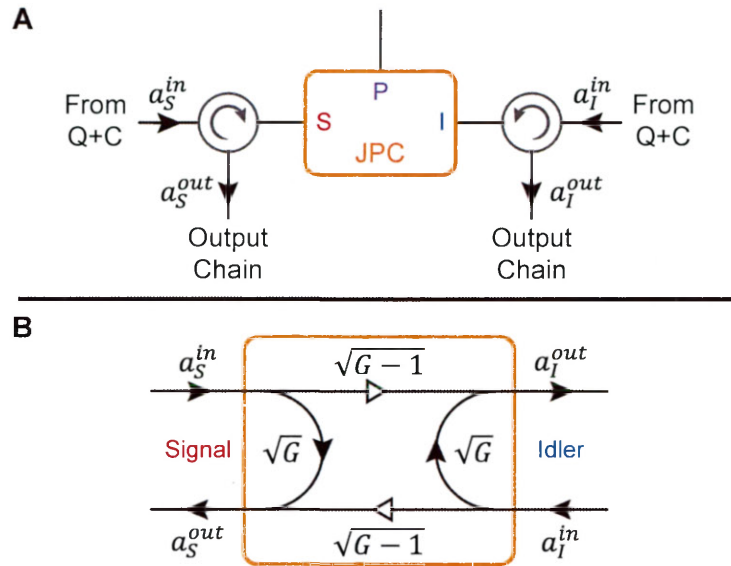


Figure 2.3 | **Effective Block Diagram for the JPC.** A) Connection schematic of a JPC in an experimental system. For representation in circuit schematic diagrams, the JPC circuit of Fig. 2.2 is depicted as a block with three ports: idler (I), signal (S), and pump (P). Microwave tones incident on these ports couple to the X, Y and Z modes of the JPC (see Fig. 2.2). A non-resonant microwave drive applied at  $\omega_P = \omega_S + \omega_I$  on the pump port is used to operate the JPC as a phase-preserving reflection amplifier. The spatial separation of incoming and outgoing microwave tones on the signal and idler ports is achieved by circulators. One port of each circulator is connected to the qubit-cavity system and the other is connected to the output chain for further amplification and demodulation. B) Visual representation of the scattering matrix for a JPC operated as a phase-preserving amplifier. A non-resonant drive on the pump port at frequency  $\omega_P = \omega_S + \omega_I$  results in the JPC operating as a phase-preserving amplifier. The resulting output on the signal (idler) port,  $a_S^{out}$  ( $a_I^{out}$ ), is the sum of a reflection gain component, tones incident on the signal (idler),  $a_S^{in}$  ( $a_I^{in}$ ), reflected with power gain,  $G$ , and a transmission gain component, tones incident on the idler (signal) transmitted with power gain,  $G - 1$ , and frequency conversion.

of the amplifiers greater than the linewidths of the cavities they were connected to.

Usually, the JPC is operated in continuous-wave (CW) mode where the pump tone is always on and the JPC provides gain at all times; however, in all the experiments in this thesis, the JPC was instead operated in a pulsed mode. The pump tone was pulsed so that the JPC provided gain only when it was being used to perform readout or other operations; otherwise, the pump tone was off and JPC behaved as a unit-reflector. This pulsed mode of operation is advantageous to prevent heating of the base stage of the dilution fridge from pump power dissipation as well

as in some experiments where turning on the JPC reduced the relaxation times or coherence times of the qubits. When operated in pulsed mode, it is important that the gain of the JPC is constant over the duration of the microwave pulse it is amplifying; to this end, the pump tone is turned on before and switched off after the readout tone. Since the JPC rings up to its operating gain point on a time scale given by its instantaneous bandwidth, for the JPCs that we use with typical 20 dB gain bandwidths of 5 MHz, this ring-up and ring-down time is chosen to be around 200 ns. Experimentally, the buffer time between when the JPC pump tone and readout tone are turned on or off is varied to find the shortest time that does not affect the measurement strength or fidelity.

Although the JPC is a robust and versatile plug-and-play module in the superconducting quantum circuit toolbox, it does suffer from a few limitations that adversely affect the experiments of this thesis<sup>3</sup> (for a detailed discussion of this and potential solutions, see Ref. [123]). One of the primary problems is the limited instantaneous bandwidth and 1-dB compression power for this amplifier; ideally, increased bandwidth could be obtained by using larger coupling capacitors to lower  $Q_c$  and increased saturation power could be obtained from using Josephson junction with larger critical currents. However, since the JPCs used here have microstrip resonators, they suffer from  $p \sim 0.1$  and either of those two would result in  $Q_c p$  falling below the safe value of 10. One explored strategy is to replace the microstrip resonators with a lower impedance embedding structure, such as parallel-plate capacitors, to increase the participation ratio to  $p \sim 0.5$ . This would enable devices with smaller  $Q_c$  or larger critical current junctions, which would in turn lower  $p$ . However, this strategy requires further optimization [1].

A second major problem with the JPC is its limited efficiency arising both from the internal losses of the device and its operation as a reflection amplifier. As it is currently fabricated [123, 131], the JPC suffers from a low internal quality factor  $Q_{\text{int}} \sim 3000$  to 5000 limiting the efficiency of the JPC due to losses to  $\eta_{\text{JPC}} \sim 0.9$ . In fact, as a result of the materials used in their fabrication, the internal quality factors of most Josephson junction parametric amplifiers are limited to this level, underscoring a need for lower-loss dielectrics and circuits. Moreover, as a

<sup>3</sup>Note that the limitations described for the JPC are not unique to this amplifier. Instead, they are common to many parametric amplifiers and overcoming them is the subject of active research.

reflection amplifier, the JPC necessitates the use of lossy circulators which introduce loss and are a primary limitation to the overall measurement efficiency (see Ch. 1.5 and Ch. 3). Directional amplifiers that provide gain in transmission (and not in reflection) would obviate the need for such lossy elements and are an area of intense research but have not matured in performance and ease of use and fabrication to entirely replace reflection amplifiers [69, 84, 132].

Addressing these limitations of the JPC, and parametric amplifiers in general, remains an area of active research, and will be essential to achieving improved measurement fidelity and efficiency beyond what is presented in this thesis.

## 2.4 Dispersive Readout of a Qubit in Circuit QED

We now put the tools discussed in the previous two sections together to describe how the dispersive interaction of cQED can be used to perform quantum non-demolition readout of the qubit, the underlying operational primitive for all the experiments in this thesis. This readout protocol is summarized as a quantum algorithm in Fig. 2.4. The qubit to be measured, here also referred to as Alice, begins in some arbitrary state  $\psi$ , for example  $\psi = \alpha |g\rangle + \beta |e\rangle$  where  $|\alpha|^2 + |\beta|^2 = 1$ <sup>4</sup>. As was described in Fig. 1.1, the measurement process begins by entangling Alice with a pointer variable, here a traveling coherent state  $|\alpha\rangle$  (containing an average number of photons  $\bar{n} = |\alpha|^2$ ); the entanglement between Alice and the coherent state is a result of the interaction term  $\chi a^\dagger a b^\dagger b$  in the cQED Hamiltonian which imparts the cavity with a qubit-state dependent frequency. Thus, the coherent incident on the system, upon interacting with the cavity, acquires a qubit-state dependent amplitude and phase response. The interaction between Alice and the pointer variable is described by

$$U_{\text{cQED}} = e^{-i\theta\sigma_z a^\dagger a/2} \quad (2.11)$$

<sup>4</sup>Since our transmon is not a true two-level system, the qubit state could also have components in other states like  $|f\rangle$  and higher

where  $\theta$  is the shift acquired by the coherent state. Note that in writing  $U_{\text{cQED}}$ , we are now treating the qubit as a true two-level system by using the Pauli operator  $\sigma_z$ . After this interaction, the total system state of qubit and pointer variable is  $\alpha |g\rangle |\alpha_g\rangle + \beta |e\rangle |\alpha_e\rangle$ .

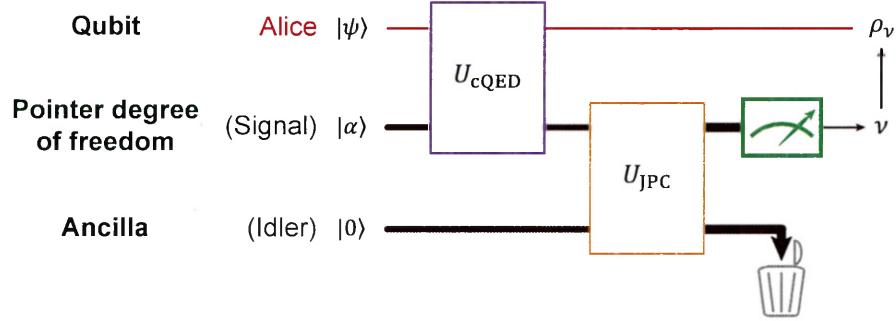


Figure 2.4 | **Single Qubit Measurement Schematic in circuit-QED.** The measurement of a superconducting qubit in cQED is very similar to that described in Fig. 1.1. First, the stationary qubit, Alice, is entangled with a pointer variable, in this case a coherent state  $|\alpha\rangle$ , by the dispersive qubit-cavity interaction described by the unitary operation  $U_{\text{cQED}}$ . Next, the pointer variable is amplified by a parametric amplifier, in this case the JPC, which has two modes, the signal and the idler. The coherent state entangled with the qubit enters the amplifier as the signal mode whereas the idler mode input is the vacuum state  $|0\rangle$ . The action performed by the amplifier is described by the unitary operation  $U_{\text{JPC}}$ . Finally, the measurement of the qubit is completed when the signal output of the JPC is measured and the idler output discarded.

Since the pointer variable has a higher-dimensional Hilbert space than that of the qubit, this interaction already serves as a first stage of amplification as it maps one bit of information encoded in a two-level system onto a multi-level system. Following this, the pointer variable enters the signal port of the JPC and undergoes further amplification. The JPC is operated as a phase-preserving amplifier (described in the previous section) with the idler input, here called the ancilla, in the vacuum state  $|0\rangle$ . The amplification operation performed by the JPC is summarized by the unitary:

$$U_{\text{JPC}} = e^{\Lambda a^\dagger b^\dagger - \Lambda^* a b} \quad (2.12)$$

where  $\Lambda = \lambda e^{i\phi}$ . Here  $\phi = -\phi_p + \pi/2$  is related to the phase of the pump tone  $\phi_p$  and  $\lambda = \ln(\sqrt{G} + \sqrt{(G-1)})$  depends on the power gain of the amplifier  $G$ . After  $U_{\text{JPC}}$ , the pointer variable is amplified to the larger coherent state with average photon number  $G\bar{n}$ , pictorially

represented by the increased thickness of the black line in Fig. 2.4. Alice is now entangled with both the signal and idler degrees of freedom but in the high-gain limit where we operate, the signal and idler contain the same information [51]. Thus, we throw away the information in the idler by terminating its output in a matched cold load ( $Z = 50 \Omega$ ) and measure only the signal resulting in a measurement outcome  $\nu_i$ . From this measurement outcome, the final state of the qubit, written as the density matrix  $\rho_f$ , as a result of measuring  $\nu_i$  is calculated using the generalized measurement formalism [50]

$$\rho_f | \nu_i = \frac{M_{\nu_i} \rho_i M_{\nu_i}^\dagger}{\text{Tr} (M_{\nu_i} \rho_i M_{\nu_i}^\dagger)} \quad (2.13)$$

Here  $M_{\nu_i}$  is the measurement operator for the outcome  $\nu_i$  whose exact form depends on the measurement process<sup>5</sup>. The probability of measuring an outcome  $\nu_i$  is given by

$$P_{\nu_i} = \text{Tr} (M_{\nu_i} \rho_i M_{\nu_i}^\dagger) \quad (2.14)$$

This generalized measurement formalism yields the projective measurements described in Ch. 1.2 when  $M_{\nu_i}$  is an orthogonal, Hermitian projector  $\Pi_{\nu_i}$  satisfying the normalization condition  $\sum_i M_{\nu_i}^\dagger M_{\nu_i} = \sum_i \Pi_{\nu_i} = 1$  [50].

For a more concrete picture of the dispersive cQED measurement, let us recast this process in terms of the experimental setup as shown in Figs. 2.5 and 2.6. The traveling coherent state  $|\alpha\rangle$  is a microwave frequency pulse with an average photon number  $\bar{n} = |\alpha|^2$ . This pulse is incident on the weakly-coupled port of the cavity, for the case of measurement in transmission (Fig. 2.5A), or the strongly-coupled port for the case of measurement in reflection (Fig. 2.6A). When measured in transmission, the cavity has a Lorentzian line shape with a bandwidth  $\kappa$  and a qubit-state dependent center frequency. The cavity resonance frequency is shifted by  $\chi$  to the left of  $f_c^g$  for every excitation in the transmon. Thus, an incident coherent state will acquire a phase and amplitude response dependent on the state of the cavity, and hence the qubit. As

<sup>5</sup>The exact form of the measurement operator for the dispersive readout described here is derived in Refs. [51, 131]. As another example, the measurement operators for a single photon detector are described in Ch. 5.8.

shown in Fig. 2.6B, a readout pulse at  $(f_c^g + f_c^e)/2$ , for example, will acquire a phase shift of  $\pm\vartheta/2$  for the qubit being in  $|g\rangle$  or  $|e\rangle$  respectively, encoding the qubit state onto the phase of the output coherent state. This strategy is used for the single qubit measurements discussed in Ch. 3 where  $\kappa \sim \chi$ . An alternative method for readout where the qubit state is encoded purely in the amplitude is also discussed in that chapter. In the case of measurement in reflection on the other hand, as shown in Fig. 2.6B, there is no amplitude response since the cavity is over-coupled; instead there is only a phase response. Reflections measurements of qubits and some of the advantages they offer are further discussed in Ch. 4. Since our transmon has higher levels, this measurement can learn some information about the qubit in those states; for the analysis below, we restrict ourselves to a measurement distinguishing only between  $|g\rangle$  and  $|e\rangle$ , and reserve the discussion for the effects of the higher order states to the end of the section.

Once entangled with Alice (shown by the color of the pulse changing to purple in Figs. 2.5A and 2.6A), they enter the signal port of the JPC and are amplified in reflection. Microwave circulators between the qubit-cavity and the JPC separate the incoming and outgoing signals while also providing reverse isolation to prevent the amplified reflected signal from reaching the qubit-cavity (although only one or two circulators are shown in the figures, up to three may be used in an experiment for adequate reverse isolation). The amplified coherent state then travels to higher temperature stages and is further amplified by a low-noise commercial HEMT amplifier. It is then further amplified at room temperature before it is down-converted and demodulated using a reference signal to measure the in-phase (I) and quadrature (Q) components of the pulse. This results in a measurement outcome  $\nu = (I_m, Q_m)$  that informs the observer about the state of the qubit.

To see how the final qubit state is inferred from the measurement outcome, we return to the measurement operator picture. This formalism is crucial to understanding that the measurement is not just a textbook projective measurement of the qubit, but actually a general quantum operation. The measurement operator for this dispersive readout process of a single qubit with a phase preserving amplifier where the other input is the vacuum state is  $M_{I_m, Q_m}$  (derived in

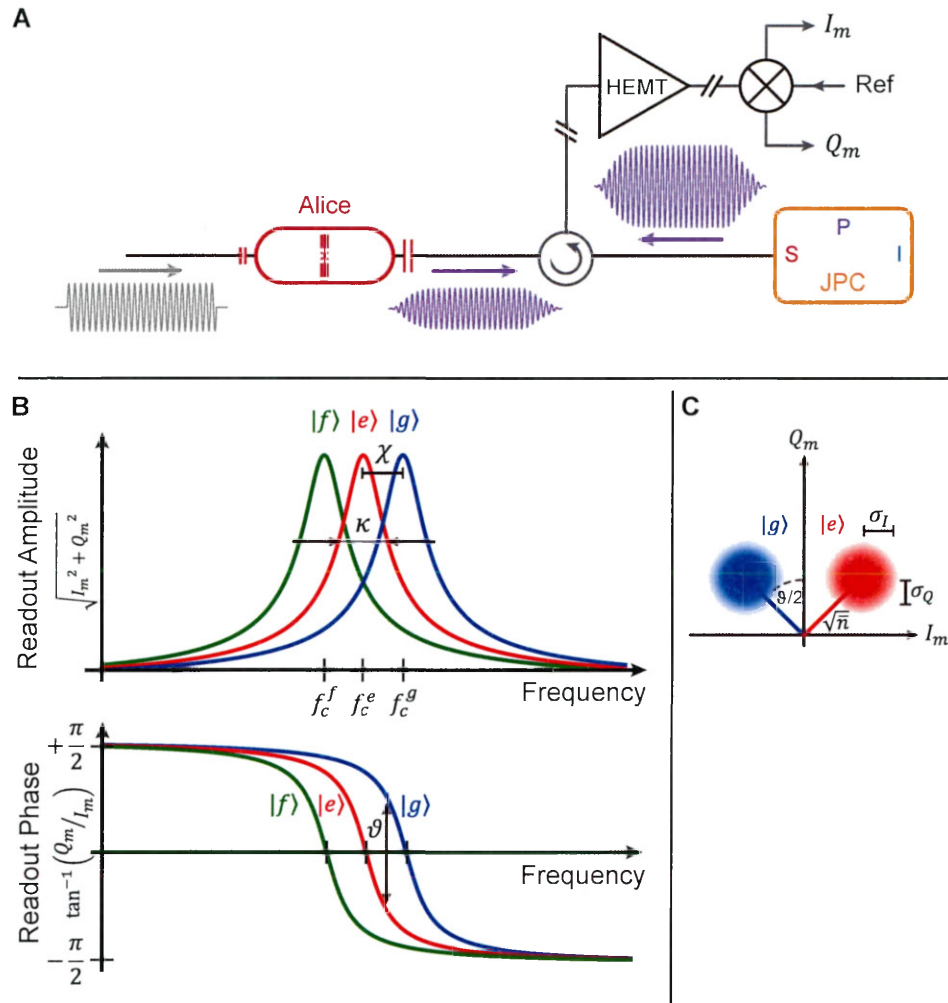


Figure 2.5 | **Transmission Measurement in circuit-QED.** A) Schematic of dispersive qubit readout in transmission. To measure the state of a 3D transmon qubit, a microwave pulse (a flying coherent state) is sent into the weakly coupled port of the cavity. Inside the cavity, the state of the qubit is entangled with the flying pulse as a result of the dispersive qubit-cavity interaction. The pulse leaves the cavity through the strongly coupled port and travels to a JPC where it is amplified before being directed by a circulator to further amplification at higher temperatures. Demodulating this signal and measuring its phase and amplitude completes the measurement process, thus allowing an observer to measure the state of the qubit. B) Amplitude and phase response of a dispersively coupled qubit-cavity system in transmission. As a result of the dispersive interaction between the qubit and cavity, the cavity acquires a qubit-state dependent frequency shift. The cavity resonance frequency, centered at  $f_c^g$  with linewidth  $\kappa$ , shifts by the dispersive shift  $\chi$  for every excitation in the qubit mode. C)  $IQ$ -space representation of the pointer variable. The state of the qubit is encoded in the color of the pointer variable (blue for  $|g\rangle$  and red for  $|e\rangle$ ). The measurement outcome  $\nu = (I_m, Q_m)$  informs the observer about the state of the qubit.

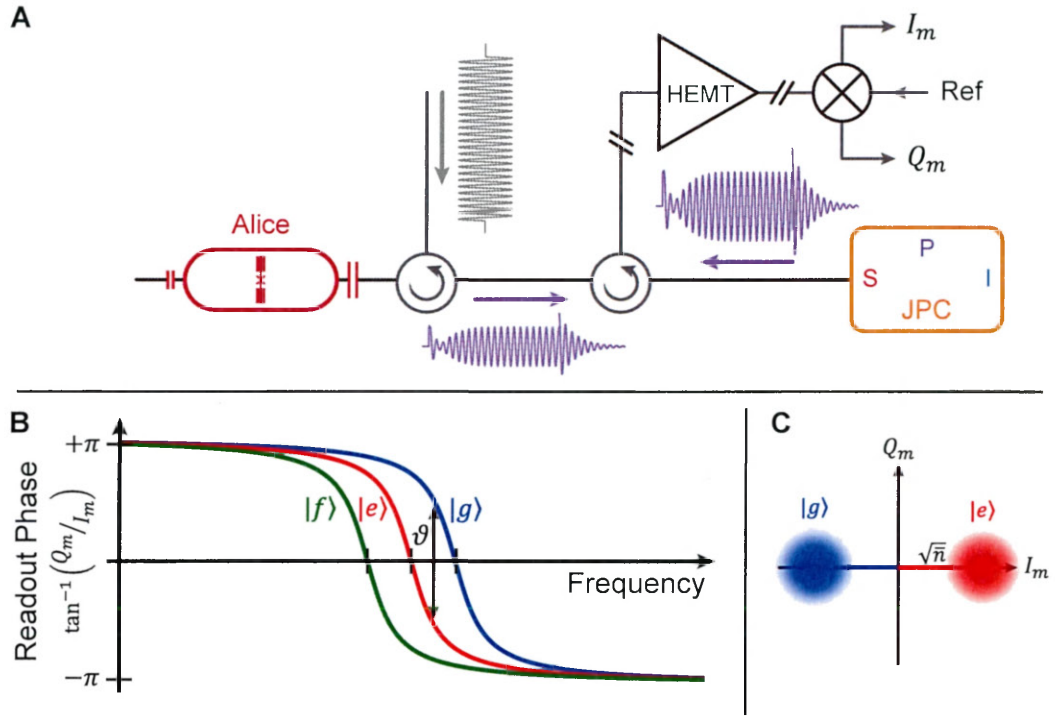


Figure 2.6 | **Reflection Measurement in circuit-QED.** A) Schematic of dispersive qubit readout in reflection. The measurement of a qubit-cavity system in reflection is identical to the process described in Fig. 2.5 except that in this case, the microwave pulse is incident on the strongly coupled port of the cavity instead. B) Phase response of a dispersively coupled qubit-cavity system in reflection. Unlike the case of measurement in transmission, when a cavity, specifically an over-coupled cavity, is measured in reflection, there is only a phase response and no amplitude response. This, the output coherent state acquires a qubit-state dependent phase shift that is measured to determine the state of the qubit. C)  $IQ$ -space representation of the pointer variable. The state of the qubit is encoded in the color of the pointer variable (blue for  $|g\rangle$  and red for  $|e\rangle$ ). The measurement outcome  $\nu = (I_m, Q_m)$  informs the observer about the state of the qubit.

Refs. [51, 131]<sup>6</sup>):

$$M_{I_m, Q_m} = \frac{1}{\sqrt{\pi}} e^{-\frac{(Q_m - \bar{Q}_m)^2}{4\sigma_m^2}} \begin{pmatrix} e^{-\frac{(I_m + \bar{I}_m)^2}{4\sigma_m^2}} e^{\frac{iI_m Q_m}{2\sigma_m^2}} & 0 \\ 0 & e^{-\frac{(I_m - \bar{I}_m)^2}{4\sigma_m^2}} e^{-\frac{iI_m Q_m}{2\sigma_m^2}} \end{pmatrix} \quad (2.15)$$

Here  $\sigma_m^2 = 1/2$ . Assuming a qubit that starts pointed along the  $+Y$ -axis of the Bloch sphere,  $|\psi\rangle_i = |+Y\rangle$ , and a perfect measurement process where no information is lost, the distribution

<sup>6</sup>A discussion of this measurement process for phase sensitive amplification can be found in Ref. [131].

of possible measurement outcomes is:

$$P(I_m, Q_m) = \text{Tr} \left( \mathbf{M}_{I_m, Q_m} \rho_i \mathbf{M}_{I_m, Q_m}^\dagger \right) \quad (2.16)$$

$$= \frac{1}{8\pi\sigma_m^2} \exp \left\{ -\frac{(Q_m - \bar{Q}_m)^2}{2\sigma_m^2} \right\} \left[ \exp \left\{ -\frac{(I_m - \bar{I}_m)^2}{2\sigma_m^2} \right\} + \exp \left\{ -\frac{(I_m + \bar{I}_m)^2}{2\sigma_m^2} \right\} \right] \quad (2.17)$$

We find that  $P(I_m, Q_m)$  is an equal superposition of two Gaussian distributions, one centered around  $(-\bar{I}_m, \bar{Q}_m)$  and the other around  $(\bar{I}_m, \bar{Q}_m)$ . This corresponds to the equal probability of measuring the qubit in  $|g\rangle$  or  $|e\rangle$ ; indeed, if the qubit is prepared in some arbitrary superposition state, the weights of the two Gaussian distributions will change accordingly. Moreover, these distributions have a variance  $\sigma_m^2 = 1/2$  that is twice the variance of a coherent state  $\sigma_I^2 = \sigma_Q^2 = 1/4$  corresponding to the added half-photon of noise from phase preserving amplification [20, 51]. Paralleling the discussion in Ch. 1.2, we see that a discrete state of a qubit can be recovered from a continuous variable measurement outcome by thresholding the outcomes, here at  $I_m = 0$ ; outcomes to the left (right) correspond to measuring the qubit in  $|g\rangle$  ( $|e\rangle$ ) as shown in Fig. 2.5C and Fig. 2.6C.

Furthermore, we can also calculate the final state of the qubit for a measurement outcome using

$$\rho_f(I_m, Q_m) = \frac{\mathbf{M}_{I_m, Q_m} \rho_i \mathbf{M}_{I_m, Q_m}^\dagger}{\text{Tr} \left( \mathbf{M}_{I_m, Q_m} \rho_i \mathbf{M}_{I_m, Q_m}^\dagger \right)} \quad (2.18)$$

The final qubit state in the two-level Bloch vector basis as a function of the measurement outcome is:

$$x_f(I_m, Q_m) = \text{sech} \left( \frac{I_m \bar{I}_m}{\sigma^2} \right) \sin \left( \frac{Q_m \bar{I}_m}{\sigma^2} \right) \quad (2.19)$$

$$y_f(I_m, Q_m) = \text{sech} \left( \frac{I_m \bar{I}_m}{\sigma^2} \right) \cos \left( \frac{Q_m \bar{I}_m}{\sigma^2} \right) \quad (2.20)$$

$$z_f(I_m, Q_m) = \tanh \left( \frac{I_m \bar{I}_m}{\sigma^2} \right) \quad (2.21)$$

From this, we can see that the  $I_m$  component of the measurement outcome informs the observers about the  $Z$  component, i.e. the polarization, of the qubit state. On the other hand, the  $Q_m$

component encodes the phase of the resulting qubit state. Indeed, when  $I_m$  is very large, for example, the final qubit state has  $x_f = y_f = 0$ , realizing a projective measurement. In general, the back-action of such a perfect measurement is to kick the qubit to an unpredictable location on the Bloch sphere; however, from the measurement outcome  $\nu = (I_m, Q_m)$ , an observer has perfect knowledge of the final state of the qubit. Moreover, this happens despite the added half photon of noise from the JPC; this is because the added noise only changes the back-action of the measurement but, as long as no information is lost, the qubit state remains pure<sup>7</sup>.

So far we have dealt with the case of a perfect measurement of a two-level system where no information is lost. However, in practice, not only does our measurement suffer from a loss of information due to imperfections in the output amplification chain, our transmon qubit has more than two levels. We address each of these problems in the next two sections.

### 2.4.1 Finite Efficiency - The cost of information loss

The coherent state pulse we use as a pointer variable suffers from photon loss as it travels from the qubit-cavity system to the measurement apparatus at room temperature. As a result, the observer only gains a fraction of the information about the qubit state, losing the rest to unmonitored information channels. The fraction of the total information gained by the observer is characterized by the measurement efficiency  $\eta$ ; it can be understood as the addition of extra noise to the measurement inflating the measured Gaussian distributions to an observed variance  $\sigma$ . Thus,  $\eta = \sigma_m^2 / \sigma^2$  is the ratio of the ideal to the measured variance.

In the presence of this information loss, a measurement leaves the qubit in the final state in

---

<sup>7</sup>For a discussion of the back action of a phase sensitive amplifier and how it differs from the phase preserving case, see Ref. [131].

the Bloch vector basis:

$$x_f(I_m, Q_m) = \operatorname{sech}\left(\frac{I_m \bar{I}_m}{\sigma^2}\right) \sin\left(\frac{Q_m \bar{I}_m}{\sigma^2} + \frac{\bar{Q}_m \bar{I}_m}{\sigma^2} \left(\frac{1-\eta}{\eta}\right)\right) e^{-\frac{\bar{I}_m^2}{\sigma^2} \left(\frac{1-\eta}{\eta}\right)} \quad (2.22)$$

$$y_f(I_m, Q_m) = \operatorname{sech}\left(\frac{I_m \bar{I}_m}{\sigma^2}\right) \cos\left(\frac{Q_m \bar{I}_m}{\sigma^2} + \frac{\bar{Q}_m \bar{I}_m}{\sigma^2} \left(\frac{1-\eta}{\eta}\right)\right) e^{-\frac{\bar{I}_m^2}{\sigma^2} \left(\frac{1-\eta}{\eta}\right)} \quad (2.23)$$

$$z_f(I_m, Q_m) = \tanh\left(\frac{I_m \bar{I}_m}{\sigma^2}\right) \quad (2.24)$$

From these equations, we can see that an inefficient measurement reduces the Bloch vector amplitude

$$\langle R \rangle_c^2 = \langle X \rangle_c^2 + \langle Y \rangle_c^2 + \langle Z \rangle_c^2 = 1 - \operatorname{sech}\left(\frac{I_m \bar{I}_m}{\sigma^2}\right) \left(1 - \exp\left\{-\frac{2\bar{I}_m^2}{\sigma^2} \frac{1-\eta}{\eta}\right\}\right)^2 \quad (2.25)$$

Unlike an efficient measurement where the state of the qubit remained pure, the loss of information during an inefficient measurement results in the dephasing of the qubit. Hence, the qubit Bloch vector amplitude shrinks to  $R^2 < 1$  depending on the amount of information lost. However, from the unchanged form of  $z_f$ , we can see that, in the limit where the argument of the  $\tanh$  becomes very large, the qubit ends up in  $z_f = \pm 1$  with  $x_f = y_f = 0$ . The limit of a projective measurement where the outcome is an eigenstate of the measurement is recovered; what is more, in this limit, even a finite efficiency measurement can yield a final qubit state that is pure.

A useful parameter to characterize these measurements is the measurement strength

$$\frac{\bar{I}_m}{\sigma} = \sqrt{2\bar{n}\eta\kappa T_m} \sin \vartheta/2 \quad (2.26)$$

where  $\bar{n}$  is the average photon number in the pulse,  $T_m$  is the pulse length and  $\vartheta = 2 \arctan \chi/\kappa$ . When the value of  $\bar{I}_m/\sigma$  is small, the measurement is considered to be weak and the resulting qubit state suffers from dephasing. It is only when the strength of the measurement increases and  $\bar{I}_m/\sigma$  is large that the Bloch vector amplitude recovers. In fact, it is the projectiveness of the measurement that ends up purifying the final qubit state.

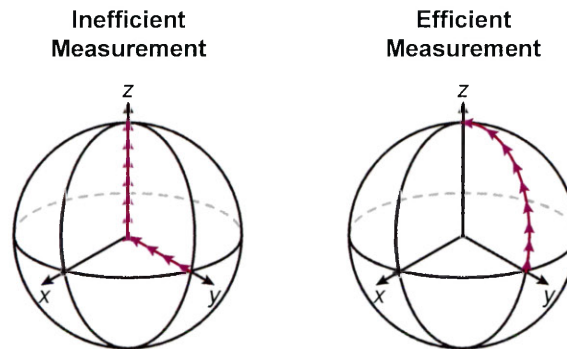


Figure 2.7 | **Contrasting Efficient and Inefficient Measurements.** Left: An inefficient measurement process causes the qubit state to first decohere driving it from a superposition state  $|y\rangle$  to the origin before projecting it to an eigenstate corresponding to the measurement outcome. Right: In contrast, an efficient measurement causes the state of the qubit to always remain on the surface of the Bloch sphere as it is projected to an eigenstate. Because no information about the state of the qubit is lost during the measurement, the qubit always remains in a pure state characterized by a unit Bloch vector.

The effect of measurement efficiency is represented as a trajectory in the Bloch sphere in Fig. 2.7. Shown on the left is a trajectory for an inefficient measurement; when a qubit is measured inefficiently, it initially dephases since information about its state is lost to the observer. As the strength of the measurement increases, the observer slowly learns about the state of the qubit and, in the limit of a projective measurement, the measurement actually purifies the qubit state until it ends up in an eigenstate of the measurement. On the other hand, when the measurement is efficient, the qubit always stays in a pure state and does not experience any dephasing (right in Fig. 2.7) as it is eventually projected to an eigenstate of the measurement.

Since information about the state is first lost during an inefficient measurement, and then only slowly learned, this process is slow, unlike an efficient measurement. It is for this reason that efficiency is intricately linked to the speed of a measurement. Moreover, this information picture also illustrates why efficient measurements are crucial when they are the basis for generating entanglement; any dephasing due to information loss would reduce the fidelity of the entangled state, and in the worst case scenario, result in separable state instead of an entangled one.

### 2.4.2 Higher Qubit Levels

A further source of complexity is that our transmon is not a true qubit, but instead a multi-level system. As shown in Figs. 2.5 and 2.6, the qubit being in a state like  $|f\rangle$  or higher results in the coherent state acquiring a different phase and amplitude shift. In principle, this dispersive readout could be used to gain information about the qubit state beyond just the  $|g\rangle$  and  $|e\rangle$  manifold of state; for example, instead of using a readout tone at  $(f_c^g + f_c^e)/2$ , a readout tone at  $f_c^e$  would result in a phase shift of  $+\vartheta/2$  for  $|g\rangle$ , 0 for  $|e\rangle$ , and  $+\vartheta/2$  for  $|f\rangle$ . This could enable readout that distinguishes between three states. However, for qubit states of excitations higher than  $|f\rangle$ , the output phase and amplitude response would be difficult to distinguish. Thus, in practice, the readout would actually inform an observer of the outcome  $|g\rangle$ ,  $|e\rangle$  or neither.

In fact, this is true with all measurements in this regime of dispersive cQED readout. Higher order qubit states that result in cavity resonance frequencies far from the readout frequency will be difficult to distinguish because of the phase and amplitude responses they cause will be indiscernible. Thus, we tailor the readout to maximize the information gained about the lowest two levels of the transmon. To learn about higher order states, we instead use qubit pulses that maps populations between the various states of interest to measure the transmon in a multi-state basis. Even when treated this way, it is always important to realize what information the measurement actually yields, which depends on the readout frequency in relation to  $\chi$  and  $\kappa$  as well as the thresholding used. We outline the cases of interest to this thesis below:

- $\chi \gg \kappa$  - In this regime (for experimental data, see Ch. 5.2), the separation between the lorentzian cavity responses  $\chi$  is much larger than the linewidth  $\kappa$ . This favors transmission readout on resonance with one of the cavity response frequencies,  $f_c^g$  for example, encoding the qubit state entirely in the amplitude and not the phase. Since the cavity phase response is thus indistinguishable for the states  $|e\rangle$  and higher, the readout actually distinguishes between the outcomes of measuring the ground state  $|G\rangle$  and not the ground state, expressed as  $|\bar{G}\rangle$ . By moving the readout frequency to the cavity resonance frequency corresponding to the state  $|i\rangle$  of the transmon at  $f_c^i$ , the readout informs the

observer about  $|i\rangle$  vs.  $|\bar{i}\rangle$ .

- $\chi \sim \kappa$  - In this case (experimental data in Ch. 3.8), the readout is more susceptible to learning a little information about nearby higher order states like  $|f\rangle$ . For example, the histograms in Fig. 1.6 show outcomes where the qubit was measured in  $|f\rangle$  or higher. However, by using a line threshold equidistant between the outcome distributions corresponding to  $|g\rangle$  and  $|e\rangle$ , these higher order states will also be recorded as  $|e\rangle$ . This reduces the measurement to one whose outcomes are again either the ground state,  $|G\rangle$ , or not,  $|\bar{G}\rangle$ .

Since many applications use only the lowest two levels of the qubit as the computational states (and even some operations that depend on higher order states only use them as an intermediary without encoding information in them), this effective readout that only discriminates between them and provides a single bit of information is sufficient. Even the joint readout techniques of Ch. 4.3 and Ch. 5.2 which provide more than a bit of information still only gain a single bit of information about each individual qubit.

# 3

## Efficient Single Qubit Measurements

Fast, fun, and efficient.

---

Alex the Grimm

### 3.1 Overview

Having established our choice of the superconducting quantum circuit toolbox in Ch. 2 and summarized the results for measurement fidelities and efficiencies in Ch. 1.5, in this chapter, we explore in further the techniques used to achieve these results. We begin in Ch. 3.2 by establishing an experimental checklist that outlines the requirements for high-fidelity and high-efficiency readout in the regime of dispersive cQED. Then, in Ch 3.3, we outline how to build experimental systems for high qubit coherence and readout performance. Next we expound upon how to enhance qubit lifetimes in fast cavities with Purcell filter in Ch. 3.1, shaping drives to minimize readout time with overdrive pulses in Ch. 3.6, and using a shaped demodulation window to minimize information loss in Ch. 3.7. With these tools, we take a more detailed look first at achieving high-fidelity QND readout of qubit-cavity systems in different regimes of  $\chi$  and  $\kappa$ .

in Ch. 3.4 and second at measurement efficiency in Ch. 3.9. Finally, we explore an alternative method to characterizing the measurement efficiency in a continuous-wave experiment using the quantum Zeno effect in Ch. 3.10.

## 3.2 Optimizing Qubit-Cavity Systems for Readout

From the results outlined in the discussion of QND dispersive readout of superconducting qubits in Ch. 2.4, we can translate the desires of high fidelity and efficiency readout into a set of requirements to be experimentally realized and optimized. Starting with Eq.2.26 for the apparent measurement strength, which is effectively a voltage signal-to-noise ratio (SNR), we define a power SNR:

$$\text{SNR} = \left( \frac{\bar{I}_m}{\sigma} \right)^2 = 2\bar{n}\eta\kappa T_m \sin^2 \left( \frac{\vartheta}{2} \right) = 2\bar{n}\eta\kappa T_m \frac{\chi^2}{\chi^2 + \kappa^2} \quad (3.1)$$

Since the measurement or readout fidelity is the faithfulness with which the outcome corresponds to the state of the qubit after it has been measured, maximizing the fidelity necessitates maximizing the SNR. Moreover, since the qubit relaxes at a rate  $\Gamma_1 = 1/T_1$ , the readout must be performed in a time much shorter than this relaxation time. To arrive at a SNR rate, we can divide the expression for the SNR above by the product  $\kappa T_m$ , which is the number of cavity lifetimes that the measurement takes:

$$\text{SNR per cavity lifetime} = \text{SNR}_{\text{rate}} = 2\bar{n}\eta \frac{\chi^2}{\chi^2 + \kappa^2} \quad (3.2)$$

Therefore, the number of bits of information about the qubit that can be acquired in  $T_1$  is

$$\text{number of bits per } T_1 = \frac{T_1}{T_m} \log_2 (1 + \kappa T_m \text{SNR}_{\text{rate}}) \quad (3.3)$$

Thus, not only do we want to achieve  $T_1 \gg T_m$  to minimize errors from qubit relaxation during the measurement, we also want to maximize the number of bits of information acquired during each measurement by maximizing  $\kappa T_m \text{SNR}_{\text{rate}}$ . However, this optimization must be done under constraints imposed by properties of the following JPC amplifier and the cQED Hamiltonian:

- **Limitations to  $\bar{n}$**  - Ideally, the  $\text{SNR}_{\text{rate}}$  can be increased by using a larger average photon number  $\bar{n}$  in the readout pulse. However,  $\bar{n}$  is experimentally limited to  $\bar{n} \sim 1$  to 10 by a combination of three factors: (1) the compression power of the JPC, usually on the order of a few photons in the amplifier bandwidth [123, 131]; (2) the breakdown of the dispersive regime of cQED; (3) the non-QNDness of the readout resulting from increased qubit relaxation rates when the cavity is populated with photons [13, 14], colloquially referred to as  $T_1$  versus  $\bar{n}$ .
- **Limitations to  $\chi$**  - Qubit-cavity systems with large  $\chi$  suffer from cavities with undesirably large non-linearities, which can be detrimental to readout. In the extreme case of readout cavity that is too non-linear, the addition of a single photon in the cavity will prevent any further photons at that frequency from entering the cavity (thus making the cavity behave like a qubit). Moreover, large dispersive shifts can also result in lower qubit relaxation times because of the Purcell effect [57]. Thus, in practice, the dispersive shift is often chosen such that  $\chi/2\pi < 10$  MHz.
- **Limitations to  $\kappa$**  - The cavity bandwidth must necessarily be smaller than the instantaneous bandwidth of the following amplifier, about 10 MHz for a JPC operated at  $G = 20$  dB, so that the information content of the readout pulse is amplified uniformly without distortion or loss.

Under these constraints, the design choices made to achieve high-fidelity and efficiency QND readout can be summarized as follows:

- **Maximize information per measurement  $\kappa T_m \text{SNR}_{\text{rate}}$**  - The cavity linewidth is maximized and designed to be  $\kappa/2\pi \sim 1$  to 5 MHz. While  $\kappa \sim \chi$  is preferred for large readout contrast, sometimes systems need to be engineered with  $\chi \gg \kappa$  to enable cavity-state-selective operations on the qubit (like the qubit-cavity systems used in Ch. 5). High fidelity measurement data for systems in both regimes are discussed in Ch. 3.8.
- **Maximize number of possible measurements  $T_1/T_m$**  - To minimize the measurement

infidelity due to qubit relaxation  $\mathcal{F}_{\text{msmt}} = e^{(-T_m/T_1)}$ , the systems are designed to maximize  $T_1$  (with the Purcell filters described in Ch. 3.1, for example) and minimize  $T_m$  (for example, with the shaped measurement pulses detailed in Ch. 3.6). While Eq. 3.3 would suggest choosing  $T_m \rightarrow 0$ , the lower limit on  $T_m$  is ultimately bounded by the bandwidth of the output measurement chain.

- **Minimize information loss to maximize  $\eta$**  - In addition to being crucial for using measurements as quantum operations, to generate remote entanglement for example, maximizing the measurement efficiency directly increases the SNR. One method for maximizing  $\eta$  for pulsed measurement is using the shaped demodulation described in Ch. 3.7.

With these constraints and design choices, we have a path towards achieving high-fidelity, QND readout of our transmon qubits using the dispersive interaction. Before proceeding to discuss the measurement fidelity in Ch. 3.8, we first discuss the microwave and cryogenic hygiene required for superconducting quantum circuit experiments, especially in the 3D cQED regime, to maximize qubit lifetimes and optimize for other system parameters that directly determine performance.

### 3.3 Engineering Experimental Systems - Cryogenic, Microwave and Quantum Hygiene

Superconducting quantum circuit experiments are performed at millikelvin temperatures for two reasons: (1) the circuits need to be cooled to below the superconducting critical temperature, which for aluminum is  $T_c \sim 1$  K; (2) they also need to be cooled to a temperature where the system is in the quantum ground state and thermal fluctuations are much smaller than the qubit or cavity transition frequency. For typical mode frequencies of  $\omega/2\pi = 5$  to 10 GHz, this requires cooling the circuits to below  $\hbar\omega/k_B \sim 200$  mK. Moreover, once cold, the transmon qubit would ideally only be coupled to the few modes to which it is designed to be coupled and are specified in the Hamiltonian (Eq. 2.3, for example). In the case of the experiments in this chapter and

thesis, the qubit should only be coupled to the  $TE_{101}$  mode of the rectangular cavity that it is placed in.

Of course, as is the nature of experimental physics, would that it were so simple. Cryogenic technology has advanced significantly in the past few decades, making commercially available dilution refrigerators that used to border on art form at the forefront of experimental physics. However, ensuring that all parts of the experiment are cooled to the base temperature of a dilution cryostat, around 20 mK, is still challenging. For example, a number of components used in superconducting quantum circuits experiments were not meant for cryogenic applications, consisting of dielectrics and other materials that are hard to cool down. This problem is further exacerbated by the need to get microwave signals in and out of the cryostat; design considerations for these input and output lines are discussed in the following subsections.

Furthermore, the environment seen by our qubit is not as simple as the Hamiltonian we use to describe it. Unfortunately, not only are the cavities themselves multi-mode objects, but the qubit is also coupled a plethora of other systems and environments. For example, there are defects in the substrate or the Josephson junction insulator that can couple to the qubit mode. Stray photons, ranging from radio-frequency to optical frequencies and beyond, can also be a problem. These unmonitored couplings will result in these systems extracting energy or information from the qubit, causing relaxation (characterized by  $T_1$ ) and dephasing (characterized by  $T_\phi$ ) respectively.

Addressing these various considerations is critical when designing and engineering a superconducting quantum circuit experiment. As the first step towards a successful experiment, we outline below the design choices made in the experiments of this thesis. The methods and practices were chosen to balance between competing considerations of cryogenic, microwave and quantum hygiene and experimental ease of assembly and use. Over the course of many experiments, there is empirical evidence that these choices have improved system performance, like qubit coherences.

### 3.3.1 Thermalization

Ensuring that all the experimental mounted to the base stage of the dilution cryostat are cooled to the base temperature of 20 mK begins by using, wherever possible (which is ideally everywhere),

materials with high thermal conductivity at low temperatures [108]. The material of choice in our experiments is oxygen-free high-conductivity (OFHC) copper, from which all the hardware to mount and thermalize samples is made. Once machined, the surfaces of the parts are sanded, in stages with increasingly fine (higher grit) sandpaper, to achieve a smooth surface with minimal residual tool marks. The parts are then cleaned by sonication in baths of detergent (Alconox), acetone and isopropanol to remove grease and other surface contaminants. Parts may also be plated with a 2 to 5  $\mu\text{m}$  thick gold layer (by electroplating with no nickel strike layer) for improved surface quality. When mounted in the cryostat, the quality of the thermal joint made between the part and the fridge is primarily determined by the point of contact, and especially the contact pressure. Parts are bolted to the fridge with stainless screws and nuts to maximize the fastening force that can be applied; furthermore, molybdenum washers are used at all joints because their low contraction with temperature [108] ensures that joints become tighter as the system cools. The number of thermal joints is also minimized where possible, especially between crucial components like cavities and the cold head of the dilution stage.

One of the main challenges encountered in thermalizing the various experimental components is materials whose cryogenic performance is questionable. Commercially used components in the experiments, as well as 3D superconducting quantum circuits, commonly contain metals with low thermal conductivity, like stainless steel, or dielectrics, like polytetrafluoroethylene and sapphire. Moreover, the very superconductors at the heart of our experiments have poor thermal conductivities below their critical temperature [2]. How these materials thermalize and behave at cryogenic temperatures and what, if any, effects they have remains an open question that needs to be investigated to ensure that they are not limiting experimental performance.

### 3.3.2 Magnetic Shielding

Magnetic fields can be detrimental to the behavior of superconductors; in the worst case scenario, if the applied magnetic field exceeds the critical field of the superconductor, the field can disrupt the superconducting state entirely [2]. To protect against external magnetic fields, like the Earth's field or ones arising from ferrite based components like circulators, the samples are housed inside

shields of Ammumetal 4K, a high magnetic permeability material. Additionally, shields made of aluminum can also be used to provide further screening of magnetic fields. Inside the shields, no magnetic components are used, where ever possible [144]. Microwave components like coaxial cables and SMA connectors as well as mounting hardware is carefully chosen to avoid magnetic materials like stainless steel. Of course, this introduces a conflict with the desire to thermalize components well, which favors using stainless steel fasteners. Compromises may be found in using brass or aluminum fasteners instead although this remains the topic of some debate.

### 3.3.3 Filtering against Radiation

Undesired stray electromagnetic radiation can be a large problem for the large frequency, and hence energy, range that it can span. While low energy radio-frequency radiation could be a source of noise in the experiment that induces qubit relaxation or dephasing, high energy infrared and optical radiation can generate quasiparticles and heat up experimental components [2, 144]. The cavities that our transmons are housed in form the first stage of radiation-tight shielding; seals made of indium wire are used minimize the amount of radiation that can leak in through any seams. Indeed, there is empirical evidence that qubit coherence suffers when the cavities are poorly designed and leaky to radiation. However, there remains room for improvement in cavity design by, for example, implementing radiation baffles composed of knife-edge seals along the cavity seams.

The samples are further shielded by wrapping them in layers of aluminized mylar and housing them in shields whose insides were coated in radiation absorptive material. This coating is made of epoxy (Stycast 2850) loaded with carbon black. While the cavities could be better shielded by potting the entire sample in this loaded epoxy material [5, 115], that has the undesirable consequences of making the cavity non-reusable. Alternatively, some samples are mounted in shields that are themselves hermetically sealed to make them radiation-tight. However, no difference in coherence and relaxation times has been observed for qubits in the two different types of shielding.

### 3.3.4 Fabrication and Sample Design

Perhaps inarguably the most opaque and challenging aspect of the field and the experimental process is sample fabrication. Often described as a dark art, the fabrication of Josephson junctions and other microwave frequency circuit elements involves multiple steps, like electron-beam lithography and electron-beam evaporation deposition, to name the two most common tools used for the samples in this thesis. Understanding how the vast number of fabrication parameters affect qubit coherence is an area of active research. We pursue an alternative strategy of carefully designing systems to minimize sensitivity to sources of loss; for example, embedding qubits in 3D cavities [103] or appropriate design of transmon antenna geometry [145] can reduce the participation ratio of lossy dielectrics suspected to limit relaxation times. However, further improving coherence properties may require revisiting some of the fabrication techniques. A suspected candidate for loss is the polymer based electron-beam resist used for lithography which may be hard to entirely remove before and after the deposition of aluminum.

### 3.3.5 Input Lines

The next challenge arises from the need to connect this carefully engineered experimental system at 20 mK with room temperature control and measurement hardware at 300 K. Signals travel to the experiment down what are called input lines, stages of coaxial cable anchored to the all temperature stages of the dilution cryostat (40 K, 3 K, 700 mK, 100 mK, and 20 mK) for thermalization. These inner and outer conductors of these cables are typically made of low thermal conductivity metals like stainless steel inner or niobium-titanium, a superconductor. The cables are designed with U-shaped bends to provide strain relief between cryostat temperature stages as well as increase the overall cable length, and thus decrease the thermal load between states.

To prevent these input lines from carrying radiation to the experiment, a number of filters are used. First, a microwave low-pass filter (K&L 6L250-12000/T26000-OP/O) is used to attenuate microwave frequency signals above 12 GHz. Ideally, a bandpass filter that with a lower cutoff

frequency around 4 GHz would be used to also filter low-frequency radiation but these filters are not readily available commercially in cryogenically compatible designs in low-profile packages. Additionally, homemade Eccosorb filters are used to attenuate infrared and optical frequency radiation; these filters are small section of coaxial cable with copper as the inner and outer conductor and Eccosorb CR-110 as the dielectric.

Additionally, the experiment must also be protected from microwave frequency noise incident on the experiment from the high-temperature stages. This is accomplished by adding broadband attenuators to the input lines to ensure that all the circuits see signals whose noise temperature is dominated by quantum, instead of thermal, fluctuations. The noise seen by the experiment is expressed in terms of a thermal photon number  $n_{th}$ . An attenuator will decrease power at its output by its attenuation  $A$  while adding thermal noise photons corresponding to its physical temperature  $n(T) = (\exp [hf/k_B T] - 1)^{-1}$ . Here  $h$  is the Planck constant,  $f$  is the operating frequency,  $k_B$  is the Boltzmann constant, and  $T$  is the physical temperature of the attenuator. Thus, the total number of thermal photons incident at the 20 mK stage is

$$n_{th}^{20mK} = \sum_i A_i n(T_i) \quad (3.4)$$

where  $i$  is the index of the cryostat temperature stages, each at temperature  $T_i$ ,  $A_i$  is the attenuation between the  $i^{\text{th}}$  and base stage, and  $n(T_i)$  is the thermal photon number of that stage. Since thermal photons in the cavity coupled to a qubit can result in measurement induced dephasing, limiting the qubit dephasing time to  $T_\phi = 1/n_{th}\kappa$ , where  $\kappa$  is the cavity bandwidth. Thus, we want to choose the attenuation at the various temperature stages to ensure that the thermal-photon-induced dephasing time is as long as possible. In practice, we design the lines so that the number of thermal photons is limited to around  $10^{-3}$  at most.

For most input lines, this is achieved with a 20 dB attenuator at the 3 K stage, a 10 dB attenuator at the 700 mK stage and a variable amount at the 20 mK base stage. The attenuation used at the base stage depends on the function of the input line; for input lines connected to the weakly coupled input port of a qubit-cavity, the attenuation is typically 20 dB since the weak

input coupling acts as further attenuation. On the other hand, for input lines connected to the strongly coupled port of the qubit-cavity (for diagnostics or measuring in reflection for example), the attenuation is typically 50 dB.

Two further important considerations that can drastically alter the amount of attenuation needed are the physical temperature of each attenuator as well as the noise temperature of the room temperature microwave signals. Since the commercial attenuators used have stainless steel housings, it is feared that they do not thermalize to the temperature stage that they are anchored. Similarly, as applications demand increased microwave signal power at the base stage (for example, to generate single photons with sideband transitions as discussed in Ch. 5.3), amplifiers used at room temperature can increase the signal noise temperature by many orders of magnitude. Careful filtering can be used to ensure that this large signal noise temperature is limited to a small bandwidth. In general, balancing the need to deliver adequate power with low thermal noise without heating up the fridge, while tractable, needs to be considered, especially as demands for experiments change with advances in system complexity.

### 3.3.6 Output Lines

Signals from the experiment travel back to room temperature for measurement and processing via output lines; these output lines need to satisfy the same requirements that the input lines do: thermalization, filtering, and minimal radiation and heat loads to the cryostat and experiment. Of course, this needs to be accomplished while amplifying small quantum signals into large classical ones with ultra-low added noise. Consequently, unlike the input lines with attenuators, the output lines rely on directional elements, like circulators and isolators. While the reverse isolation provided by these directional components attenuates thermal noise incident on the base stage from higher temperature stages of the cryostat, the low-insertion loss experienced by forward traveling signals does not degrade the signal to noise ratio (SNR). The loss encountered by signals as they traverse the output lines is also crucial in determining the system measurement efficiency; since any insertion loss of attenuation is a channel to which we lose information, mitigating these losses is crucial to achieving high measurement efficiency.

Examples of typical output lines can be seen in Fig. 4.1 and Fig. 5.1. After exiting the qubit-cavity system, signals are directed to the Josephson Parametric Converter (JPC) via a bank of two to three circulators (chosen so that the signals lie within their operating bandwidth). The output signal is amplified in reflection by the JPC and directed to a microwave low-pass filter and homemade Eccosorb filters (like those used on the input lines). Next, the signals pass through two broadband isolators (Quinstar CWJ1019-K414) which together provide about 36 dB of reverse isolation (hence providing a similar amount of attenuation to signals from higher temperature stages as that on the input lines). The signals travel from the 20 mK to the 3 K stage of the cryostat on superconducting coaxial cables (Coax Co. SC-219/50-NbTi-NbTi). At the 3 K stage, they are amplified by commercial high-electron mobility transistor (HEMT) amplifiers (from Low Noise Factory or Caltech). After the HEMT, the output signals are carried by stainless steel coaxial cables, like those used on the input lines, to room temperature for further amplification and demodulation.

To understand why the output lines were constructed this way, we look at the noise power  $P_{\text{out}}$  at the output of the HEMT amplifier as a function of the parameters of the output line. Consider a simplified model of the output consisting of the JPC, followed by some attenuation and then the HEMT; for now, we ignore any attenuation before the JPC for simplicity. The JPC and HEMT amplifiers have gains of  $G_{\text{JPC}}$  and  $G_{\text{HEMT}}$  respectively with noise temperatures of  $T_Q$  and  $T_N$  respectively. Here we are assuming that the JPC is quantum limited, adding only the minimal half-photon of noise for phase-preserving amplification [20],  $T_Q = \hbar\omega/2k_B$ . The attenuator has an attenuation  $A$  and has a physical temperature of  $T_A$ . Finally, we assume that the noise incident on the JPC has a temperature  $T_{in}$ . Thus, the output noise power after the second amplifier is

$$P_{\text{out}} = k_B B G_{\text{HEMT}} G_{\text{JPC}} \left[ T_{in} + T_Q + \frac{A}{G_{\text{JPC}}} (T_A + T_N) \right] \quad (3.5)$$

where  $k_B$  is the Boltzmann constant and  $B$  is the bandwidth of the amplification chain [109, 131]. To simplify this expression, we can define the system noise temperature  $T_N^{\text{sys}} = \frac{A}{G_{\text{JPC}}} (T_A + T_N)$ .

Thus we see that any attenuation before the HEMT worsens the system noise temperature and we rely on the gain of the JPC to counteract this. Since, in practice, the JPC can be operated with  $G_{\text{JPC}} \sim 20$  dB, making this attenuation as low as possible is imperative to ensuring SNR integrity. Consequently, the filters and other components between the JPC and HEMT are chosen to have the lowest possible insertion loss. For example, the Eccosorb filters used on the output lines have lower attenuations than the ones used on input lines. Moreover, each coaxial cable used on the output lines is carefully chosen to have the lowest possible insertion and reflection loss. Using superconducting coaxial cables with negligible attenuation, instead of stainless steel cables with about 10 dB of loss, keeps the system noise temperature close to the HEMT noise temperature  $T_N^{\text{sys}} \sim T_N \sim 3$  K. A useful proxy for the noise temperature is the noise visibility ratio (NVR), the ratio of the noise power measured at room temperature on a spectrum analyzer when the JPC is on to when it is off [96, 131]. For example, when the NVR= 10 dB, then the amplified signals from the JPC that a factor of ten larger than the added noise of the HEMT.

A second key takeaway from Eq. 3.5 is that without the JPC, signals would not be protected against losses before the HEMT. Similarly, although ignored in this calculation, signals are not protected against any losses encountered before the JPC. Since these losses also reduce measurement efficiency, minimizing these losses is crucial to achieving high measurement fidelity and efficiency. To this end, all filters are placed after the JPC. The number of joints between microwave components is kept to a minimum by directly attaching circulators to each other as well as using only two coaxial cables, one from the cavity to the circulator bank and the other from the circulator bank to the JPC. The lengths of these cables are kept as short as possible by efficient cable routing at the base stage as well as careful relative placement of the qubit-cavity and the JPC. Using superconducting cables instead of a copper ones also offers some improvement in insertion loss.

### 3.4 System Parameters

The data presented in this chapter comes from two different experimental systems: the first, called System 1, was used for the coherent state based remote entanglement experiment of Ch. 4; the second, called System 2, was used for the single photon based remote entanglement experiment of Ch. 5. Detailed experimental setups for these systems are shown in Fig. 4.1 and described in Ch. 4.2 for System 1 and Fig. 5.1 and Ch. 5.2 for System 2 respectively. Instead of repeating discussions of the setup (which are also outlined in the previous section), we instead just summarize the relevant system parameters:

Parameter	System 1	System 2
Cavity frequency $\omega_c^g/2\pi$ (GHz)	7.4813	7.6222
Cavity bandwidth $\kappa/2\pi$ (MHz)	4.9	0.9
Readout frequency $\omega_r/2\pi$ (GHz)	7.4794	7.6222
Qubit frequency $\omega_{ge}/2\pi$ (GHz)	5.0038	4.7664
Anharmonicity $\chi_{qq}/2\pi$ (MHz)	220	240
Dispersive shift $\chi/2\pi$ (MHz)	3.8	3
$T_1$ ( $\mu\text{s}$ )	70-90	90
$T_{2R}$ ( $\mu\text{s}$ )	10	25
$T_{2E}$ ( $\mu\text{s}$ )	25	30

Table 3.1 | High-fidelity measurements - qubit and cavity parameters

With these two qubit-cavity system, we explore the realization of high-fidelity readout in the two different regimes of  $\chi \sim \kappa$  for System 1 and  $\chi \gg \kappa$  for System 2.

### 3.5 Purcell Filters - Long Lived Qubits in Fast Cavities

Designing qubit-cavity systems that simultaneously have long qubit relaxation times  $T_1$  and strong coupling to a fast cavity  $\chi \sim \kappa \sim 1$  to 5 MHz for high-fidelity readout requires overcoming the Purcell effect [110]. When a system with quantized levels, like a qubit, is coupled to an environment with a continuum of modes, through a cavity, the relaxation rate of the qubit can be enhanced or suppressed [57, 114]; based on the frequencies of the qubit and cavity and their detuning, the density of states seen by the qubit is modified, thus affecting the relaxation rate

of the qubit. Since the cavity that our qubit is coupled to has many modes, the analysis of the Purcell limited qubit relaxation rate requires a multi-mode analysis [57]. This can be calculated using the circuit model of Ref. [57] where the qubit  $T_1$  depends on the qubit capacitance  $C$  and the admittance of the environment it is coupled to  $Y(\omega)$ :

$$T_1^{\text{Purcell}} = \frac{C}{\text{Re}[Y(\omega)]} \quad (3.6)$$

A strategy to minimize  $\text{Re}[Y(\omega)]$  is to build a Purcell filter which suppresses qubit relaxation by reducing the density of states in the environment at the qubit frequency without changing the environment at the cavity frequency to preserve  $\kappa$  [114]. Realizations of such Purcell filters have ranged from band-reject filters centered around the qubit frequency [114] to a bandpass filter centered near the cavity frequency [3, 63]. To implement a filter compatible with the 3D cQED architecture of our qubit-cavity systems that minimizes the number of added (lossy) components without introducing other microwave environments like printed-circuit boards, 2D resonators or 2D transmission lines, we use 3D rectangular waveguides, as shown in Fig. 3.1A. Since rectangular waveguides have a cutoff frequency below which microwave modes cannot propagate [109], they behave like a high-pass filter. Above this cutoff frequency, they are a very-loss transmission line. Thus, a Purcell filter can be realized by choosing the cutoff frequency to be above the qubit frequency but below the cavity frequency.

For our systems with cavity frequencies around 7.5 GHz and qubit frequencies around 5 GHz, we use a section of straight WR-102 (1.02 in wide by 0.51 in tall) rectangular waveguide since it has a cutoff frequency of  $f_{\text{cutoff}} = 5.8$  GHz and single-mode propagation frequency range of 7 to 11 GHz. The waveguides were made of either 6061 alloy Al or oxygen-free high-conductivity copper. The  $\text{TE}_{101}$  mode of the cavity is over-coupled to the waveguide by an aperture located at the anti-node of the mode. The aperture size determines  $\kappa_{\text{out}}$  and hence the cavity bandwidth  $\kappa$ . Using finite element electromagnetics simulations in HFSS, the aperture was designed to realize  $\kappa/2\pi \sim 5$  MHz for the cavity shown in Fig. 3.1<sup>1</sup>. The other end of the waveguide is

<sup>1</sup>Purcell filtered devices with  $\kappa/2\pi \sim 1$  MHz were used for the single-photon based remote entanglement experiment of Ch. 5

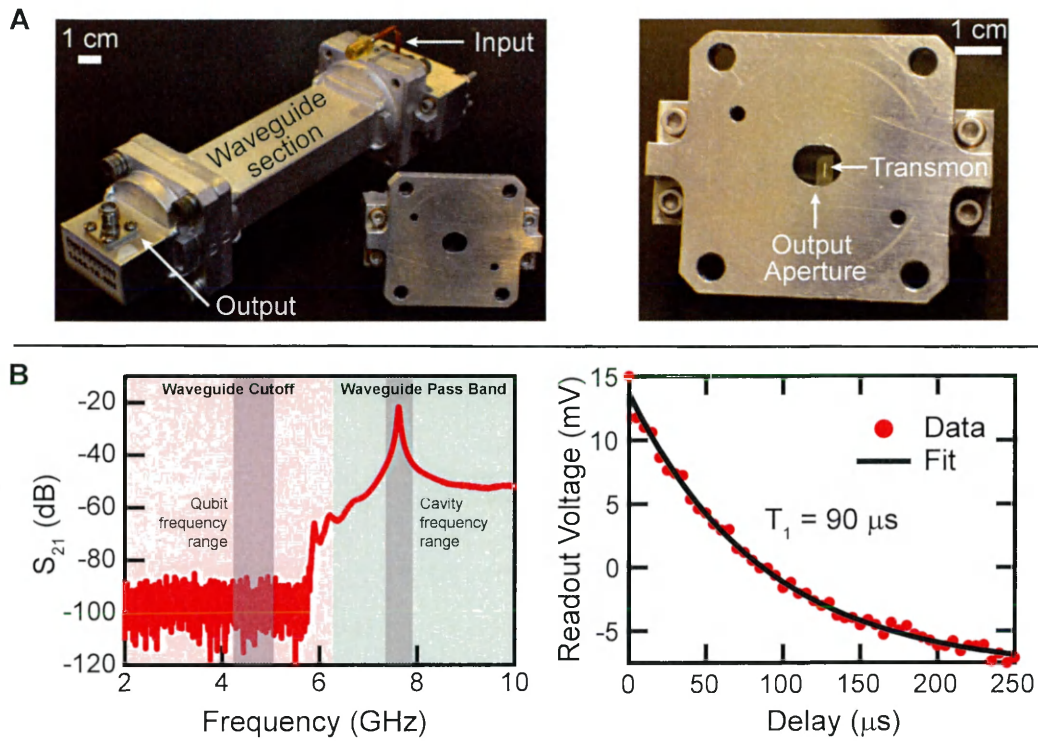


Figure 3.1 | **Waveguide Based Purcell Filters for 3D Transmon Qubits.** A) Pictures of waveguide Purcell-filtered 3D transmon devices. A Purcell filter for a 3D transmon is realized by a section of rectangular waveguide (WR102) on the output port of the qubit-cavity system. Signals enter the system from the weakly coupled input port and then interact with the qubit-cavity system. The microwave field in the cavity leaks into the waveguide through the output aperture (see right) whose size determines the output coupling  $\kappa_{\text{out}}$ . After passing through a length of waveguide, a waveguide-SMA adapter is used to return the output to coaxial cable. B) Spectroscopy of a waveguide and cavity in transmission and example  $T_1$  measurement for a Purcell-filtered qubit. The waveguide is chosen so that its cutoff frequency ( $f_{\text{cutoff}} = 5.8$  GHz) is above the qubit frequency ( $f_{ge} \sim 5$  GHz) and below the cavity frequency ( $f_c \sim 7.5$  GHz) (see left). Thus, whereas the qubit is isolated from the  $50 \Omega$  microwave environment, the cavity remains unaffected. This preserves the qubit lifetime while maintaining its coupling to a fast cavity. An example of a measured  $T_1$  for such a Purcell-filtered system is plotted on the right. The measured qubit relaxation time of  $T_1 = 90 \mu\text{s}$  is about three orders of magnitude slower than the cavity decay rate of  $1/\kappa = 160$  ns.

connected to a waveguide to SMA adapter to return signals to coaxial cables that are connected a JPC and then the output line chain via circulators (for a full experimental setup, see Fig. 4.1). Microwave signals enter the qubit-cavity system through a weakly coupled coaxial coupler as shown in Fig. 3.1A.

Measuring the transmission between the input and output ports of the system at room temperature on a vector network analyzer (VNA), we confirm that below the cutoff frequency of 5.8 GHz, the waveguide does not transmit signals and they are attenuated to below the noise floor of the measurement shown in Fig. 3.1B. On the other hand, around the cavity frequency, the waveguide behaves like a  $50 \Omega$  transmission line. The measured cavity bandwidth of  $\kappa/2\pi \sim 4.9$  MHz agreed closely with simulations. Other systems with different aperture sizes and hence different cavity bandwidths are used in the experiments described in Ch. 5. A qubit with a  $ge$  transition frequency of  $\omega_{ge}/2\pi = 5.1038$  GHz and dispersive shift  $\chi/2\pi = 3.8$  MHz to the cavity was measured with this Purcell filter (detailed experimental system shown in Fig. 4.1) and measured to have a  $T_1 = 90 \mu\text{s}$  (as shown in Fig. 3.1B). Thus, we realize  $\kappa T_1 \sim 2800$  an almost 10-fold increase over  $\kappa T_1 \sim 300$  for measured for systems without Purcell filters. In this system, high-fidelity measurements could be performed in  $T_m \sim 400$  ns (see Ch. 1.5 and Ch. 3.8) realizing  $T_1/T_m \sim 200$ . Beyond the data shown here, these waveguide Purcell filters have been used for a variety of qubit-cavity systems in this thesis and have consistently realized  $T_1 \sim 70$  to  $140 \mu\text{s}$  for systems with bandwidths that ranged from  $\kappa/2\pi = 1$  to  $5$  MHz.

While the increase in qubit  $T_1$  realized by these Purcell filters and their simple implementation makes them attractive in the experiments discussed here, these waveguide Purcell filters are not without their disadvantages. First, all the Purcell filtered qubits were measured to have very high thermal populations around 10 to 20%. Although it is not well understood and required further investigation, it is suspected that the qubits are hot because they are now isolated from the cold microwave environment they would have been coupled to in the absence of the Purcell filter and are instead now thermalized to some other environment at a higher temperature. While the increased qubit temperatures did not adversely affect the experiments in this thesis, they can be detrimental in other systems, for example high- $Q$  cavities coupled to qubits [101]. Secondly, our implementation of the Purcell filter with a single aperture only controls the coupling of the  $\text{TE}_{101}$  mode. Since higher frequency modes of the cavity will also couple to the waveguide and thus limit the qubit  $T_1$ , ideally a Purcell filter should also strongly suppress these couplings, for example using a bandpass filter [3]. However, finite-element electromagnetics simulations using

a multi-mode Purcell analysis estimate  $T_1 \sim 1$  ms, suggesting that the relaxation times of the measured qubits are not currently limited by the Purcell effect.

### 3.6 Overdrive Pulses

A second strategy to increasing the ratio  $T_1/T_m$  is to reduce the measurement time  $T_m$ ; albeit, this has to be done without reducing the SNR, since  $\text{SNR} \propto T_m$  (see Eq. 3.1). Decreasing the time needed to perform a measurement is especially important in applications that depend on feedback, like some forms of quantum error correction that use measurements to detect and correct for errors [30, 43, 63, 101, 117]. One of the main factors that limits  $T_m$  is the amount of time it takes for a cavity starting in vacuum to ring-up to a steady state and to ring-down to vacuum again. Moreover, the cavity ring-down also limits the amount of time required between measurements as the observer has to wait for photons to leak out of the cavity before performing a second measurement. Typically, cavities are excited with square pulses; the exponential ring-up and ring-down of a cavity under this drive have a time scale of  $1/\kappa$ , where  $\kappa$  is the cavity bandwidth. Along with the limit to  $\bar{n}$  in the measurement imposed by the JPC, measurement pulses are usually limited to  $\kappa T_m \sim 5$  to 10.

One strategy to reducing  $T_m$  is to change the shape of the drive applied to the cavity to force it to reach steady state in a time scale faster than its natural response rate of  $1/\kappa$ . Similar pulses could also be used to speed up the ring-down of a cavity and return it to vacuum, enabling a higher measurement cadence by reducing the amount of time required between measurements [86]. We refer to these types of drives as overdrive pulses. The exact form of the overdrive pulses depends on the intended outcome, and system parameters like the drive frequency  $f_r$ , the cavity bandwidth  $\kappa$  and the qubit-cavity dispersive shift  $\chi$ . For example, the pulse needed to rapidly empty a cavity independent of the qubit state when  $\chi \sim \kappa$  is different from that required for rapidly ringing up and down a cavity with the qubit in  $|g\rangle$  that has  $\chi \gg \kappa$ . However, all these cases involve applying large impulses of varying phase to coax the cavity to respond faster than its natural time scale.

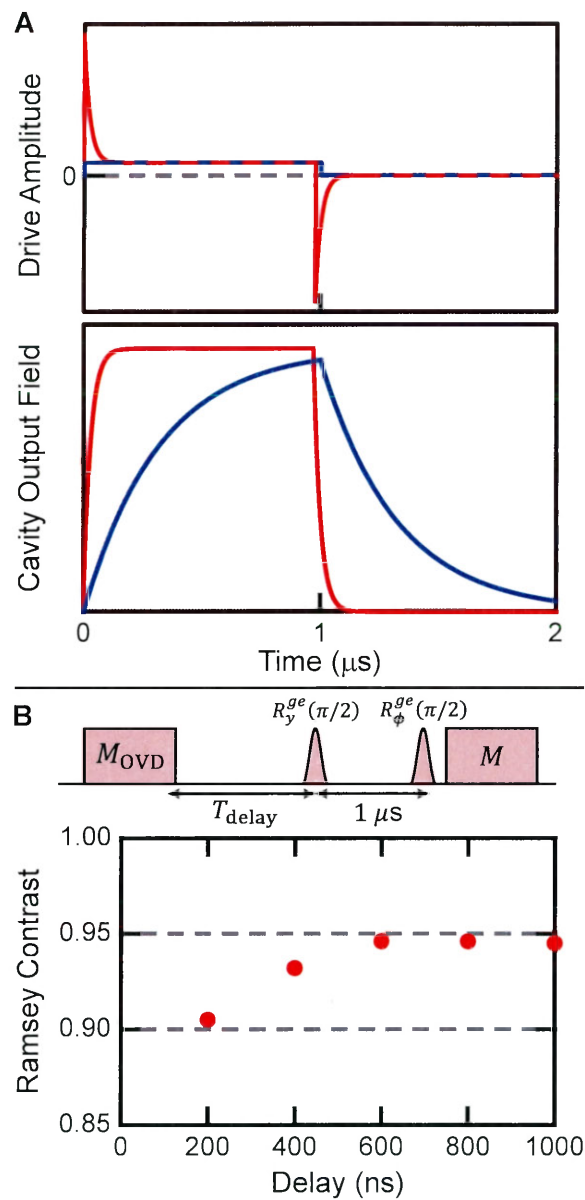


**Figure 3.2 | Overdrive Pulses for Qubit Readout.** A) Simulated cavity drive (top) and response (bottom). Unlike the square pulses (blue) typically used to interrogate a cavity to measure the state of a qubit, an overdrive pulse (red) has a drive shape modified to reduce the time taken to ring-up and ring-down the cavity (top). The output field of a cavity with  $\kappa/2\pi = 1$  MHz driven in transmission by these pulses is plotted in the bottom graph. B) Ramsey dephasing amplitude as a function of delay after a measurement. To characterize how quickly a subsequent measurement can be performed, a Ramsey experiment is performed where two  $\pi/2$  pulses separated by  $1 \mu\text{s}$  are performed a variable time  $T_{\text{delay}}$  after the end of the overdrive pulse. The phase of the second  $\pi/2$  pulse is swept from  $-2\pi$  to  $2\pi$  resulting in a sinusoidal output signal whose amplitude is sensitive to measurement induced dephasing from photons in the cavity. With the overdrive pulse, the delay between the subsequent measurements can be reduced to 400 ns, much shorter than the  $1 \mu\text{s}$  delay required for a square pulse, while incurring less than a 1% loss in contrast.

For this discussion, we consider the specific case of System 2 (see Ch. 3.4) where  $\kappa/2\pi = 1$  MHz and  $\chi/2\pi = 2$  MHz to illustrate the operation of the overdrive pulses. The intended goal is to reduce the total measurement time  $T_m$  as well as increase the measurement cadence. To this end, we apply an overdrive pulse that starts at time  $t_i$  and ends at time  $t_f$  with the functional form

$$A(t) = C_0 \left\{ H[t_i] (1 + C_1 e^{-\kappa_{OVD} t}) - H[t - (t_f - t_i) - n_\tau \kappa_{OVD}^{-1}] (1 + C_1 e^{-(t - (t_f - t_i) - n_\tau \kappa_{OVD}^{-1})}) \right\} \quad (3.7)$$

Here  $H[t]$  is the Heaviside step function,  $C_0$  is the steady state pulse amplitude,  $C_1$  is the overdrive pulse amplitude,  $\kappa_{OVD} = \tau_{OVD}^{-1}$  is the time constant of the overdrive pulse, and  $n_\tau$  is the number of time constants for which the overdrive exponential is applied. A plot of this pulse (red) in relation to a square pulse (blue) of the same steady state amplitude and total pulse time is shown in the top plot of Fig. 3.2A. Here  $C_0 = 1$ ,  $C_1 = 10$ ,  $\kappa_{OVD} = 5.5\kappa$ , and  $n_\tau = 1$ . Both pulses had a total duration of  $1 \mu\text{s}$ , starting at  $t_i = 0$  and ending at  $t_f = 1 \mu\text{s}$ . Shown in the bottom plot of Fig. 3.2A is the simulated output field of the cavity when these pulses were applied to a cavity in transmission at  $f_r = f_c^g$ , the cavity frequency when the qubit is in  $|g\rangle$ . For the case of the square pulse (blue), the cavity barely reaches steady state; instead, it spends the first microsecond ringing up and the second microsecond ringing down back to vacuum. On the other hand, with the overdrive pulse (red), the cavity ring-up and ring-down last about 100 ns. The cavity spends most of its time at steady state when the overdrive pulse is applied and quickly returns to vacuum once it is turned off. Consequently, the state of the qubit is entangled with a pointer variable of larger photon number for the same measurement time, and measurements can be repeated more quickly since the cavity is rapidly reset to vacuum.

A version overdrive pulse, with  $C_1 = 13C_0$ ,  $\tau_{OVD} = 20$  ns ( $\kappa_{OVD} = 8\kappa$ ), and  $n_\tau = 5$ , was applied to the qubit-cavity of System 2, used as the detector qubit in the single-photon remote entanglement experiment of Ch. 5. The pulse parameters were chosen to yield an experimentally measured cavity response that had the most rapid ring-up and ring-down. Differences between

the experimental pulse parameters from those used from simulation are attributed to system imperfections like saturation effects of amplifier and mixer components, uncertainty in the values of  $\kappa$  and  $\chi$ . With this overdrive pulse, a readout fidelity of  $\mathcal{F}_{\text{det}} \sim 0.99$  achieved with a  $1 \mu\text{s}$  square pulse could now be achieved with a 700 ns overdrive pulse.

Furthermore, since the cavity also rings-down faster than for a square pulse, two time between two successive measurements of the system could be reduced to 400 ns from about  $1 \mu\text{s}$ . To quantify this, we perform the experiment outlined in Fig. 3.2B. The number of residual photons in the cavity at a time  $T_{\text{delay}}$  after the overdrive pulse was characterized by the measurement-induced dephasing that they caused. To measure the dephasing resulting from residual photons, a  $R_y^{ge}(\pi/2)$  pulse and a  $R_\phi^{ge}(\pi/2)$  pulse separated by  $1 \mu\text{s}$  were applied to the qubit in the cavity; the phase of the second pulse was varied from  $-2\pi$  to  $2\pi$ . Finally a projective measurement was performed. Each experiment results in Ramsey oscillations of the qubit whose amplitude informs us about the amount of dephasing experienced by the qubit due to information learned by unmonitored photons. This experiment was then repeated for different values of  $T_{\text{delay}}$  and the Ramsey oscillation amplitude was plotted as a function of the delay as shown in the plot in Fig. 3.2B. Measurements performed with square pulses required  $T_{\text{delay}} = 1 \mu\text{s}$ ; however, with the overdrive pulses, the delay could be reduced to 400 ns with only a 1% hit to the Ramsey contrast.

The combination of reduced measurement time and increased measurement cadence were crucial to increasing the fidelity of the entangled state generated in the experiment discussed in Ch. 5. Of course, these overdrive pulses can be applied to other systems; they were also used in the experiments of Ch. 3.8 and Ch. 4 to achieve the similar improvements although we do not present data for those systems. It is worth noting that overdrive pulses need to be carefully tailored for the system. Simulations are an important tool in understanding the cavity response and are a first step to a candidate overdrive pulse. Special care must be taken for certain situation, for example when the overdrive pulse needs to reset a cavity to the vacuum independent of the state of the qubit, an essential tool for high-cadence measurements. Moreover, since these pulses necessarily result in large powers, care must be taken not to saturate amplifiers, especially the

JPC for example.

### 3.7 Shaped Demodulation

Another important consideration when performing pulsed dispersive readout of a qubit is the filtering used to perform demodulation. The signal measured at room temperature during the measurement process is a voltage as a function of time,  $V(t)$ . It is down-converted from the cavity readout frequency,  $f_r$ , by mixing it with a slightly detuned room temperature reference signal,  $f_r + 50$  MHz, to produce a radio-frequency signal, at 50 MHz for the experiments in this thesis (see Fig. 4.1 or Fig. 5.1 for example). To convert this 50 MHz voltage signal into a measurement outcome  $\nu = (I_m, Q_m)$ , it is demodulated and integrated

$$I_m = \int_0^{T_m} V(t) \cos(\omega_{LO}t) dt \quad (3.8)$$

$$Q_m = \int_0^{T_m} V(t) \sin(\omega_{LO}t) dt \quad (3.9)$$

Here  $T_m$  is the measurement time, set by how long the signal is integrated for, and  $\omega_{LO}/2\pi = 50$  MHz. The measurement outcome is then thresholded to determine the measurement outcome of the qubit observable being interrogated.

However, as discussed in Ch. 3.6, when the cavity is driven with pulses, it has transient ring-up and ring-down responses as it changes between the vacuum state and the steady state under the drive and back. This raises the question of how best to choose the bounds of the integration window. Retaining only the part of the signal record when the cavity is in steady state would excise out the ring-up and ring-down periods which contain some information about the state of the qubit. On the other hand, expanding the integration window to the entire cavity response would treat equally the steady state and transient parts of the response, which have different amounts of information about the qubit as the number of average photons in the cavity  $\bar{n}$  is different.

A better strategy to the boxcar integration window of Eq. 3.9 is to use a shaped window

function  $W(t)$  for the demodulation, thus modifying the integration being performed to

$$I_m = \int_0^{T_m} W_I(t) V(t) \cos(\omega_{LO} t) dt \quad (3.10)$$

$$Q_m = \int_0^{T_m} W_Q(t) V(t) \sin(\omega_{LO} t) dt \quad (3.11)$$

where  $W_I(t)$  and  $W_Q(t)$  are the I and Q components of the window function respectively. Of course, the new question is what the shape of  $W(t)$  should be. Here we choose that window function to be the difference between the cavity response when is in  $|g\rangle$  and when it is in  $|e\rangle$  [44]

$$W(t) = a_{out}^{|g\rangle}(t) - a_{out}^{|e\rangle}(t) \quad (3.12)$$

Here  $a_{out}^{|g\rangle}(t)$  ( $a_{out}^{|e\rangle}(t)$ ) is the cavity output field as a function of time when the qubit is in  $|g\rangle$  ( $|e\rangle$ ). To understand this choice of the window function, we step back to consider the measurement process (outlined in Ch. 1.2 and Ch. 2.4). Consider the case of performing a measurement of  $Z$  of a qubit; the possible measurement outcomes of  $Z = +1$  and  $Z = -1$  correspond to finding the qubit in  $|e\rangle$  and  $|g\rangle$  respectively. During the measurement of a transmon, the state of the qubit is mapped onto the coherent states  $|\alpha_g\rangle$  and  $|\alpha_e\rangle$  for  $|g\rangle$  and  $|e\rangle$  respectively. As the coherent state pointer variable is amplified, it is turned into a classically distinguishable signal as the distance in phase-space between the two different pointer variables increases. Thus, the information about the state of the qubit is captured by the difference between the two pointer variable states. When the distance in phase-space between  $|\alpha_g\rangle$  and  $|\alpha_e\rangle$  is small, during the ring-up and ring-down for example, so is the amount of information acquired by the observer. Another way to understand this is the measurement formalism of Ch. 2.4 where the distance between the Gaussian distributions corresponding to the outcomes  $|g\rangle$  and  $|e\rangle$  is the strength of a measurement  $\bar{I}_m/\sigma$ .

A crucial simplification made in this choice of  $W(t)$  is assuming infinite qubit relaxation and decoherence times; for qubits with finite  $T_1$ , the increased probability of the qubit having relaxed for later times and longer measurements affects the shape of the demodulation window

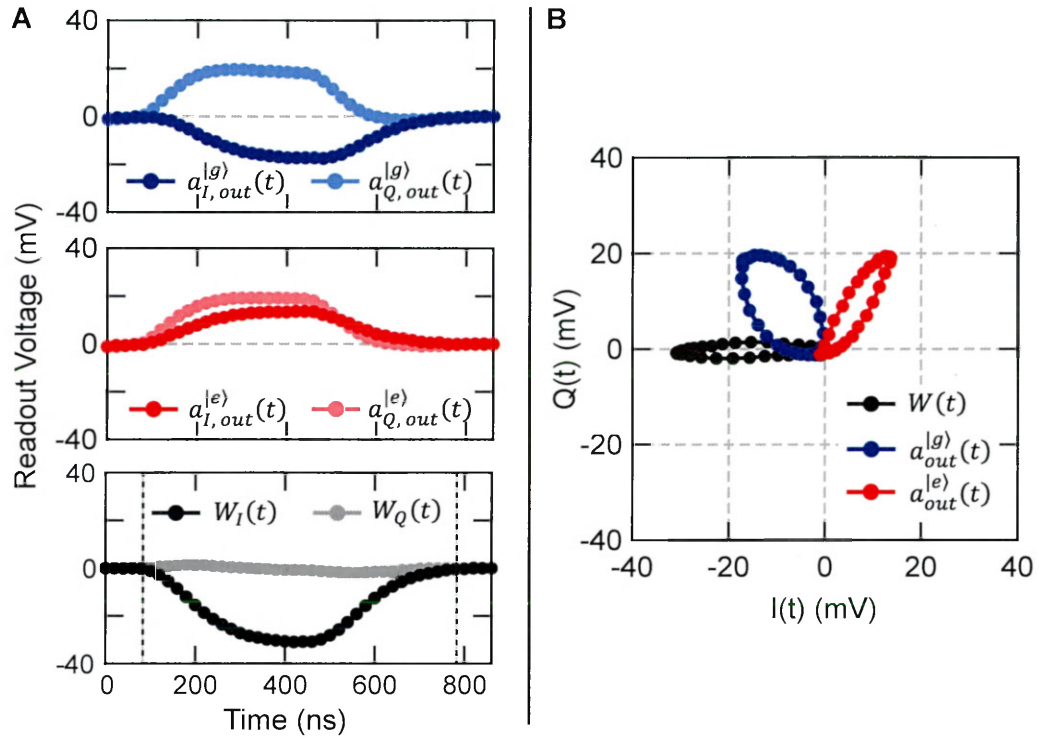


Figure 3.3 | **Cavity Response and Demodulation Waveforms.** A) Measured cavity response and demodulation envelopes. The measured I and Q components of the cavity output field  $a_{out}(t)$  as a function of time are shown for the qubit being prepared in  $|g\rangle$  (top graph) or  $|e\rangle$  (middle graph). The demodulation envelope  $W(t)$  (bottom graph) is constructed by calculating the difference  $a_{out}^{(g)}(t) - a_{out}^{(e)}(t)$ . The envelope, excited to the area between the dotted lines in the bottom plot, is then used as the demodulation window function. B) IQ-plane representation of cavity response and demodulation envelopes. The data shown in the three plots in A is now plotted on the IQ-plane.

function [44, 130]. However, incorporating these effects makes calculating the window function more challenging, especially in the presence of non-QND effects like the reduction in  $T_1$  during readout due to the presence of photons in the cavity [14].

An example of this demodulation window function is shown in Fig. 3.3 for the qubit-cavity of System 1 (see Table. 3.1). To construct  $W(t)$ , the qubit was prepared in the state  $|g\rangle$  (or  $|e\rangle$ ) by scrambling and post-selection (see Ch. 1.5) and a 500 ns readout pulse was applied at  $\omega_r/2\pi = (\omega_c^g - \chi/2)/2\pi = 7.4794$  GHz, halfway between the cavity frequency when the qubit was in  $|g\rangle$  and  $|e\rangle$ . The cavity output signal was demodulated in 20 ns intervals using a boxcar filter for each interval. The experiment was repeated to accumulate at least  $10^5$  successful signal

records for each qubit state. The records were averaged to produce the averaged cavity output when the qubit was in  $|g\rangle$ ,  $a_{out}^{(g)}(t)$  (blue traces), and when it was in  $|e\rangle$ ,  $a_{out}^{(e)}(t)$  (red traces). Plots of the I and Q components of the cavity response as a function of time are shown in the top and middle plots of Fig. 3.3A; the same traces are also plotted on the IQ-plane in Fig. 3.3B.

From these two averaged signal records, the demodulation window function was constructed; the difference of the I and Q components between the  $|g\rangle$  and  $|e\rangle$  records was calculated point-by-point. The resulting window function is shown in the bottom plot of Fig. 3.3A and as the black trace in Fig. 3.3B. Since the difference between the  $|g\rangle$  and  $|e\rangle$  response lies mostly along the I-axis,  $W_Q(t)$  is close to zero and  $W(t)$  lies mostly along the I-axis. Finally, the calculated difference is excised, keeping only the part between the black dotted black lines as the final  $W(t)$ . This envelope is then used as the demodulation window function for measurements in subsequent experiments with this the qubit-cavity system.

The idea of constructing the demodulation waveform from the difference between the cavity response for different states of the qubit is generally applicable beyond the specific system discussed here. For example, the same procedure was also used for System 2 to generate the demodulation envelopes used for the measurements discussed in Ch. 3.8 and Ch. 5. Moreover, a modified version of this envelope was used for the joint two-qubit readout performed in Ch. 4.3 and Ch. 5.2. In these cases, the I and Q axis encode information about two different qubits, Alice and Bob, respectively; hence, the Q-component of the window function was calculated from the difference in the joint cavity response for the qubits prepared in  $|gg\rangle$  and  $\geq$  to contain information only about the state of Bob. On the other hand, the I-component was constructed from the difference in the joint cavity response for  $|gg\rangle$  and  $|eg\rangle$  to be sensitive to the state of Alice.

## 3.8 Single Qubit Measurement Fidelity

We now turn our discussion to how to wield the tools presented above within the constraints discussed in Ch. 3.2 to tune up high-fidelity dispersive readout of transmon qubits. Once the

qubit-cavity system has been fabricated, assembled and cooled to 20 mK, the only part of the experimental system that can be varied is the pulse used to interrogate the cavity and perform readout. Specifically, an experimenter has control over the average photon number  $\bar{n}$  in the pulse, the length of the pulse  $T_m$ , and the pulse shape. To begin, a square pulse with  $T_m \sim 10/\kappa$ , where  $\kappa$  is the cavity bandwidth, is chosen as a starting candidate measurement pulse; a 500 ns and 2  $\mu$ s long readout pulse was used for System 1 and System 2 respectively. The average photon number in this candidate pulse is chosen to be on the order of 1 to 5 photons; one way to choose the pulse amplitude would be to calibrate the amplitude in terms of photon number using a version of the Ramsey measurement-induced dephasing experiment described in Ch. 3.6. In practice, a more commonly used method is to perform single-tone spectroscopy on the cavity with different pulse amplitudes to find the largest amplitude that can be used before the cavity line-shape deviates from a linear Lorentzian response [114].

For the experiments in this section, the cavity readout pulses were applied to the weakly coupled input port to measure the systems in transmission. However, the optimization outlined below is equally valid for performing measurements in reflection. The choice between transmission versus reflection measurements is a somewhat open choice to the experimenter, dependent on other factors in the experiment, for example, avoiding amplifier saturation (see Ch. 4.3) or power availability due to attenuation on input lines.

The frequency at which the readout pulse is applied depends on the ratio of  $\kappa$  and the qubit-cavity dispersive shift  $\chi$ . For System 1 where  $\chi \sim \kappa$ , the pulses were applied at  $\omega_r = \omega_c^g - \chi/2$ , halfway between the cavity frequency for the qubit in  $|g\rangle$  and  $|e\rangle$ . In this case, as outlined in Ch. 2.4, the state of the qubit is mapped onto only the phase of the coherent state pointer variable, and not the amplitude. This results in two Gaussian outcome distributions for  $|g\rangle$  and  $|e\rangle$  equidistant from the  $Q_m$  axis, as shown in Fig. 1.5; this choice is made to ensure that any saturation effects in the output amplification and demodulation chain treats the two outcome distributions equally, without introducing bias. On the other hand, for the case of System 2 where  $\chi \gg \kappa$ , applying the readout tone at  $\omega_r = \omega_c^g - \chi/2$  would necessitate using very large pulse amplitudes at room temperature since very few photons would enter the cavity at this

frequency. Thus, the readout pulse is instead applied at  $\omega_r = \omega_c^g$ . Now, the state of the qubit is encoded entirely in the amplitude of the measured coherent state; when the qubit is in  $|g\rangle$ , the cavity is energized with photons and the output is a coherent state offset from the origin of the IQ-plane. On the other hand, when the qubit is in  $|e\rangle$ , few (if any) photons enter the cavity and hence the output coherent state is close to the vacuum state. It is important to note that especially in the latter case of System 2, as a result of measuring at  $\omega_r = \omega_c^g$ , the two Gaussian distributions actually correspond to the outcomes  $|G\rangle$  and  $|\bar{G}\rangle$  (for a more detailed discussion, see Ch. 2.4).

With this candidate measurement readout pulse, the experiment outlined by the pulse sequence in Fig. 3.4A is performed. At the beginning of the protocol, the state of the qubit is scrambled with a measurement pulse (not shown) followed by a  $R_y^{ge}(\pi/2)$  to initialize the qubit in an equal superposition state of  $|g\rangle$  and  $|e\rangle$ . Since this erases the history of the qubit, it allows for the experiment to be repeated at  $T_{\text{rep}} = 20 \mu\text{s}$  without needing for the qubits to relax to the ground state naturally. Subsequently, a measurement is performed to post-select on outcomes where the qubit was measured to be in  $|g\rangle$ . The selection was performed by using a circular threshold centered around the Gaussian distribution associated with the outcome  $|G\rangle$ . The radius of the circular threshold was chosen to be about the measured standard deviation of the Gaussian distribution. Ideally, since the qubit starts in  $|g\rangle$  half the time due to scrambling, this post-selection should retain half the data; in practice, the choice of the threshold results in only about 30% to 40% of the data being retained. Next, one of three single qubit rotations,  $Id$ ,  $R_y^{ge}(\pi/2)$  or  $R_y^{ge}(\pi)$ , was applied to prepare the qubit in the states  $|g\rangle$ ,  $1/\sqrt{2}(|g\rangle + |e\rangle)$ , or  $|e\rangle$ . Then a second measurement is performed to verify the state that was prepared. The demodulated measurement outcome  $\nu = (I_m, Q_m)$  is converted into binary measurement outcome of  $|G\rangle$  or  $|E\rangle$  based on a threshold halfway between the two measurement outcome Gaussian distributions (depicted by the dashed white lines in Fig. 3.4). The experiment is repeated to accumulate successful shots for each qubit preparation pulse and binned as counts,  $C_g$  and  $C_e$ .

At the end of the experiment, the expectation value of the observable being measured, in this case  $Z$ , was calculated  $\langle Z \rangle = (C_e - C_g) / (C_e + C_g)$ . Here, we use the convention that

$\langle Z \rangle = -1$  ( $\langle Z \rangle = +1$ ) corresponds to  $|g\rangle$  ( $|e\rangle$ ). From the measured  $Z$  expectation value when the qubit was prepared in  $|g\rangle$ , called  $\langle Z \rangle_{|G\rangle}$  and in  $|e\rangle$ ,  $\langle Z \rangle_{|E\rangle}$ , the fidelity of the measurement can be calculated using  $\mathcal{F} = \frac{1}{2} \left( \langle Z \rangle_{|E\rangle} - \langle Z \rangle_{|G\rangle} \right)$ . This fidelity is otherwise known as the blind measurement fidelity (or assignment fidelity) which is just the fraction of times the measurement outcome,  $|G\rangle$  or  $|E\rangle$ , agreed with the prepared qubit state,  $|g\rangle$  and  $|e\rangle$ . Thus another way to calculate this blind fidelity is  $\mathcal{F} = 1 - P(|G\rangle | |e\rangle) - P(|E\rangle | |g\rangle)$  where  $P(|G\rangle | |e\rangle)$  ( $P(|E\rangle | |g\rangle)$ ) is the probability of measuring the outcome  $|G\rangle$  ( $|E\rangle$ ) when the qubit was prepared in the state  $|e\rangle$  ( $|g\rangle$ ).

In the absence of finite qubit lifetimes  $T_1$  and decoherence times  $T_2$ , as well as any other imperfections like state preparation errors, the measurement fidelity would then be entirely determined by the separation of the two Gaussian distributions. Given two Gaussian distributions centered at  $I_m = \pm \bar{I}_m / \sigma$  each with standard deviation  $\sigma$ , the fidelity would be limited by their separation  $2\bar{I}_m / \sigma$  to  $\mathcal{F} = \text{erf} \left( \frac{\bar{I}_m}{\sqrt{2}\sigma} \right)$  where  $\text{erf}(x)$  is the error function. Thus, a higher measurement fidelity could be simply achieved by increasing  $\bar{I}_m / \sigma$  by using a longer measurement pulse or one with a higher average photon number.

However, when  $T_1$  is finite, a longer measurement suffers from an increased probability of the qubit relaxation. The error due to qubit relaxation scales according to  $\exp[-T_m / T_1]$ . On the other hand, the separation-limited fidelity scales as  $\text{erf}[\sqrt{T_m}]$  (since  $\bar{I}_m / \sigma \propto \sqrt{T_m}$  according to Eq. 2.26). The total fidelity in the presence of  $T_1$  will be a product of the two contributions. As the  $T_m$  increases from zero, so too will the fidelity since the growing separation of the Gaussian distributions will increase the observer's ability to accurately assign outcomes. However, as the separation continues to increase with  $T_m$ , the infidelity due to  $T_1$  dominates and the measurement fidelity decreases again. Thus, by finding the maximum in this product as a function of the measurement time  $T_m$ , the optimal pulse length can be calculated. Using this, we chose square pulses with  $T_m = 500$  ns for System 1 and  $T_m = 1$   $\mu$ s for System 2. Of course, the pulse lengths can be made shorter still by using the overdrive pulse shapes discussed in Ch. 3.6.

The next available degree of freedom is the photon number used in the pulse,  $\bar{n}$ . While the separation-limited fidelity scales as  $\text{erf}[\sqrt{\bar{n}}]$  (since  $\bar{I}_m / \sigma \propto \sqrt{\bar{n}}$  according to Eq. 2.26), this must

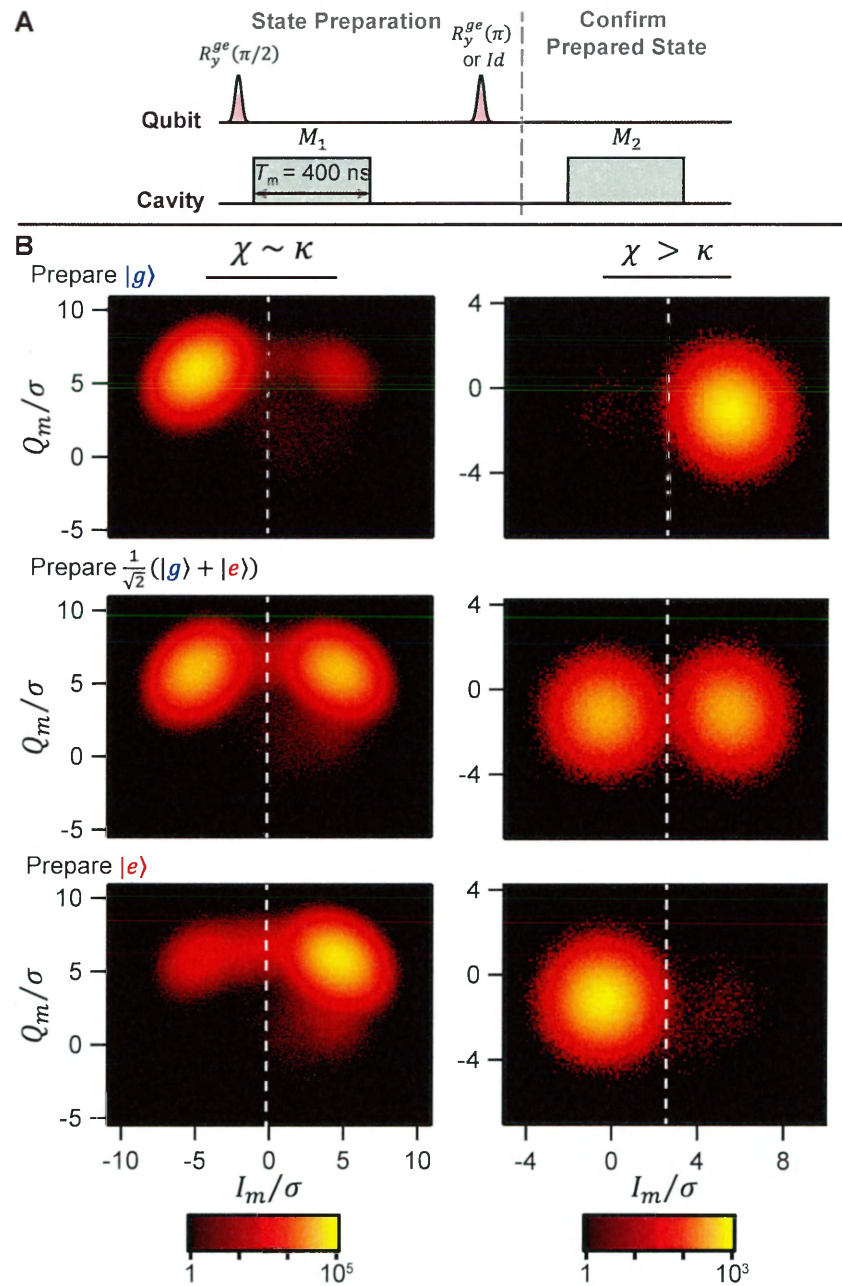


Figure 3.4 | **Single Qubit State Preparation and Measurement.** A) Pulse sequence to prepare and confirm the state of a single qubit. After a  $R_y^{ge}(\pi/2)$  pulse to scramble the history of the qubit and rotate it to  $1/\sqrt{2}(|g\rangle + |e\rangle)$ , a measurement is performed to initialize the qubit in  $|g\rangle$  by post-selection. The qubit is then prepared in the desired state by a second qubit rotation pulse, in this case either  $Id$  or  $R_y^{ge}(\pi)$  for  $|g\rangle$  or  $|e\rangle$  respectively. Finally, state preparation is confirmed by a second measurement pulse. B) Single-shot histograms (on a logarithmic scale) of the measurement of a qubit state after it was prepared in  $|g\rangle$  (top row),  $1/\sqrt{2}(|g\rangle + |e\rangle)$  (middle row), and  $|e\rangle$  (bottom row) for the case of  $\chi \sim \kappa$  (left column) and  $\chi > \kappa$  (right column). In both cases, the qubit could be prepared and measured with  $\mathcal{F} \sim 99\%$ .

be balanced against effects of amplifier saturation and reduction in  $T_1$  during readout. Although both these can be measured experimentally, the more common experimental practice is to choose  $\bar{n}$  based on the resulting measurement fidelity. Specifically, the smallest pulse amplitude required for a desired measurement fidelity is chosen.

The result of applying this procedure to System 1 and 2 are shown in Fig. 3.4. Data for System 1 is shown on the left and for System 2 on the right. The histograms are the measured distributions on a logarithmic scale for preparing the qubit in  $|g\rangle$  (top row),  $1/\sqrt{2}(|g\rangle + |e\rangle)$  (middle row), and  $|e\rangle$  (bottom row). The values of  $\langle Z \rangle$  for each of these measurement is summarized in Table. 3.2. We calculate a measurement fidelity of  $\mathcal{F} = 0.992 \pm 0.001$  for System 1 and  $\mathcal{F} = 0.989 \pm 0.002$  for System 2 respectively. The error bars in the measurement fidelity were dominantly due to statistical error from the finite number of successful outcomes.

Prepared State	System 1	System 2
$ g\rangle$	-0.997	-0.993
$\frac{1}{\sqrt{2}}( g\rangle +  e\rangle)$	0.020	0.012
$ e\rangle$	0.986	0.985

Table 3.2 | **High-fidelity measurements - measured  $\langle Z \rangle$**

From the data in Fig. 3.4 and Table. 3.2, we can see that the fidelity is dominantly limited by our ability to accurately measure the qubit when it was prepared in  $|e\rangle$ . The asymmetry in the measured expectation values  $|\langle Z \rangle_{|E\rangle}| < |\langle Z \rangle_{|G\rangle}|$  suggests that our measurement is primarily limited by errors due to  $T_1$  during the readout; as a consequence, the qubit relaxes during the readout and an outcome of  $|G\rangle$  is recorded although the system was prepared in  $|e\rangle$ . This is despite  $T_1/T_m = 140$  to  $160$  for System 1 and  $T_1/T_m = 130$  with our efforts with Purcell filters and shaped readout pulses. Errors due to qubit relaxation are further exacerbated by the observation that the presence of photons in the cavity can result in non-QNDness in the dispersive readout process, evidenced by a reduction in  $T_1$  [14]. Rectifying this cavity photon-number dependent qubit relaxation time and increasing qubit  $T_1$  will be essential to further improving measurement fidelity.

A second source of error in this system is the initial state preparation - the fidelity with which

the system was measured to be in  $|g\rangle$  and then prepared in the initial state with a qubit rotation will affect the measured blind fidelity. To estimate the former, i.e the fidelity of initializing the qubit to  $|g\rangle$ , we look at the data when no rotation was performed and the observed value of  $\langle Z \rangle$  in that case<sup>2</sup>. The threshold used to select outcomes that were recorded as  $|g\rangle$  and retained was changed from the circular threshold to a linear separatrix between the two Gaussian distributions. Starting from a separatrix halfway between the distributions for  $|G\rangle$  and  $|E\rangle$ , the location of the separatrix was swept towards the distribution for  $|G\rangle$  to set a more stringent threshold that excluded more and more counts. The observed value of  $\langle Z \rangle$  was calculated as a function of the threshold and was found not to change, indicating that the fidelity of the first measurement is not limiting the overall blind fidelity. As further evidence of this, in a separate experiment (performed on System 1), a measurement tone that much longer than many cavity lifetimes,  $T_m \sim 2 \mu s$ , was applied with no qubit pulses; when two 500 ns intervals of the record were integrated and thresholded, then the outcome of the second measurement was  $\langle Z \rangle \sim 0.999$  when the first measurement resulted in  $|g\rangle$ . However, when the delay between the two measurements was increased to 300 ns to be similar to that of the pulse sequence that yielded the data in Fig. 3.4, the result of the second measurement fell to  $\langle Z \rangle \sim 0.997$ ; this indicates that error in the measurement of  $|g\rangle$  is dominantly limited by  $T_1$ , specifically the rate at which the qubit jumps to  $|e\rangle$  from  $|g\rangle$ .

To estimate the limitation to the measurement fidelity arising from the single-qubit pulses used to prepare the qubit computational states, we compared the observed value of  $\langle Z \rangle$  when the qubit was prepared in  $|g\rangle$  with and without a scrambling  $R_y^{ge}(\pi/2)$  pulse before the first measurement. From that, we estimate an error of about  $10^{-3}$  to the overall fidelity from the single qubit rotations. This is despite the use of tuneup protocols to correct for various sources of error in the pulses [112, 141]. Since tuning up high-fidelity pulses requires high-fidelity measurements and vice-versa, this presents a problem that needs to be approached with bootstrapping techniques that incrementally improve both the measurements and pulses. Especially as the fidelity improves, independently measuring the various sources of error also grows more challenging and requires

<sup>2</sup>The data for this measurement are not presented in this thesis and were only performed for System 1

alternate protocols than the ones described above. Techniques based on the readout correction discussed in Ch. 5.6 could be one potential way to separate the effects of imperfect measurement and state preparation and better quantitatively understand their individual contributions to the error budget. Moreover, techniques like randomized benchmarking [73] can also provide an independent measure of the state preparation fidelity. However, with measurements currently limited by qubit relaxation, these techniques are not yet as essential.

### 3.9 Measurement as a Quantum Operation

Next we address the last requirement of measurements for quantum information, as outlined in Ch. 1.3: they need to be efficient. The measurement efficiency  $\eta$  is the fraction of information about a system that is learned by the experimenter instead of being lost to unmonitored information channels. Quantifying this fraction requires measuring the amount of loss experienced by a signal as it travels from the plane of the qubit-cavity system through the output amplification chain to the room temperature demodulation and measurement apparatus. This can be accomplished with a calibrated power source that emits signals of known power at the plane of the qubit-cavity system and measuring the power observed at room temperature. Among the options for calibrated cryogenic-compatible microwave frequency noise or power sources [84, 133], the most straightforward to the use with our experimental system is the qubit. The coherent states that are entangled with our qubits have a standard deviation of  $\sigma = 1/2$  corresponding to a half-photon of noise  $T_Q = \hbar\omega/2k_B$  at frequency  $\omega$ . Thus analyzing the loss experience by this signal and the increase in the noise offers a method for measuring  $\eta$ .

Indeed, as discussed in Ch. 2.4, the apparent measurement strength  $\bar{I}_m/\sigma$ , obtained from the separation of the observed Gaussian distributions, depends on the measurement efficiency (see Eq. 2.26) and offers one method for extracting  $\eta$ . However, this method requires independently measuring other parameters like the average number of photons  $\bar{n}$  used in the measurement which lasts  $T_m$ . While this can be obtained using measurement-induced dephasing experiments to calibrate the photon number, the errors in this experiment can easily exceed  $\sim 10\%$  because

of the systematic and random error involved.

Instead, analyzing the back-action of a variable-strength measurement offers a self-calibrating method for measuring  $\eta$  [51, 131]. In this method, the observer can extract  $\eta$  by quantifying the amount of dephasing experienced by a qubit undergoing a measurement. Since the observer can simultaneously also extract the measurement strength from this observation of the back-action, no other calibration is required, offering a more precise value of  $\eta$ . The back-action on the qubit of a variable-strength measurement with phase-preserving amplification is summarized by Eq. 2.24<sup>3</sup>; upon measuring an outcome  $\nu = (I_m, Q_m)$ , the final state of the qubit as Bloch vector coordinates is  $(x_f, y_f, z_f)$ .

To measure this experimentally, the pulse sequence shown in Fig. 3.5A was used. Here we show data for the specific case of System 1, although the method could be applied to other qubit-cavity systems as well. Like the protocol to quantify single qubit measurement fidelity, it begins by initializing the qubit to  $|g\rangle$  by scrambling and post-selection. After initializing the qubit to  $Y = +1$  with a  $R_x^{ge}(\pi/2)$  pulse, a variable-strength measurement is performed; this is realized by applying a measurement pulse at the readout frequency on the cavity and sweeping the pulse amplitude to vary the average photon number  $\bar{n}$  in the pulse. Finally, the back-action of this measurement is determined by performing full single-qubit tomography. This consists of applying one of three rotations on the qubit,  $Id$ ,  $R_y^{ge}(\pi/2)$  or  $R_x^{ge}(-\pi/2)$ , to measure the  $Z$ ,  $X$ , and  $Y$  components respectively of the qubit state in the Bloch vector basis. Like discussed above in Ch. 3.8, the result of this measurement was converted into a binary outcome of  $+1$  or  $-1$  for each trial; by repeating these measurements on an ensemble of identically prepared states, the counts were converted into expectation values of the observable being measured. The experiments were repeated to accumulate at least  $10^3$  successful shots of each trial.

The resulting data is shown in Fig. 3.5B. Histograms of the outcome of the variable-strength measurement,  $\nu = (I_m, Q_m)$ , are shown in the left-most column of the figure for three different measurement strengths,  $\bar{I}_m/\sigma = 0$ ,  $\bar{I}_m/\sigma = 1.0$ , and  $\bar{I}_m/\sigma = 2.6$ . The strengths of the variable-strength measurements were calculated from the separation of the observed Gaussian

<sup>3</sup>This method of extracting the measurement efficiency can also be used when the measurement is performed with phase-preserving amplification. A derivation of the back-action in that case can be found in Ref. [131].

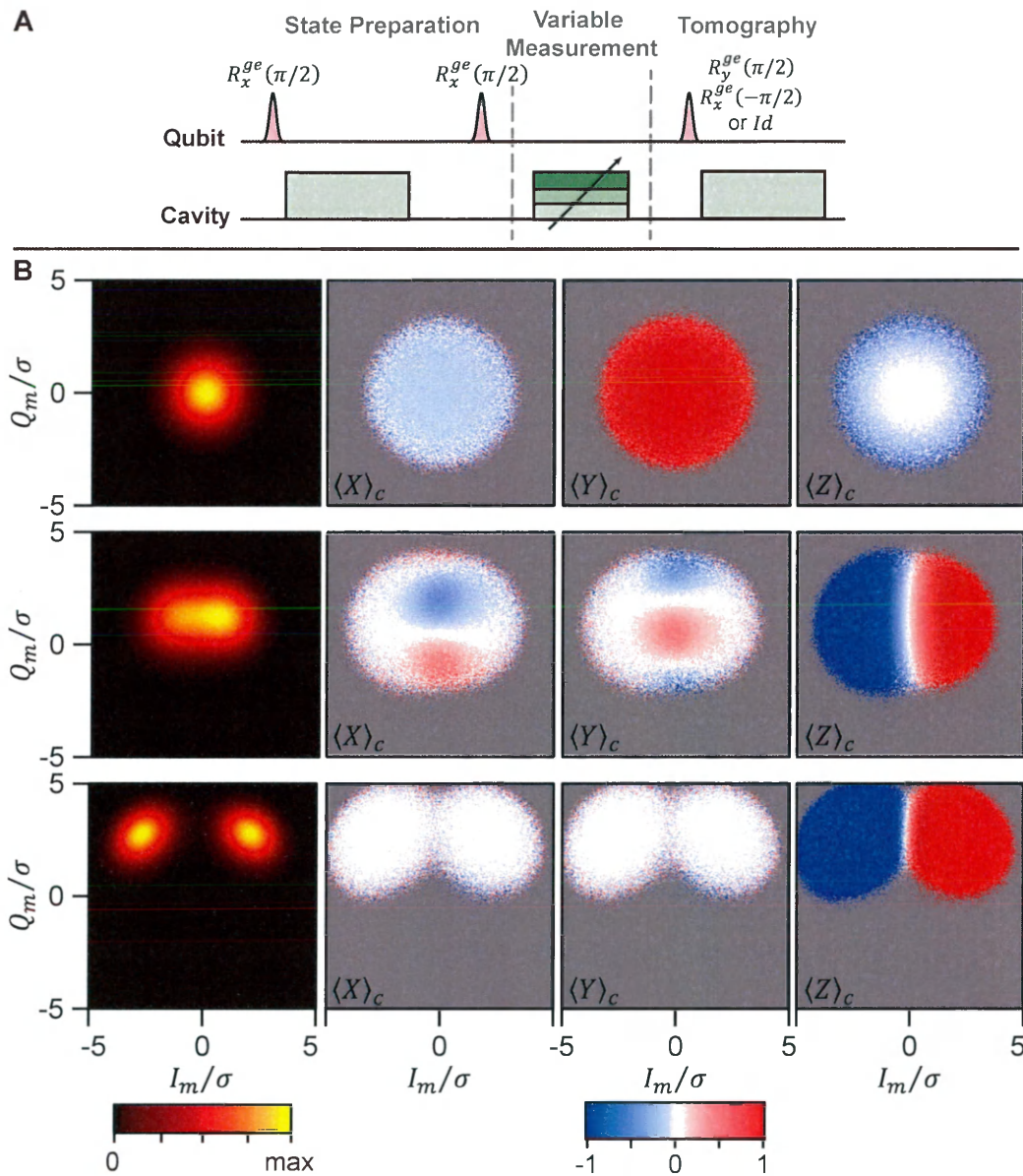


**Figure 3.5 | Variable Strength Measurement Back-action Histograms and Tomograms.** A) Pulse sequence to measure the measurement efficiency  $\eta$  using the back-action of a variable-strength measurement. The qubit is prepared in the state  $Y = +1$  ( $1/\sqrt{2}(|g\rangle + i|e\rangle)$ ) with a  $R_x^{ge}(\pi/2)$  pulse after scrambling the qubit state and post-selecting on outcomes where the qubit is found in  $|g\rangle$  after the first measurement, using the same method described in Fig. 3.4A. Subsequently, a variable-strength measurement is performed; the back-action of this measurement is determined by performing full single-qubit state tomography using one of three rotations,  $R_y^{ge}(\pi/2)$ ,  $R_x^{ge}(-\pi/2)$  or  $Id$  to measure the  $X$ ,  $Y$ , and  $Z$  components respectively of the qubit Bloch vector. B) Histograms (first column) and conditional tomograms  $\langle X \rangle_c$  (second column),  $\langle Y \rangle_c$  (third column), and  $\langle Z \rangle_c$  (fourth column) for increasing measurement strength  $I_m/\sigma$ . The measured average final qubit state is plotted for each measurement outcome  $(I_m/\sigma, Q_m/\sigma)$ .

distributions for  $|g\rangle$  and  $|e\rangle$ . The measurement outcomes were sorted into a  $201 \times 201$  bin histogram. For each measurement outcome, the final qubit state was calculated in the Bloch vector basis by averaging the single-shot tomography measurement outcomes. Since the final qubit state depends on the measurement outcome, they are referred to as conditional Bloch vector components and are plotted in the tomograms for  $\langle X \rangle_c$  (second column),  $\langle Y \rangle_c$  (third column) and  $\langle Z \rangle_c$  (last column). In the case of a very weak measurement  $\bar{I}_m/\sigma = 0$ , the measurement does not perturb the qubit and leaves it in the initially prepared state of  $Y = +1$ . A slight rotation towards  $X = -1$  (indicated by the light blue in the tomogram for  $\langle X \rangle_c$ ) is attributed to a detuning in the qubit pulse resulting in rotation of the qubit along the equator of the Bloch sphere.

As the measurement strength is increased to  $\bar{I}_m/\sigma = 1.0$ , we observe the behavior described in Ch. 1.5. For measurement outcomes where  $I_m \ll 0$  ( $I_m \gg 0$ ) were observed, the qubit is projected towards  $Z = -1$  ( $Z = +1$ ), this leaving it in  $|g\rangle$  ( $|e\rangle$ ); at the same time, the equatorial Bloch vector components vanish  $\langle X \rangle_c = \langle Y \rangle_c = 0$ . This shows that the measurement is projective along the  $I_m$  axis which encodes the  $Z$  parity of the single qubit. On the other hand, for measurement outcomes near  $I_m = 0$ , the back-action of the measurement is very different. Now, the qubit experiences a stochastic impulse that rotates it along the equator of the Bloch sphere, as shown by the oscillations in  $\langle X \rangle_c$  and  $\langle Y \rangle_c$  with the outcome  $Q_m$ . However, this back-action does not project, and hence purify, the qubit state; instead, the  $Q_m$  outcome encodes the phase of the qubit state along  $X$  and  $Y$ . This is revealed by reduction in the amplitude of  $\langle X \rangle_c$  and  $\langle Y \rangle_c$  arising from the qubit dephasing as a result of information loss.

Finally, for strong measurements, here with  $\bar{I}_m/\sigma = 2.6$ , the projective measurement limit is recovered. The histograms reveal two well separated Gaussian distributions with the one on the left (right) corresponding to the qubit being projected to  $Z = -1$  ( $Z = +1$ ) corresponding to a final qubit state of  $|g\rangle$  ( $|e\rangle$ ). Since the qubit is driven to the poles of the Bloch sphere in this case, the equatorial components vanish entirely  $\langle X \rangle_c = \langle Y \rangle_c = 0$ . Indeed, this is identical to what was observed in Fig. 3.4 when the qubit was prepared in  $1/\sqrt{2}(|g\rangle + |e\rangle)$ ; the measurement results in two symmetric distributions of equal probability since the qubit is projected to  $|g\rangle$  and

$|e\rangle$  half the time.

One significant imperfection visible in the data is that the separatrix along the  $Q_m$  axis that is halfway between the two Gaussian distributions is not a straight line as would be expected. This can also be seen in the histogram in the middle row where the Gaussian distribution on the right appears to be larger than the one on the left. This is suspected to be a result of the following Josephson Parametric Converter (JPC) used to perform phase-preserving amplification having different gain for when the qubit was in  $|g\rangle$  and in  $|e\rangle$ . Although it remains to be verified, simulations of the system incorporating this effect resulted in the same observed behavior. This effect appears to be a result of insufficient reverse isolation between the JPC and the qubit-cavity system resulting in what is effectively entanglement between the gain of the amplifier and the qubit state.

To extract the measurement efficiency from this general operation, we use two methods. The first is to measure the amount of dephasing experienced by a qubit for a intermediate-strength measurement that results in stochastic oscillations around the equator of the Bloch sphere (the case of the middle row in Fig. 3.5). Specifically, we look at the case of outcomes near  $I_m\sigma = 0$  resulting in the data shown in Fig. 1.8A. The amplitude of these oscillations can be derived from Eq. 2.24 by setting  $I_m = 0$ . Furthermore, since the decoherence time of the qubit  $T_{2R}$  will also contribute to dephasing, and hence a reduction in the Bloch vector amplitude, we incorporate its effects into the equation for the amplitudes of  $\langle X \rangle_c$  and  $\langle Y \rangle_c$ , resulting in Eq. 1.3. By separating the effects of finite  $T_{2R}$ , we extract a more accurate measure of  $\eta$ . From the form of Eq. 1.3, we also find another method to measure  $\bar{I}_m/\sigma$ : the frequency of the oscillations. We find good quantitative agreement between the values of  $\bar{I}_m/\sigma$  extracted from the oscillation frequency and separation of the observed Gaussian distributions.

A second method for extracting the measurement efficiency is to ignore the variable-strength measurement. The now unrecorded measurement is a source of measurement-induced dephasing; thus analyzing the qubit Bloch vector amplitude as a function of the strength of the ignored variable-strength measurement provides another measure of  $\eta$ . The result of this unrecorded measurement is to dephase the qubit by the amount  $\exp[-\Gamma_m]$  where  $\Gamma_m = 2\bar{n}\kappa T_m \sin^2(\vartheta/2) =$

$(\bar{I}_m/\sigma)^2/\eta$ . Here  $\Gamma_m$  is the measurement-induced dephasing rate,  $\bar{n}$  is the average number of photons in the unrecorded measurement,  $T_m$  is the length of the measurement pulse, and  $\vartheta$  is the dispersive phase shift during the readout. We instead express  $\Gamma_m$  as a function of the measurement strength and the efficiency; since the latter has already been measured in two different ways for the experiment,  $\eta$  is the only remaining fit parameter. Thus, the Bloch vector amplitude  $\langle R \rangle_c$  was fit to  $A \exp [-(\bar{I}_m/\sigma)^2/\eta]$  as shown in Fig. 1.8B.

While this protocol has the advantages of being self-calibrating and offering two different ways of extracting  $\bar{I}_m/\sigma$  and  $\eta$  each from the same data set, it also suffers from some imperfections. Since it is a pulsed protocol, it is sensitive to all the imperfections resulting from transient responses. First, although a shaped demodulation window is employed, some information in the readout pulse may still be lost. Additionally, the bandwidth of the following amplification chain, set primarily by the instantaneous bandwidth of the JPC at its operating gain of 20 dB can also limit the efficiency. As in the case of this experiment, the JPC bandwidth, 6 MHz, was not much larger than the cavity bandwidth, 4.7 MHz, introducing errors resulting from different frequency components of the pulse experiencing different amount of gain. Band-limiting the spectral content of the measurement pulse by slowing it down could alleviate these errors but would involve using slower measurements more susceptible to relaxation and dephasing errors.

### 3.10 Extracting Measurement Efficiency from Observation of the Quantum Zeno Effect

An alternative method for characterizing the measurement efficiency of a system is to use a continuous-wave (CW) protocol. Unlike the pulsed-protocol described above, a CW-protocol is insensitive to imperfections arising from effects like shaped demodulation or the finite bandwidth of the following amplifier. In this CW-protocol, a qubit is simultaneously and continuously driven and measured resulting in the quantum Zeno effect. The quantum Zeno effect is the competition between the unitary evolution of a qubit due to a continuous Rabi drive and the stochastic back-action of a continuous, finite-strength measurement [62, 90]. Whereas the drive on a qubit

will cause it to coherently evolve and undergo Rabi oscillations, the measurement will inhibit this evolution by driving the qubit to an eigenstate of the measurement operator. Under these competing effects, a measure of the efficiency can be obtained by analyzing the back action on a qubit and characterizing the amount of information about the system gained by the observer.

### 3.10.1 Theory

Our system consists of a qubit that is subjected to a continuous drive, resulting in Rabi oscillations with frequency  $\Omega_R$ , and a variable-strength measurement, characterized by a measurement rate  $\Gamma_m$ . The power spectrum observed from such a system is derived in Ref. [75, 76]<sup>4</sup> The measured power spectrum  $S[\omega]$  is

$$\frac{S[\omega]}{S_0} = 1 + \frac{4\eta\Gamma_m^2\Omega_R^2}{(\omega - \Omega_R)^2 + \Gamma_m^2\omega^2} \quad (3.13)$$

where,  $\eta$  is the measurement efficiency and  $S_0$  is the power spectrum when no drive or measurement is applied.

To understand the behavior of this system as the measurement strength  $\Gamma_m$  is varied, we plot this expression for a Rabi drive of strength  $\Omega_R/2\pi = 1$  MHz and assuming a perfect measurement efficiency  $\eta = 1$  (shown in Fig. 3.6A). The measurement strength, expressed in terms of the Rabi drive strength  $\Omega_R$  is varied from the limit of no measurement being performed  $\Gamma_m = 0$  to a strong measurement  $\Gamma_m = 4.3\Omega_R$ .

When the measurement is off,  $\Gamma_m = 0$  (red trace), no information about the qubit is learned by the observer and we measure only quantum noise. Thus, the output power spectrum is a flat line, indicated by the noise floor in Fig. 3.6A. As the measurement strength increases and becomes finite but still weak compared to the Rabi drive,  $\Gamma_m \ll \Omega_R$  (orange and yellow traces), the cavity output, in the time domain, continues to look at first like pure quantum noise. However, its power spectral density reveals a sharp peak centered at the Rabi frequency. This is indicative of the qubit undergoing Rabi oscillations while only being weakly perturbed by the measurement drive. The peak of these curves is called the fixed point.

<sup>4</sup>Although in the reference the specific system being considered is an electron in quantum dots, the treatment can also be applied to a superconducting qubit like the transmon.

As the measurement strength increases further,  $\Gamma_m \sim \Omega_R$  (green and light blue traces), we observe that the measurement begins to perturb the Rabi oscillations. This is demonstrated by the peak in the power spectrum moving to lower frequency as the coherent oscillations are inhibited by the measurement. In the limit of a measurement rate much stronger than the Rabi drive,  $\Gamma_m \gg \Omega_R$  (blue and purple traces), the curves become Lorentzians centered at  $\omega = 0$ ; the qubit no longer evolves coherently. Instead, it is now pinned to an eigenstate by the measurement and only stochastically jumps because of the Rabi drive. In other words, the qubit undergoes quantum jumps between the eigenstates of the measurement.

We can further see how this experiment informs us about the measurement efficiency by looking at the behavior of the peak in the power spectrum at the Rabi frequency. Evaluating Eq. 3.13 for  $\omega = \Omega_R$ , we find that  $S[\Omega_R]/S_0 = 1 + 4\eta$ . Consequently, for the case of a perfectly efficient measurement,  $\eta = 1$ , shown in Fig. 3.6A, the ratio of the height of the fixed point to the height of the noise floor is 5. However, in the case of an inefficient measurement, this contrast is reduced and the height of the fixed point decreases. Consequently, the ratio  $S[\Omega_R]/S_0$  serves as a good experimental calibration of the system's measurement efficiency.

So far, we have ignored the effects of the finite lifetimes and coherence times of the qubit. The decay and decoherence that the qubit undergoes as it is being driven and measured will further change the measured spectrum. The expression for the output power spectrum, incorporating the effects of the qubit lifetime  $T_1$  and the decoherence time  $T_{2R}$ , is obtained from Ref. [104]:

$$\frac{S[\omega]}{S_0} = 1 + \frac{4\eta\Gamma_m}{\gamma^2 + (\omega\Omega - \Omega_{eff})^2 [\gamma^2 + (\omega\Omega + \Omega_{eff})^2]} \left\{ \gamma(1 - z_{st}^2) [\gamma^2 + \Omega_{eff}^2 + (\omega\Omega)^2] + \left( \left[ (1 - z_{st})^2 \left( \frac{\Gamma_2 - \Gamma_1}{2} \right) - \frac{\Omega^2 z_{st}^2}{2} \right] [\gamma^2 + \Omega_{eff}^2 - (\omega\Omega)^2] \right) \right\} \quad (3.14)$$

Here  $\gamma = (\Gamma_1 + \Gamma_2)/2$ ,  $\Omega_{eff} = \sqrt{\Omega^2 - (\Gamma_2 - \Gamma_1)^2/4}$ , and  $z_{st} = -1/(1 + \Gamma_1 + \Omega^2\Gamma_{2R})$  with  $\Gamma_1 = 1/T_1$ ,  $\Gamma_2 = 1/T_{2R} + \Gamma_m$ , and  $\Gamma_{2R} = 1/T_{2R}$ . As before,  $\Gamma_m$  is the measurement rate,  $\Omega_R$  is the Rabi oscillation frequency, and  $\eta$  is the measurement efficiency.

First, we verify that by simplifying this expression under the limit that  $T_1 = T_{2R} = \infty$ ,

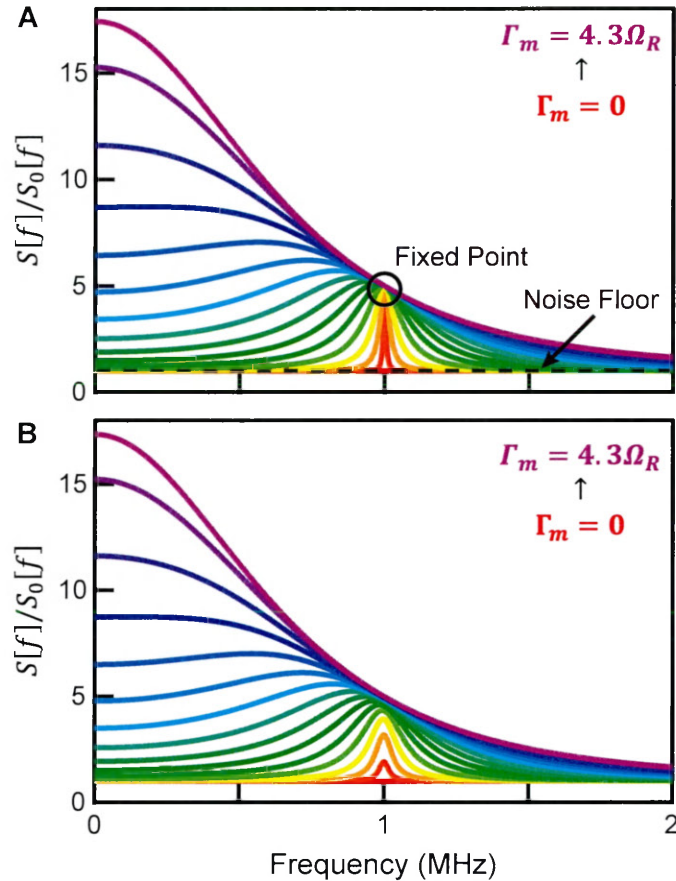


Figure 3.6 | **Theoretical Quantum Zeno Behavior of a Driven Monitored Qubit.** A) Theory without qubit lifetimes. The output power spectrum for a qubit that is simultaneously driven by a continuous Rabi drive and measured by a readout drive for a perfect measurement chain, i.e.  $\eta = 1$ . When the measurement strength,  $\Gamma_m$ , is much smaller than the Rabi drive,  $\Omega_R$ , the spectrum is a sharp peak at the Rabi frequency rising to the fixed point above the noise floor. This corresponds to the qubit undergoing coherent Rabi oscillations. In the limit that the measurement is much stronger than the Rabi drive, the qubit is pinned to an eigenstate by the measurement. It now stochastically jumps between the two eigenstates leading to Lorentzian shaped curves centered at  $\omega = 0$  B) Theory with finite qubit lifetimes. When the finite lifetime  $T_1$  and coherence  $T_2$  times of the qubit are included in the theory, all the curves no longer pass through the fixed point. Although, the location of the fixed point remains unchanged. For weak measurement strengths, the Rabi signal only slowly grows out of the noise floor since the measurement is not strong enough to discern the Rabi oscillations from the noise before the qubit decoheres. The behavior for strong measurement, however, remains unchanged.

Eq. 3.14 reduces to Eq. 3.13. Next, to understand the effects of the finite qubit relaxation and coherence times, we plot the new expression, as shown in Fig. 3.6B. Once again we choose

$\Omega_R/2\pi = 1$  MHz, vary  $\Gamma_m = 0$  to  $4.3\Omega_R$ , and assume  $\eta = 1$ . The values of  $T_1 = 20 \mu\text{s}$  and  $T_{2R} = 7 \mu\text{s}$  were chosen to match experimentally measured qubit parameters.

Comparing this to Fig. 3.6A, we find that the effects of  $T_1$  and  $T_{2R}$  are to smear out the fixed point and broaden the peaks for  $\Gamma_m \ll \Omega_R$ . Moreover, we find that instead of the peaks at  $\Omega_R$  always rising to the fixed point for any  $\Gamma_m$  as in Fig. 3.6A, the signal now only slowly grows out of the noise floor. This is because, for very small measurement strengths, the Rabi oscillations decay and dephase before they can be resolved. However, once the measurement strength increases a little further, these oscillations can be observed and the peak eventually rises to the fixed point. The behavior for the limit of very strong measurement  $\Gamma_m \gg \Omega_R$  remains unchanged; the qubit still undergoes stochastic jumps.

A noteworthy feature of this equation is that the effects of finite qubit lifetimes and imperfect measurement efficiency manifest differently; while the former results in not all the power spectrum curves passing through the fixed point, the latter actually changes the height of the fixed. As a result, this technique is somewhat robust to qubit decoherence as long as the peak at the Rabi frequency can be resolved. In fact, since all the other quantities in Eq. 3.14 can be independently measured and calibrated, the only free parameter is the measurement efficiency  $\eta$ . Thus, by fitting the measured spectrum to Eq. 3.14,  $\eta$  can be extracted.

### 3.10.2 Experimental Results

To implement this protocol, a slightly different system was used than the ones used in the rest of the experiments of this chapter (and thesis) - a qubit measured by a phase-sensitive amplifier (instead of the phase-preserving amplifier used in all the other experiment).

The system, cooled to 20 mK at the base stage of a dilution fridge, consisted of a transmon qubit, with frequency  $\omega_{ge}/2\pi = 4.416$  GHz, in a 3D rectangular cavity, with frequency  $\omega_c^g/2\pi = 7.431$  GHz and bandwidth  $\kappa/2\pi = 4.7$  MHz. The qubit-cavity dispersive shift was  $\chi/2\pi = 3.3$  MHz. A variable-strength measurement tone was applied to the weakly coupled input port ( $Q_{in} \sim 10^5$ ) of the cavity at  $(\omega_c^g - \chi/2)/2\pi = 7.429$  GHz, halfway between the cavity frequency for the qubit in  $|g\rangle$  and  $|e\rangle$ . The measurement tone exited the cavity through the strongly coupled

output port ( $Q_{out} = 1700$ ).

The output was routed via circulators to a double-pumped Josephson bifurcation amplifier (DP-JBA) operated as a reflection phase-sensitive amplifier. Unlike a phase-preserving amplifier, a phase-sensitive amplifier with gain  $G$  amplifies only a single quadrature of the incident microwave signal, ideally adding no noise to that quadrature of the amplified output [20]. The other quadrature is de-amplified, i.e. squeezed, by the same gain factor  $G$ . The experimental setup was otherwise identical to that used for the measurements described earlier in this chapter. Detailed theory and experiments about the operation of this amplifier can be found in Refs. [67, 131]. Measuring a qubit with a phase-sensitive amplifier results in different back-action than when the qubit is measured with a phase-preserving amplifier [131]. As a result of the unequal treatment of the two quadratures, the qubit now experiences back action that restricts its motion to a great circle of the Bloch sphere; the orientation of this great circle depends on the phase of the amplified quadrature relative to the phase of the readout. In this experiment, the phases are chosen to perform a measurement of the  $Z$  component of the qubit thereby restricting the back-action to a great circle passing through the poles of the Bloch sphere.

The amplifier was operated at a gain of  $G = 20$  dB where it had a bandwidth of 20 MHz and noise visibility ratio (NVR) of  $> 10$  dB. After the DP-JBA, the output signals were routed to a commercial cryogenic high electron mobility (HEMT) amplifier at 3 K for additional amplification before subsequent room-temperature amplification and demodulation. The input lines, room-temperature electronics, and shielding for this experimental system were similar to that used in other experiments in this thesis.

To implement this CW protocol, first the strengths of the Rabi drive and the measurement tone were calibrated. The amplitude of the tone applied at  $\omega_{ge}$  was chosen to achieve  $\Omega_R/2\pi = 1$  MHz. On the other hand, the measurement strength was calibrated using the expression for the measurement induced dephasing rate under phase-sensitive amplification  $\Gamma_m = \bar{n}\kappa\chi^2/(\chi^2 + \kappa^2)$ . It is expressed in terms of the average photon number in the readout tone,  $\bar{n}$ . The protocol, shown at the top of Fig. 3.7, consisted of concurrently imposing the 1 MHz Rabi drive on the qubit and a variable-strength cavity drive and recording the amplified cavity output

for a period of 1 ms. The experiment was repeated to acquire  $10^3$  records and the measured power spectrum was averaged over all the trials.

The measured average power spectrum scaled by the average power spectrum for  $\Gamma_m = 0$  is shown in Fig. 3.7; the inset shows a close-up of the region around  $\omega = \Omega_R$ . Solid lines are data with the color representing the strength of the measurement, which is varied from  $\bar{n} = 0$  (black) to  $\bar{n} = 1.36$  (purple). The dashed lines are plot of Eq. 3.14 using the experimentally measured qubit parameters of  $T_1 = 20 \mu\text{s}$ ,  $T_{2R} = 7 \mu\text{s}$  and  $\Gamma_m = \bar{n}\kappa\chi^2/(\chi^2 + \kappa^2)$ . The only free parameter in the equations was  $\eta$ .

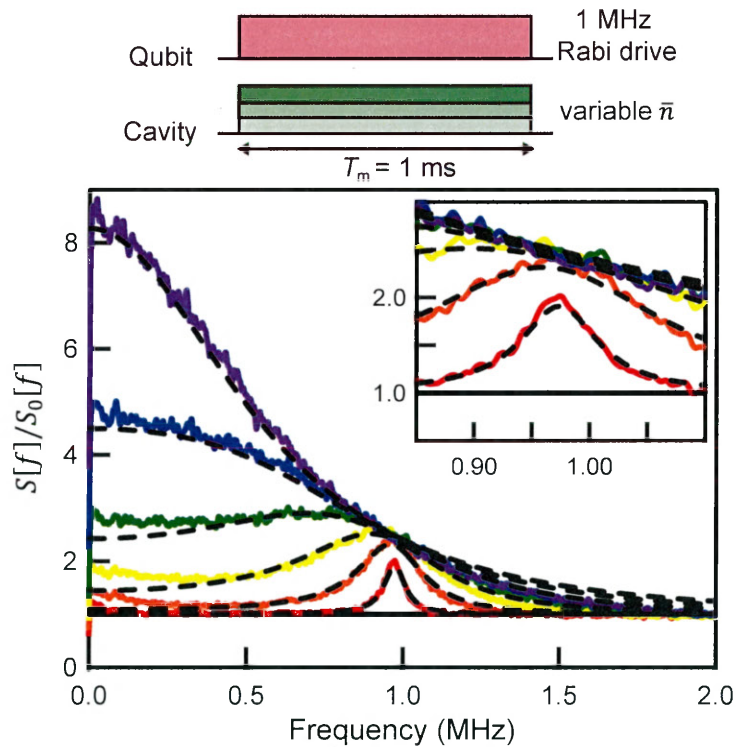


Figure 3.7 | **Extracting Quantum Measurement Efficiency from the Quantum Zeno Effect.** A) Pulse sequence for the observation of the quantum Zeno effect. A 1 MHz Rabi drive is applied to the qubit while a variable-strength measurement tone is concurrently applied to the cavity, whose output is recorded over a period of 1 ms. B) Power spectral density of Rabi oscillations in the presence of measurement versus cavity drive strength  $\bar{n}$  from weak (red curve) to strong (purple), along with theoretical fit (dashed lines) from which we extract  $\eta = 0.37 \pm 0.03$ . Inset: Detail of region about  $\omega/2\pi = 1$  MHz showing the expected fixed-point behavior.

We find good quantitative and qualitative agreement between the experimentally measured

power spectra and theoretical results. For small measurement strengths ( $\bar{n} = 0$  to  $\bar{n} = 0.14$ ), we obtain the expected narrow peak centered at the Rabi frequency, corresponding to the qubit undergoing weakly perturbed Rabi oscillation. As the measurement strength increases, the peak broadens and shifts left until it becomes a broad Lorentzian centered around  $\omega = 0$ .

To extract  $\eta$ , we fit  $S[\omega]/S_0$  with the measurement efficiency  $\eta$  as the only free parameter. These fits (shown as black superimposed lines in Fig. 3.7) show good agreement to the experimental data and correspond to  $\eta = 0.37 \pm 0.03$ . Independently, the measurement efficiency was also extracted by performing a version of the pulsed measurement back action protocol of Ch. 3.9 which yielded  $\eta = 0.32 \pm 0.02$ , in reasonable agreement with the CW quantum Zeno effect based protocol. Discrepancies in the two measurement efficiencies are suspected to be a result of imperfections in the shaped demodulation used in the pulsed protocol as well as ignored effects of amplified bandwidth and saturation in the CW protocol. Imperfections aside, this CW protocol offers a robust, alternative method for measuring the measurement efficiency of a qubit-cavity system.

# 4

## Coherent State Based Remote Entanglement Mediated by a JPC

Coherent states die many times before their death. Fock states taste of death but once.

---

Michael the Bard

### 4.1 Overview

Building upon the single qubit measurements with a JPC discussed in Ch. 3, we now use the coherent state pointer variable and the JPC to generate remote entanglement between two 3D transmon systems. We begin, in Ch. 4.2, by describing the experimental setup, parameters for the qubits and cavities, and a general overview of the entanglement generation protocol. Next, in Ch. 4.3, we discuss the two types of measurements performed in this system: a joint tomography measurement and an entangling measurement. In Ch. 4.4, we present the experimental results, expanding upon the discussion of Ch. 1.6. Finally, in Ch. 4.5, we discuss the future prospects of this specific remote entanglement protocol as well as other continuous variable based schemes.

## 4.2 Experimental Setup

The experiment, cooled to below 20 mK on the base stage of a dilution refrigerator, consists of two different superconducting transmon qubits in separate 3D cavities, referred to as Alice and Bob. A detailed experimental setup is shown in Fig. 4.1. The transmon qubits consist of Al/AlO<sub>x</sub>/Al Josephson-junctions fabricated using a bridge-free electron-beam lithography technique[79]; they were fabricated on double-side-polished chips of *c*-plane sapphire that were 3 mm by 7 mm for Alice and 3 mm by 10 mm for Bob. The junctions are connected via 1 μm leads to two rectangular pads (540 μm × 500 μm for Alice and 1100 μm × 250 μm for Bob) separated by 100 μm. The qubit chips are placed in their respective rectangular cavities, made of copper for Alice and aluminum for Bob. The transmon parameters and couplings to the TE<sub>101</sub> cavity mode were designed using using finite-element simulations and black-box quantization[100]. Experimentally measured device parameters are listed in Table 4.1.

Parameter	Alice (Signal)	Bob (Idler)
Cavity frequency $\omega_c^g/2\pi$ (GHz)	9.1632	7.4818
Cavity bandwidth $\kappa/2\pi$ (MHz)	3.4	4.7
Readout frequency $\omega_r/2\pi$ (GHz)	9.1624	7.4798
Qubit frequency $\omega_{ge}/2\pi$ (GHz)	5.3800	5.0252
Anharmonicity $\chi_{qq}/2\pi$ (MHz)	200	220
Dispersive shift $\chi/2\pi$ (MHz)	1.6	3.8
$T_1$ (μs)	60	70
$T_{2R}$ (μs)	8	10
$T_{2E}$ (μs)	40	20

Table 4.1 | Coherent state based remote entanglement - Alice and Bob qubit and cavity parameters

The two cavities (17.78 mm × 5.08 mm × 36.65 mm for Alice and 21.34 mm × 7.62 mm × 43.18 mm for Bob) had resonance frequencies  $\omega_A^g/2\pi = 9.1632$  GHz,  $\omega_B^g/2\pi = 7.4818$  GHz, and bandwidths  $\kappa_A/2\pi = 3.4$  MHz,  $\kappa_B/2\pi = 4.7$  MHz. For both Alice and Bob, a coaxial coupler was used as the input port with the length of pin determining the input coupling quality factors  $Q_{in, A} \sim 10^5$  and  $Q_{in, B} \sim 5 \times 10^5$ . The output port for Alice was also a coaxial coupler chosen to realize  $Q_{out, A} \sim 2400$ ; on the other hand, the output port for Bob was an aperture

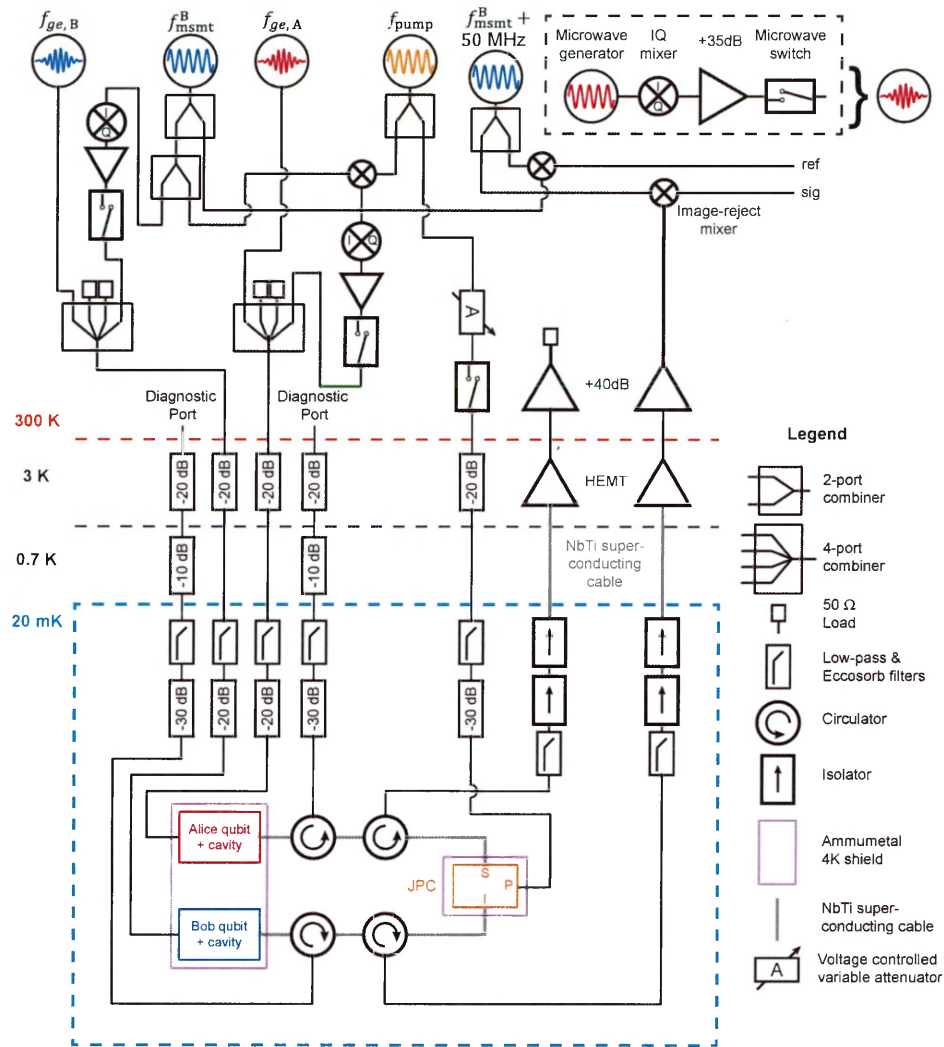


Figure 4.1 | **Detailed Experimental Setup.** The experiment (bottom) was cooled down to below 20 mK on the base-stage of a dilution refrigerator. Input lines carrying signals to the systems were attenuated and filtered using commercial low-pass filters and homemade lossy Eccosorb filters. The room temperature electronics used to produce and shape the input signals are shown at the top of the figure. The basic setup to produce shaped signals was a microwave generator driving an IQ mixer followed by an amplifier and a switch to gate the signal (box in top right corner). The signals were shaped by channels from two Arbitrary Waveform Generators (AWGs) (not shown) which also provided the digital markers for all the switches. Copies of this setup (denoted by the shorthand notation of a circle with a shaped pulse) were used to generate the drive signals (color-coded) for Alice (red) and Bob (blue). The Alice and Bob modules had 2 inputs each, the cavity readout tone and the qubit signals. The Alice and Bob systems were connected to the signal and idler ports respectively of a JPC amplifier which was used to perform both the entanglement generation as well as high-fidelity joint single-shot readout of both systems. The output signals were down-converted and then digitized and demodulated along with a room-temperature reference copy.

in the cavity wall at the anti-node of the  $TE_{101}$  mode to couple to a 76.2 mm long section of aluminum WR-102 waveguide Purcell filter (see Ch. 3.5). The size of the aperture was chosen so that  $Q_{\text{out}, B} \sim 1500$ . A waveguide to coaxial cable adapter (WR-102 to SMA) was connected to the other end of the straight waveguide section, serving as the output port. The output ports of the Alice and Bob cavities were connected to the signal and idler ports of a Josephson Parametric Converter (JPC) using Nb-Ti superconducting coaxial cables to reduce photon loss. Operated as a phase-preserving amplifier, the JPC was used to perform high-fidelity single shot readout of the two qubit cavity systems for qubit state tomography, and to generate entanglement by measurement between Alice and Bob. Microwave circulators were used to enforce directionality, separating between incoming and outgoing signals from the JPC.

The resonance frequencies of Alice and Bob were designed and then precisely tuned so that the JPC could simultaneously provide gain centered at the Alice and Bob readout frequencies  $(\omega_A^g - \chi/2)/2\pi = 9.1624$  GHz, and Bob,  $(\omega_B^g - \chi/2)/2\pi = 7.4798$  GHz respectively. A pump tone was applied at the sum frequency,  $\omega_p/2\pi = 16.6422$  GHz, to the JPC; the pump tone power and the magnetic flux bias of the JPC were tuned so that it provided 20 dB of gain with 5.7 MHz of bandwidth on the signal centered at 9.1619 GHz and 20 dB of gain with 5.8 MHz on the signal centered at 7.4798 GHz. The measured noise visibility ratio (NVR) was 5.5 dB on the signal and 8 dB on the idler.

This frequency tuning of the cavities was achieved by placing an aluminum tuning screw (#4 – 40) at the anti-node of the  $TE_{101}$ ; by increasing the amount that screw penetrated into the cavity, the frequency of the mode could be lowered. With this, the frequency of the  $TE_{101}$  mode could be lowered by around 200 MHz with no measured change to the internal or coupling quality factors at room temperature. To tune a cavity to a desired frequency within its tunable range of 200 MHz, the cavity frequency (when containing the qubit being used) was at 20 mK. Calculating the detuning from the desired frequency, the cavity frequency is then screw-tuned at room temperature; the screw is adjusted to move the measured resonance frequency by the calculated detuning. Then, the system is cooled down to 20 mK; this procedure can repeatedly

enable tuning the cavity resonance frequency to within about  $0.2 \times \kappa$  of the desired frequency<sup>1</sup>.

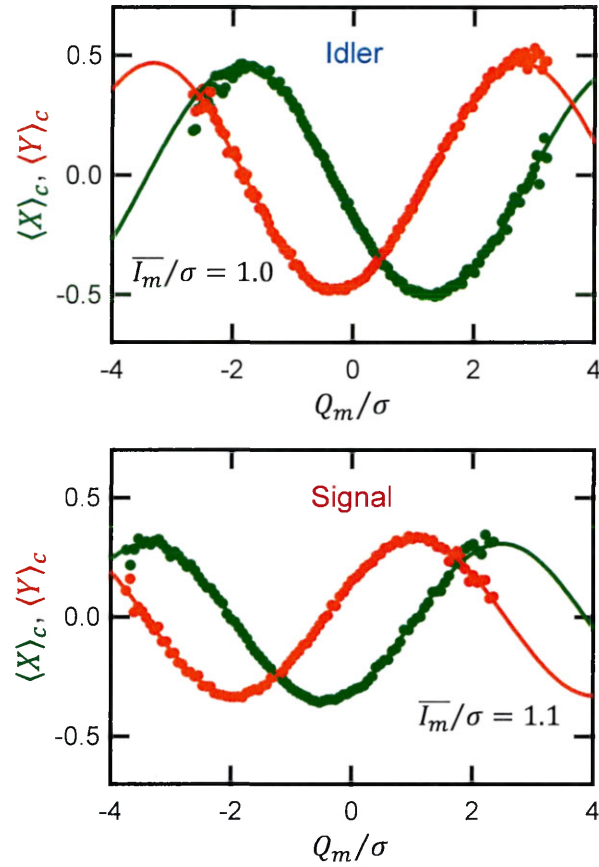


Figure 4.2 | **Signal and Idler Quantum Measurement Efficiencies.** The  $\langle X \rangle_c$  and  $\langle Y \rangle_c$  as a result of a weak measurement ( $\bar{I}_m/\sigma \sim 1$ ) on the signal, or Alice, (bottom) and idler, or Bob, (top) qubit are shown for weak measurement outcomes near  $I_m/\sigma \sim 0$ . From a fit to these stochastic Ramsey oscillations (data in points, fit in solid lines), we extract a quantum measurement efficiency of  $\eta_{\text{Alice}} = 0.53 \pm 0.01$  and  $\eta_{\text{Bob}} = 0.60 \pm 0.01$ .

As shown in Fig. 4.1, the qubits were housed inside the same  $\mu$ -metal (Amumetal A4K) can to shield them from magnetic fields. The input and output lines connected to the experiment were filtered with home-made lossy Eccosorb filters, commercial low-pass microwave filters, attenuators and isolators to attenuate radiation incident on the experiment. The signal and idler outputs from the JPCs were each connected to a commercial cryogenic high electron mobility (HEMT) amplifier at 3 K to additionally amplify the output signals before subsequent room-temperature

<sup>1</sup>A similar tuning procedure was used to adjust the frequencies of the qubit cavity systems used in single photon based remote entanglement experiment of Ch. 5.

amplification and demodulation. Although both the signal and idler outputs contain identical information in the high-gain limit (see Ch. 2.4), we choose to only use the idler output chain because the measured NVR (8 dB) was higher than on the signal side (5.5 dB) for the same gain (20 dB). This is due to the lower noise temperature of the HEMT amplifier used on the idler output line (LNF-LNC4\_8C) compared to the one used on the signal output line (LNF-LNC7\_10C). Also, the insertion loss of the components between the JPC and the HEMTs is lower at 7.5 GHz than at 9 GHz. Consequently, the lower added noise of the idler output line results in an increased overall quantum efficiency than the signal output line. For all the experimental data discussed hereafter, only the idler output line was used; thus the Bob system was measured using the reflection gain of the JPC whereas the Alice system was measuring using transmission gain.

The room temperature microwave hardware shown in Fig. 4.1 offered independent amplitude and phase control over the qubit control pulses and the cavity readout pulses for the Alice and Bob system. Two arbitrary waveform generators (AWGs) were used to provide the envelopes for the qubit and cavity control pulses. Separate IQ-mixers were used for each of the four (one each for the Alice and Bob qubits and cavities) microwave tones. The local oscillators for the IQ-mixers for all but the Alice cavity tone were independent microwave signal generators; the local oscillator input for the Alice cavity tone was generated by mixing the signal from a microwave generator for the JPC pump tone and the Bob cavity readout tone (for more details see Ch. 4.3). The generated readout and control pulses were then amplified and gated by room temperature microwave switches before being sent to the input lines connected to the strongly-coupled ports of the Alice and Bob cavities via circulators. The power of the JPC pump tone was controlled by a combination of a constant-gain linear amplifier and a voltage-variable attenuator to achieve 20 dB of gain. The pump tone was also gated by a microwave switch to enable pulsed operation of the JPC.

A crucial determinant of whether remote entanglement can be generated is the measurement efficiency (as discussed in Ch. 1.6). The measurement efficiency of the Alice and Bob systems were independently measured using the stochastic Ramsey fringes observed during the back-

action of a weak measurement (discussed in Ch. 1.5 and Ch. 3.9). Both qubit cavity systems were measured in reflection, i.e. the readout tones entered and left the cavity through the strongly coupled output port. The cavities were driven with 500 ns square pulses and demodulated with 700 ns long shaped  $|g\rangle - |e\rangle$  waveforms (discussed in Ch. 3.7). The measured stochastic Ramsey oscillations for a measurement strength around  $\bar{I}_m/\sigma \sim 1$  are shown in Fig. 4.2 with the data Alice (the signal side) on the bottom and Bob (the idler side) on the top. From fits to the oscillations, we measured  $\eta_{\text{Alice}} = 0.53 \pm 0.01$  and  $\eta_{\text{Bob}} = 0.60 \pm 0.01$ . Like the data for single qubit measurement efficiency in Ch. 3.9, here too, the reduction in the stochastic Ramsey oscillation contrast from qubit dephasing was included to provide a more accurate estimate of the measurement efficiency. The lower measurement efficiency of the signal side is suspected to be due to the increased insertion loss of the components between the qubit-cavity system and the JPC than the idler side. Although even higher efficiencies are desirable, the measured values are just beyond the threshold of  $\eta > 0.5$  required for generating remote entanglement [122, 130].

### 4.3 Joint and Entangling Measurements

At its core, this experiment depends on how the JPC processes its signal and idler inputs, which are flying coherent states pointer variables entangled with the Alice and Bob qubits. Indeed, by choosing, on the fly, how this processing is done, we use the JPC to first generate remote entanglement between Alice and Bob and then characterize the final two-qubit state using single-shot high-fidelity joint readout. The first step towards realizing this joint microwave signal processing is technical: the phases of the Alice and Bob readout tones and the JPC pump tone must be locked to each other. When the JPC converts microwave signals between the signal and idler frequencies, it also imparts the phase of the pump,  $\phi_p$  as described by Eq. 2.10. Since the Alice system is measured in transmission gain, the readout pulse at the signal frequency will acquire this phase shift when it is converted to the idler frequency. To ensure that the phase of readout signal does not drift with time, this pump phase must be subtracted out before the readout signal is demodulated with a reference signal near the idler frequency (see Fig. 4.1). This

is accomplished by mixing the pump tone (phase  $\phi_p$ ) with the Bob readout signal (phase  $\phi_B$ ) to generate the Alice readout signal, as shown in Fig. 4.1; moreover, the phase shift that the Alice signal acquires from this mixing ( $\phi_A = \phi_B - \phi_p$ ) is chosen such that the phase shift acquired from the JPC is canceled out. With this, not only are the readout phases of Alice and Bob locked and stable with time, but a relative phase  $\phi_{\text{rel}}$  could be set on the two readout signals on demand.

Next, the amplitudes of the readout pulses applied at room temperature were tuned so that they resulted in the same observed measurement strength  $\bar{I}_m/\sigma$  for the Alice and Bob modules. Furthermore, due to the differences in signal path lengths on the Alice and Bob sides of the system, the overall phase of the readout signals will be different as well. The offset phase between the two was also experimentally measured to calibrate the system.

Both the cavities were driven with 500 ns long readout pulses at  $\omega_c^g - \chi/2$ , halfway between the cavity resonance frequency for the qubit in  $|g\rangle$  and  $|e\rangle$ . The state of qubit was mapped onto the phase of the incident coherent state, the pointer variable. As discussed in Ch. 2.4, the joint stationary-qubit flying-coherent state can be written as  $\alpha |g\rangle |\alpha_g\rangle + \beta |e\rangle |\alpha_e\rangle$  with  $|\alpha|^2 + |\beta|^2 = 1$ . Representations in  $IQ$ -space of the pointer variables after they are entangled with the Alice and Bob qubits are shown in the center and left columns respectively of Fig. 4.3A. These coherent states are then incident on the JPC; operated as a phase-preserving amplifier, the output of the JPC is the amplified sum of its signal and idler inputs (see Eq. 2.10). The JPC output is shown in the right column of Fig. 4.3A. By changing the relative phase between the signal and idler inputs to the JPC, the operation performed by the JPC also changes and is used to realize either an entangling measurement (top row of Fig. 4.3A) or a joint measurement (bottom row).

### 4.3.1 Which-Path Erasing Measurements for Entanglement Generation

When the relative phase between the Alice and Bob readout tones is chosen to be  $\phi_{\text{rel}} = 0$ , both the signal and idler inputs to the JPC lies along the same axis, the  $I_m$  axis for example in Fig. 4.3A and the JPC generated entanglement between the Alice and Bob qubits for certain measurement outcomes. In the  $IQ$ -plane representation, the output of the JPC is just the vector sum of its signal and idler inputs. Thus, when both input are  $|\alpha_g\rangle$  ( $|\alpha_e\rangle$ ) corresponding to Alice and Bob

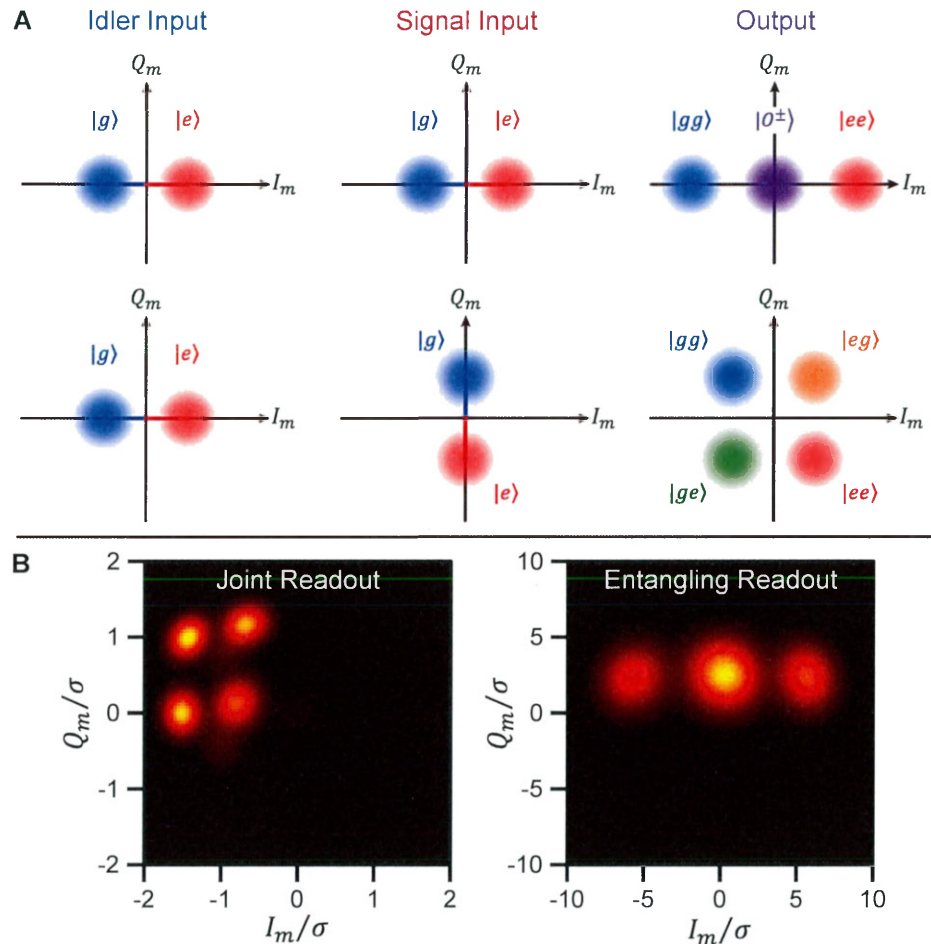


Figure 4.3 | **Two Qubit Joint and Entangling Readout with a JPC.** A)  $IQ$ -plane representation of the coherent state pointer variables incident on the JPC (left for Bob and center for Alice) and after the JPC (right) for an entangling (top) and joint (bottom) measurement. The states of the Alice and Bob qubits are entangled with the phases of the coherent state pointer variables. After being emitted by each qubit-cavity system, these flying coherent states are incident on the signal and idler ports of the JPC where they are coherently summed and multiplied. When the relative phase between the two inputs is zero (i.e. both input lie along the  $I_m$  axis), the JPC performs an entangling measurement because the output does not distinguish between  $|ge\rangle$  and  $|eg\rangle$ , instead performing a half-parity measurement and projecting the qubits into the manifold of odd Bell states. On the other hand, when the two input have a relative phase of  $\pi/2$  (i.e. one input lies along the  $I_m$  axis and the other along the  $Q_m$  axis), the JPC implements a joint measurement where the four two-qubit computational states ( $|gg\rangle$ ,  $|ge\rangle$ ,  $|eg\rangle$ , and  $|ee\rangle$ ) are mapped onto distinguishable outcomes. B) Measured histograms for a joint (left) and entangling (right) readout. The experimentally realized joint and entangling measurements produce histograms that resemble those shown in A. The distortion of the output coherent states for the joint readout are a result of saturation effects of the JPC.

both in  $|g\rangle$  ( $|e\rangle$ ), the output is a coherent state of increased negative (positive) displacement shown in red (blue), corresponding to the two-qubit computation state  $|gg\rangle$  ( $|ee\rangle$ ). On the other hand, when one of the qubits is in  $|g\rangle$  and the other in  $|e\rangle$ , the inputs are  $|\alpha_g\rangle$  and  $|\alpha_e\rangle$ , and the output is a coherent state (in purple) near the origin of  $IQ$ -plane. Moreover, the output state is the same regardless of which qubit is in  $|g\rangle$  and  $|e\rangle$ . In the limit that no information is lost, i.e. perfect measurement efficiency, when an outcome  $(I_m, Q_m)$  is from the center distribution (purple), no information about the individual qubits is learned. Instead, the observer only learns that the two qubits are in an odd  $ZZ$  parity state. Consequently, the measurement leaves Alice and Bob in an eigenstate associated with that outcome with is an odd Bell state. Since the three possible outcomes, one each for  $|gg\rangle$ ,  $|ee\rangle$ , and an odd Bell state of arbitrary phase,  $|O^\pm\rangle$ , are separated along the  $I_m$  axis, this corresponds to a measurement of  $ZI + IZ$  of the two qubits.

On the other hand, the  $Q_m$  axis encodes the phase of the resulting odd Bell state; this can be understood as the two qubit extension to the measurement of a single qubit where the  $Q_m$  outcome encodes the phase (see Eq. 2.21) of the final qubit state informing the observer about the back-action along the  $X$  and  $Y$  components of the Bloch sphere. In the two-qubit case, for outcomes inside the distribution corresponding to an odd Bell state (purple distribution in Fig. 4.3A), the phase of the generated odd Bell state oscillates with  $Q_m$ . Moreover, like the single qubit case, the frequency of the oscillations of this phase increase with the measurement strength. Consequently this non-projective stochastic phase kick is sensitive to information loss, which will appear as dephasing of the Bell state. If sufficient information is lost, i.e. the measurement efficiency is low, this dephasing reduces the Bell state to a separable state. It is for this reason that the measurement efficiency is one of the crucial determinants of the success of this protocol.

As discussed in Ch. 1.6, the other vital requirement for this experiment is to erase the which path information contained in the traveling coherent states so that the output from the JPC associated with the state  $|ge\rangle$  and  $|eg\rangle$  are indistinguishable. So far, in the description of the measurement outcomes and back action presented above, we have assumed that this requirement has been satisfied. To realize this which path erasure experimentally requires matching the amplitudes and aligning the phases of the Alice and Bob coherent state pointer variables. Their

amplitudes were matched by adjusting the room temperature voltages used for the Alice and Bob readout pulses until the observed measurement strength  $\bar{I}_m/\sigma$  was found to be the same. The  $\bar{I}_m/\sigma$  was measured by finding the separation of the Gaussian distributions obtained when the qubit was prepared in  $|g\rangle$  and  $|e\rangle$  followed by a 500 ns readout pulse in transmission. For this experiment, the measurement strength was chosen to be  $\bar{I}_m/\sigma = 2.00$ ; moreover, the observed measurement strength for Alice and Bob differed by only about a 1%. This measurement strength was chosen to minimize saturation effects from the JPC while providing sufficient separation for high fidelity tomography. While performing readout in reflection would have alleviated these saturation effects, the requirement for overdrive pulses (discussed below) necessitated performing the measurements in transmission.

The results of this amplitude matching are shown in the top plot of Fig. 4.4; after preparing the Alice (Bob) qubit in  $|g\rangle$  or  $|e\rangle$ , a 500 ns readout pulse was applied to the Alice (Bob) cavity with the Bob (Alice) cavity not energized. The cavity output field was demodulated in 20 ns intervals and plotted on the  $IQ$ -plane. As expected for performing readout in transmission at  $\omega_r = \omega_c^g - \chi/2$ , we find that the amplitudes of the coherent states for  $|g\rangle$  and  $|e\rangle$  are identical and differ only in phase; moreover, the coherent state amplitudes, as well as their separation, are identical for Alice and Bob.

Next, the phases were aligned by calibrating the angle of the vector pointing from the Gaussian distribution for  $|g\rangle$  to the one for  $|e\rangle$ ; from that, a relative offset angle between Alice and Bob was calculated and the phase of the readout tone applied to the Alice system was rotated by that amount to align the output phases. Together, this amplitude and phase calibration resulted in the entangling readout histogram shown on the right of Fig. 4.3B; as expected, when the Alice and Bob qubits were each prepared in the state  $Y = +1$ , we observed three different distributions, one each for the states  $|gg\rangle$  and  $|ee\rangle$  at negative and positive  $I_m/\sigma$  respectively and one for the manifold of odd Bell states near the origin.

However, this amplitude and phase matching only ensure that the which-path information is erased in steady state, i.e the states  $|ge\rangle$  and  $|eg\rangle$  look identical once the Alice and Bob cavities are rung up. Since the readout is performed with a 500 ns pulse, the ring-up and ring-down,

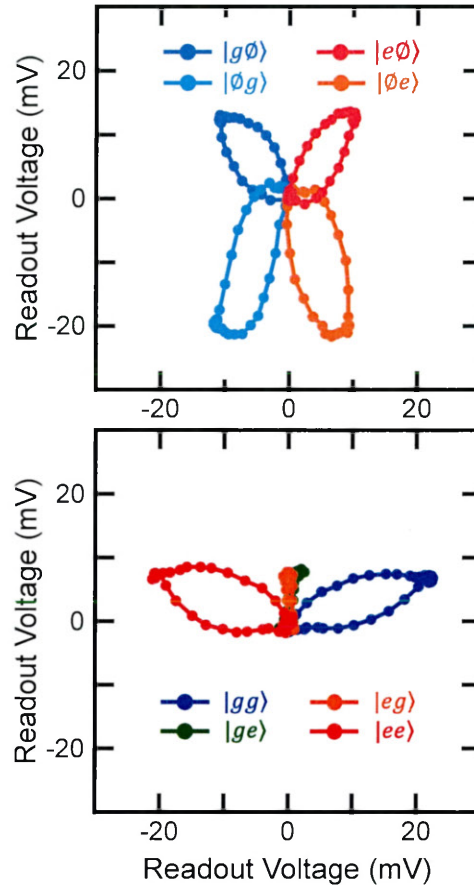


Figure 4.4 | **Erasing Which-Path Information by Tuning Cavity Output Fields.** A) Individual cavity response plotted as a trajectory in  $IQ$ -space. The response for the Alice and Bob cavity when individually energized with the qubit prepared in either  $|g\rangle$  (blue for Bob, cyan for Alice) or  $|e\rangle$  (red for Bob, orange for Alice) is demodulated in 20 ns intervals, averaged and plotted in  $IQ$ -space. The drive amplitudes for Alice and Bob were chosen to match the resulting separation between  $|g\rangle$  and  $|e\rangle$  in  $IQ$ -space; the relative phase of the drives was chosen so that the output states lie parallel to the  $I_m/\sigma$  axis. B) Matching the measured trajectories for  $|ge\rangle$  and  $|eg\rangle$  in  $IQ$ -space. The relative amplitude and phase of the entangling readout was chosen to maximize the overlap of the  $|ge\rangle$  and  $|eg\rangle$  trajectories. This minimizes the ability of the JPC to resolve single qubit information when an outcome associated with a state of odd-parity is measured.

around  $5/\kappa \sim 200$  ns are not negligible, constituting a fair fraction of the total demodulated pulse. As a result, not only do the steady state responses of the cavities need to be matched but so do their transient behavior to ensure that which-path information is obscured at all times. This was achieved by using overdrive pulses (see Ch. 3.6) to effectively speed up the output field of the slower Alice cavity and make it look identical to the faster Bob cavity. In addition, the

relative amplitude and phase between the Alice and Bob readout pulses were also adjusted. To quantify the similarity of the system response for the states  $|ge\rangle$  and  $|eg\rangle$ , the Alice and Bob systems were prepared in the computational states ( $|gg\rangle$ ,  $|ge\rangle$ ,  $|eg\rangle$ , and  $|ee\rangle$ ) and the output field was measured by demodulating it in 20 ns intervals. The efficacy of the which-path erasure was quantified by the ratio of the magnitude of the vector separating the states  $|ge\rangle$  and  $|eg\rangle$  integrated over the duration of the readout pulse, called  $\bar{I}_m^{\text{dist}}$ , to the magnitude of the vector separating the states  $|ge\rangle$  and  $|gg\rangle$ , called  $\bar{I}_m^{\text{ent}}$ . By minimizing the ratio, the entangling readout was experimentally tuned to learn the least amount of information that could distinguish between  $|ge\rangle$  and  $|eg\rangle$ ; as shown in the bottom of Fig.4.4, this tuning makes the trajectories associated with  $|ge\rangle$  and  $|eg\rangle$  overlap although some residual distinguishability remains. In the experiment, a ratio of  $\bar{I}_m^{\text{dist}}/\bar{I}_m^{\text{ent}} \sim 0.1$  was achieved; this indicates that the distinguishability of the states will limit the fidelity of the generated odd Bell state to  $\mathcal{F} \sim 0.9$ .

### 4.3.2 Joint Measurements for Two-Qubit Tomography

Choosing a relative phase of  $\phi_{\text{rel}} = \pi/2$  between the Alice and Bob readout drives results in the joint readout shown in the bottom row of Fig. 4.3A. The readout maps the computational states,  $|gg\rangle$ ,  $|ge\rangle$ ,  $|eg\rangle$  and  $|ee\rangle$ , to four different output distributions; thus the observer gains a bit each of information about the state of Alice and Bob as well as correlations between the states of the two, making this measurement ideal for two-qubit tomography. As shown in Fig. 4.3A, the  $I_m$  axis encodes information about the parity of Bob and the  $Q_m$  axis encodes information about the parity of Alice. While the orthogonal quadrature ( $Q_m$  for Bob and  $I_m$  for Alice) should encode information of the phase of each qubit, according to measurement back action discussed in Ch. 2.4, here we limit ourselves to the case of projective measurements where the measurement strength is large and phase information is destroyed. An experimentally measured joint histogram when both qubits are prepared in the state  $Y = +1$  is shown on the left of Fig. 4.3B; that the four distributions do not lie in a perfect square (as we would expect for identical measurement strengths on Alice and Bob) and the distortion of the distributions is a result of saturation from the JPC. The number of photons being processed by the JPC for this type of readout exceeds

its 1 dB compression power and distributions with larger displacements from the center,  $|gg\rangle$  for example, are affected worse than ones with smaller displacements,  $|ee\rangle$  for example.

To perform qubit state tomography, the pulses  $Id$ ,  $R_y(\pi/2)$  and  $R_x(\pi/2)$  were performed on the Alice or Bob qubits to measure the  $Z$ ,  $X$  and  $Y$  components respectively of each qubit Bloch vector. Furthermore, by applying all 9 possible combinations of those pre-rotations on Alice and Bob, as well as 3 each where one of Alice or Bob was not measured, all combinations of correlations between the  $I$ ,  $Z$ ,  $X$ , and  $Y$  components were measured. Two separatrices, the first along the  $Q_m$  axis and the second along the  $I_m$  axis, were used to threshold the output voltage of the Alice and Bob qubits respectively to an outcome of  $+1$  or  $-1$ . In addition, the two-qubit correlation was calculated on a shot-by-shot basis. By performing measurements on an ensemble of identically prepared states, these counts were converted into expectation values of the observable being measured. With this, the two-qubit density matrix was measured in the Pauli basis.

## 4.4 Experimental Results and Analysis

The pulse sequence to generate remote entanglement (shown in Fig. 4.5A) is very similar to that used to examine the back action of a variable-strength measurement on a single qubit; the protocol consists of three steps: (1) qubit state preparation; (2) entanglement generation by measurement; (3) two-qubit tomography. At the beginning for the remote entanglement protocol, the Alice and Bob qubits were initialized in  $|g\rangle$  by post selection using a method similar to that used for the single qubit protocols discussed in Ch. 1.5 and Ch. 3.8. First, after performing a joint projective measurement of Alice and Bob, a  $R_x^{ge}(\pi/2)$  pulse was applied to each qubit to rotate the qubit to  $Y = +1$ . Together, this scrambles the state of the two qubits, erasing information about the past state of the qubit. Then, another joint measurement was performed to post-select on experiments where both qubits were found to be in  $|g\rangle$ . This state initialization by post-selection had a success probability of 19%, slightly lower than the expected 25%, and allowed the experiment to be repeated at  $T_{\text{rep}} = 10 \mu\text{s}$ , much faster than the relaxation time of

any qubit.

Next, single qubit pulses were applied to the Alice and Bob qubits to prepare them in the desired initial state. For entanglement generation, a  $R_x^{ge}(\pi/2)$  pulse was applied to each qubit to prepare them in  $Y = +1$ ; in addition, for control experiments, single qubit pulses were used to also prepare the two in the computational states,  $|gg\rangle$ ,  $|ge\rangle$ ,  $|eg\rangle$ , and  $|ee\rangle$ . Subsequently, an entangling measurement of varying amplitude was performed by applying a 500 ns long pulse to each of the Alice and Bob cavities, and the measurement outcome  $(I_m, Q_m)$  was recorded; the amplitude of the entangling measurement was varied linearly from  $\bar{I}_m/\sigma = 0.3$  to 4.0, where, as before,  $\bar{I}_m/\sigma$  is the distance of the  $|gg\rangle$  distribution along the  $I_m$  axis from the origin scaled by the variance of the distribution. The relative phase and amplitude of the drives on Alice and Bob were chosen to erase the which-path information about the qubits, as discussed above in Ch. 4.3.

Next, a  $R_x^{ge}(\pi)$  pulse was applied to each of the Alice and Bob qubits to act as a spin echo refocusing pulse; the pulse was located at the midpoint of the protocol, halfway between the single qubit pulses used to prepare the qubit state and the pre-rotation pulse before joint tomography. To ensure that the pulse was at the protocol midpoint, a delay was introduced after this pulse, resulting in an overall time of  $T_{\text{seq}} = 1.65 \mu\text{s}$ . Since the echo decoherence time of the two qubits exceeded the Ramsey dephasing time (see Table. 4.1), using the echo pulses reduces the infidelity of the final Bell state due to qubit decoherence.

Finally, two-qubit tomography was performed by applying one of 15 combinations of single qubit pulses on Alice and Bob followed by a joint projective measurement. The outcome of the tomography was thresholded using two separatrices, one for Alice and one for Bob, to obtain a tomography measurement outcome for Alice, Bob, and the correlation between the two. Furthermore, the tomography outcomes were binned by the entangling measurement outcome. The experiments were repeated to accumulate at least  $3 \times 10^5$  successful shots of each sequence, i.e. each initial state, entangling measurement strength and tomography outcome.

The outcomes of the variable-strength entangling measurement were sorted into a  $201 \times 201$  bin histogram for each measurement strength. Measured histograms are shown in the left column

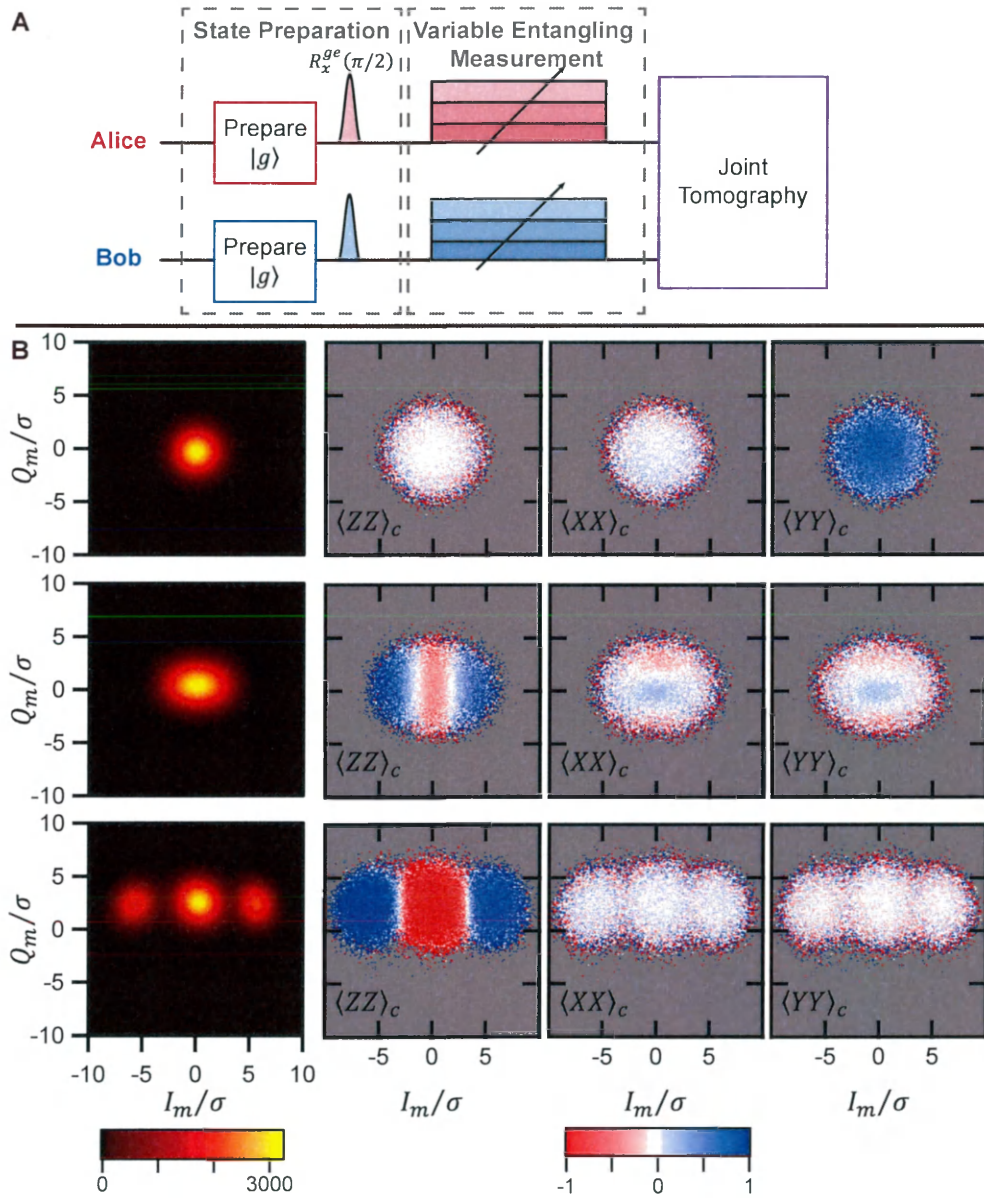


**Figure 4.5 | Histograms and Tomograms of Select Pauli Components.** A) Pulse sequence for generating remote entanglement by measurement with a JPC. Using a protocol similar to that outlined in Fig. 1.5, the two qubits were each prepared in  $1/\sqrt{2}(|g\rangle + i|e\rangle)$ . Next, a variable-strength entangling measurement was performed whose outcome  $(I_m/\sigma, Q_m/\sigma)$  was recorded. Finally, full two-qubit state tomography was performed by a combination of 15 pre-rotation pulses and a joint measurement of the two qubits to construct the final density matrix obtained for each entangling measurement outcome. B) Histograms (left column) show the probability of a particular measurement outcome  $(I_m/\sigma, Q_m/\sigma)$  of the variable-strength entangling measurement. For each measurement outcome, the two-qubit density in the Pauli basis was calculated from joint tomography of the two qubits. The measured  $\langle XX \rangle_c$  (second column),  $\langle YY \rangle_c$  (third column), and  $\langle ZZ \rangle_c$  (right column) components are shown for each measurement outcome.

of Fig. 4.5B for measurement strengths of  $\bar{I}_m/\sigma = 0.3$  (top row), 1.3 (middle row), and 4.0 (bottom row). For each measurement outcome bin, the resulting two-qubit density matrix was measured in the Pauli basis by calculating the average values of the tomography outcomes. Shown in the other three columns of Fig. 4.5B are selected conditional tomograms for  $\langle ZZ \rangle_c$  (second column),  $\langle XX \rangle_c$  (third column), and  $\langle YY \rangle_c$  (right column).

As the strength of the measurement is increased, we find that projectiveness of the half-parity measurement, encoded by  $I_m$ , also increases. This is the expected two-qubit analog of the single qubit measurement back action, where increasing the measurement strength increases the projectiveness of the  $Z$  measurement (see Ch. 2.4). Not only is this illustrated by the observed increase in separation between the  $|gg\rangle$  and  $|ee\rangle$  from the odd state manifold, but also by the change in the  $\langle ZZ \rangle_c$  tomograms. For weak measurements, the final state has no parity and  $\langle ZZ \rangle_c \sim 0$  for all measurement outcomes; on the other hand, as the measurement strength increases outcomes near  $I_m \sim 0$  are projected to a state of negative (odd) parity and ones with  $|I_m| > 0$  are projected to positive (even) parity. Moreover, as demonstrated by the difference between the  $\langle ZZ \rangle_c$  tomograms in the middle and bottom rows, the resulting  $ZZ$  parity increases with measurements, approaching  $ZZ = \pm 1$  for  $\bar{I}_m/\sigma = 4.0$ .

On the other hand, the  $Q_m$  axis encodes the phase of the generated odd Bell state and is sensitive to the measurement efficiency, once again paralleling the single qubit case. For the case of a very weak measurement strength of  $\bar{I}_m/\sigma = 0.3$  (top row), we find that  $\langle XX \rangle_c = 0$  and  $\langle YY \rangle_c \sim 0.7$  corresponding to the initial separable state of the two qubits both pointing along  $+Y$ . The reduction in  $\langle YY \rangle_c$  is attributed to dephasing and imperfect state preparation and tomography although a more detailed quantitative analysis is needed to provide an accurate error budget which was not possible from the data acquired for this system. From the As the measurement strength is increased to  $\bar{I}_m/\sigma = 1.3$  (middle row), oscillations in  $\langle XX \rangle_c$  and  $\langle YY \rangle_c$  as a function of  $Q_m$  are observed for outcomes near  $I_m \sim 0$ . Crucially, these oscillations decrease in amplitude for outcomes with  $|I_m| > 0$  since the states  $|gg\rangle$  and  $|ee\rangle$  have  $\langle XX \rangle_c = \langle YY \rangle_c = 0$ . However, increasing the measurement strength further to  $\bar{I}_m/\sigma = 4.0$  (bottom row), these oscillations disappear because their frequency increases and the measurement

inefficiency of the Alice and Bob side of the system causes the Bell state to dephase, destroying the coherence of the state.

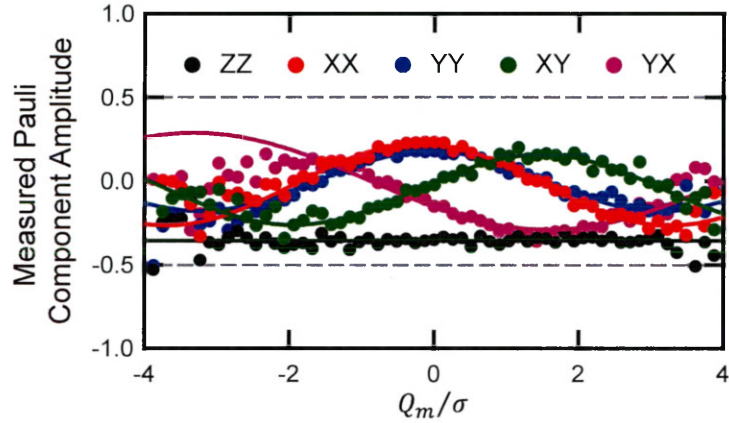


Figure 4.6 | **Histograms and Tomograms of Select Pauli Components.** Select two qubit density matrix components in the Pauli basis for a weak entangling measurement of strength  $\bar{I}_m/\sigma \sim 1$  (middle row of Fig. 4.5) for measurement outcomes corresponding to  $I_m/\sigma = 0$ . The resulting states have odd parity indicated by negative  $ZZ$  and the components of the Pauli vector oscillate with  $Q_m/\sigma$  as expected. From the amplitude of the oscillations, we extract a raw fidelity of  $\mathcal{F} = 0.46$  to an odd Bell state.

For an arbitrary Bell state, the only non-zero density matrix components in the Pauli basis are  $\langle ZZ \rangle$ ,  $\langle XX \rangle$ ,  $\langle YY \rangle$ ,  $\langle XY \rangle$ , and  $\langle YZ \rangle$ . To quantify the quality of the entangled state that is generated with this protocol, we examine these Pauli components for outcomes along  $I_m = 0$  for  $\bar{I}_m/\sigma = 1.3$ . Shown in Fig. 4.6 are the measured values of  $\langle ZZ \rangle_c$ ,  $\langle XX \rangle_c$ ,  $\langle YY \rangle_c$ ,  $\langle XY \rangle_c$ , and  $\langle YZ \rangle_c$  as a function of the  $Q_m$  measurement outcome. We find that  $\langle ZZ \rangle_c < 1$  indicating a state of odd parity, as expected. The deviation of  $\langle ZZ \rangle_c$  from  $-1$  is attributed to the finite projectiveness of the measurement, i.e. some poisoning from states of even parity, as well as imperfect tomography and the finite  $T_1$ 's of the two qubits. The other four Pauli components follow the expected sinusoidal behavior, oscillating with  $Q_m$  as the phase of the Bell state changes. From these Pauli components, we can estimate the fidelity  $\mathcal{F} = \text{Tr}(\rho_{\text{meas}} |O^{\text{arb}}\rangle \langle O^{\text{arb}}|)$  to an odd Bell state of arbitrary phase  $\phi$ ,  $|O^{\text{arb}}\rangle = \frac{1}{\sqrt{2}}(|ge\rangle + e^{i\phi}|eg\rangle)$ . We measure a fidelity  $\mathcal{F} = 0.45 \pm 0.02$  lower than the threshold of  $\mathcal{F} = 0.5$  for provable entanglement.

An alternative metric to characterize whether the final state has quantifiable entanglement

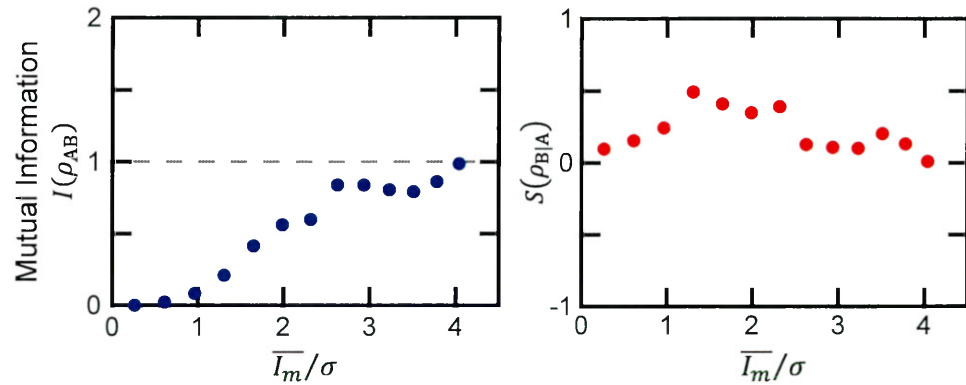


Figure 4.7 | **Mutual Information from an Entangling Measurement.** The mutual information  $I(\rho_{AB})$  (left) and von Neumann entropy  $S(\rho_{B|A})$  generated for an entangling measurement as a function of the entangling measurement strength  $\bar{I}_m/\sigma$  for measurement outcomes at the center of the odd Bell state distribution. Provably entangled states necessarily have a mutual information  $I(\rho_{AB}) > 1$  and  $S(\rho_{B|A}) < 0$ ; this threshold is not exceeded for any strength of the entangling measurement.

beyond classical correlations is the mutual information

$$I(\rho_{AB}) = S(\rho_A) + S(\rho_B) - S(\rho_{AB}) \quad (4.1)$$

Here,  $S(\rho) = -\text{Tr}[\rho \log(\rho)]$  is the von Neumann entropy,  $\rho_{AB}$  is the two-qubit density matrix of the Alice and Bob qubits, and  $\rho_A = \text{Tr}_B \rho_{AB}$  ( $\rho_B = \text{Tr}_A \rho_{AB}$ ) is density matrix for the Alice (Bob) subsystem obtained by taking the partial trace over Bob (Alice) [99]. For a pure, two-qubit entangled state  $S(\rho_A) = S(\rho_B) = 1$  and  $S(\rho_{AB}) = 0$ ; in general, a two-qubit state is entangled if and only if the quantity  $S(\rho_{B|A}) = S(\rho_{AB}) - S(\rho_A)$  is negative, with an extremal value of  $-1$  for a pure entangled state [99]. This threshold can be recast in terms of the mutual information as  $I(\rho_{AB}) > 1$ . This entanglement metric is attractive because it is agnostic to the type of entangled state but offers a threshold for provable entanglement.

Shown in Fig. 4.7 is the mutual information  $I(\rho_{AB}) > 1$  (left) and the quantity  $S(\rho_{B|A})$  as a function of the strength of the entangling measurement  $\bar{I}_m/\sigma$  for measurement outcomes at the center of the odd Bell state distribution. We find that at no measurement strength does the resulting two-qubit state cross either threshold, confirming that we do not generate provable

entanglement.

As discussed in Ch. 1.6, this fidelity is a result of a number of different imperfections but is primarily dominated by the finite measurement efficiency of the system. From the data, only an estimate of the infidelity due to the various sources of error is possible, not a detailed analysis of the error channels using a quantum circuit model like that discussed in Ch. 5.8. Moreover, since this system involves continuous variable coherent states as pointer variables, a quantitative analysis would require using master equation simulations to fully analyze the sources of error [130]. Instead, here we only present an outline of the various sources of error and how they impact the fidelity.

The first contribution to the infidelity of the final Bell state is the decoherence of the two qubits. From the individual qubit echo dephasing times,  $T_{2E}^{\text{Alice}} \sim 40 \mu\text{s}$  and  $T_{2E}^{\text{Bob}} \sim 20 \mu\text{s}$ , we calculate a Bell state coherence time of  $T_{2\text{Bell}} \sim 15 \mu\text{s}$ . From this, the maximum Bell state fidelity limited by qubit decoherence is  $\mathcal{F}_{T_{2\text{Bell}}} \cong 0.95$ . The contribution to the infidelity from the finite distinguishability of the states  $|ge\rangle$  and  $|ge\rangle$  can be estimated from the ratio of  $\bar{I}_m^{\text{dist}} / \bar{I}_m^{\text{ent}} \sim 0.1$ . This is a measure of the amount by which the outputs  $|ge\rangle$  and  $|eg\rangle$  differ compared to the difference between  $|ge\rangle$  and  $|gg\rangle$ ; thus, the state distinguishability limited fidelity is  $\mathcal{F}_{\text{dist}} \cong 0.9$ . Another imperfection in the system is the state preparation and tomography; unfortunately, from the data collected for this system, it is not possible to extract a quantitative value of the measurement fidelity. This also precludes correcting for systematic errors in tomography as described in Ch. 5.6. Instead, we can only estimate that the joint measurement fidelity was  $\mathcal{F}_{\text{joint}} < 90\%$ .

None of these sources of error are enough, on their own or even combined, to account for the measured Bell state fidelity. Indeed, the dominant source of error is the information loss suffered by the coherent states as they travel from the Alice and Bob modules to the JPC. As in the case of a single qubit, this loss of information results in dephasing of the final qubit state. The measured efficiencies of  $\eta_{\text{Alice}} = 0.53 \pm 0.01$  and  $\eta_{\text{Bob}} = 0.60 \pm 0.01$  just exceed the minimal viable threshold of  $\eta > 0.5$  needed for achieving entanglement assuming no other imperfections, like qubit decoherence, and identical losses on the Alice and Bob sides. A better

metric for a system like the one used in this experiment is a combined measurement efficiency  $\eta_t = \eta_{\text{Alice}}\eta_{\text{Bob}} / (\eta_{\text{Alice}} + \eta_{\text{Bob}} - \eta_{\text{Alice}}\eta_{\text{Bob}})$ ; provable entanglement generation in the absence of qubit decoherence requires that  $\eta_t > 1/3$  [130] which our system just exceeds  $\eta_t = 0.39$ . Since there are additional sources of error, together, the system parameters are still not sufficient to generate provable remote entanglement.

## 4.5 Perspectives and Future Directions

Although coherent states are a natural choice for a pointer variable, i.e flying qubit, for remote entanglement generation because they are easy to entangle with stationary qubits and process with linear amplifiers, the protocols described here based on them are notoriously susceptible to photon loss. More precisely, this is a direct consequence of the back action of the phase-preserving amplification that we use, which only encodes the phase on the  $Q_m$  quadrature but does not actually measure the phase unlike how it measures the  $ZZ$  parity. In other words, while the measurement of  $ZZ$  is increasingly projective with measurement strength, the measurement of  $XX$  and  $YY$  is never projective; instead, it is better to think of the back action associated with the  $Q_m$  outcome as a stochastic impulse to the qubit, ultimately sensitive to dephasing due to information loss. As a result, this remote entanglement protocol mediated by coherent states processed by a JPC does not implement the measurement along  $X$  of the flying qubit described in Fig. 1.2.

This is not to say that a remote entanglement protocol based on continuous variable states cannot be made insensitive to loss. For example, suppose it were possible to design a system where there are four distinct measurement outcome distributions, one each for the states  $|O^+\rangle$ ,  $|O^-\rangle$ ,  $|E^+\rangle$ , and  $|E^-\rangle$ ; each Bell state is mapped onto a different coherent state output. In this hypothetical system, the  $I_m$  axis would encode the parity along  $ZZ$  and the  $Q_m$  axis would encode the parity along  $XX$ . Although each is a continuous variable outcome, the back action of the measurement would be projective, and hence purifying, along both quadratures. In this case, the fidelity of the Bell state would no longer be sensitive to photon loss since the projectiveness

of the measurement would purify the state, protecting it against any information loss (just like the single qubit measurement in the strong projective measurement limit). Realizing this would require implementing a true CNOT gate between the flying qubits as shown in Fig. 1.2, which remains an open challenge.

Of course, increasing the measurement efficiency is an alternative strategy to achieving higher entanglement fidelities. As discussed in Ch. 1.5 and Ch. 3.9, the measurement efficiency is dominantly limited by the losses between the qubit-cavity module and the JPC, arising, for example, from the use of bulky and lossy commercial circulators. On-chip circulators and direction amplifiers offer a path to realizing higher system efficiencies by obviating these lossy components and interconnects [21, 69, 132]. However, these devices still do not offer isolation comparable to commercially available circulators and introduce additional hardware and experimental complexity. Another avenue is to use reduce the losses between the qubit-cavity module and the JPC with either commercially available lower insertion-loss interconnects and circulators, or changing the architecture of those intermediary elements, to waveguide for example [96]. However, no experiment has yet demonstrated a significant increase in measurement efficiency beyond  $\eta \sim 0.6$ ; moreover, any improvements in fidelity will require further decreasing these losses, requiring the entire measurement system to be constantly improved. As the complexity of quantum information systems grows, especially in applications like a modular architecture described in Ch. 1.3, the losses will necessarily increase as more components are introduced to advance functionality. While coherent states are undeniable advantageous for being easily compatible with the superconducting quantum circuit toolbox and the high generation rates possible with continuous variable flying qubits, their sensitivity to information loss makes these protocols ones that are more attractive once systems have been engineered to be extremely low-loss and efficient.



# Remote Entanglement with Single Flying Microwave Photons

... we are not experimenting with single particles any more than we can raise Ichthyosauria in the zoo.

---

Erwin Schrödiner

## 5.1 Overview

In the absence of continuous-variable based remote entanglement protocols that are robust to photon loss [122], protocols that instead rely on single photons as the carriers of quantum information are preferable since their robustness to loss makes them a compelling choice for use in current quantum information and computation systems where transmission losses are a challenge. Moreover, the robustness to loss also makes these protocols conducive to scaling to larger and more complex systems where losses will inevitably increase. The single microwave photon based remote entanglement protocol described in Ch. 1.7, based a proposal designed for nitrogen-vacancy center based systems [6], is robust to loss because the detection of a single photon in each round of the experiment is uniquely associated with the generation of a Bell state

of Alice and Bob of a definite phase (unlike the coherent state based protocol where the phase oscillated with  $Q_m$ ).

For the full protocol using two single photon detectors, the maximum success probability is 50%, assuming perfectly efficient detectors and no transmission losses. This can be understood from the total system state after the beam-splitter in the first round of the protocol  $|\psi\rangle_2 = \frac{1}{2} \left( |gg\rangle |00\rangle + |O^+\rangle |10\rangle + |O^-\rangle |01\rangle + \frac{1}{\sqrt{2}} |ee\rangle (|02\rangle - |20\rangle) \right)$ ; half of the 4 possible outcomes for the states of Alice and Bob are entangled states. It is worth noting that the success probability here is identical to that of the coherent state based protocol.

Therefore, by using only a single detector in our experiment, the maximum success probability is reduced to 25%. Incorporating the finite efficiency of the detector of approximately 50% (justified in Ch.5.4) and the transmission efficiency of the system 80%, the probability of success estimated for this experiment is  $P_{\text{success}} = 0.25 \times (0.5)^2 \times (0.8)^2 = 0.04$ . Here the detector efficiency and the transmission efficiency appear squared because they affect each of the two rounds of the protocol. Although this success probability of 4% may seem low compared to the coherent state based protocol, it is worth noting that even that protocol's actual success probability is well below 50% since only a narrow sliver of outcomes centered around  $I_m/\sigma \sim 0$  produce a viable Bell state, assuming, of course, a sufficiently high system efficiency.

In this chapter, we delve deeper into the experimental implementation of the single photon based remote entanglement protocol. Starting with describing the experimental system in Ch. 5.2, we then describe how to generate single photons in Ch. 5.3 and how to detect these single photons in Ch. 5.4. We then demonstrate in Ch. 5.5 that the single photon generation process is actually the desired CNOT-like operation (discussed in Ch.1.7). After describing how we perform tomography and correct for systematic measurement errors in Ch. 5.6, we present the experimental results and control data in Ch.5.7 discussing the various sources of error in Ch. 5.8. Finally we offer perspectives on improving the fidelity and generation rate in Ch. 5.9.

## 5.2 Experimental Implementation

The three transmon qubits in the experiment consist of Al/AIO<sub>x</sub>/Al Josephson-junctions fabricated using a bridge-free electron-beam lithography technique[79] on double-side-polished 3 mm by 13 mm chips of *c*-plane sapphire. The junctions are connected via 1 μm leads to two rectangular pads (1900 μm × 145 μm for Alice and Bob, 1100 μm × 250 μm for the detector) separated by 100 μm. The qubit chips are placed in their respective rectangular indium-plated copper cavities (21.34 mm × 7.62 mm × 43.18 mm). The transmon parameters and couplings to the TE<sub>101</sub> cavity mode were designed using finite-element simulations and black-box quantization[100]. Experimentally measured device parameters are listed in Table 5.1.

A coaxial coupler was used as the input port of each cavity with the length of pin determining the input coupling quality factor  $Q_{\text{in}} \sim 10^6$ . The output port for each cavity was an aperture in the cavity wall at the anti-node of the TE<sub>101</sub> mode. The size of the aperture was chosen so that  $Q_{\text{out}} = 7.5 \times 10^3$  yielding a total cavity bandwidth  $\kappa \simeq 1/Q_{\text{out}}$ . Waveguide to coaxial cable adapters (WR-102 to SMA) were used on the output port of the cavities; since the qubit frequency is below the cutoff frequency of the waveguide while the cavity frequency is inside the passband, this section of waveguide acts as a Purcell filter for the qubit.

Parameter	Alice	Bob	Detector
Cavity frequency $\omega_c^g/2\pi$ (GHz)	7.6314	7.6316	7.6222
Cavity bandwidth $\kappa/2\pi$ (MHz)	0.9	1.2	0.9
Qubit frequency $\omega_{ge}/2\pi$ (GHz)	4.6968	4.6620	4.7664
Anharmonicity $\chi_{qq}/2\pi$ (MHz)	197	199	240
Dispersive shift $\chi/2\pi$ (MHz)	9	9	3
$T_1$ (μs)	140	85	90
$T_{2, \text{Echo}}$ (μs)	9	16	30

Table 5.1 | **Single photon based remote entanglement - Alice, Bob, and Detector qubit and cavity parameters**

As shown in Fig. 5.1, the qubits were mounted to the base stage of a cryogen-free dilution fridge maintained below 50 mK. The cavities were housed inside μ-metal (Amumetal A4K) cans to shield them from magnetic fields. The input and output lines connected to the experiment were

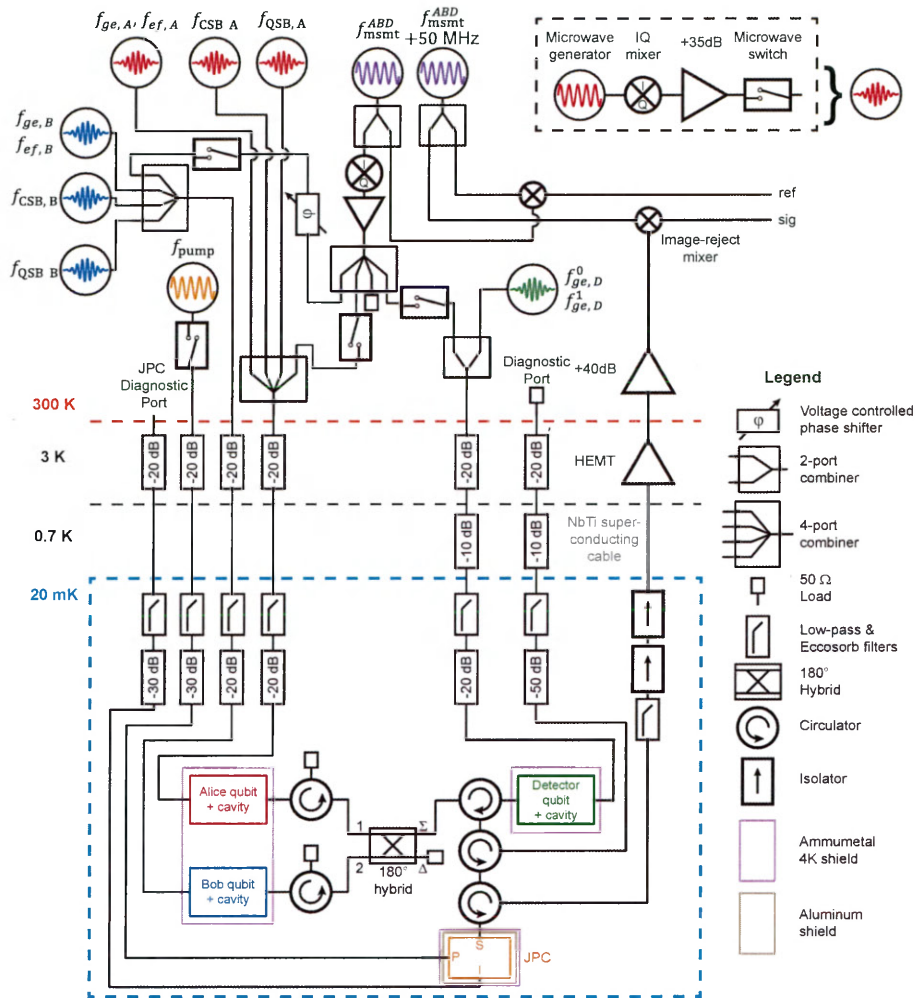


**Figure 5.1 | Detailed Experimental Setup.** The experiment (bottom) was cooled down on the base-stage ( $< 50 \text{ mK}$ ) of a dilution refrigerator. Input lines carrying signals to the systems were attenuated and filtered using commercial low-pass filters and homemade lossy Eccosorb filters. The room temperature electronics used to produce and shape the input signals are shown at the top of the figure. The basic setup to produce shaped signals was a microwave generator driving an IQ mixer followed by an amplifier and finally a switch to gate the signal (box in top right corner). The signals were shaped by channels from four Arbitrary Waveform Generators (AWGs) (not shown) which also provided the digital markers for the switches. Copies of this setup (denoted by the shorthand notation of a circle with a shaped pulse) were used to generate the drive signals (color-coded) for three modules, Alice (red), Bob (blue) and the detector (green). The Alice and Bob modules had 4 inputs each: the cavity readout tone, the qubit signals and the pair of sideband pulses for photon generation. On the other hand, the detector module had 2 inputs: the cavity readout tone and the qubit signals. All the modules were readout using a single output line that had multiple stages of amplification. High-fidelity single-shot readout was enabled by the JPC amplifier. The output signals were down-converted and then digitized and demodulated along with a room-temperature reference copy.

filtered with home-made lossy Eccosorb filters, commercial low-pass microwave filters, attenuators and isolators to attenuate radiation incident on the experiment. A commercial cryogenic HEMT amplifier was used at 3 K to additionally amplify the output signals before subsequent room-temperature amplification and demodulation.

A critical requirement for the experiment was matching the frequencies of the Alice and Bob cavities to render the flying single photons indistinguishable. In addition, the detector cavity frequency needs to also be matched to the Alice and Bob cavity frequencies so that incident photons can enter the detector cavity. This was achieved by an aluminum screw inserted into each cavity at the  $TE_{101}$  anti-node to fine-tune the cavity frequencies until they satisfied  $\omega_A^e = \omega_B^e = \omega_D^g$  (see Fig. 5.2A).

All three qubit-cavity systems were measured on the same output line using a single Josephson Parametric Converter (JPC) operated as a nearly-quantum-limited phase-preserving amplifier. The JPC was biased to provide 20 dB of gain with a bandwidth of 8 MHz centered at 7.6314 GHz to realize high-fidelity single-shot readout of all three qubit-cavity system. At this operating point, a noise visibility ratio (NVR)[96] of 8 dB was measured, indicating that 86% of the noise measured at room temperature was amplified quantum fluctuations from the JPC.

As shown in Fig. 5.1, readout pulses for the three cavities were generated using a single microwave generator powering an IQ-mixer. The output of the mixer was split and sent to each cavity on separate input lines with the relative room temperature attenuation on each line adjusted so that an applied readout amplitude at room temperature resulted in the same measured signal-to-noise ratio (SNR) for each qubit-cavity system. Room temperature microwave switches were used on each line to gate the pulses generated by the IQ-mixer. The amplified cavity outputs were mixed down to radio frequencies along with a copy of the generator tone that did not pass through the cryostat to provide a reference. The signal and reference were digitized and demodulated to yield in-phase and quadrature components ( $I(t)$ ,  $Q(t)$ ) that are insensitive to drifts in the generator and other microwave components. With this setup, high-fidelity readout of all the modules in the fridge was possible with minimal hardware and complexity. In the experiments described in this chapter, two types of measurements were performed: (1) joint

measurement of the Alice and Bob qubits and (2) single qubit measurement of the detector.

### 5.2.1 Joint Alice and Bob measurement

The Alice and Bob cavities were measured jointly by energizing them with  $2 \mu\text{s}$  pulses at  $f_{msmt}^{ABC} = \omega_A^g/2\pi = 7.6314 \text{ GHz}$ . Using a phase shifter on the Bob cavity arm, the relative phase of the pulses on the Alice and Bob cavities (including all system path lengths) was adjusted to  $\pi/2$ . The output signals from each cavity then passed through the hybrid whose output was the sum of the two cavity signals but with half the power from each signal was lost in the cold  $50 \Omega$  load. This joint output signal reflects off the detector cavity (since it is  $\chi_A$  above  $\omega_D^g$ ) and was amplified by the JPC. As a result, the output signal demodulated at  $50 \text{ MHz}$  contained information about both qubit states along orthogonal axes (see Fig. 5.2B). Two separatrices (white dashed lines), the first along the  $Q_m$  axis and the second along  $I_m$  axis, were used to measure the state of the Alice and Bob qubits respectively. In addition, the two-qubit correlation was calculated on a shot-by-shot basis. This resulted in an overall fidelity  $\mathcal{F}_{\text{joint}} > 90\%$ . A primary limitation in achieving a higher fidelity was the loss of half the information in the cold-load after the hybrid. This can be improved in future experiments by the use of a second detector and output line. While these joint tomography imperfections will ultimately impact the measured entanglement fidelity, they can be calibrated out (as we discuss later in the Joint Tomography and Calibration section).

### 5.2.2 Detector qubit measurement

To measure the state of the detector qubit, an IF-frequency of  $-9.2 \text{ MHz}$  was used on the IQ-mixer to generate  $700 \text{ ns}$  pulses at  $\omega_D^g = 7.6222 \text{ GHz}$ . Since this is equal to  $\omega_A^e$  and  $\omega_B^e$ , this readout is not performed simultaneously with the joint measurement of Alice and Bob described above to avoid signal interference. The amplified output from the cavity was demodulated at  $59.2 \text{ MHz}$  resulting in the histogram shown in Fig. 5.2C. As explained in Ch. 1.7, measuring the qubit in  $|e\rangle$  corresponds to a click in the detector. In this case, the measurement fidelity,  $\mathcal{F}_{\text{det}} > 99\%$ . The measurement was optimized for maximal fidelity in the shortest possible time

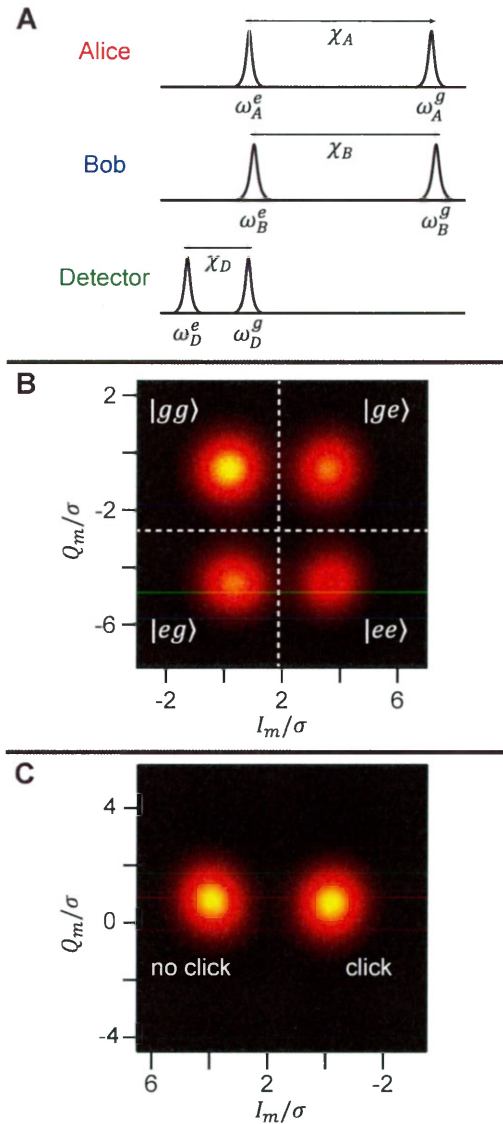


Figure 5.2 | **Alice, Bob and Detector Qubit Readout Spectra and Histograms.** A) Alice, Bob and Detector cavity frequency spectra. The Alice and Bob cavities had nearly identical frequencies ( $\omega_A^g \approx \omega_B^g$ ) and dispersive shifts ( $\chi_A \approx \chi_B$ ). To perform joint readout of Alice and Bob, microwave pulses were simultaneously applied on each cavity at  $\omega_A^g$  with a relative phase of  $\pi/2$  between the two pulses. The detector module cavity frequency  $\omega_D^g$  was tuned to match the frequency of the photons in the experiment,  $\omega_A^e$ . The detector was readout at  $\omega_D^g$ . B) Joint readout histogram for Alice and Bob. A  $2 \mu\text{s}$  measurement pulse was used to measure the state of both qubits. The resulting output contained information about the state of Alice and Bob along the  $Q_m$  and  $I_m$  axes respectively. Thus, the measurement provided single-shot readout of both qubit states as well as the correlation between the two qubit states with  $\mathcal{F}_{\text{joint}} > 90\%$ . C) Readout histogram for the detector. The state of the detector qubit was measured with  $\mathcal{F}_{\text{det}} > 99\%$  in 700 ns.

by using a shaped pulse that minimized the cavity ring-up and ring-down time (as discussed previously in Ch. 3) [86]. Since the pulse-shape also decreased the time taken to depopulate the cavity, operations on the detector could be performed 400 ns after the readout instead of having to wait for the natural ring-down time.

### 5.3 Generating Single Photons

As discussed in Ch. 1.7, the first key technical requirement is generating flying single photons that are entangled with the stationary transmon qubits, i.e a CNOT operation between the stationary and flying qubits. Under the system constraints that single photons cannot directly be created in the cavity (the linear drives at our disposal only provide control of the average position of a harmonic oscillator, not of populations in specific states [89]) and that only the cavity (not the transmon) is coupled to the external environment, flying single photons can be generated by first creating an excitation in the qubit, swapping the excitation into the cavity and then allowing leak out the cavity to become a traveling photon [58, 77]. The exchange of excitations between the qubit and cavity, which are otherwise only dispersively coupled, is achieved by the application of two detuned microwave pump tones on the system, which enable four-wave mixing between the qubit and cavity, to drive sideband transitions [71, 142]; the advantage of this approach is all microwave control of the system without requiring magnetically tunable qubits with fast flux control [42, 58, 136].

The cQED Hamiltonian of the qubit (designated by mode  $b$  with frequency  $\omega_q$ ) and cavity (designated by mode  $a$  with frequency  $\omega_c$ ) system expanded to fourth-order in the cosine potential of the junction is given by [74, 81]:

$$\mathbf{H}_{\text{cQED}}/\hbar = \omega_c \mathbf{a}^\dagger \mathbf{a} + \omega_q \mathbf{b}^\dagger \mathbf{b} - \frac{1}{2} \chi_{qq} \mathbf{b}^{\dagger 2} \mathbf{b}^2 - \chi \mathbf{a}^\dagger \mathbf{a} \mathbf{b}^\dagger \mathbf{b} \quad (5.1)$$

To this system, we apply two microwave drives, called QSB and CSB (since they are detuned from the qubit and cavity modes), with complex amplitudes  $\xi_{\text{QSB}}$  and  $\xi_{\text{CSB}}$ , at frequencies  $\omega_{\text{QSB}}$

and  $\omega_{\text{CSB}}$  respectively. This adds the term  $\mathbf{H}_{\text{drive}}$  to the system Hamiltonian:

$$\mathbf{H}_{\text{drive}}/\hbar = \xi_{\text{QSB}} e^{i\omega_{\text{QSB}}t} \mathbf{b} + \xi_{\text{QSB}}^* e^{-i\omega_{\text{QSB}}t} \mathbf{b}^\dagger + \xi_{\text{CSB}} e^{i\omega_{\text{CSB}}t} \mathbf{a} + \xi_{\text{CSB}}^* e^{-i\omega_{\text{CSB}}t} \mathbf{a}^\dagger \quad (5.2)$$

Here, we have assumed that the QSB drive couples to the qubit mode  $\mathbf{b}$  and that the CSB drive couples to the cavity mode  $\mathbf{a}$  since the QSB and CSB drives are detuned by  $\Delta \sim 100$  MHz from the qubit and cavity modes respectively. Moving to a displaced frame under these drives [81]:

$$\mathbf{a} \rightarrow \tilde{\mathbf{a}} - \frac{\xi_{\text{CSB}}^*}{\Delta_a} e^{-i\omega_{\text{CSB}}t} \quad (5.3)$$

$$\mathbf{b} \rightarrow \tilde{\mathbf{b}} - \frac{\xi_{\text{QSB}}^*}{\Delta_b} e^{-i\omega_{\text{QSB}}t} \quad (5.4)$$

We now go to the interaction frame with respect to  $\mathbf{H}_0 = \omega_c \tilde{\mathbf{a}}^\dagger \tilde{\mathbf{a}} + \omega_q \tilde{\mathbf{b}}^\dagger \tilde{\mathbf{b}}$ . In this frame, we can identify terms that are resonant based on our choice of the frequencies of the two drives. Note that, here for clarity and brevity, we are omitting all the terms corresponding to frequency shifts of the modes as a result of the drives; these Stark shifts are important because they need to be accounted for when tuning up these transitions as we discuss later.

For  $\omega_{\text{CSB}} - \omega_{\text{QSB}} = \omega_c - \omega_q$ :

$$\mathbf{H}_{\text{int}} = \chi \frac{\xi_{\text{CSB}}}{\Delta_a} \frac{\xi_{\text{QSB}}}{\Delta_b} (\mathbf{a}\mathbf{b}^\dagger + \mathbf{b}\mathbf{a}^\dagger) \quad (5.5)$$

we obtain a conversion-like, also known as a red sideband, process that swaps excitations between the qubit and cavity modes.

On the other hand, for  $\omega_c - \omega_{\text{CSB}} = \omega_q - \omega_{\text{QSB}}$

$$\mathbf{H}_{\text{int}} = \chi \frac{\xi_{\text{CSB}}}{\Delta_a} \frac{\xi_{\text{QSB}}}{\Delta_b} (\mathbf{a}\mathbf{b} + \mathbf{a}^\dagger \mathbf{b}^\dagger) \quad (5.6)$$

we obtain a gain-like, or a blue sideband, process that generates or destroys excitations, in pairs, one in the qubit and one in the cavity mode.

Thus, in general, the application of two detuned pumps results in a two-photon interaction

rate between the qubit and cavity modes were the couplings strength is

$$g_{2\text{ph}} = \chi \frac{\xi_{\text{CSB}}}{\Delta_a} \frac{\xi_{\text{QSB}}}{\Delta_b} \quad (5.7)$$

with the type of two-photon process, red or blue sideband, depending on the frequency relation between the pumps and qubit and cavity modes.

From this, the most straightforward way to generate a photon would seem to be to use pumps that drive a blue sideband transition between  $|g0\rangle \leftrightarrow |e1\rangle$ . However, this transition does not actually implement a CNOT between the qubit and the generated photon; although it can be used to map  $|g0\rangle \rightarrow \frac{1}{\sqrt{2}}(|g0\rangle + |e1\rangle)$ , it does not in general map  $\alpha|g\rangle + \beta|e\rangle \rightarrow \alpha|g0\rangle + \beta|e1\rangle$  as desired to generate qubit-photon entanglement. This can be illustrated concretely by considering what happens when this transition is applied to a Bell state of the Alice and Bob qubits like we have at the beginning at the second round of the protocol; this transition maps the initial state  $|O^+\rangle|00\rangle$  to  $|O^+\rangle|00\rangle + |ee\rangle|o^+\rangle$  not  $|O^+\rangle|o^+\rangle + |O^-\rangle|o^-\rangle$  as a CNOT should.

Instead, to generate flying photons entangled with the qubit, we exploit the second excited state of the qubit,  $|f\rangle$ , and the  $|f0\rangle \leftrightarrow |e1\rangle$  red sideband transition. Summarized in Fig. 5.3, the operation, which is identical for the Alice and Bob systems, starts with the qubit in  $\alpha|g\rangle + \beta|e\rangle$  and the cavity in the vacuum state  $|0\rangle$ . First a  $R_{ef}^y(\pi)$  pulse is applied, taking the qubit to  $\alpha|g\rangle + \beta|f\rangle$ . Then, two pump tones, one called the the QSB pump, detuned by  $\Delta$  above  $\omega_{ef}$  and the other called the CSB pump, detuned by  $\Delta$  above  $\omega_{A/B}^e$ , are applied to drive the  $|f0\rangle \leftrightarrow |e1\rangle$  transition. The choice of positive detuning for both pumps (the same process could be driven by using a negative detuning where both pumps are detuned by  $\Delta$  below the qubit and cavity modes) resulted from wanting to maximize the detuning between the pumps and higher order transitions of the qubit cavity system which all like at lower frequencies. The amplitudes and length of the applied pump tones are tuned (described further below) to implement a  $\pi$ -pulse, thus taking the system to  $\alpha|g0\rangle + \beta|e1\rangle$ , generating an intra-cavity photon. Finally, the operation is completed with the photon state leaking out of the cavity to become a flying photon entangled with the qubit. This operation is only a CNOT-like operation (not a true CNOT) since it

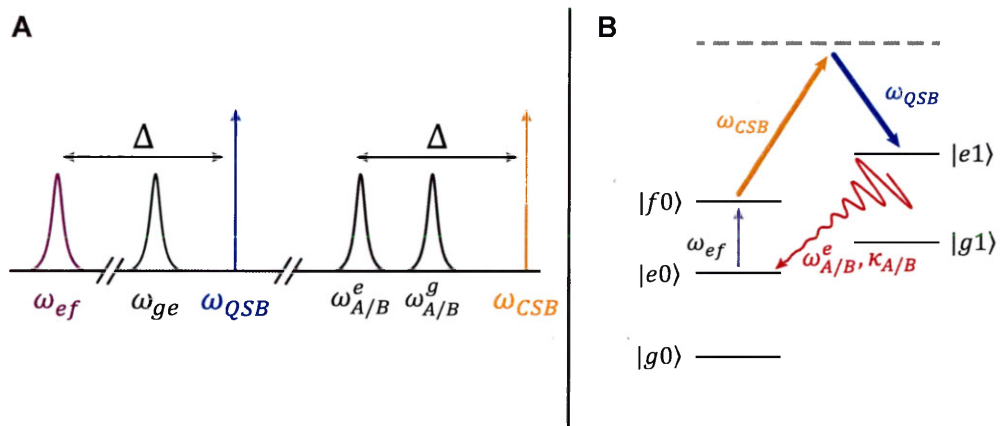


Figure 5.3 | **Single Photon Generation with Sideband Pumps.** A) Frequency spectra of the Alice/Bob qubit-cavity systems. The colors denote transitions which are driven to perform the CNOT-like operation that generates entanglement between the stationary transmon qubit and the flying single microwave photon. B) Energy level diagram for the Alice/Bob qubit-cavity systems. Beginning with the qubit in an arbitrary superposition state  $\alpha|g\rangle + \beta|e\rangle$  and the cavity in the vacuum state  $|0\rangle$ , the pulse  $R_y^{ef}(\pi)$  at  $\omega_{ef}$  transfers the population from  $|e\rangle$  to  $|f\rangle$ . Subsequently, a pair of sideband pulses are applied at  $\omega_{QSB}$ , detuned by  $\Delta$  from  $\omega_{ef}$ , and  $\omega_{CSB}$ , detuned by  $\Delta$  from  $\omega_{A/B}^e$ . They transfer population from  $|f0\rangle$  to  $|e1\rangle$ , generating an intra-cavity photon and resulting in the joint qubit-cavity state  $\alpha|g0\rangle + \beta|e1\rangle$ . The intra-cavity photon is converted into a flying photon by over-coupling the cavity to the environment; the photon leaks out of the cavity at a rate  $\kappa_{A/B}$  with an exponentially decaying temporal waveform.

takes  $|e1\rangle$  to  $|f1\rangle$  (not  $|e0\rangle$  as CNOT should). Thus the operation is not a unitary in the manifold  $\{|g0\rangle, |g1\rangle, |e0\rangle, |e1\rangle\}$ ; however, this has no effects on the protocol since the cavity always starts in  $|0\rangle$  whenever we perform this operation in the remote entanglement generation protocol.

At the crux of this CNOT-like operation, then, is performing a  $\pi$ -pulse on the  $|f0\rangle \leftrightarrow |e1\rangle$  transition which requires experimentally determining two things: (1) the frequencies  $\omega_{\text{QSB}}$  and  $\omega_{\text{CSB}}$  to satisfy  $\omega_{\text{CSB}} - \omega_{\text{QSB}} = \omega_{A/B}^e - \omega_{ef}$  accounting for the Stark shifts that these drives cause on the qubit and cavity frequency; (2) the amplitudes  $\xi_{\text{QSB}}$  and  $\xi_{\text{CSB}}$  and the pulse length  $T_{\text{SB}}$  to perform a  $\pi$ -pulse. The procedure for tuning up this  $R_{f0-e1}(\pi)$  pulse is outlined in Fig. 5.4, with the data shown here for the Alice system (we omit data for Bob since it looks very similar). Since the frequency matching condition changes as a function of the applied pump powers, the tuneup procedure begins by finding  $\omega_{\text{CSB}}$  that drives  $|f0\rangle \leftrightarrow |e1\rangle$  for a fixed amplitude  $\xi_{\text{QSB}}$  and frequency  $\omega_{\text{QSB}}$ . The amplitude  $\xi_{\text{QSB}}$  is chosen to be the maximum that can be generated by the setup described in Fig. 5.1; consequently, by changing only  $\xi_{\text{CSB}}$ ,  $g_{2\text{ph}}$  can be changed, thus reducing the number of control knobs by one. In this experiment, the pump tones were detuned by  $\Delta_A \sim 700$  MHz and  $\Delta_B \sim 500$  MHz to strike a balance between providing adequate power to drive transitions sufficiently quickly ( $T_{\text{SB}} \sim 250$  ns) and avoiding undesirable dephasing and heating effects or higher-order transitions observed when applying the pumps too close in frequency to the qubit and cavity modes.

To find  $\omega_{\text{CSB}}$  that satisfies the required frequency matching condition, the qubit  $ef$ -polarization is measured as a function of  $\omega_{\text{CSB}}$  (bottom axis of Fig. 5.4A) and  $\xi_{\text{CSB}}$  (left axis of Fig. 5.4A), after initializing it in  $|f\rangle$  and turning on both sideband pumps for  $T_{\text{SB}} = 3 \mu\text{s}$ , which is much longer than the cavity decay time of  $1/(2\pi\kappa_{A/B}) = 160$  ns. When  $\omega_{\text{CSB}} - \omega_{\text{QSB}} = \omega_{A/B}^e - \omega_{ef}$  is satisfied, the sidebands drive  $|f0\rangle \leftrightarrow |e1\rangle$  repeatedly, while the generated photon also leaks out of the cavity, eventually leaving the qubit in  $|e\rangle$  (blue on graph), i.e saturating the transition; otherwise, the qubit remains in  $|f\rangle$  (red on graph). Thus, by identifying the frequency at which the qubit is left in  $|e\rangle$  for each CSB amplitude  $\xi_{\text{CSB}}$ , we coarsely determine  $\omega_{\text{CSB}}$ . The width of the transition seen in this saturation spectroscopy experiment is a measure of  $g_{2\text{ph}}$ .

Next, we proceed to time-domain measurements to determine the pulse length required to

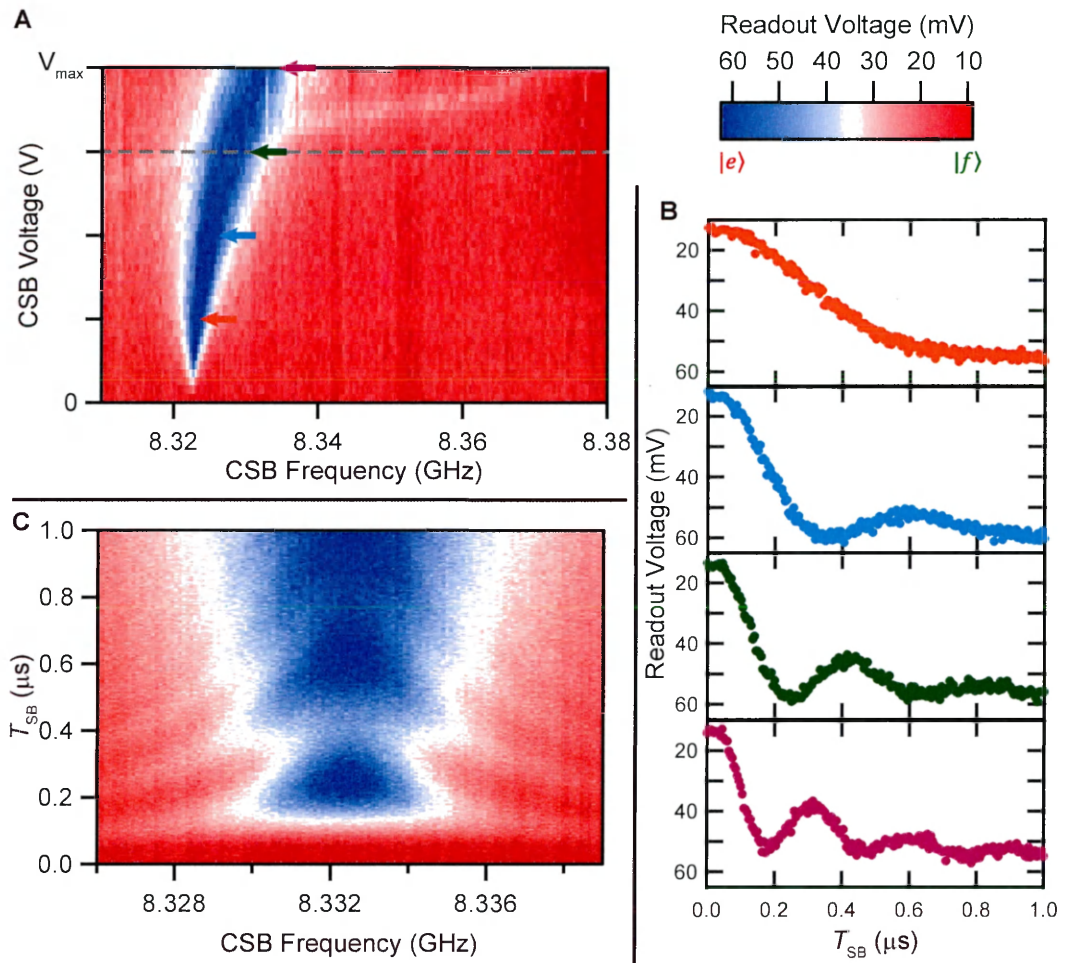


Figure 5.4 | **Spectroscopy and Damped Rabi Oscillations for Two-Photon Sideband Transitions on Alice.** A) Spectroscopy of the  $|f0\rangle \rightarrow |e1\rangle$  transition. Coherent oscillations between the states  $|f0\rangle$  and  $|e1\rangle$  are driven when the frequency condition  $\omega_{\text{CSB}} - \omega_{\text{QSB}} = \omega_A^e - \omega_{ef}$  is satisfied. To experimentally determine  $\omega_{\text{CSB}}$  for a chosen  $\omega_{\text{QSB}}$  held at fixed amplitude, the Alice qubit  $ef$  polarization was measured as a function of the amplitude and frequency of the CSB pump (left and bottom axes respectively), after starting with Alice in  $|f\rangle$  and applying both sideband pumps for  $3 \mu\text{s}$ . When the frequency condition is satisfied, the qubit is found in  $|e\rangle$  at the end of the experiment. B) Time domain measurements of the  $|f0\rangle \rightarrow |e1\rangle$  transition rates for different amplitudes of the sideband pump at  $\omega_{\text{CSB}}$ . The Alice qubit  $ef$  polarization is measured as a function of the sideband pulse length  $T_{\text{SB}}$  for different amplitudes of the CSB drive (indicated by the colored arrows in A). For each amplitude, the frequency of the CSB drive was chosen to satisfy the frequency condition mentioned above (i.e CSB pump on resonance). As the amplitude of the CSB drive was increased (orange to purple trace), the transition rate  $g_{2\text{ph}}$  from  $|f0\rangle \rightarrow |e1\rangle$  also increases. C) Time domain measurement of the  $|f0\rangle \rightarrow |e1\rangle$  transition rate versus  $\omega_{\text{CSB}}$ . The Alice qubit  $ef$  polarization is measured as a function of the sideband pulse length  $T_{\text{SB}}$  (left axis) and  $\omega_{\text{CSB}}$  for the amplitude of the CSB drive given by the dashed line in A. The contrast of the oscillations between  $|f0\rangle \rightarrow |e1\rangle$  is maximized when the CSB drive is on resonance.

implement  $R_{f0 \rightarrow e1}(\pi)$  at a chosen  $\xi_{\text{CSB}}$ , as shown in Fig. 5.4B. For a chosen value of  $\xi_{\text{CSB}}$ , the qubit  $ef$ -polarization is measured after initializing the qubit in  $|f\rangle$  and applying both sideband pumps for a varying time  $T_{\text{SB}}$  (bottom axis of graphs), with the CSB tone applied at the value of  $\omega_{\text{CSB}}$  determined from the saturation spectroscopy experiment of Fig. 5.4A. The pump tones applied to the system were constant amplitude pulses with a ring-up and ring-down defined by a tanh function; the time constant of the ring-up and ring-down (in this experiment, 8 ns) was chosen to be slow compared to the inverse of the detuning of the drives to constrain the spectral content of the pulse from directly driving a qubit or cavity mode (i.e.  $\sigma_{\text{SB}} \gg \frac{1}{\Delta}$ ) [106]. This resulted in the damped sideband Rabi oscillations shown in the traces in Fig. 5.4B, the oscillation frequency increasing with  $\xi_{\text{CSB}}$  as expected (in the figure, the color of the trace indicates the value of  $\xi_{\text{CSB}}$  at which it was taken, shown by the correspondingly colored arrows in Fig. 5.4A). For the full remote entanglement experiment,  $\xi_{\text{CSB}}$  was chosen so that a  $\pi$ -pulse on  $|f0\rangle \leftrightarrow |e1\rangle$  was performed in  $T_{\text{SB}} = 254$  ns (green trace).

With this choice of  $\xi_{\text{CSB}}$  and  $T_{\text{SB}}$ , a more sensitive tuneup of  $\omega_{\text{CSB}}$  is performed in the final step, as shown in Fig. 5.4C. The time-domain measurement of Fig. 5.4B (specifically, the green trace) is performed as a function of  $\omega_{\text{CSB}}$  (bottom axis). When the CSB tone is applied away from resonance, the oscillations between  $|f0\rangle$  and  $|e1\rangle$  have a reduced contrast but increased apparent frequency. As the CSB tone is brought on resonance to satisfy  $\omega_{\text{CSB}} - \omega_{\text{QSB}} = \omega_{A/B}^e - \omega_{ef}$ , the oscillation frequency between  $|f0\rangle$  and  $|e1\rangle$  decreases but the contrast increases. Thus,  $\omega_{\text{CSB}}$  is chosen to maximize the contrast.

Finally, this tuneup procedure also provides a direct measure of the coupling rate  $g_{2\text{ph}}$  generated in the experiment from fitting to the damped sideband Rabi oscillations of Fig. 5.4B. Under this coupling between the qubit and cavity, the system of two modes that can exchange energy while one mode, the cavity, also has a decay rate to the environment, can be modeled by the coupled differential equations [106]:

$$\delta_t \mathbf{a} = -i[\mathbf{a}, \mathbf{H}_{\text{int}}] - \frac{\kappa_{\text{out}}}{2} \mathbf{a} = -ig_{2\text{ph}} \mathbf{b} - \frac{\kappa_{\text{out}}}{2} \mathbf{a} \quad (5.8)$$

$$\delta_t \mathbf{b} = -i [\mathbf{b}, \mathbf{H}_{\text{int}}] = -ig_{2\text{ph}} \mathbf{a} \quad (5.9)$$

Under the initial conditions that the cavity mode starts in the vacuum state  $\mathbf{a}(t=0) = 0$  and the qubit mode starts in some initial state  $\mathbf{b}(t=0) = \mathbf{b}(0)$ , the differential equations can be solved exactly for the qubit and cavity fields as function of time:

$$\mathbf{a}(t) = -i \frac{4g_{2\text{ph}} \mathbf{b}(0)}{\beta} e^{-\kappa_{\text{out}} t/4} \sinh \frac{\beta t}{4} \quad (5.10)$$

$$\mathbf{b}(t) = \frac{\mathbf{b}(0)}{\beta} e^{-\kappa_{\text{out}} t/4} \left( \beta \cosh \frac{\beta t}{4} + \kappa_{\text{out}} \sinh \frac{\beta t}{4} \right) \quad (5.11)$$

where  $\beta = \sqrt{\kappa_{\text{out}}^2 - (4g_{2\text{ph}})^2}$ . Specifically, the time traces of Fig. 5.4B are a measure the average population of the qubit mode  $\langle \mathbf{b}^\dagger \mathbf{b} \rangle$ . Thus, from fitting the measured traces to the expression for  $\langle \mathbf{b}^\dagger \mathbf{b} \rangle$ , we obtain  $g_{2\text{ph}}$ , the only free parameter in these equations since  $\kappa_{\text{out}}$ , the bandwidth of the cavity, can be independently measured. On the other hand, a theoretical value for  $g_{2\text{ph}}$  can be calculated from Eq. 5.7 by calibrating  $\xi_{\text{CSB}}/\Delta_a = \sqrt{\bar{n}_{\text{CSB}}}$  and  $\xi_{\text{QSB}}/\Delta_b = \sqrt{\bar{n}_{\text{QSB}}}$  from the Stark shifts that each pump individually induces on the qubit frequency [81, 106].

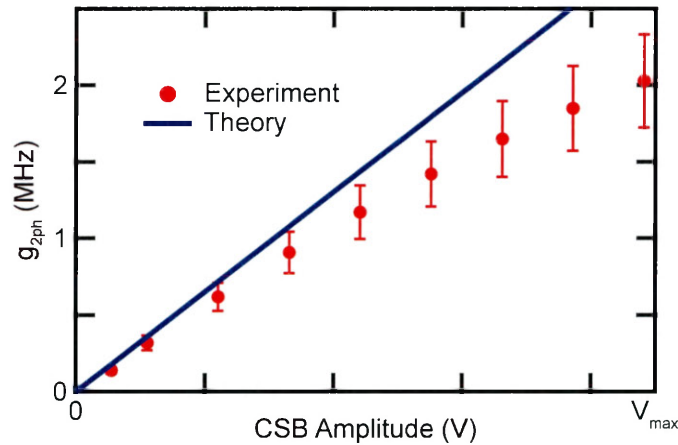


Figure 5.5 | **Calibrating the Two-Photon Coupling Rate.** Comparison of experimentally measured (red points) and theoretically calculated  $g_{2\text{ph}}$  (blue line). The experimentally measured values of  $g_{2\text{ph}}$  are from fits to damped sideband oscillations when the  $|g0\rangle \leftrightarrow |e1\rangle$  is driven as a function of the CSB amplitude  $\xi_{\text{QSB}}$ . Errors bars for the experimental data were obtained from the uncertainty in  $\chi$  of  $\sim 15\%$  for the system. The theoretically expected  $g_{2\text{ph}}$  was calculated using the pump amplitudes, independently calibrated using the Stark shifts they induced on the qubit.

A comparison of the experimentally measured and theoretically calculated  $g_{2\text{ph}}$  using this method are shown in Fig. 5.5 from the  $|g0\rangle \leftrightarrow |e1\rangle$  transition (note that this data was taken what is called the Bob qubit in Fig. 5.1 in a different cooldown of the experiment when its configuration was changed for the experiment outlined in Fig. 5.14). The experimentally measured values of  $g_{2\text{ph}}$  have error bars of 15% dominated primarily by the uncertainty in the value of  $\chi = 7.5 \pm 1$  MHz. Moreover, with increasing CSB amplitude, the error in the fit also increased as the measured sideband oscillation curves deviated further from the solutions of Eq. 5.11. Even with this error, we find that the experimentally measured rate is lower than the theoretically calculated one from the Stark shift calibration of the two pump amplitudes. The source of this discrepancy is not entirely understood and is suspected to be related to the pumps driving higher order transitions and population leakage into other undesired states. In fact, as we discuss later in Ch. 5.9, this same behavior is suspected to also limit the fidelity of the CNOT-like operation.

Thus, sideband transitions are a powerful part of the cQED toolbox enabling the generation of single excitations in the cavity using the non-linearity of the transmon. However, the fidelity of these transitions ( $\sim 90\%$ ), and hence the gates that depends upon them, is not as high as that of single qubit rotations ( $\sim 90\%$ ) and so require further investigation into their imperfections and how to rectify them to prevent them from becoming the limiting factor in the cQED tool set.

## 5.4 Detecting Single Photons

Having established how we generate flying single photons, we now proceed to the second key technical requirement of detecting these single photons. Specifically, we need to be able to perform high-fidelity, single-shot readout of a photon, in a microwave analog of the photomultipliers used in similar remote entanglement experiments with optical photons. As discussed in Ch. 1.7, our single-photon detector consists of another qubit-cavity system. Using a selective  $\pi$ -pulse to excite the qubit only if a single photon is in the cavity, we map the presence or absence of the flying photon on the  $|e\rangle$  or  $|g\rangle$  state respectively of the detector qubit. Subsequently, by

performing the standard dispersive readout of the detector qubit described in Ch. 5.2, the state of the qubit is measured, informing the observer of a photon detection event, called a 'click', or not, called a 'no-click'.

### 5.4.1 Simulations

A cascaded quantum system simulation[17, 40, 45] was performed to understand the operation of the detector and how two characteristics, dark counts and detector efficiency, depend on system parameters. We simulate a simplified model of the experiment consisting of a single emitter cavity, Alice, and the detector qubit-cavity module. The master equation for this system was solved for various initial states of Alice modeling the inputs seen by the detector in the experiment. The simulations were performed with the experimentally measured parameters (see Table 1). However, unlike the experiment, the two cavities had identical cavity frequencies.

As shown in Fig. 5.6, the simulation began by initializing the Alice cavity in the  $|0\rangle$  (red trace),  $|1\rangle$  (blue trace) or  $|2\rangle$  (green trace) Fock state (top panel). The photon leaked out and excited the detector cavity (second panel). Simultaneously, a selective  $\pi$ -pulse, timed to start at the beginning of the simulation, with  $\sigma = 120$  ns was applied at  $\omega_{ge}^1$  to selectively excite the detector qubit conditioned on the presence of an intra-cavity photon (third panel). Finally,  $P_{\text{click}}$  was extracted by calculating the probability that the detector qubit state was  $|e\rangle$  at the end of the simulation (bottom panel). The first detector characteristic, its dark count fraction  $P_d$ , is the probability that the detector clicks when the input is  $|0\rangle$ . When no photons were sent to the detector (red trace),  $P_{\text{click}} < 0.01$  at the end of the simulation. The transient increase in the probability of the detector qubit being in  $|e\rangle$  observed during the course of the qubit pulse is a result of the finite selectivity of the  $\pi$ -pulse which was confirmed by varying  $\sigma$  or  $\chi$ . Thus, the dark count probability,  $P_d$ , can be decreased by increasing  $\sigma$  at the cost of slowing down the detection process (and hence the detection probability).

The second detector characteristic is its efficiency,  $\eta$ , the probability that the detector clicks when the input is  $|1\rangle$ . When one photon was sent to the detector, the qubit was excited by the selective  $\pi$ -pulse resulting in  $P_{\text{click}} = 0.4$ . On the other hand, when two photons were sent

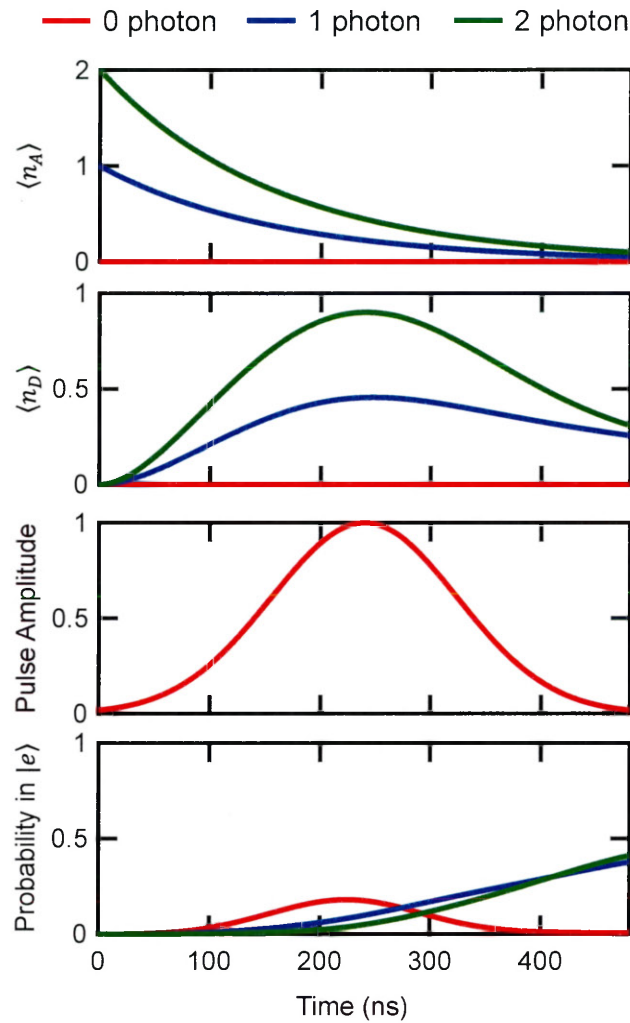


Figure 5.6 | **Single Photon Detector - Simulations.** Results from solving the master equation for a cascaded quantum system of the Alice cavity emitting Fock states into the detector qubit-cavity system. The top two panels show the expectation value of the photon number operators of the Alice,  $\langle n_A \rangle$ , and detector,  $\langle n_D \rangle$ , cavities. The Alice cavity (top panel) was initialized in  $|0\rangle$  (red trace),  $|1\rangle$  (blue trace) or  $|2\rangle$  (green trace). The third panel shows the amplitude of a selective  $\pi$ -pulse with  $\sigma = 120$  ns applied on the detector qubit to excite it conditioned on the presence of a single intra-cavity photon. Finally, the probability to find the detector qubit in  $|e\rangle$  was calculated to find  $P_{\text{click}}$  at the end of process (bottom panel). Simulations confirm that the detector has dark counts ( $P_{\text{click}}$  given  $|0\rangle$ )  $P_d < 0.01$  and an efficiency ( $P_{\text{click}}$  given  $|1\rangle$ )  $\eta \sim 0.4$ . Since  $P_{\text{click}}$  is the same for  $|1\rangle$  (blue trace) and  $|2\rangle$  (green trace), the detector is not number-resolving.

to the detector, on average a single photon entered the detector, also resulting in  $P_{\text{click}} = 0.4$ . Since  $P_{\text{click}}$  is similar for  $|1\rangle$  and  $|2\rangle$ , the detector is not photon-number resolving. Furthermore,

the simulations verified that the detector efficiency is robust to small imperfections and does not require precise tuning. When the simulation parameters, such as the mismatch between the Alice and detector cavity bandwidths and the selective pulse length and timing, were varied by 20%,  $\eta$  changed by  $< 10\%$ .

### 5.4.2 Detector Characterization

The performance of the detector was also characterized experimentally to verify that it was detecting single photons. In these experiments (see Fig. 5.7A), the Alice and Bob modules were initialized in one of the two states,  $|0\rangle$  or  $|1\rangle$ . Single photons were generated by preparing the qubit in  $|e\rangle$  and then performing the CNOT-like operation to create the state  $|e1\rangle$ . Note that the generation process takes 254 ns unlike the assumption of instantaneous generation in the simulations. Then, detection was performed by applying the selective  $\pi$ -pulse ( $\sigma = 120$  ns) on the detector followed by measuring the state of the detector qubit to find  $P_{\text{click}}$ . The frequency of the detection  $\pi$ -pulse was varied to characterize the detector response as a function of frequency. As shown in Fig. 5.7A, when the state  $|0\rangle$  (blue circles) was sent, the  $P_{\text{click}}$  was maximized at zero detuning where the pulse is selective on zero intra-cavity photons in the detector. Instead, when the input was  $|1\rangle$  (red circles), an increased response at  $\omega_{ge}^0 - \chi$  was observed. This is a direct result of the detector being excited when photon enters the detector. Due to losses and the detector inefficiency, the response at zero detuning remains but with a lower  $P_{\text{click}}$  than for  $|0\rangle$ . Moreover, the similar detector response to inputs from Alice and Bob demonstrates that the detector can detect photons from both systems and that the losses on the two arms are similar on the two paths.

In a second characterization experiment, the delay between the end of the photon generation and beginning of the photon detection steps was optimized. The probability of detecting the photon,  $P_{\text{click}}$ , is maximized when the peak of the detection pulse coincides with the time at which the photon population inside the detector cavity is maximum. To find this point experimentally, a photon was generated by Alice or Bob and sent to the detector with a variable delay between the end of the photon generation sideband pulse and the beginning of the selective detection

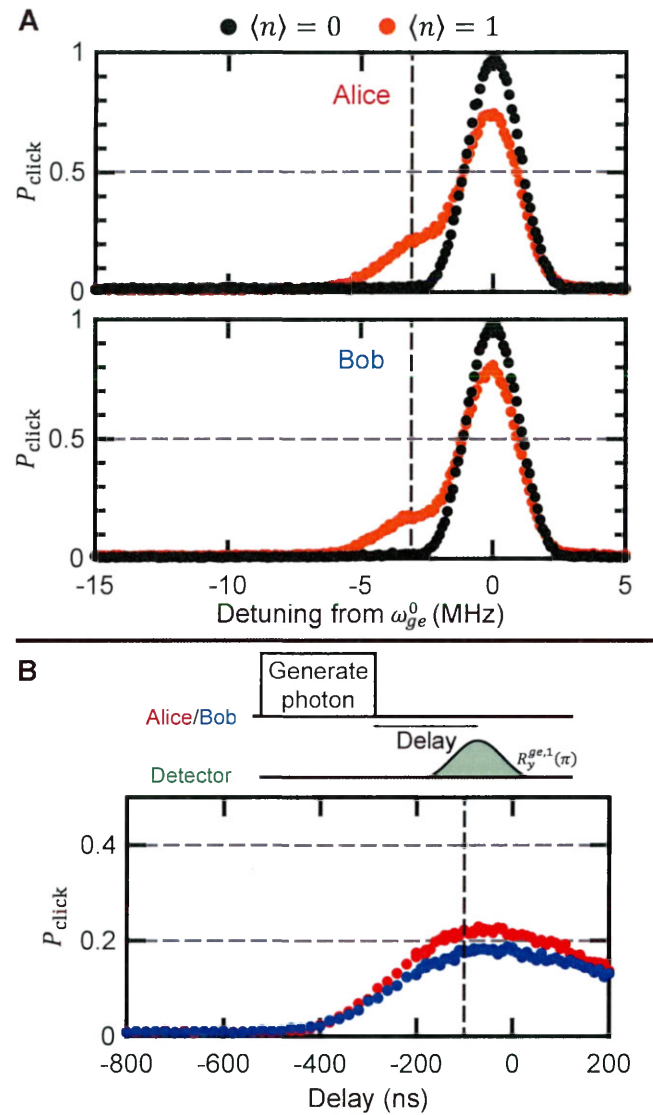


Figure 5.7 | **Single Photon Detector - Characterization.** A) Detector click probability,  $P_{\text{click}}$ , as function of the detuning of the detection pulse from  $\omega_{ge}^0$  for different input states from the Alice (top panel) and Bob (bottom panel) modules. The black dashed line indicated the frequency of the selective  $\pi$ -pulse for optimum discrimination of the state  $|1\rangle$  from the state  $|0\rangle$ . B) Detector click probability,  $P_{\text{click}}$ , as a function of the delay between the end of the photon generation pulse and the start of the selective detection  $\pi$ -pulse. In the remote entanglement experiment of Fig. 1.12, the pulses overlapped by 100 ns (black dashed line).

$\pi$ -pulse. As shown in Fig. 5.7B,  $P_{\text{click}}$  was maximized around a delay of  $-100$  ns (black dashed line), i.e when the sideband and detection pulses had 100 ns of overlap. This operation point was used in the remote entanglement experiments of Figs. 3 and 4.

We attribute the difference between the simulated detector efficiency,  $\eta = 0.4$ , and the measured  $P_{\text{click}}$  when a photon was generated in experiments to the losses in our system and dark counts. Due to the the hybrid and the insertion losses of the microwave components between the Alice/Bob modules and the detector, photons only reach the detector about 40% of the time, corresponding to an efficiency due to the loss of  $\eta_{\text{loss}} \sim 0.4$ . In addition, the detector can also click when no photon is incident on it, which occurred with a probability  $P_d = 0.01$ . Together, they result in the observed  $P_{\text{click}} \sim 0.2$  when a photon was generated.

### 5.4.3 Detector Optimization

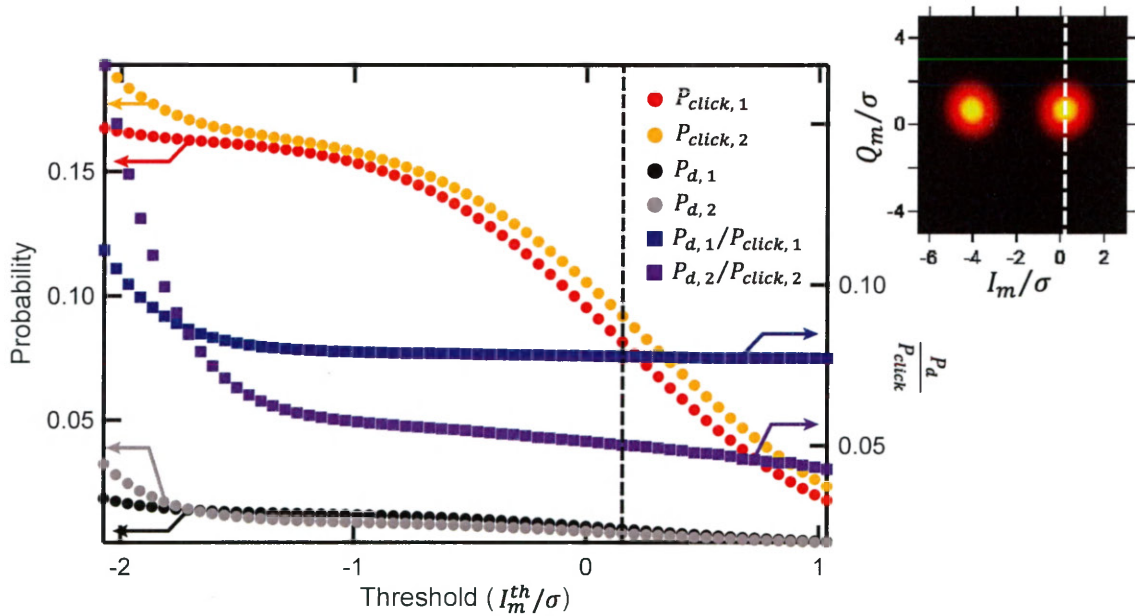


Figure 5.8 | **Single Photon Detector - Optimization.** The probability of dark counts,  $P_d$ , and detector click probability,  $P_{\text{click}}$ , (left axis) and their ratio (right axis) for each round of detection as a function of the readout threshold  $I_m^{\text{th}}/\sigma$ . The detector readout has two probability distributions (inset), one for click and one for no click. By using a more stringent threshold for outcomes to be considered a click (white dashed line/black dashed line), the ratio  $P_d/P_{\text{click}}$  can be reduced, therefore improving the fidelity of the generated Bell state.

This remote entanglement protocol is robust to loss since the generation of an entangled state is uniquely heralded by the dual detection of single photons in the detector. Hence, photon loss between Alice/Bob and the detector only affect the probability of that outcome. However,

dark counts in the detector are detrimental to this experiment (for a quantitative discussion of the effect, see Ch. 5.8) because they mix the desired Bell state with unwanted states, for example  $|gg\rangle$ . This impacts the measured fidelity. Since the desired (undesired) outcomes occur with probabilities proportional to  $P_{\text{click}}$  ( $P_d$ ), the ratio of  $P_d/P_{\text{click}}$  is the figure of merit that must be minimized for reducing the infidelity due to dark counts. Thus, it is important to minimize the probability of dark counts in the detector,  $P_d$ . In our detector, dark counts occur as a result of the finite selectivity of the detection  $\pi$ -pulse and imperfect readout of the qubit state. While the detection pulse could be made more selective by increasing its  $\sigma$ , this would increase the overall detection time. Unfortunately, this has two undesired consequences. First, the overall protocol time increases, and thus, so does the infidelity due to decoherence. Second, simulations show that the detector efficiency is maximized for  $\sigma \sim \kappa$  and thus increasing  $\sigma$  further actually increases  $P_d/P_{\text{click}}$ . Therefore, we operated with  $\sigma = 120$  ns.

Instead, we decrease the ratio  $P_d/P_{\text{click}}$  in post-selection by reducing the probability that the detector clicks when the state  $|0\rangle$  is incident on it. As discussed before, readout of the detector qubit results in two distributions, one for click and one for no click. As shown in Fig. 5.8, by moving the threshold closer to the distribution associated with a click in the detector, it was possible to decrease the dark count fraction. The data for  $P_{\text{click}}$  (red and yellow circles) and  $P_d$  (black and gray circles) were obtained from the two rounds of the remote entanglement experiment and the control experiments (see Ch. 5.7) respectively. From these two numbers, the ratio  $P_d/P_{\text{click}}$  (blue and purple squares) was calculated for each round. A threshold in the middle of the two distributions corresponds to  $I_m^{\text{th}}/\sigma = -1.8$  where  $P_d/P_{\text{click}} = 0.1$  for the second round. By moving the threshold to  $I_m^{\text{th}}/\sigma = 0.15$  (black dashed line), the ratio decreases to  $P_d/P_{\text{click}} = 0.05$ .

## 5.5 Qubit-Photon Entanglement

We now put the tools of single photon creation and generation together, first showing that the detector can indeed detect the photons generated by the Alice and Bob systems. With this, we

can also tune the photons in frequency and temporal shape to minimize their distinguishability.

### 5.5.1 Generating and Detecting Single Photons

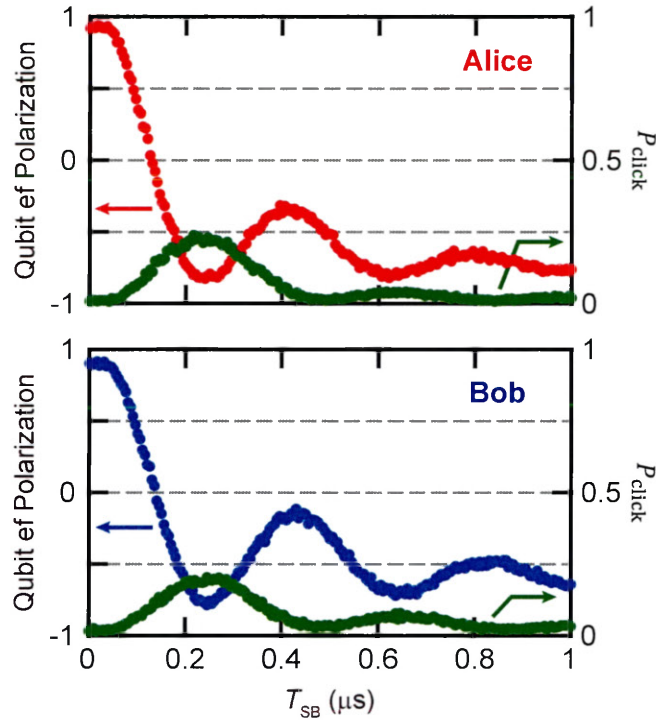


Figure 5.9 | **Single Photon Generation and Detection.** Alice (top) and Bob (bottom) qubit  $ef$  polarization (left axis) and detector click probability,  $P_{\text{click}}$ , (right axis) as a function of sideband pulse length,  $T_{\text{SB}}$ , when the qubit is prepared in  $|f\rangle$ . Two sideband drives ( $\omega_{QSB}$ ,  $\omega_{CSB}$ ) were applied, satisfying the frequency condition  $\omega_{CSB} - \omega_{QSB} = \omega_{A/B}^e - \omega_{ef}$ . The drives result in coherent oscillations between  $|f0\rangle$  and  $|e1\rangle$  with the amplitude of the drives chosen that a  $\pi$ -pulse on the transition took the same time for the Alice and Bob qubits,  $T_{\text{SB}} = 254$  ns. The generation of a photon was verified with the detector which showed a peak in  $P_{\text{click}}$  when Alice/Bob were in  $|e\rangle$ .

As discussed in Ch. 1.7, the CNOT-like operation that entangles the stationary qubits with flying microwave photons is realized by a  $\pi$ -pulse on the qubit  $ef$ -transition followed by a  $\pi$ -pulse between  $|f0\rangle \leftrightarrow |e1\rangle$  following the method in Ref. [71, 142]. To drive coherent transitions between  $|f0\rangle \leftrightarrow |e1\rangle$ , two sideband tones at  $\omega_{QSB,A}/2\pi = 5.1987$  and  $\omega_{CSB,A}/2\pi = 8.3325$  ( $\omega_{QSB,B}/2\pi = 4.9631$  and  $\omega_{CSB,B}/2\pi = 8.1302$ ) were applied to Alice (Bob). As shown in Fig. 5.9, these drives result in damped sideband Rabi oscillations of the qubit state between  $|f\rangle$

and  $|e\rangle$  (Alice top, Bob bottom). The probability of detecting a photon with the detector,  $P_{\text{click}}$ , shown on the right axes of the graphs in Fig. 5.9, peaked when the qubit was in  $|e\rangle$  confirming that a photon is generated. Thus, a  $\pi$  pulse can be performed by turning on the drives for half an oscillation, i.e. the time taken to transfer the excitation from the qubit to the cavity. The amplitudes of the CSB and QSB drives on Alice and Bob were chosen so that the  $\pi$ -pulse on  $|f0\rangle \leftrightarrow |e1\rangle$  took the same time,  $T_{\text{SB}} = 254$  ns, for both modules. While the oscillations would ideally be between  $+1$  and  $-1$ , a deviation from this behavior is observed in the data. We attribute this behavior to the QSB tone spuriously exciting the  $ge$  and  $ef$  transitions and hence driving the qubit out of  $|e\rangle$ . While increasing the detuning of the drives would lower the spurious excitation, this was not possible in our experiment because of power limitations. Similarly, the drive amplitudes could have been decreased but this would have increased the photon generation time and degraded the fidelity of two-qubit entangled state because of decoherence. Thus, the drive amplitudes and detunings were chosen to balance the two effects.

### 5.5.2 Demonstrating Qubit-Photon Entanglement

As a preliminary step towards the realization of the full remote entanglement protocol, we demonstrate in Fig. 5.10B and C signatures of entanglement between the Alice qubit and its corresponding traveling photon state by showing that the CNOT-like operation maps  $\alpha|g0\rangle + \beta|e0\rangle$  to  $\alpha|g0\rangle + \beta|e1\rangle$  (for data on the Bob qubit and simulations, see below). We first show that the relative weights of  $|g\rangle$  and  $|e\rangle$  were correctly mapped by initializing the qubit in  $\cos(\theta/2)|g\rangle + \sin(\theta/2)|e\rangle$ , followed by a  $\pi$  pulse on the  $\omega_{A,ef}^0$  and sideband pulses for a varying time  $T_{\text{SB}}$  (see Fig. 5.10A, right). The selective  $\pi$ -pulse on the detector was a 480 ns Gaussian pulse ( $\sigma = 120$  ns) and was timed such that the center of the Gaussian coincides with the end of the sideband pulse. Finally, we measured the probability of detecting a photon in the detector,  $P_{\text{click}}$ , and the Alice polarization,  $\langle Z_A \rangle$ . As shown in Fig. 5.10B (black dashed line), a  $\pi$ -pulse on the  $|f0\rangle \leftrightarrow |e1\rangle$  transition occurs for  $T_{\text{SB}} = 254$  ns when the probability of detecting a photon,  $P_{\text{click}}$  is maximized. On the other hand, for shorter sideband pulse lengths, no photons are generated and  $P_{\text{click}} = 0$ . Moreover, the observed increase in  $P_{\text{click}}$  with  $\theta$  confirms that the relative

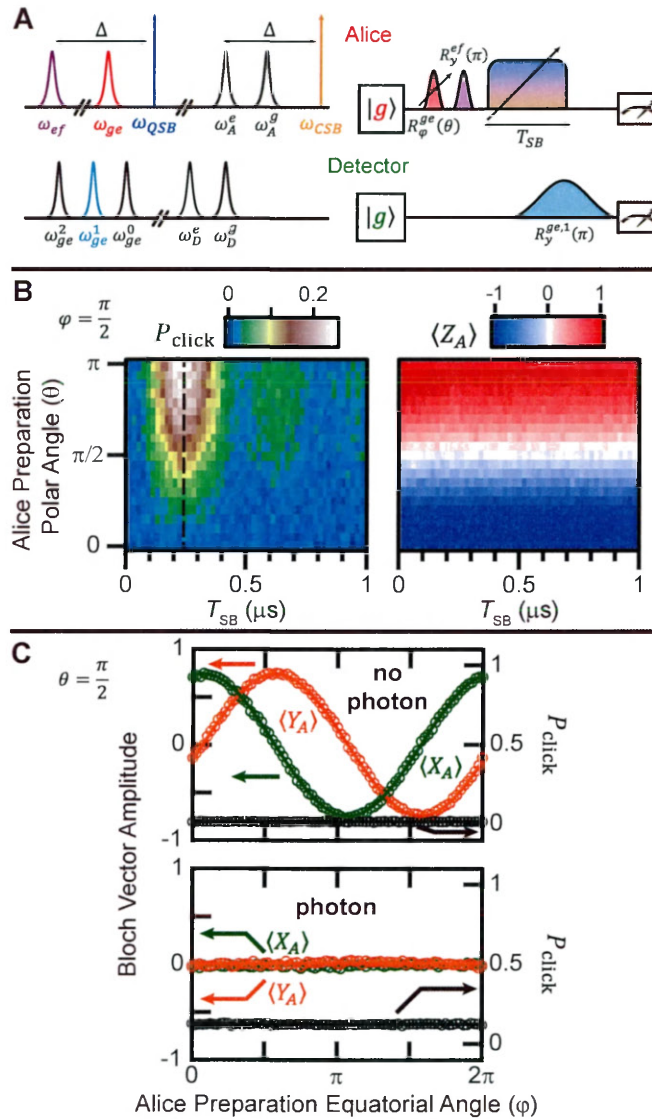


Figure 5.10 | **Signatures of Alice Qubit/Flying Photon Entanglement.** A) Frequency spectra of the Alice and detector qubit-cavity systems (left) and experimental pulse sequence (right). The colors denote transitions which are driven to perform the CNOT-like operation and flying single photon detection. The Alice qubit is prepared in an arbitrary initial state by the pulse  $R_\phi^{ge}(\theta)$  at  $\omega_{ge}$ . The CNOT-like operation consists of a  $R_y(\pi)$  pulse at  $\omega_{ef}$  followed by a pair of sideband pulses. The sideband pulses are applied at  $\omega_{QSB}$ , detuned by  $\Delta$  from  $\omega_{ef}$ , and  $\omega_{CSB}$ , detuned by  $\Delta$  from  $\omega_A^e$ . To detect flying photons, a frequency selective  $\pi$ -pulse is applied to the detector qubit at  $\omega_{ge}^1$  followed by a measurement of the qubit state. B) Color plots of the probability,  $P_{\text{click}}$ , of the detector qubit ending in  $|e\rangle$  (left) and the Alice qubit polarization,  $\langle Z_A \rangle$  (right), as a function of the sideband pulse length  $T_{\text{SB}}$  and  $\theta$  (for  $\phi = \pi/2$ ). The dashed line at  $T_{\text{SB}} = 254$  ns corresponds to a transfer  $|f0\rangle \rightarrow |e1\rangle$ , i.e. a CNOT-like operation. C) Detector click probability,  $P_{\text{click}}$ , and Alice equatorial Bloch vector components,  $\langle X_A \rangle$  and  $\langle Y_A \rangle$ , as a function of  $\phi$  for  $\theta = \pi/2$  when the CNOT-like operation is either performed (bottom) or not (top). Open circles are experimental data and lines are fits.

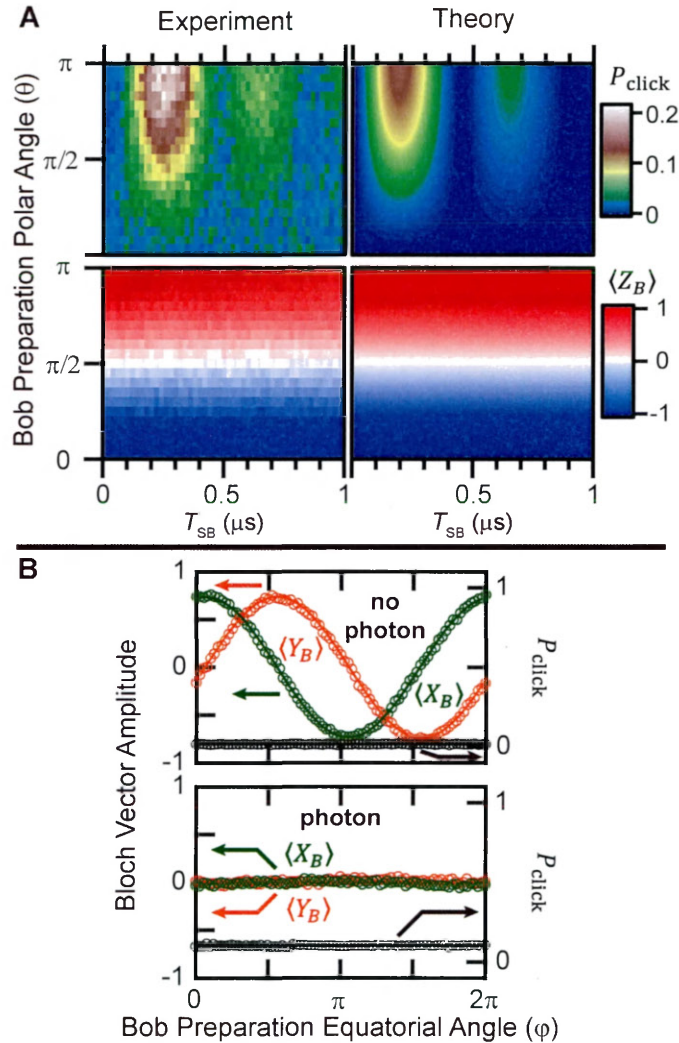


Figure 5.11 | **Signatures of Qubit-Photon Entanglement: Data vs. Theory.** This data is similar to that of Fig. 5.10 but addresses the Bob module of the experiment and its equivalence to the Alice module. A) Color plots of the probability,  $P_{\text{click}}$  (top left), of the detector qubit ending in  $|e\rangle$  and the Bob qubit polarization,  $\langle Z_B \rangle$  (bottom left), as a function of the sideband pulse length  $T_{SB}$  when Bob was prepared in  $\cos(\theta/2)|g\rangle + \sin(\theta/2)|e\rangle$ . A theoretical simulation, plotted on the right, shows good agreement. B) Detector click probability,  $P_{\text{click}}$ , and Bob equatorial Bloch vector components,  $\langle X_B \rangle$  and  $\langle Y_B \rangle$ , as a function of  $\phi$  when Bob was prepared in  $\frac{1}{\sqrt{2}}(|g\rangle + e^{i\phi}|e\rangle)$  and the CNOT-like operation was either performed (bottom) or not (top). Open circles are experimental data and lines are fits.

weight of the superposition state between  $|g\rangle$  and  $|e\rangle$  is mapped onto  $|g0\rangle$  and  $|e1\rangle$  (Fig. 5.10B, left). We also confirm that this process does not destroy the qubit state by observing that the final value of  $\langle Z_A \rangle$  agrees with the initial preparation angle  $\theta$  (Fig. 5.10B, right).

Furthermore, in Fig. 5.10C, we show that this operation also maps the phase of  $\alpha|g\rangle + \beta|e\rangle$  onto  $\alpha|g0\rangle + \beta|e1\rangle$ . Directly measuring the phase of  $|e1\rangle$  relative to  $|g0\rangle$  is not possible in this experiment since the detector only detects the presence or absence of a photon. Instead, the Alice qubit was first prepared on the equator of the Bloch sphere in  $\frac{1}{\sqrt{2}}(|g\rangle + e^{i\phi}|e\rangle)$ , the CNOT-like operation was either performed or not and finally both  $P_{\text{click}}$ , and the qubit equatorial Bloch vector components,  $\langle X_A \rangle$  and  $\langle Y_A \rangle$ , were measured. When no photon is generated,  $P_{\text{click}} = 0$  as expected and  $\langle X_A \rangle$  and  $\langle Y_A \rangle$  oscillate with the preparation phase  $\phi$  (Fig. 5.10C, top). However, when the operation is performed, a photon is generated and thus  $P_{\text{click}}$  is now non-zero. Since, the preparation phase  $\phi$  is now mapped onto the entangled state, the measurement of the photon, either by the detector or some other loss in the system, results in the unconditional dephasing of the qubit,  $\langle X_A \rangle, \langle Y_A \rangle = 0$  (Fig. 5.10B, bottom).

Similar signatures were observed for the Bob module as shown in Fig. 5.11. The observed behavior agrees with the results of a simplified theoretical model (right panels, Fig. 5.11A). In this model, the action of the sideband drives on Alice/Bob was modeled using the theory of damped vacuum Rabi oscillations described in [50]. We note that although our system uses sideband transitions between a different set of states, the coupling can still be modeled with the same formalism. Thus, the three states used here were  $|f0\rangle$ ,  $|e1\rangle$  and  $|e0\rangle$ . The sidebands drive coherent transitions between  $|f0\rangle$  and  $|e1\rangle$  while the cavity linewidth,  $\kappa$ , causes  $|e1\rangle$  to decay to  $|e0\rangle$ . For the detector signal, we made the simplification of using the state of the cavity subjected to two inefficiencies as a proxy. Thus,  $P_{\text{click}}(T_{\text{SB}}) = \eta P_{e1}(T_{\text{SB}})$ , where  $\eta$  accounts for the loss between the Alice/Bob module and the detector as well as the detector efficiency and  $P_{e1}(t)$  is the probability of the system being in  $|e1\rangle$ . We find good qualitative agreement between theory and experiment.

## 5.6 Joint Tomography and Calibration

Next, we address the joint tomography which is used to measure the state of the Alice and Bob qubits at the end of the remote entanglement protocol. To calculate the final state of the Alice and Bob qubit after a joint measurement, the measured in-phase and quadrature signal ( $I(t)$ ,  $Q(t)$ ) was converted into a digital result using two thresholds, one for Alice and one for Bob (see Fig. 5.2B). Since the four measured Gaussian distributions had equal standard deviations, these thresholds were straight lines equidistant from the two distributions. Thus, using the thresholds, the output voltage from each joint tomography measurement was converted into a final outcome of  $|G\rangle$  or  $|E\rangle$  for each qubit. By performing measurements on an ensemble of identically prepared states, these counts were converted into expectation values of the observable being measured. Fully characterizing the state of the two qubits requires measuring the 16 components of the two-qubit density matrix. This was done in the Pauli basis using the single-qubit pre-rotations  $Id$ ,  $R_y(\pi/2)$  and  $R_x(\pi/2)$  to measure the  $Z$ ,  $X$  and  $Y$  components respectively of each qubit Bloch vector and the two-qubit correlators.

However, the tomography was not perfect ( $\mathcal{F}_{\text{joint}} \neq 100\%$ ) and we next discuss how to understand the imperfect tomography and calibrate out its effects[87, 118]. The ideal joint measurement of the two-qubit state can be described using the projectors into the computational basis:

$$\Pi_{GG} = \begin{pmatrix} 1 & 0 & 0 & 0 \\ 0 & 0 & 0 & 0 \\ 0 & 0 & 0 & 0 \\ 0 & 0 & 0 & 0 \end{pmatrix}, \Pi_{GE} = \begin{pmatrix} 0 & 0 & 0 & 0 \\ 0 & 1 & 0 & 0 \\ 0 & 0 & 0 & 0 \\ 0 & 0 & 0 & 0 \end{pmatrix} \quad (5.12)$$

$$\Pi_{EG} = \begin{pmatrix} 0 & 0 & 0 & 0 \\ 0 & 0 & 0 & 0 \\ 0 & 0 & 1 & 0 \\ 0 & 0 & 0 & 0 \end{pmatrix}, \Pi_{EE} = \begin{pmatrix} 0 & 0 & 0 & 0 \\ 0 & 0 & 0 & 0 \\ 0 & 0 & 0 & 0 \\ 0 & 0 & 0 & 1 \end{pmatrix} \quad (5.13)$$

Here, the capital letters are used to denote a measurement outcome and distinguish it from a two-qubit state. The probability of each of those 4 outcomes is given by  $p(j) = \text{Tr}[\Pi_j \rho]$  where  $j = \{GG, GE, EG, EE\}$ . In the case of the imperfect measurement, the state at the end of the experiment is not faithfully converted into a measurement outcome. For example, the state  $|gg\rangle$  could be recorded as EG with some probability. This can be described by the  $4 \times 4$  matrix  $\mathbf{A}$ , where  $A_{ji}$  is the probability that the state  $i$  is recorded as outcome  $j$ . Thus, four new projectors,  $\Pi_j^{expt} = \sum_i A_{ji} \Pi_i$ , can be calculated that model this imperfection. The effects of this imperfect measurement were accounted for in the theoretically calculated density matrix in Fig. 1.12B.

To calculate  $\mathbf{A}$  for this system, a calibration experiment was performed where the 4 computational states  $|gg\rangle$ ,  $|ge\rangle$ ,  $|eg\rangle$  and  $|ee\rangle$  were prepared. Then joint-tomography was performed to calculate the probability of each measurement outcome. By measuring  $p_j$  for each of the input states, the values of  $A_{ji}$  were calculated, yielding:

$$\mathbf{A} = \begin{pmatrix} 0.941 & 0.047 & 0.031 & 0.001 \\ 0.031 & 0.925 & 0.001 & 0.030 \\ 0.027 & 0.001 & 0.931 & 0.031 \\ 0.001 & 0.027 & 0.037 & 0.938 \end{pmatrix} \quad (5.14)$$

With this matrix, the tomography for the actual experiment could be corrected. For a given tomography pre-rotation  $k$ , the outcome can be written as a vector of probabilities  $B_k = (p(GG)_k, p(GE)_k, p(EG)_k, p(EE)_k)$ . Thus, the experimental state in the computational basis,  $P_k$ , that resulted in this outcome is given by  $P_k = \mathbf{A}^{-1} B_k$ . This operation was applied to tomography outcomes to calculate a corrected density matrix,  $\rho_{\text{corr}}$ , and thus a corrected fidelity,  $\mathcal{F}_{\text{corr}} = 57\%$ .

## 5.7 Experimental Results

Having established all the tools used in the experiment, we now delve into the full experimental protocol, including control experiments to verify that remote entanglement was generated

intentionally as a result of the flying photons.

### 5.7.1 Pulse Sequence

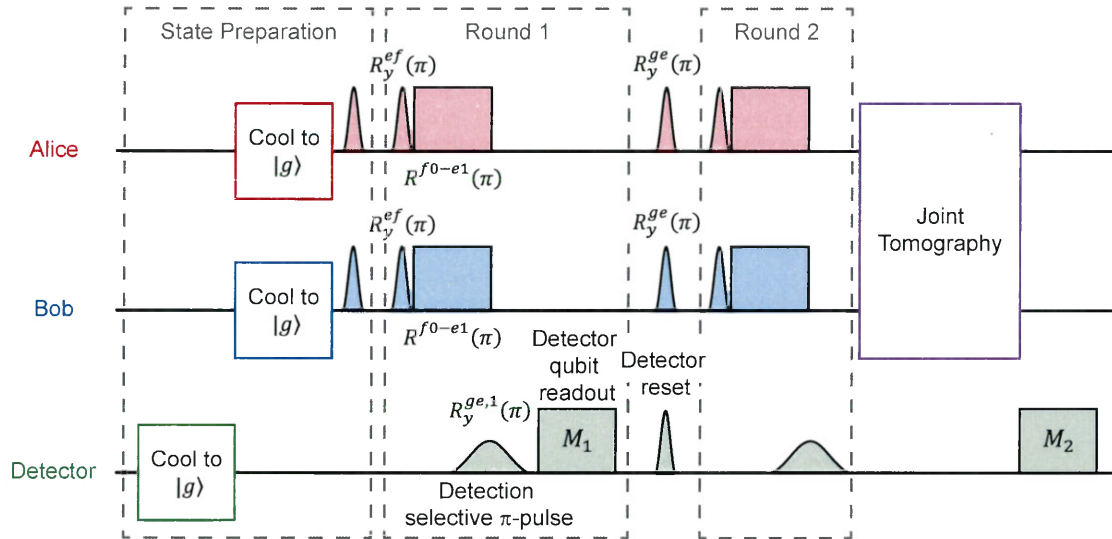


**Figure 5.12 | Detailed Pulse Sequence.** The remote entanglement protocol began with state preparation where the three qubit-cavity systems were initialized in the desired state by cooling and single-qubit rotations. Then, the first of two rounds of the protocol was performed. The qubits were entangled with flying single photons by a CNOT-like operation which then interfered on the hybrid and were detected by a selective  $\pi$ -pulse on the detector qubit. A  $\pi$ -pulse was performed on both Alice and Bob to remove the unwanted  $|ee\rangle$  state and the detector to reset it. Next, the second round of the protocol was performed followed by joint tomography to measure the state of Alice and Bob. The measurement outcomes from the two rounds of photon detection,  $M_1$  and  $M_2$ , were used to post-select successful trials for the tomographic analysis. The entire protocol was repeated with  $T_{\text{rep}} = 21 \mu\text{s}$ , much faster than the  $T_1$  time of any of qubits.

In the first step of the complete remote entanglement protocol (see Fig. 5.11), the Alice, Bob and the detector qubits were initialized in  $|g\rangle$ . They were first cooled to the ground states using a driven reset protocol [46] and then a measurement was performed to post-select on experiments where all three qubits were successfully cooled. This state initialization by post-selection had a success probability of 57%. Moreover, this also allowed the experiment to be repeated at  $T_{\text{rep}} = 21 \mu\text{s}$ , much faster than the relaxation time of any qubit. Single qubit pulses were then applied to the Alice and Bob qubits to prepare them in the desired initial state. Then, the first round of the remote entanglement protocol consisting of the CNOT-like operation and the photon

detection were performed. Before the second round, a  $\pi$ -pulse on  $\omega_{ge}$  was applied to both the Alice and Bob qubits to remove the weight in the  $|ee\rangle$  state. In addition, the detector was reset by an unselective  $\pi$ -pulse that returned the detector qubit to  $|g\rangle$  if it went click in the first round. Such an unconditional reset can be used since only those trials where the detector went click were used in the final data analysis. After a second round of the CNOT-like operation and photon detection, joint tomography of the Alice and Bob qubit state was performed conditioned on measuring two clicks in the detector. As shown in Fig. 5.12, the measurement of the detector qubit in the second round was performed after the joint tomography to reduce the protocol time and hence, the effects of decoherence. This can be done because the photon detection process is completed at the end of the detection  $\pi$ -pulse. The measurement of the qubit state is required only for the experimenter to determine the outcome of the detection event. A set of control sequences was interleaved into the above protocol to calibrate the joint tomography. These experiments were repeated to accumulate at least  $10^5$  successful shots of each sequence for adequate statistics.

### 5.7.2 Control Experiments

To verify that the experimental results observed in the data shown in Fig. 1.12 and Fig. 1.13 are a result of the which-path erasure of the flying photons by the hybrid, two control experiments were performed. In these experiments, no flying photons were generated but the experimental protocol was otherwise left unchanged. The joint tomography performed at the end of the protocol is no longer conditioned on photon detection events. To further rule out systematic error, these experiments were interleaved with the experiments performed in Fig. 1.13. The results on these experiments are shown in Fig. 5.13. In the first experiment, a control for the data in Fig. 1.13A, Bob was initialized in  $\frac{1}{\sqrt{2}}(|g\rangle + |e\rangle)$  and Alice was prepared in  $\cos(\theta/2)|g\rangle + \sin(\theta/2)|e\rangle$ . Since the qubits were not entangled with photons, no entanglement was generated for any preparation angle  $\theta$ . This is most directly demonstrated by  $\langle ZZ \rangle = 0$ , unlike in Fig. 1.13A where  $\langle ZZ \rangle < 0$ . Since Bob remained in  $\frac{1}{\sqrt{2}}(|g\rangle + |e\rangle)$  at the end of the experiment independent of  $\theta$ , the final single-qubit Bloch vector has Pauli components  $\langle Z_B \rangle = 0$ ,  $\langle X_B \rangle = 0$  and

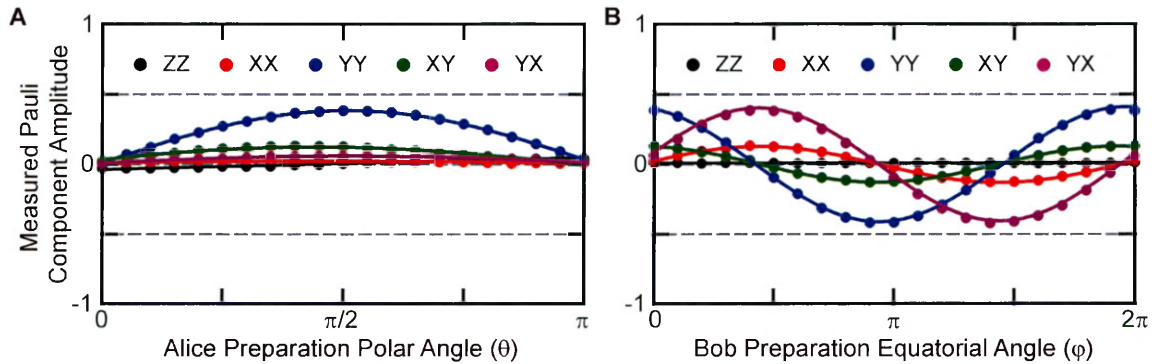


Figure 5.13 | **Control Sequence Data.** Measured amplitudes of selected two-qubit Pauli vector components as a function of qubit preparation. In experiments identical to those in Fig. 1.12, the two qubit were prepared in the desired initial state but no flying photons were generated. Joint tomography of the final two-qubit state was performed. A) With Bob always initialized in  $\frac{1}{\sqrt{2}}(|g\rangle + |e\rangle)$ , Alice was prepared in the variable state  $\cos(\theta/2)|g\rangle + \sin(\theta/2)|e\rangle$ . B) With Alice always initialized in  $\frac{1}{\sqrt{2}}(|g\rangle + |e\rangle)$ , Bob was prepared in the variable state  $\frac{1}{\sqrt{2}}(|g\rangle + e^{i\phi}|e\rangle)$ . In both cases, data (points) and fits (lines) confirm that no two-qubit entanglement is observed. This is most directly indicated by  $\langle ZZ \rangle = 0$  unlike Fig. 1.12.

$\langle Y_B \rangle = 1$ . Consequently, only  $\langle YY \rangle$  and  $\langle XY \rangle$  vary with  $\theta$  and are maximized at  $\theta = \pi/2$  while  $\langle XX \rangle = \langle YX \rangle = 0$ , unlike in Fig. 1.13A.

In the second experiment, a control for the data in Fig. 1.13B, Alice was now initialized in  $\frac{1}{\sqrt{2}}(|g\rangle + |e\rangle)$  and Bob was prepared in  $\frac{1}{\sqrt{2}}(|g\rangle + e^{i\phi}|e\rangle)$ . In the control experiment with no photons, the final two-qubit state should be the superposition of the computation states  $\frac{1}{2}(|gg\rangle + e^{i\phi}|ge\rangle + |eg\rangle + e^{i\phi}|ee\rangle)$ . Thus,  $\langle ZZ \rangle = 0$  (see Fig. 5.13B). Moreover,  $\langle XX \rangle$  and  $\langle YY \rangle$  do not have in-phase sinusoidal oscillations characteristic of an odd Bell state. Ideally,  $\langle XX \rangle = \langle XY \rangle = 0$  but a small detuning error on the Alice qubit caused oscillations in them too.

## 5.8 Entanglement Fidelity

To understand the sources of infidelity in the experiment, various sources of imperfection were built into a quantum circuit model of the entire system. The model contained both qubits, treated as two-level systems, an upper and lower branch of the experiment that could have 0, 1

or 2 flying photons and two single-photon detectors. Thus, the total system state was described by a  $36 \times 36$  density matrix. Sources of imperfections were individually introduced and their effects on this density matrix was calculated. By cascading their effects on the density matrix, their combined impact was also calculated. Finally, to compare to experiment, the photon parts of the density matrix were traced out to reduce it to a two-qubit density matrix which was expressed in the Pauli basis to generate Fig. 1.12B and calculate the expected fidelity.

### 5.8.1 Qubit Decoherence

The effects of qubit decoherence on the density matrix were modeled using phase damping. For a single qubit, this can be represented by the quantum operation  $\mathcal{E}(\rho) = E_0\rho E_0^\dagger + E_1\rho E_1^\dagger$  [99].

Here,

$$E_0 = \sqrt{\alpha} \begin{pmatrix} 1 & 0 \\ 0 & 1 \end{pmatrix}, \quad E_1 = \sqrt{1-\alpha} \begin{pmatrix} 1 & 0 \\ 0 & -1 \end{pmatrix} \quad (5.15)$$

and  $\alpha = (1 + e^{-t/T_{2E}})/2$ . The decoherence of each qubit was treated as an independent process assuming that there was no correlated noise affecting the two systems. Thus, by taking its Kronecker product with a  $2 \times 2$  identity matrix, the single-qubit phase damping operation was converted into a two-qubit operator. Two separate quantum operations,  $\mathcal{E}_A(\rho)$  and  $\mathcal{E}_B(\rho)$  for the decoherence of Alice and Bob, were calculated using  $T_{2E, A} = 10 \mu\text{s}$  and  $T_{2E, B} = 16 \mu\text{s}$  respectively. The final density matrix, obtained by cascading the two operation, resulted in a 20% infidelity due to decoherence, i.e.  $\mathcal{F}_{T_{2\text{Bell}}} \cong 0.8$ .

### 5.8.2 Dark Counts

This protocol's robustness to loss is a result of heralding on single-photon detection events which are uniquely linked to the generation of a Bell state. However dark counts mix the Bell state with other states,  $|gg\rangle$  for example, resulting in a lowered fidelity. This infidelity was calculated by modeling the impact of an imperfect detector on the two-qubit density matrix. The detector takes one of three possible input states, the flying Fock states  $|0\rangle$ ,  $|1\rangle$  and  $|2\rangle$ , and returns one of two outputs, click or no-click. In the generalized measurement formalism, this corresponds to

the three measurement operators  $\mathbf{M}_0 = |0\rangle\langle 0|$ ,  $\mathbf{M}_1 = |0\rangle\langle 1|$  and  $\mathbf{M}_2 = |0\rangle\langle 2|$  for detecting 0, 1 or 2 photons respectively[50]. To model the imperfections of dark counts and finite detector efficiency, we introduce  $P_d$ , the probability of a dark count in the detector, and  $P_{\text{real}}$ , the probability that the detector goes click when a photon arrives. Since according to simulations, the detector cannot distinguish between  $|1\rangle$  and  $|2\rangle$ , we make the assumption that either input results in a click with the same probability  $P_{\text{real}}$ . Thus, the probability of the two outcomes, no-click (NC) and click (C), are:

$$P_{\text{NC}} = \text{Tr} \left[ (1 - P_d) \mathbf{M}_0 \rho \mathbf{M}_0^\dagger + (1 - P_{\text{real}}) \left( \mathbf{M}_1 \rho \mathbf{M}_1^\dagger + \mathbf{M}_2 \rho \mathbf{M}_2^\dagger \right) \right] \quad (5.16)$$

$$P_{\text{C}} = \text{Tr} \left[ P_d \mathbf{M}_0 \rho \mathbf{M}_0^\dagger + P_{\text{real}} \left( \mathbf{M}_1 \rho \mathbf{M}_1^\dagger + \mathbf{M}_2 \rho \mathbf{M}_2^\dagger \right) \right] \quad (5.17)$$

Based on the measurement outcome, the input density matrix is projected to one of two output density matrices:

$$\rho_{\text{NC}} = \frac{\left( (1 - P_d) \mathbf{M}_0 \rho \mathbf{M}_0^\dagger + (1 - P_{\text{real}}) \left( \mathbf{M}_1 \rho \mathbf{M}_1^\dagger + \mathbf{M}_2 \rho \mathbf{M}_2^\dagger \right) \right)}{P_{\text{NC}}} \quad (5.18)$$

$$\rho_{\text{C}} = \frac{\left( P_d \mathbf{M}_0 \rho \mathbf{M}_0^\dagger + P_{\text{real}} \left( \mathbf{M}_1 \rho \mathbf{M}_1^\dagger + \mathbf{M}_2 \rho \mathbf{M}_2^\dagger \right) \right)}{P_{\text{C}}} \quad (5.19)$$

To model the experiment and calculate the fidelity limited by dark counts, the final density matrix after two rounds of the protocol and successful photon detection was calculated, resulting in a  $36 \times 36$  density matrix. The photon components of the density matrix were traced out, yielding the  $4 \times 4$  density matrix  $\rho_{\text{final}}$ . From this, the fidelity limited by dark counts,  $\mathcal{F}_d = \text{Tr}(\rho_{\text{final}} |O^+\rangle\langle O^+|)$ , was found:

$$\mathcal{F}_d = \frac{3P_{d,1}P_{d,2} + P_{d,1}P_{\text{real},2} + 4P_{\text{real},1}P_{\text{real},2}}{11P_{d,1}P_{d,2} + 8P_{d,2}P_{\text{real},1} + 9P_{d,1}P_{\text{real},2} + 4P_{\text{real},1}P_{\text{real},2}} \quad (5.20)$$

Here the numeric subscripts on  $P_d$  and  $P_{\text{real}}$  are for the two detections rounds in the experiment. The values of  $P_{\text{real}}$  and  $P_d$  for each round were extracted from the measured click proba-

bilities from the remote entanglement and the control experiments. We find  $P_{d,1} = 0.006$ ,  $P_{d,2} = 0.005$ ,  $P_{\text{real},1} = 0.21$ ,  $P_{\text{real},2} = 0.26$  and thus  $\mathcal{F}_d \cong 0.9$ . Combining the effects of decoherence and dark counts results in an expected theoretical fidelity of  $\mathcal{F}_{\text{thy}} = 0.76$ .

From this model of the experiment, it is also possible to analyze the state created at the end of the first round of the protocol which, as described in Ch. 1.7, is  $\rho_3^{\text{click}} = \mathcal{N} |O^+\rangle \langle O^+| + (1 - \mathcal{N}) |ee\rangle \langle ee|$ . In the case of a detector with no ability to distinguish between the inputs  $|1\rangle$  and  $|2\rangle$  and with no losses or dark counts, the normalization constant  $\mathcal{N} = \frac{2}{3}$ . However, in the presence of dark counts in the detector, the mixed state is further contaminated with weights in  $|gg\rangle$  and  $|O^-\rangle$ . From the values of  $P_{d,1}$  and  $P_{\text{real},1}$ , we find that the mixed state generated by detecting a click in the first round is:

$$\rho_3^{\text{click}} = 0.635 |O^+\rangle \langle O^+| + 0.327 |ee\rangle \langle ee| + 0.019 |gg\rangle \langle gg| + 0.019 |O^-\rangle \langle O^-| \quad (5.21)$$

While limiting the experiment to a single round would reduce the effects of decoherence and increase the generation rate by decreasing the protocol time, the advantages of performing a second round of the protocol are greater. In addition to increasing the overall fidelity by removing the weight in the  $|ee\rangle$ , the inclusion of the  $R_y(\pi)$  pulse on Alice and Bob stabilizes the phase of the generated Bell state, protecting it against inevitable drifts in experimental setup, such as the qubit frequencies or the phase of the various microwave generators for example.

### 5.8.3 Tomography

To model the imperfections arising from the tomography process, we used the theory described above (see Ch. 5.6) to calculate the Pauli components in Fig. 1.12. Using the experimentally measured  $\mathbf{A}$  matrix, the imperfect projectors  $\Pi_j^{\text{expt}}$  were calculated. Thus the measurement outcome is  $P_{jk} = \text{Tr} \left[ \Pi_j^{\text{expt}} \mathbf{R}_k \rho \mathbf{R}_k^\dagger \right]$  where  $\mathbf{R}_k$  is one of the 9 tomography pre-rotations. From the set of measurement outcomes, the 16 Pauli vector were calculated and plotted in Fig. 1.12B.

### 5.8.4 Error Analysis

The error bars in the quoted fidelity were dominated by statistical error from the finite number of tomography outcomes used to reconstruct the density matrix in the Pauli basis. Since around  $2 \times 10^5$  successful shots were used to calculate each Pauli component, the error was limited to around 1%. To convert the error in the Pauli components to an error in the fidelity and hence the concurrence, different density matrices were constructed by varying each Pauli component by their respective error amounts. The fidelity to  $|O^+\rangle$  and concurrence was then calculated for each of these density matrices to find the desired error bars.

## 5.9 Future Directions

We now turn our discussion to how both the remote entanglement fidelity and generation rate can be further improved, expanding upon the discussion in Ch. 1.7. To be used as a primitive for other quantum operations and gates, the operation that generates remote entanglement, which we otherwise call the remote entanglement generation gate, must have high fidelity and a large generation rate. Crucially for the latter, the generation rate must exceed the decoherence rate of the components storing quantum information ( $\sim 10$  kHz for qubits and  $\sim 200$  Hz for 3D cavities).

Starting with the fidelity of the remote entanglement generation gate, the primary source of infidelity, the decoherence times of the Alice and Bob qubits, can be reduced by readily available qubits with an order of magnitude greater coherence time [3]. However, while this improves  $\mathcal{F}_{T_{2\text{Bell}}} \sim 0.9$ , to really make the decoherence limited fidelity much smaller requires qubits with even longer decoherence times ( $T_{2\text{Bell}} \gg 100 \mu\text{s}$ ), an ever-present goal for superconducting, indeed all, qubits. Next, improving the single photon detectors to lower their dark count rate, and also increase their detection efficiency since  $\mathcal{F}_{\text{det}} \sim P_{\text{d}}/P_{\text{click}}$ . One proposal for an improved is discussed below. The remaining source of infidelity is suspected to be from the imperfect CNOT-like operation; signatures of this imperfection can be seen in Fig. 5.9 in the reduced contrast (ideally 2) sideband oscillations which suggest that the final state is not purely  $|e1\rangle$ . As mentioned

in Ch. 5.3 and Ch. 1.7, the cause for this is not well understood although it is suspected that at large power, the pumps used to drive the  $|f0\rangle \leftrightarrow |e1\rangle$  transition also drive other undesired transitions and also leakages to other states. Given the increasing use that these two-photon processes are seeing in cQED, these non-idealities are an area of active further investigation.

As for the generation rate, readily available real-time fast feedback techniques can be used to significantly reduce the protocol repetition time which is currently limited by the time it takes to initialize all three qubits in the experiment to  $|g\rangle$  by cooling and post-selection. Moreover, real-time feedback also allows us to implement an adaptive protocol that can reset all the qubits to  $|g\rangle$  if no photon is detected in the first round, instead of proceeding to the second as we currently do. Therefore, in addition to the 16-fold increase in generation possible from the use of two efficient single-photon detectors, these real-time feedback techniques could enable generation rates of  $\sim 10$  kHz. However, given the success probability of the protocol, 50%, and the fastest the protocol repetition time,  $\sim 2 \mu\text{s}$ , the maximum generation rate possible is on the order of 100 kHz. Consequently, this further emphasizes the need for significantly increased decoherence times, especially for qubits.

### 5.9.1 Improving the Single Photon Detector

While the entanglement generation rate in the experiment can be increased by a factor of 4 by using two detectors, a further almost 4-fold increase in the rate can be achieved with a higher efficiency detector. The mode mismatch between the flying photons and the the detector which currently limits its efficiency to  $\sim 50\%$  can be overcome by shaping the traveling photons to be perfectly absorbed by the detector. Since they leak out of the Alice or Bob cavities, the traveling photons have a decaying exponential temporal waveform with the decay constant  $\kappa_A$  or  $\kappa_B$ . Ideally, to perfectly enter the detector cavity without any reflections, the photons would need to have a rising exponential temporal waveform with the decay constant  $\kappa_D$ . Whereas time-reversing the photon temporal shape is challenging, an alternative strategy outlined in Fig. 5.14 involves using drives to generate and capture photons with time-symmetric temporal waveforms.

Adapting the ideas for quantum state transfer between trapped ion systems introduced in

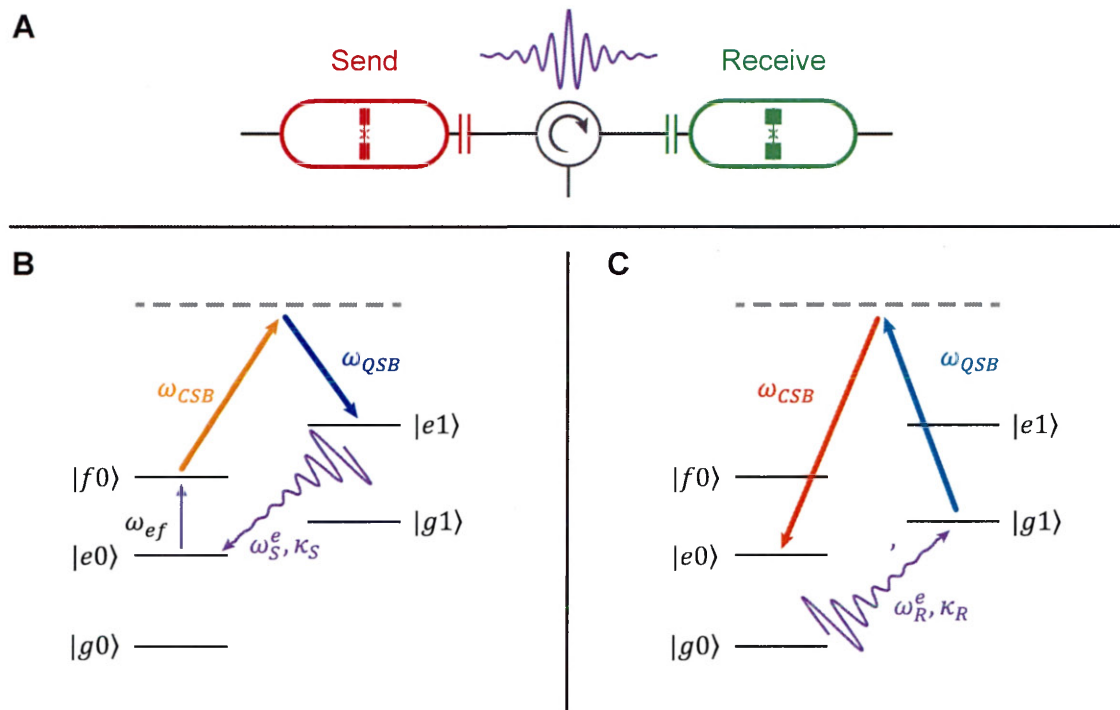


Figure 5.14 | **Schematic for Emitting and Capturing Single Photons.** A) The strongly coupled ports of two superconducting 3D transmon qubits are connected via a circulator in an example schematic for a system to efficiently emit and capture single photons using shaped sideband drives. Single photons with time-symmetric temporal waveforms are emitted by the Send system on the left and captured by the Receive system on the right. B) Energy level diagram for the Send. The protocol for generating a photon is identical to Fig. 5.3. The qubit begins in an arbitrary superposition state  $\alpha|g\rangle + \beta|e\rangle$  with the cavity in  $|0\rangle$ . A single photon is generated by first applying the pulse  $R_y^{ef}(\pi)$  at  $\omega_{ef}$  and then applying a pair of sideband pulses that drive transitions from  $|f0\rangle \leftrightarrow |e1\rangle$ . By controlling the shapes of these drives, a time-symmetric photon is emitted. C) Energy level diagram for the Receive. The photon emitted by the Send system incident on the Receive system excited it from its initial state of  $|g0\rangle$  to  $|g1\rangle$ . By applying two sideband pulses, transitions from the state  $|g1\rangle \leftrightarrow |e0\rangle$  are driven to transfer the excitation from the cavity mode to the qubit mode. At the end of the sequence, the Receive qubit is left in  $|e\rangle$  only if a photon was incident on it and otherwise remains in  $|g\rangle$ . Because these two sideband drives can be shaped to make the qubit look mode-matched to the incident photon, the flying photon can be perfectly absorbed with no reflections unlike the detector described in Fig. 5.6.

Ref. [25] to our cQED systems, we consider a simplified system of a single Send and a single Receive system, so named for the functions they perform in the experiment (see Fig. 5.14A), to outline how to realize an efficient single photon detector. The single photon generation process

in the Send system is almost identical to that described in Fig. 5.3 (Ch. 5.3); an arbitrary initial superposition state of the qubit  $\alpha |g\rangle + \beta |e\rangle$  with the cavity in  $|0\rangle$  is mapped onto  $\alpha |g0\rangle + \beta |e1\rangle$  with a  $R_y^{ef}(\pi)$  pulse followed by a sideband drive enabled  $\pi$ -pulse from  $|f0\rangle \rightarrow |e1\rangle$ . No, instead of the sideband drives being constant amplitude, they are amplitude is changed with time to generate a time-symmetric photon. To capture this photon, a similar process is used on the Receive system; the incident photon excites the Receive from its initial state of  $|g0\rangle$  to  $|g1\rangle$ . Simultaneously, another pair of sideband drives with shaped amplitudes are applied to drive the  $|g1\rangle \leftrightarrow |e0\rangle$ , swapping a cavity excitation into the qubit mode. Thus, when a photon is incident, it is absorbed by the system and the Receive qubit ends in  $|e\rangle$ ; on the other hand, when no photon is incident, the drives have no effect and the qubit remains in  $|g\rangle$ . Thus, the detection process is completed with dispersive readout of the qubit state as before followed by resetting the detector. As shown in Ref. [25], specifying the desired photon shape is sufficient to specify the necessary drive amplitudes as a function of time for the Send and Receive system. Thus, the drive amplitudes and the  $g_{2\text{ph}}$  that they generate need to be carefully calibrated to make this process work. A further advantage of this protocol is that it should have a lower dark count rate than the currently used detector since the sideband pulses should be more significantly more selective at not exciting the qubit when no photon is incident than the  $R_y^{ge,1}(\pi)$  pulse currently used. Moreover, this protocol can also be optimized to minimize the overall time to send and receive photons, balancing that with the overall efficiency, affording more control than currently available.

### 5.9.2 Single Round Protocols for Increased Generation Rate

One potential strategy towards a higher generation rate that also avoids using the  $|f0\rangle \leftrightarrow |e1\rangle$  sideband transition is an alternate remote entanglement scheme with only a single round of flying photon generation and detector [16]. The current protocol, based on Ref. [6], has two round to filter out the desired Bell state from the density matrix obtained at the end of the first round  $\rho_3^{\text{click}} = \mathcal{N} |O^+\rangle \langle O^+| + (1 - \mathcal{N}) |ee\rangle \langle ee|$  (see Ch. 1.7); the contamination of  $|ee\rangle$  results from losses in the system and the inability of the detector to distinguish between  $|1\rangle$

and  $|2\rangle$ . However, an alternative is to instead reduce the weight of  $|ee\rangle$  in  $\rho_3^{click}$  by initializing both the Alice and Bob qubit-flying photon system each in the state  $(1 - \epsilon) |g0\rangle + \epsilon |e1\rangle$  where  $\epsilon$  is a small number. After the photons interfere on the hybrid, the total system state is now  $|\psi\rangle_2 = (1 - \epsilon)^2 |gg\rangle |00\rangle + (1 - \epsilon)\epsilon |O^+\rangle |10\rangle + (1 - \epsilon)\epsilon |O^-\rangle |01\rangle + \epsilon^2 |ee\rangle (|02\rangle - |20\rangle)$ . When a single flying photon is detected, the resulting state is dominantly a Bell state with only small contamination of  $|ee\rangle$ , since  $\epsilon$  is small. The value of  $\epsilon$  to maximize the fidelity of the generated entangled state depends on the losses in the system and the properties of the detector like its dark count rate. However, because the qubits do not start in an equal superposition state, the success probability of this weak excitation single-round protocol is lower than the 50% possible in the two-round protocol. Still, this weak excitation protocol can achieve a higher generation rate since it can be repeated faster due to the shorter protocol time, and it also suffers less from inefficiencies in the detector and single photon transmission losses.

Since the qubit systems need to be initialized in the  $(1 - \epsilon) |g0\rangle + \epsilon |e1\rangle$  with no second round, the required CNOT operation between the stationary and flying qubits can be performed by driving the  $|g0\rangle \leftrightarrow |e1\rangle$  transition to create the necessary weak excitation, which can be driven with higher fidelity than the  $|f0\rangle \leftrightarrow |e1\rangle$  transition. However, in using the  $|g0\rangle \leftrightarrow |e1\rangle$  transition, the CNOT is not realized exclusively from a combination of  $\pi$ -pulses. Moreover, since there is only a single round, the  $\pi$ -pulse in the two-round protocol is also absent removing an important re-focusing pulse in the protocol that stabilized the generated Bell state phase. While superconducting qubit systems do not suffer from drifts in path lengths that can plague experiments using optical photons, the transmon qubits themselves drift in frequency over time; as a consequence, the Bell state phase of the single-round protocol is susceptible to this additional dephasing mechanism, not being protected by the  $\pi$ -pulse of the two-round protocol. Thus, successfully implementing a weak excitation protocol for superconducting qubits would require borrowing yet another strategy from the optical experiments - tracking the qubit frequencies over time. By interleaving the remote entanglement experiment with a Ramsey dephasing protocol to measure the qubit frequency periodically, the frequency of the control pulses applied to the experiment can be dynamically changed to follow the qubit, mitigating these dephasing effects.



# Perspectives of this Work Towards Entanglement Distillation, and Beyond

Civilization begins with distillation.

---

William Faulkner

## 6.1 Overview of Entanglement Distillation

Along with local single qubit operations, the tools of high-fidelity, QND measurements and robust concurrent remote entanglement generation form the operations necessary for non-local, i.e. teleported, two-qubit gates in a distributed quantum system, like the modular architecture presented in Ch. 1.3. An arbitrary remote gate between the data qubits of two modules can be performed by implementing the quantum circuit shown in Fig. 6.1. Similar to the protocol for the remote-CNOT gate shown in Fig. 1.4, the operation between the data qubits uses a remote entangled state between communications qubits of the two modules as a resource. After the remote entangled state is generated, only local operations and control are required to complete the

protocol. The remote unitary gate is implemented by performing controlled operations between the data and communication qubits within a module as well as operations on the data qubits conditioned on the measurements of the communication qubits in the other module.

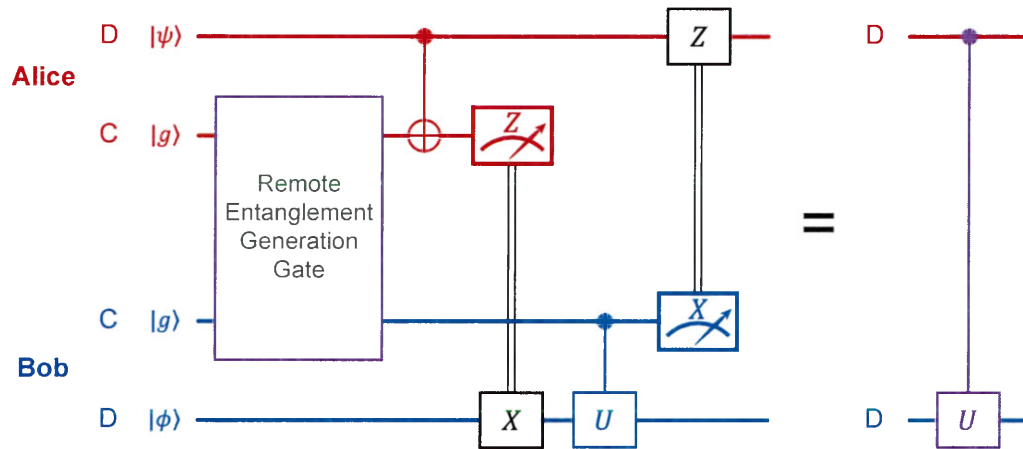


Figure 6.1 | **Quantum Circuit for a Remote Unitary Gate between Modules.** Circuit for a remote arbitrary unitary gate between modules. Using an entangled state between the communication qubits of two modules as a resource, an arbitrary unitary gate  $U$  between the two data qubits in the modules can be implemented using only local operations and classical communication between the modules. After a CNOT gate between the data and communication qubits in the first module, the communication bit is measured in the  $Z$  basis. An  $X$  gate, conditioned on the measurement outcome, is performed on the data qubit. Then, a controlled-unitary is performed between the communication and data qubit before completing the operation with a measurement of the communication bit in the  $X$  basis and performing a conditional  $Z$  gate on the data qubit in the first module.

The fidelity of the two-qubit gate crucially depends on various constituents of the remote gate shown in Fig. 6.1: (1) the fidelity of the local operations performed in each module; (2) the lifetimes and coherence times of the quantum modes involved in the circuit; (3) the fidelity of the remote entangled state used as a resource state [7, 65, 93, 97]. With demonstrated single qubit operation fidelities of  $\mathcal{F} \sim 0.99$  [12, 53, 112, 141], the first of the three constituents is the least concerning. On the other hand, the coherence times, especially of transmon qubits, can be limiting to the remote-gate fidelity. While concerning, the most debilitating of the three is the fidelity of the remote entangled resource state. The achieved fidelity of  $\mathcal{F} \sim 0.57$  (see Ch. 5) would be insufficient to demonstrate a successful gate. Even with all the improvements

described in Ch. 5.9, the entangled state fidelity would still contribute to imperfections on par with decoherence. Moreover, as the size and complexity of the modular systems increases, it will be crucial to ensure that the remote entangled state fidelity doesn't degrade. This necessitates implementing what is effectively a form of error correction; high-quality entangled states can be generated using many copies of lower-quality ones in a process called entanglement distillation [7, 32].

Also known as entanglement purification, this distillation procedure consists of performing unitary operations on the starting copies of the two-qubit entangled states followed by single-qubit measurements; conditioned on the measurement outcomes, the final state is an entangled state of higher fidelity, making this a probabilistic process. To illustrate how this works concretely, consider the case of Alice and Bob who share two Bell pairs, each with fidelity  $\mathcal{F} = F$  to the odd Bell state  $|O^+\rangle$ . Expressed as a density matrix:

$$\rho_i = F |O^+\rangle \langle O^+| + \frac{1-F}{3} (|O^-\rangle \langle O^-| + |E^+\rangle \langle E^+| + |E^-\rangle \langle E^-|) \quad (6.1)$$

Here  $O$  and  $E$  correspond to the odd and even Bell states respectively and  $+$  and  $-$  indicate the phase of that Bell state. This initial state is not too different than the one we obtain from the experiment discussed in Ch. 5; in fact, the only difference is that for the state obtained in the experiment, the weight in  $|O^-\rangle$  was larger than that in  $|E^\pm\rangle$ . First, Alice and Bob perform a  $X$  rotation on the qubit that transforms  $|O^\pm\rangle \leftrightarrow |E^\pm\rangle$ . The density matrix of each Bell state copy thus becomes:

$$\rho_i = F |E^+\rangle \langle E^+| + \frac{1-F}{3} (|E^-\rangle \langle E^-| + |O^+\rangle \langle O^+| + |O^-\rangle \langle O^-|) \quad (6.2)$$

Thus, the Bell state has gone from being dominantly  $|O^+\rangle$  to  $|E^+\rangle$ . Next, Alice and Bob perform a CNOT between the two qubits they have. In other words, they perform the gate using their qubit from one Bell pair as the control and their qubit from the second Bell pair as the target. The effect of this operation is summarized in Ref. [7]. Finally, Alice and Bob each measure their target qubit in the  $Z$  basis; if they find that their measurement outcomes agree, then the unmeasured

pair (the control qubits) is a Bell state of improved fidelity  $\mathcal{F} = F' > F$ . A sufficient requirement for  $F' > F$  is that the fidelity of the initial Bell pairs exceed  $\mathcal{F} = F > 0.5$ . It is important to note that this protocol is inherently probabilistic and the success probability depends on the fidelity of the input entangled states, with higher fidelity pairs resulting in an increased success probability [7].

The combination of the CNOT operation and the measurement is to effectively redistribute the weights of the density matrix and select outcomes that increase the weight in the desired Bell state. This can be understood by seeing what happens as a result of the CNOT operation. When the qubits that Alice and Bob use as the controls start in the Bell state  $|E^\pm\rangle$  and the target Bell pair are in  $|E^+\rangle$ , then the this CNOT operation has no effect and the source and target remain unchanged. However, when the source pair is in  $|O^\pm\rangle$  and the target pair is in  $|E^+\rangle$ , the CNOT leaves the source unchanged but changes the target to  $|O^+\rangle$ . In the first case, a measurement of the  $Z$  component of the Alice and Bob target qubits will yield identical outcomes. However, in the second case, the measurement will result in anti-correlated outcomes. By only keeping attempts where the target qubit measurement outcomes agree, the protocol filters out density matrix weights in undesired Bell pair components, like  $|E^+\rangle$  for example. As a result, the fidelity of the desired Bell pair increases.

However, this implementation of entanglement distillation suffers from a few shortcomings. Most importantly, it does not correct all the possible errors that the input Bell state to be purified may suffer from. The Bell pair can suffer one of three possible types of errors: a bit-flip error (also called an  $X$  error); a phase-flip error (a  $Z$  error); and a simultaneous bit-flip and phase-flip error (a  $Y$  error). The protocol outlined above with a single round of local operations and measurements, creating what is sometimes referred to as a level-1 purified pair, corrects only two of the three possible error [65]. Thus, even with repeated rounds of distillation, this protocol would be limited in the ultimate fidelity of Bell state is produced if the input state is the one of Eq. 6.1; however, if, for example, one of the error rates was very low and the Bell state only suffered from only two error channels, this protocol could be effective.

An alternative entanglement distillation protocol (see Ref. [65]) that can correct all three

possible errors relies on concatenating the above procedure. After a single round of distillation is performed to produce a level-1 pair, the process is repeated to generate a second level-1 distilled entangled pair. Subsequently, the two level-1 pairs are used as the input for yet another round of distillation resulting in a level-2 pair. This would necessitate having at least two storage modes in each module so that two entangled states may be simultaneously stored. Other entanglement distillation procedures that can only correct arbitrary errors in the input Bell pairs but also protect, to some level, against imperfect local operations have also been explored [32, 38, 98]. In general, the choice of what distillation procedure to implement is strongly dependent on the errors that the input Bell pairs are prone to as well as the errors in the local operations (for systems where the errors due to local operations dominate the errors in the Bell states, longer distillation protocols with more operations will induce more errors that they may fix).

Since the errors that our experiment is prone to will depend upon the physical system that is used (for example, the properties of our transmon qubit) as well as the protocol used to generate entanglement (for example, while the Bell state generated in the single photon based remote entanglement experiment of Ch. 5 was primarily limited by dephasing, future iterations of the experiment could be limited by other things like dark counts), the choice of what distillation protocol to implement will depend on the platform we choose to use to perform distillation. Thus, temporarily setting aside discussions about the distillation protocol, we now turn to address what the hardware requirements for implementing this general class of protocols is, specifically for the distillation of remote entangled states for use in a distributed, modular architecture (like that in Ch. 1.3). In the outlined architecture, remote entanglement can directly be generated only between communication qubits; the data qubits, containing the quantum information to be processed, must be left alone until the remote entangled state is ready to be consumed as a resource for non-local gates. Therefore, generating multiple copies of remote entangled Bell pairs would require either having multiple communication qubits per module or adding storage modes to the module which can be loaded with Bell pairs. The former strategy introduces the new challenges or a more complex router capable of connecting modules with multiple outputs to the measurement apparatus. Moreover, introducing more modes to a module that are capable of

communicating with the environment potentially opens up new loss and decoherence channels. Thus, the latter strategy of adding storage mode(s) to the module where a Bell state can be stored and operated (see Fig. 1.14A) seems the more immediately tractable. Crucially, since even the more advanced distillation protocols only require operations on up to three Bell pairs at a time, modules with the ability to store three bits would have sufficient hardware flexibility to implement a range of distillation protocols. Indeed, this method of using storage modes has been proposed [65, 93, 98] and implemented [66] for remote entanglement distillation in other hardware platforms for quantum information.

With this new object in the module, the remote entanglement distillation protocol would be modified to what is shown in Fig. 1.14B where remote entanglement is first generated between the communication qubits of two modules, Alice and Bob. It is then transferred into one of the storage qubits using a SWAP operation. This process can be repeated between the communication qubit and the storage qubits to generate and load as many resource entangled pairs as the distillation protocol requires. Furthermore, it would also be necessary to be able to perform gates between the various storage qubits as well as measurements of these storage qubits to complete the set of operations required for distillation. The choice of which distillation protocol to implement in this hardware would then depend on the characteristics of the system like the fidelity of the local operations and of course, the fidelity of the resource entangled pair. Since the requirements of a distillation procedure become less challenging as the fidelity of the input Bell pairs increases [7, 32, 38, 65, 98], improving the fidelity of the remote entanglement generation operation remains imperative. Moreover, improving the generation rate is also crucial to enable multiple resource states to be generated and consumed by the purification protocol in a time much shorter than the coherence and relaxation times of the data qubits.

With this set of requirements in mind, we can now explore how to extend the functionality of a module to enable entanglement distillation. While the choice of which protocol to use will ultimately depend on the hardware capability and performance, it is still possible to design a general enough system, i.e. consisting of a communication qubit with a few storage qubits, that is flexible enough to be used across a range of possible distillation protocol implementation. As

a first step, even adding a single storage mode to the system would enable testing the basic functionality required for distillation. Even though it would probably enable testing only a limited distillation protocol that can fix only some errors, it would serve as an invaluable testing ground for new module capabilities as well as potentially directing our understanding of how to design future iterations of the distillation protocol.

## 6.2 Modules for Remote Entanglement Distillation

The key technical challenge to realizing the remote entanglement distillation protocol shown in Fig. 1.14B is adding one or more storage modes to the module. Crucially, this storage mode must have a long relaxation lifetime,  $T_1$ , and decoherence time,  $T_2$ , to be able to hold a Bell pair without degrading its fidelity; specifically, they must exceed the time scale on which entanglement is generated,  $R_{\text{ent}}^{-1}$ , so that multiple rounds of distillation can be performed before decoherence effects dominate. However, for a first experiment, achieving  $T_1, T_2 \sim R_{\text{ent}}^{-1}$  would be sufficient to demonstrate at least one round of entanglement distillation. In addition, the protocol also requires that both single-qubit operations on the storage and two-qubit operations between the storage and the communication can be performed in this module. Furthermore, operations between storage qubits would also need to be possible. Thus, control over the storage is needed as is some coupling to the communication qubit, which itself must be able to interact with the environment for remote entanglement generation. For the purposes of the following discussion, we will assume that the remote entanglement generation protocol will be the single-photon based one of Ch. 1.7 and Ch. 5.

A promising candidate for a storage qubit is a three-dimensional (3D) cavity, specifically a cylindrical coaxial cavity, for the demonstrated long coherence times [111], ease of integration with other components of the module [3], and the ability to perform universal operations [53]. Moreover, as a system with a larger Hilbert space than a qubit, the cavity could potentially store multiple Bell pairs, realizing a hardware-efficient storage mode. Such a cavity-based storage qubit could be straightforwardly integrated with the qubit-cavity systems used in the thesis as shown

in Fig. 6.2A; the transmon qubit (green) is now coupled to two cavities, one is a rectangular readout cavity (blue) as before and the second is the added cylindrical storage cavity (orange), closely paralleling the system of Ref. [101]. The colors in the diagram are used to illustrate the roles played by each mode: green for communication qubit, orange for storage qubit, blue for readout resonator, and gray for any other mode. With this system, the single-photon based remote entanglement protocol would remain unchanged, as would the parameters of the qubit and readout cavity. Once entanglement is generated, it would be loaded in the storage, encoded, for example, in the Fock states of the cavity, or even cat states [141]. Operations like the SWAP and CNOT, as well as single-qubit rotations on the storage could all be performed using the coupling between the storage and the transmon [53, 141], which we choose to be  $\chi_{sq} \sim 2$  MHz to parallel the system of Ref. [101]. A dispersive shift of  $\chi_{qr} \sim 10$  MHz is required between the qubit and readout modes for the sideband transitions of the entanglement generation protocol (see Ch. 5.3). As a result, the direct coupling between the storage and readout modes would be  $\chi_{sr} = -2\sqrt{\chi_{ss}\chi_{rr}} = -2\sqrt{\frac{\chi_{sq}^2}{4\chi_{qq}} \frac{\chi_{qr}^2}{4\chi_{qq}}} \sim 50$  kHz. This imposes a coupling-induced dephasing rate of  $\Gamma = \frac{2\chi_{sr}^2}{\kappa_r} \sim 5$  kHz for a single photon in the readout cavity; in other words, the presence of a single photon in the readout would limit the storage lifetime to  $30 \mu\text{s}$ . Since the entanglement generation protocol populates the readout with a photon to make a flying photon, this would significantly dephase a Bell state in the storage. Moreover, as rotations are performed on the transmon, it will become entangled with the storage [101, 141], further adding to dephasing of the state in the storage. Together, these undesired effects make this idea for a module and unlikely choice for distillation.

Unsurprisingly, strong, direct coupling between a long-lived mode (like the storage) and a short-lived mode (like the readout) cause the coherence times of the former to suffer. This problem of putting modes of vastly disparate coherence properties in the same box with coupling between them is not unique to superconducting qubits; other hardware platforms for modular and distributed quantum information have to contend with it as well, demanding careful engineering [60] and using, for example, clever encodings to minimize spurious interactions [66].

One strategy for the hardware at our disposal is to use a system where the direct coupling

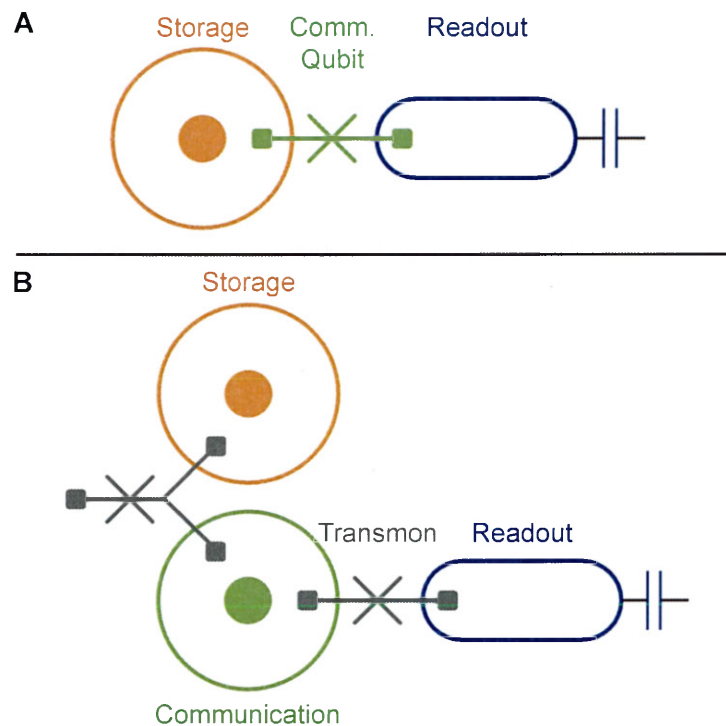


Figure 6.2 | **Schematics for Modules to Implement Remote Entanglement Distillation.** A) Schematic for a module using a cylindrical coaxial cavity as a storage qubit and a 3D transmon as the communication qubit. Remote entanglement is generated between communication bits and swapped into the cavity. After a second round of entanglement generation, distillation can be performed by performing local operations between the transmons and storage cavity. However, the static couplings between the various modes are detrimental to realizing this design imposing crippling limits to the coherence of modes, especially when entangling operations are performed on the communication qubit while the storage qubit contains another quantum state. B) Schematic for a module using two cylindrical coaxial cavities as the storage and communication qubits. While direct couplings between modes can be mitigated in this design for a module, using a very weakly harmonic cavity as a qubit to generate single flying photons entangled with the qubit is not compatible with the sideband transitions used to implement the CNOT-like gate.

between two modes can be minimized while still being able to perform operations on them [145]. As shown in Fig. 6.2B, now, both the storage and communication qubits are coaxial cavities. A transmon is coupled to the communication and readout cavities to mediate coupling and enable remote entanglement generation. Another transmon connects the storage and communication cavities to enable single and two-qubit operations to be performed. Replacing the communication qubit with a cavity requires modifying the single-photon remote entanglement protocol; for

simplicity, we assume that the communication qubit is encoded in the Fock basis of the cavity. Thus, flying photons could be generated using sideband transitions that now transfer excitations between the communication and readout cavities [106]; the sideband transitions now implement the unitary performed a beam splitter, with the transmission coefficient of the beam splitter depending on the length of time that the sideband drives are applied for. Thus, for a communication qubit starting in the equal superposition state  $|0\rangle + |1\rangle$  (paralleling the state  $|g\rangle + |e\rangle$ , ignoring normalization) and a readout in the vacuum state  $|0\rangle$ , the sideband transitions would generate the state  $|00\rangle + |01\rangle + |10\rangle$  if turned on for a time corresponding to a 50 – 50 beam splitter. Unfortunately, this is not equal to a CNOT operation which would produce the joint storage-readout state  $|00\rangle + |11\rangle$ . Furthermore, if we tried to use higher levels of the communication cavity by starting in  $|0\rangle + |2\rangle$ , the sideband transitions would still implement the desired gate, instead yielding the final state  $|00\rangle + |11\rangle + \frac{1}{2}(|02\rangle + |20\rangle)$ . The problem arises from performing the sideband operations on a harmonic mode like the cavity instead of an anharmonic mode like the qubit where they selectively address only one state of the qubit. In short, this example illustrates that, in order to use the single-photon based remote entanglement protocol as currently implemented with sideband transitions, requires that the communication qubit be a strongly anharmonic mode like the transmon.

A module that has a transmon as a communication qubit with manageable coupling to a storage mode is shown in Fig. 6.3A. Now, both the communication and storage qubits are transmons with a coaxial cavity acting as a bus resonator between the two. This system closely parallels that used in Ref. [12] where it was also demonstrated that the direct coupling between the communication and storage could be made to be very small,  $\chi_{sq} \sim 1\text{kHz}$ . Although the storage qubit would not have lifetimes anywhere close to the 1 ms possible for coaxial cavities, they can still achieve  $T_1, T_2 \sim 50$  to  $100 \mu\text{s}$ , sufficient for an initial few-round demonstration of the basic distillation protocol discussed above with generation rates of  $R_{\text{ent}} \sim 10\text{kHz}$  (i.e characteristic time of  $\sim 15 \mu\text{s}$ ). Yet another disadvantage of using a transmon as a storage mode is that it can only hold one Bell pair; thus, realizing more sophisticated distillation protocols would require adding more transmon based storage modes. While adding more transmon storage modes

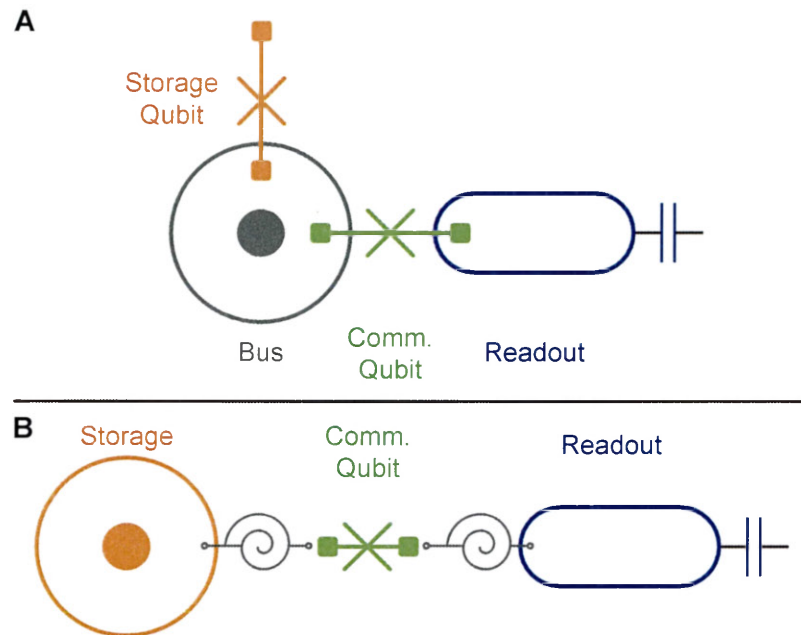


Figure 6.3 | **Schematics for Modules to Implement Remote Entanglement Distillation.**

A) Schematic for a module based on multiple transmon qubits. To address the problems with the modules described in Fig. 6.2, two different transmons are used as the communication bit and the storage bit. A coaxial cavity coupled to both qubits acts as a bus to enable operations between the two qubits while minimizing direct coupling. B) Schematic for a module with tunable couplings. An alternative strategy to managing undesirable couplings without introducing buffer modes relies on being able to turn the couplings on and off as desired. Here, this is enabled by the use of SNAILs to mediate the coupling between the storage, communication and readout modes in the modules. Since a SNAIL only allows three-wave mixing, couplings between elements can be turned on with the application of a pump tones and otherwise left off.

would be possible, it may not be as hardware-efficient as using a 3D cavity as the storage, as discussed below.

On the other hand, an advantage of using a transmon storage mode is that operations between the two qubits can be implemented using bus-resonator induced phase (RIP) gates, which have demonstrated high-fidelity and fast operation times [102]. It is worth noting that this proposal for a module still does not contain an actual data qubit, which would likely be another 3D cylindrical coaxial cavity; moreover, the coupling between this data qubit and the storage or communication qubit would also need to be carefully engineered to protect against any degradation to the mode lifetime or coherence time. This would probably require adding yet more modes to both act as

buffers between the storage and data qubits as well as enable control over the data qubit. It quickly becomes apparent that as more components with different properties and functions are added to the modules, greater care must be taken to ensure that each behaves as desired without affecting properties of the other.

It was actually this exact problem that led to the pursuit of a modular architecture. In scaling up quantum information systems to larger numbers of qubits, managing the interactions between them becomes increasingly challenging. By enclosing qubits in their own boxes, these interactions were greatly mitigated while retaining the ability to control each individual qubit. A similar principle can be, and probably will need to be, applied within a module. Instead of relying on, and carefully engineering, static couplings between the various objects in a module, incorporating tunable couplings between the objects would enable achieving a large on-off ratio. By turning on interactions between objects only as needed, the coherence properties of the modes could be preserved while still allowing operations to be performed between them. One avenue towards this lies in utilizing three-wave mixing to mediate all the couplings between objects instead of the current method of using the non-linearity and four-wave mixing elements of the transmon. Such a three-wave mixing interaction could be realized by using superconducting non-linear asymmetric inductive elements (SNAILs) as the coupling elements between modes, as shown in Fig. 6.3B. Of course, this adds the complications of now needing to introduce a magnetic flux into a module of superconducting devices in order to appropriately bias the SNAILs; the magnetic field has to be applied without affecting the coherence of any of the neighboring modes. However, this may still be more tractable than engineering the coupling between a multitude of modes. Moreover, such a system may benefit from improved transmon coherence properties since it is only transiently coupled to the readout resonator, making this a compelling system to investigate.

Even the most advanced module proposal would still only enable the implementation of a modest distillation protocol capable of correcting some errors and of only a few rounds of distillation. One reason for this is that so far we have assumed a storage capable of holding a single qubit of information. An advantage of using a 3D coaxial cavity as a storage is its large Hilbert space; indeed, many entangled pairs could be stored in the storage simultaneously.

For example, the  $|0\rangle$  and  $|1\rangle$  Fock states could encode one qubit, the  $|2\rangle$  and  $|3\rangle$  Fock states a second qubit and so on. Such a multi-mode storage would enable the implementation of distillation protocols that can correct for all errors in the resource Bell pair while also being robust to local operation errors [32, 37, 98]. Implementing this would require understanding how to perform these operations and measurements in the multi-mode storage, although the universal control of an oscillator demonstrated in Ref. [53] offers one potential strategy.

Yet another option maybe to use an entirely different method to generate remote entanglement; the Josephson Parametric Converter (see Ch. 2.3) can be used to generate entanglement between two modes, the signal and idler [123]. However, the entanglement is between two continuous variable coherent states that are susceptible to loss. Still, a protocol could be designed to capture this entangled state in the storage cavities of two modules and distill it into a Bell pair of higher fidelity. Of course, this remains an open challenge. However, it is attractive because it uses a resource unique to superconducting quantum circuits, the generation and control over continuous variable states. Although, there are many open questions, investigating approaches to implementing remote entanglement distillation will be crucial to the success of a modular architecture for quantum computing, especially as the requirements for the Bell state fidelity increase.

### 6.3 Future Challenges and Prospects

A recurrent theme of this thesis has been describing the systems and operations being used as tools for quantum information and communication with superconducting quantum circuits. As this field has matured over the last two decades or so, these tools have becomes increasingly well understood and characterized, enabling them to become more standardized and usable as plug-and-play components in experiments. Having, till now, focused on a few of these tools in detail, we now turn to a more macroscopic view, looking at imminent and interesting challenges as well as future prospects. A key idea underlining these next steps is understanding how to put these devices together in increasingly larger and more complex systems for quantum information.

### 6.3.1 Increased Coherence

A (sometimes significant) source of error in all the experiments discussed in this thesis, and common to many superconducting quantum circuit experiments in general, is qubit relaxation and decoherence. What is more, as the now low-coherence object, the transmon also limits the coherence of high-Q 3D cavities [111], which are promising quantum memories and logical qubits [3, 80, 101]. For these two reasons, improving the coherence of these qubits is critical.

Currently, (3D) transmon qubits have typical relaxation times of  $T_1 \sim 100 \mu\text{s}$  and decoherence times of  $T_2 \sim 20 - 100 \mu\text{s}$ . Of the two, the latter is the more immediate and concerning problem since the achieved decoherence times are much lower than the theoretical limit of  $T_2 = 2T_1$ . This indicates that the qubits suffer from low pure dephasing times,  $T_\phi$ , suspected to be limited by thermal photons in the cavity/resonator modes to which the qubits are coupled. The measured thermal occupancy of about  $10^{-3}$  [125] greatly exceeds the number of thermal photons expected in a mode ( $f \sim 5$  to  $10$  GHz) cooled to around  $20$  mK. This abnormally high thermal occupancy is thought to be a result of improperly thermalized objects like attenuators and coaxial cables. Confirming this hypothesis and designing microwave input and output lines that are well thermalized while retaining the properties described in Ch. 3.3 will be crucial to improving coherence times.

On the other hand, while the relaxation time of these qubits is almost two to three orders of magnitude larger typical protocol or measurement times, improving  $T_1$  is also necessary to further improving measurement and other operation fidelities. Currently, transmon relaxation times are suspected to be limited by loss mechanism like quasiparticles and dielectrics; reducing the effects of these decay channels will require exploring new fabrication techniques, like metal masks for fabrication without electron beam resist, as well as improved filtering and shielding techniques. Even more detrimental than  $T_1$  is the non-QNDness of the dispersive measurement, experimentally observed as a reduction in  $T_1$  when photons are present in the cavity. Although there are a few theoretical ideas about the origin of this behavior [13], this remains an open challenge and the dominant limitation to achieving higher measurement fidelity. Thus, understanding

and rectifying this source of error is critical to improving the performance of superconducting quantum circuit technologies.

In general, as we are better able to control both the non-linear qubit modes and the linear resonator modes they are coupled to, we will also need to better understand and engineer spurious higher-order interactions arising from terms ignored in the fourth-order expansion of the cQED Hamiltonian. Especially as coherences improve and more pumps are used to drive interactions, mitigating unwanted transitions will be vital. Moreover, these advances will require improvements in a wide range of technologies like circuit fabrication as well as incorporating novel tools, for example active monitoring and stabilization of qubit frequency.

### 6.3.2 Small Modules

Together with the work demonstrating the use of high-coherence 3D cavities as hardware-efficient logical qubits [80, 88, 101] and the ability to control them [53, 145], the (high-fidelity measurements and robust remote entanglement generation) results in this thesis are a demonstration of all the individual quantum objects and operations required for a module, as described in Ch. 1.3. An important next step is to put these ingredients together to realize a module containing both a high-coherence data qubit and a communication qubit, which has the ability to communicate with the external world. As already alluded to above in Ch. 6.2, putting high-coherence (long-lived) and low-coherence (short-lived) objects, with couplings between them, in the same box is challenging; the necessary coupling between the objects required to perform operations can also adversely affect the coherence of the data qubit. Thus, understanding how to incorporate these quantum objects of very disparate function, form, and properties in the same module while maintaining their desired performance is a crucial next step towards a modular architecture. Even as work continues to improve the individual building blocks within a module, exploring how these objects work in conjunction is useful to reveal any weak links in the module as a whole. This provides an invaluable tool in directing future research to tackle problems that arise when assembling modules.

### 6.3.3 Routers and Integrated Directional Components

Taking a still more global view of the modular architecture described in Ch. 1.3, one of the least developed aspects is the router that connects modules and mediates the flying quantum information between modules and the measurement apparatus. Although there have been demonstrations of some basic building blocks that could be used to realize a router [21, 69, 132], incorporating them into a device that can route signals in the architecture shown in Fig. 1.3 is an open challenge. Understanding the properties this router would have, bandwidth, insertion loss, and connectivity for example, would be important in designing compatible modules and measurement hardware, as well as informing the choice of what remote entanglement protocol to use.

In that vein, the development of more advanced directional components, i.e circulators, isolators and amplifiers, compatible with, ideally on-chip for example, superconducting quantum circuits that obviate commercially available ferrite-based directional elements is vital. A number of such devices have been shown [21, 69, 84, 132] but they still require further development to be usable with current experiments; suffering from low bandwidth, or reverse isolation, for example, they still require some commercial directional components and are often complex systems that need to be carefully tuned. Developing these devices into robust plug-and-play tools that can be widely incorporated into experiments will be essential for building larger-scale distributed systems that rely on transferring quantum information between remote objects.

### 6.3.4 Channel Cost and Hardware Complexity

Superconducting quantum circuits have benefited greatly from readily available commercial microwave test equipment, which have been straightforwardly re-purposed to control and measure quantum systems. However, this equipment is expensive since it was originally designed to address a much broader application range than just for superconducting quantum information. As this field has matured, the need for custom microwave control and readout hardware has also grown. This has spurred the development of real-time feedback technologies based on field programmable gate arrays (FPGAs) [82, 101, 116] which are essential for quantum error correction.

The past few years have also seen the development of custom microwave setups for control and readout based on a combination of lower-cost commercial and home-made components explicitly designed for with applications to this field in mind. These have significantly reduced the cost per qubit/quantum mode channel by more than order of magnitude. This was essential to realizing the current generation of experiments with control over of order  $\sim 10$  modes. However, to realize the next generation of experiments consisting of an order of magnitude more modes will require a corresponding decrease in channel cost.

Beyond the cost of these channels, as the number of signals entering and leaving the base stage of a dilution fridge increases, the requirements for each of them, noise characteristics and power dissipation for example, become stricter as well. More microwave lines need to be fit into a fridge while, at the very least, maintaining (if not actually improving) the microwave and cryogenic hygiene essential for high coherence. Increasingly, the specifications needed of these microwave components for superconducting quantum information systems is exceeding what is commercially available. In some cases, the components being used were never designed for operation as cryogenic temperatures or with ultra-low noise applications in mind.

Together with the push towards realizing ever larger systems, these requirements necessitate moving away from commercially available solutions and developing custom interconnects, filters, attenuators, cryogenic packages, shields, to name but a few. These components will need to be more integrated and miniaturized, by using smaller form factors than SMA for coaxial cables for example, for higher channel density. Moreover, their packaging and mounting will need to be engineered specifically for quantum information applications, like ensuring that all components are well thermalized to the base temperature of 20 mK by using appropriate materials. It is worth noting that what the exact specifications required of these components for desired quantum information performance is still a somewhat open question and the topic of further research. Still, some understanding of what the requirements are exists and should form the basis for initial versions of these custom components. These technological developments are especially important as an increasing number of applications rely on high-power pump tones to drive processes like parametric amplification (see Ch. 2.3) or two-photon interaction (see Ch. 5.3), to cite just two

relevant examples. Indeed, to certain degree, the same care of engineering will need to be applied to the microwave hardware carrying signals to and from the experiment as has been invested in the quantum objects themselves.

There are still many open challenges towards the realization of quantum computers and quantum communication networks but the prospects are promising. Beyond these compelling applications, quantum science and engineering, in general, are themselves fascinating since they represent some of the most advanced understanding and control we have over quantum devices. It is still sometimes mind-boggling to this author that we can control and entangle quantum objects that are, for example, composed of machined blocks of aluminium separated by many centimeters and observe quantum behavior on instruments at room temperature. So, it is exciting to be able to add, through this work, to the measurement and remote entanglement generation toolbox of superconducting quantum circuits and contribute to the amazing progress made by this field so far, with hopefully much more still to come.

# Bibliography

- [1] B. Abdo, A. Kamal, and M. H. Devoret (2013), “Nondegenerate three-wave mixing with the Josephson ring modulator,” *Physical Review B* **87** (1), 14508.
- [2] N. W. Ashcroft, and N. D. Mermin (1976), *Solid State Physics* (Harcourt College Publishers).
- [3] C. Axline, M. Reagor, R. Heeres, P. Reinhold, C. Wang, K. Shain, W. Pfaff, Y. Chu, L. Frunzio, and R. J. Schoelkopf (2016), “An architecture for integrating planar and 3D cQED devices,” *Applied Physics Letters* **109** (4), 8.
- [4] D. Bacon (2006), “Operator quantum error-correcting subsystems for self-correcting quantum memories,” *Physical Review A* **73** (1), 012340.
- [5] R. Barends, J. Wenner, M. Lenander, Y. Chen, R. C. Bialczak, J. Kelly, E. Lucero, P. O’Malley, M. Mariantoni, D. Sank, H. Wang, T. C. White, Y. Yin, J. Zhao, A. N. Cleland, J. M. Martinis, and J. J. A. Baselmans (2011), “Minimizing quasiparticle generation from stray infrared light in superconducting quantum circuits,” *Applied Physics Letters* **99** (11), 113507.
- [6] S. D. Barrett, and P. Kok (2005), “Efficient high-fidelity quantum computation using matter qubits and linear optics,” *Physical Review A* **71** (6), 060310.
- [7] C. H. Bennett, G. Brassard, S. Popescu, B. Schumacher, J. A. Smolin, and W. K. Wootters (1996), “Purification of Noisy Entanglement and Faithful Teleportation via Noisy Channels,” *Physical Review Letters* **76** (5), 722–725.
- [8] N. Bergeal, F. Schackert, M. Metcalfe, R. Vijay, V. E. Manucharyan, L. Frunzio, D. E. Prober, R. J. Schoelkopf, S. M. Girvin, and M. H. Devoret (2010), “Phase-preserving amplification near the quantum limit with a Josephson ring modulator,” *Nature* **465** (7294), 64–68.
- [9] N. Bergeal, R. Vijay, V. E. Manucharyan, I. Siddiqi, R. J. Schoelkopf, S. M. Girvin, and M. H. Devoret (2010), “Analog information processing at the quantum limit with a Josephson ring modulator,” *Nature Physics* **6** (4), 296–302.
- [10] H. Bernien, B. Hensen, W. Pfaff, G. Koolstra, M. S. Blok, L. Robledo, T. H. Taminiau, M. Markham, D. J. Twitchen, L. Childress, and R. Hanson (2012), “Heralded entanglement between solid-state qubits separated by 3 meters,” *Nature* **497** (7447), 86–90.

- [11] A. Blais, R. S. Huang, A. Wallraff, S. M. Girvin, and R. J. Schoelkopf (2004), “Cavity quantum electrodynamics for superconducting electrical circuits: An architecture for quantum computation,” *Physical Review A* **69** (6), 62320.
- [12] J. Blumoff, K. Chou, C. Shen, M. Reagor, C. Axline, R. Brierley, M. Silveri, C. Wang, B. Vlastakis, S. Nigg, L. Frunzio, M. Devoret, L. Jiang, S. Girvin, and R. Schoelkopf (2016), “Implementing and Characterizing Precise Multiqubit Measurements,” *Physical Review X* **6** (3), 031041.
- [13] M. Boissonneault, J. M. Gambetta, and A. Blais (2008), “Nonlinear dispersive regime of cavity QED: The dressed dephasing model,” *Physical Review A* **77** (6), 060305.
- [14] M. Boissonneault, J. M. Gambetta, and A. Blais (2009), “Dispersive regime of circuit QED: Photon-dependent qubit dephasing and relaxation rates,” *Physical Review A* **79** (1), 013819.
- [15] D. Bozyigit, C. Lang, L. Steffen, J. M. Fink, M. Baur, R. Bianchetti, P. J. Leek, S. Filipp, M. P. da Silva, A. Blais, and A. Wallraff (2010), “Measurements of the Correlation Function of a Microwave Frequency Single Photon Source,” *Nature Physics* **7** (2), 154–158.
- [16] C. Cabrillo, J. I. Cirac, P. García-Fernández, and P. Zoller (1999), “Creation of entangled states of distant atoms by interference,” *Physical Review A* **59** (2), 1025–1033.
- [17] H. J. Carmichael (1991), *An Open Systems Approach To Quantum Optics* (Springer-Verlag).
- [18] M. A. Castellanos-Beltran, K. D. Irwin, G. C. Hilton, L. R. Vale, and K. W. Lehnert (2008), “Amplification and squeezing of quantum noise with a tunable Josephson metamaterial,” *Nature Physics* **4** (12), 929–931.
- [19] M. A. Castellanos-Beltran, and K. W. Lehnert (2007), “Widely tunable parametric amplifier based on a superconducting quantum interference device array resonator,” *Applied Physics Letters* **91** (8), 083509.
- [20] C. M. Caves (1982), “Quantum limits on noise in linear amplifiers,” *Physics Review D* **26** (8), 1817–1839.
- [21] B. J. Chapman, B. A. Moores, E. I. Rosenthal, J. Kerckhoff, and K. W. Lehnert (2016), “General purpose multiplexing device for cryogenic microwave systems,” *Applied Physics Letters* **108** (22), 222602.
- [22] Y. F. Chen, D. Hover, S. Sendelbach, L. Maurer, S. T. Merkel, E. J. Pritchett, F. K. Wilhelm, and R. McDermott (2011), “Microwave photon counter based on josephson junctions,” *Physical Review Letters* **107** (21), 217401.
- [23] Y. Chu, C. Axline, C. Wang, T. Brecht, Y. Y. Gao, L. Frunzio, and R. J. Schoelkopf (2016), “Suspending superconducting qubits by silicon micromachining,” *Applied Physics Letters* **109** (11), 112601.

- [24] I. L. Chuang, and D. Gottesman (1999), "Demonstrating the viability of universal quantum computation using teleportation and single-qubit operations," *Nature* **402** (6760), 390–393.
- [25] J. I. Cirac, P. Zoller, H. J. Kimble, and H. Mabuchi (1997), "Quantum State Transfer and Entanglement Distribution among Distant Nodes in a Quantum Network," *Physical Review Letters* **78** (16), 3221–3224.
- [26] C. Cohen-Tannoudji, B. Diu, and F. Laloe (1977), *Quantum Mechanics* (Hermann, John Wiley & Sons Inc., Paris).
- [27] C. Cohen-Tannoudji, J. Dupont-Roc, and G. Grynberg (2004), *Atom-Photon Interactions*, 1st ed. (Wiley-Interscience).
- [28] A. D. Córcoles, E. Magesan, S. J. Srinivasan, A. W. Cross, M. Steffen, J. M. Gambetta, and J. M. Chow (2015), "Demonstration of a quantum error detection code using a square lattice of four superconducting qubits," *Nature Communications* **6**, 6979.
- [29] D. G. Cory, M. D. Price, W. Maas, E. Knill, R. Laflamme, W. H. Zurek, T. F. Havel, and S. S. Somaroo (1998), "Experimental Quantum Error Correction," *Physical Review Letters* **81** (10), 2152–2155.
- [30] J. Cramer, N. Kalb, M. A. Rol, B. Hensen, M. S. Blok, M. Markham, D. J. Twitchen, R. Hanson, and T. H. Taminiau (2016), "Repeated quantum error correction on a continuously encoded qubit by real-time feedback," *Nature Communications* **7**, 11526.
- [31] A. Delteil, Z. Sun, W.-b. Gao, E. Togan, S. Faelt, and A. Imamoglu (2015), "Generation of heralded entanglement between distant hole spins," *Nature Physics* **12** (3), 218–223.
- [32] D. Deutsch, A. Ekert, R. Jozsa, C. Macchiavello, S. Popescu, and A. Sanpera (1996), "Quantum Privacy Amplification and the Security of Quantum Cryptography over Noisy Channels," *Physical Review Letters* **77** (13), 2818–2821.
- [33] M. H. Devoret, and R. J. Schoelkopf (2013), "Superconducting Circuits for Quantum Information: An Outlook," *Science* **339** (6124), 1169–1174.
- [34] D. P. DiVincenzo (2000), "The Physical Implementation of Quantum Computation," *Fortschr. Phys.* **48**, 771.
- [35] G. J. Dolan (1977), "Offset masks for lift-off photoprocessing," *Applied Physics Letters* **31** (5), 337–339.
- [36] L. M. Duan, and C. Monroe (2010), "Colloquium: Quantum networks with trapped ions," *Reviews of Modern Physics* **82** (2), 1209–1224.
- [37] W. Dür, and H.-J. Briegel (2003), "Entanglement Purification for Quantum Computation," *Physical Review Letters* **90** (6), 067901.
- [38] W. Dür, H. J. Briegel, J. I. Cirac, and P. Zoller (1998), "Quantum repeaters based on entanglement purification," *Physical Review A* **59** (1), 169–181.

- [39] A. Einstein (1905), "The Photoelectric Effect," *Annalen der Physik* **4**, 132.
- [40] B. Fan, G. Johansson, J. Combes, G. J. Milburn, and T. M. Stace (2014), "Nonabsorbing high-efficiency counter for itinerant microwave photons," *Physical Review B* **90** (3), 035132.
- [41] R. P. Feynman (1982), "Simulating physics with computers," *International Journal of Theoretical Physics* **21** (6-7), 467–488.
- [42] P. Forn-Díaz, C. W. Warren, C. W. S. Chang, A. M. Vadiraj, and C. M. Wilson (2017), "Shaped, on-demand microwave single-photon generator," arXiv:1706.06688 .
- [43] A. G. Fowler, M. Mariantoni, J. M. Martinis, and A. N. Cleland (2012), "Surface codes: Towards practical large-scale quantum computation," *Physical Review A* **86** (3), 032324.
- [44] J. Gambetta, W. A. Braff, A. Wallraff, S. M. Girvin, and R. J. Schoelkopf (2007), "Protocols for optimal readout of qubits using a continuous quantum nondemolition measurement," *Physical Review A* **76** (1), 012325.
- [45] G. W. Gardiner (1991), *Quantum Noise* (Springer).
- [46] K. Geerlings, Z. Leghtas, I. M. Pop, S. Shankar, L. Frunzio, R. J. Schoelkopf, M. Mirrahimi, and M. H. Devoret (2013), "Demonstrating a driven reset protocol for a superconducting qubit," *Physical Review Letters* **110** (12), 120501.
- [47] M. Giustina, M. A. M. Versteegh, S. Wengerowsky, J. Handsteiner, A. Hochrainer, K. Phe-lan, F. Steinlechner, J. Kofler, J.-Å. Larsson, C. Abellán, W. Amaya, V. Pruneri, M. W. Mitchell, J. Beyer, T. Gerrits, A. E. Lita, L. K. Shalm, S. W. Nam, T. Scheidl, R. Ursin, B. Wittmann, and A. Zeilinger (2015), "Significant-Loophole-Free Test of Bell's Theorem with Entangled Photons." *Physical Review Letters* **115** (25), 250401.
- [48] R. J. Glauber (1963), "The quantum theory of optical coherence," *Physical Review* **130** (6), 2529–2539.
- [49] D. J. Griffiths (1995), *Introduction to Quantum Mechanics*, 2nd ed. (Pearson Prentice Hall).
- [50] S. Haroche, and J.-M. Raimond (2006), *Exploring the Quantum*, 1st ed. (Oxford University Press).
- [51] M. Hatridge, S. Shankar, M. Mirrahimi, F. Schackert, K. Geerlings, T. Brecht, K. M. Sliwa, B. Abdo, L. Frunzio, S. M. Girvin, R. J. Schoelkopf, and M. H. Devoret (2013), "Quantum Back-Action of an Individual Variable-Strength Measurement," *Science* **339** (6116), 178–181.
- [52] M. Hatridge, R. Vijay, D. H. Slichter, J. Clarke, and I. Siddiqi (2011), "Dispersive magnetometry with a quantum limited SQUID parametric amplifier," *Physical Review B* **83** (13), 1–8.
- [53] R. W. Heeres, P. Reinhold, N. Ofek, L. Frunzio, L. Jiang, M. H. Devoret, and R. J. Schoelkopf (2017), "Implementing a universal gate set on a logical qubit encoded in an oscillator," *Nature Communications* **8** (1), 94.

- [54] B. Hensen, H. Bernien, A. E. Dréau, A. Reiserer, N. Kalb, M. S. Blok, J. Ruitenber, R. F. L. Vermeulen, R. N. Schouten, C. Abellán, W. Amaya, V. Pruneri, M. W. Mitchell, M. Markham, D. J. Twitchen, D. Elkouss, S. Wehner, T. H. Taminiau, and R. Hanson (2015), “Experimental loophole-free violation of a Bell inequality using entangled electron spins separated by 1.3 km,” *Nature* **526** (7575), 682–686.
- [55] J. Hofmann, M. Krug, N. Ortegel, L. Gerard, M. Weber, W. Rosenfeld, and H. Weinfurter (2012), “Heralded Entanglement Between Widely Separated Atoms,” *Science* **337** (6090), 72–75.
- [56] C. K. Hong, Z. Y. Ou, and L. Mandel (1987), “Measurement of subpicosecond time intervals between two photons by interference,” *Physical Review Letters* **59** (18), 2044–2046.
- [57] A. A. Houck, J. A. Schreier, B. R. Johnson, J. M. Chow, J. Koch, J. M. Gambetta, D. I. Schuster, L. Frunzio, M. H. Devoret, S. M. Girvin, and R. J. Schoelkopf (2008), “Controlling the Spontaneous Emission of a Superconducting Transmon Qubit,” *Physical Review Letters* **101** (8), 080502.
- [58] A. A. Houck, D. I. Schuster, J. M. Gambetta, J. A. Schreier, B. R. Johnson, J. M. Chow, J. Majer, L. Frunzio, M. H. Devoret, S. M. Girvin, and R. J. Schoelkopf (2007), “Generating Single Microwave Photons in a Circuit,” *Nature* **449** (7160), 328–331.
- [59] D. Hucul, I. V. Inlek, G. Vittorini, C. Crocker, S. Debnath, S. M. Clark, and C. Monroe (2014), “Modular entanglement of atomic qubits using photons and phonons,” *Nature Physics* **11** (1), 37–42.
- [60] I. Inlek, C. Crocker, M. Lichtman, K. Sosnova, and C. Monroe (2017), “Multispecies Trapped-Ion Node for Quantum Networking,” *Physical Review Letters* **118** (25), 250502.
- [61] K. Inomata, Z. Lin, K. Koshino, W. D. Oliver, J.-S. Tsai, T. Yamamoto, and Y. Nakamura (2016), “Single microwave-photon detector using an artificial  $\Lambda$ -type three-level system,” *Nature Communications* **7**, 12303.
- [62] W. M. Itano, D. J. Heinzen, J. J. Bollinger, and D. J. Wineland (1990), “Quantum Zeno effect,” *Physical Review A* **41** (5), 2295–2300.
- [63] E. Jeffrey, D. Sank, J. Mutus, T. White, J. Kelly, R. Barends, Y. Chen, Z. Chen, B. Chiaro, A. Dunsworth, A. Megrant, P. O’Malley, C. Neill, P. Roushan, A. Vainsencher, J. Wenner, A. Cleland, and J. M. Martinis (2014), “Fast Accurate State Measurement with Superconducting Qubits,” *Physical Review Letters* **112** (19), 190504.
- [64] L. Jiang, J. M. Taylor, and M. D. Lukin (2006), “A fast and robust approach to long-distance quantum communication with atomic ensembles,” *Physical Review A* **76** (1), 012301.
- [65] L. Jiang, J. M. Taylor, A. S. Sørensen, and M. D. Lukin (2007), “Distributed quantum computation based on small quantum registers,” *Physical Review A* **76** (6), 062323.

- [66] N. Kalb, A. A. Reiserer, P. C. Humphreys, J. J. W. Bakermans, S. J. Kamerling, N. H. Nickerson, S. C. Benjamin, D. J. Twitchen, M. Markham, and R. Hanson (2017), “Entanglement distillation between solid-state quantum network nodes,” *Science* **356** (6341), 10.1126/science.aan0070.
- [67] A. Kamal, A. Marblestone, and M. Devoret (2009), “Signal-to-pump back action and self-oscillation in double-pump Josephson parametric amplifier,” .
- [68] J. Kelly, R. Barends, A. G. Fowler, A. Megrant, E. Jeffrey, T. C. White, D. Sank, J. Y. Mutus, B. Campbell, Y. Chen, Z. Chen, B. Chiaro, A. Dunsworth, I.-C. Hoi, C. Neill, P. J. J. O’Malley, C. Quintana, P. Roushan, A. Vainsencher, J. Wenner, A. N. Cleland, and J. M. Martinis (2015), “State preservation by repetitive error detection in a superconducting quantum circuit,” *Nature* **519** (7541), 66–69.
- [69] J. Kerckhoff, K. Lalumiere, B. J. Chapman, A. Blais, and K. W. Lehnert (2015), “On-Chip Superconducting Microwave Circulator from Synthetic Rotation,” *Physical Review Applied* **4** (3), 034002.
- [70] H. J. Kimble (2008), “The Quantum Internet,” *Nature* **453** (7198), 1023–30.
- [71] W. F. Kindel, M. D. Schroer, and K. W. Lehnert (2016), “Generation and efficient measurement of single photons from fixed-frequency superconducting qubits,” *Physical Review A* **93** (3), 9.
- [72] E. Knill, R. Laflamme, and G. J. Milburn (2001), “A scheme for efficient quantum computation with linear optics,” *Nature* **409** (6816), 46–52.
- [73] E. Knill, D. Leibfried, R. Reichle, J. Britton, R. B. Blakestad, J. D. Jost, C. Langer, R. Ozeri, S. Seidelin, and D. J. Wineland (2008), “Randomized benchmarking of quantum gates,” *Physical Review A* **77** (1), 012307.
- [74] J. Koch, T. M. Yu, J. Gambetta, A. A. Houck, D. I. Schuster, J. Majer, A. Blais, M. H. Devoret, S. M. Girvin, and R. J. Schoelkopf (2007), “Charge-insensitive qubit design derived from the Cooper pair box,” *Physical Review A* **76** (4), 42319.
- [75] A. N. Korotkov (2001), “Output spectrum of a detector measuring quantum oscillations,” *Physical Review B* **63** (8), 085312.
- [76] A. N. Korotkov, and D. V. Averin (2001), “Continuous weak measurement of quantum coherent oscillations,” *Physical Review B* **64** (16), 165310.
- [77] C. Lang, C. Eichler, L. Steffen, J. M. Fink, M. J. Woolley, A. Blais, and A. Wallraff (2013), “Correlations, indistinguishability and entanglement in Hong–Ou–Mandel experiments at microwave frequencies,” *Nature Physics* **9** (6), 345–348.
- [78] G. de Lange, D. Ristè, M. J. J. Tiggelman, C. Eichler, L. Tornberg, G. Johansson, A. Wallraff, R. N. N. Schouten, and L. DiCarlo (2014), “Reversing quantum trajectories with analog feedback,” *Physical Review Letters* **112** (8), 080501.

- [79] F. Lecocq, I. M. Pop, Z. Peng, I. Matei, T. Crozes, T. Fournier, C. Naud, W. Guichard, and O. Buisson (2011), "Junction fabrication by shadow evaporation without a suspended bridge," *Nanotechnology* **22** (31), 315302.
- [80] Z. Leghtas, G. Kirchmair, B. Vlastakis, R. J. Schoelkopf, M. H. Devoret, and M. Mirrahimi (2013), "Hardware-efficient autonomous quantum memory protection," *Physical Review Letters* **111** (12), 120501.
- [81] Z. Leghtas, S. Touzard, I. M. Pop, A. Kou, B. Vlastakis, A. Petrenko, K. M. Sliwa, A. Narla, S. Shankar, M. J. Hatridge, M. Reagor, L. Frunzio, R. J. Schoelkopf, M. Mirrahimi, and M. H. Devoret (2015), "Confining the state of light to a quantum manifold by engineered two-photon loss," *Science* **347** (6224), 853–857.
- [82] Y. Liu (2016), *Quantum Feedback Control of Multiple Superconducting Qubits*, Ph.D. thesis (Yale University).
- [83] Y. Liu, S. Shankar, N. Ofek, M. Hatridge, A. Narla, K. M. Sliwa, L. Frunzio, R. J. Schoelkopf, and M. H. Devoret (2016), "Comparing and combining measurement-based and driven-dissipative entanglement stabilization," *Physical Review X* **6** (1), 40.
- [84] C. Macklin, K. O'Brien, D. Hover, M. E. Schwartz, V. Bolkhovskiy, X. Zhang, W. D. Oliver, and I. Siddiqi (2015), "A near-quantum-limited Josephson traveling-wave parametric amplifier," *Science* **350** (6258).
- [85] P. Maioli, T. Meunier, S. Gleyzes, A. Auffeves, G. Nogues, M. Brune, J. M. Raimond, and S. Haroche (2005), "Nondestructive rydberg atom counting with mesoscopic fields in a cavity," *Physical Review Letters* **94** (11), 113601.
- [86] D. T. McClure, H. Paik, L. S. Bishop, M. Steffen, J. M. Chow, and J. M. Gambetta (2016), "Rapid Driven Reset of a Qubit Readout Resonator," *Physical Review Applied* **5** (1), 011001.
- [87] D. C. McKay, R. Naik, P. Reinhold, L. S. Bishop, and D. I. Schuster (2015), "High-contrast qubit interactions using multimode cavity qed," *Physical Review Letters* **114** (8), 080501.
- [88] M. Mirrahimi, Z. Leghtas, V. V. Albert, S. Touzard, R. J. Schoelkopf, L. Jiang, and M. H. Devoret (2014), "Dynamically protected cat-qubits: A new paradigm for universal quantum computation," *New Journal of Physics* **16**, 10.1088/1367-2630/16/4/045014.
- [89] M. Mirrahimi, and P. Rouchon (2004), "Controllability of Quantum Harmonic Oscillators," *IEEE Transactions on Automatic Control* **49** (5), 745–747.
- [90] B. Misra, and E. C. G. Sudarshan (1977), "The Zeno's paradox in quantum theory," *Journal of Mathematical Physics* **18** (4), 756–763.
- [91] D. L. Moehring, P. Maunz, S. Olmschenk, K. C. Younge, D. N. Matsukevich, L.-M. Duan, and C. Monroe (2007), "Entanglement of single-atom quantum bits at a distance," *Nature* **449** (7158), 68–71.

- [92] C. Monroe, and J. Kim (2013), “Scaling the Ion Trap Quantum Processor,” *Science* **339** (6124).
- [93] C. Monroe, R. Raussendorf, A. Ruthven, K. R. Brown, P. Maunz, L. M. Duan, and J. Kim (2014), “Large-scale modular quantum-computer architecture with atomic memory and photonic interconnects,” *Physical Review A* **89** (2), 022317.
- [94] K. W. Murch, S. J. Weber, C. Macklin, and I. Siddiqi (2013), “Observing single quantum trajectories of a superconducting quantum bit,” *Nature* **502**, 211–214.
- [95] A. H. Myerson, D. J. Szwer, S. C. Webster, D. T. C. Allcock, M. J. Curtis, G. Imreh, J. A. Sherman, D. N. Stacey, A. M. Steane, and D. M. Lucas (2008), “High-fidelity readout of trapped-ion qubits,” *Physical Review Letters* **100** (20), 200502.
- [96] A. Narla, K. M. Sliwa, M. Hatridge, S. Shankar, L. Frunzio, R. J. Schoelkopf, and M. H. Devoret (2014), “Wireless Josephson amplifier,” *Applied Physics Letters* **104** (23), 232605.
- [97] N. H. Nickerson, J. F. Fitzsimons, and S. C. Benjamin (2014), “Freely Scalable Quantum Technologies Using Cells of 5-to-50 Qubits with Very Lossy and Noisy Photonic Links,” *Physical Review X* **4** (4), 041041.
- [98] N. H. Nickerson, Y. Li, and S. C. Benjamin (2013), “Topological quantum computing with a very noisy network and local error rates approaching one percent.” *Nature Communications* **4**, 1756.
- [99] M. I. Nielsen, and I. L. Chuang (2000), *Quantum Computation and Quantum Information*, 10th ed. (Cambridge University Press, New York).
- [100] S. E. Nigg, H. Paik, B. Vlastakis, G. Kirchmair, S. Shankar, L. Frunzio, M. H. Devoret, R. J. Schoelkopf, and S. M. Girvin (2012), “Black-box superconducting circuit quantization,” *Physical Review Letters* **108** (24), 240502.
- [101] N. Ofek, A. Petrenko, R. Heeres, P. Reinhold, Z. Leghtas, B. Vlastakis, Y. Liu, L. Frunzio, S. M. Girvin, L. Jiang, M. Mirrahimi, M. H. Devoret, and R. J. Schoelkopf (2016), “Demonstrating Quantum Error Correction that Extends the Lifetime of Quantum Information,” *Nature* **536** (7617), 441–445.
- [102] H. Paik, A. Mezzacapo, M. Sandberg, D. McClure, B. Abdo, A. Córcoles, O. Dial, D. Bogorin, B. Plourde, M. Steffen, A. Cross, J. Gambetta, and J. M. Chow (2016), “Experimental Demonstration of a Resonator-Induced Phase Gate in a Multiqubit Circuit-QED System,” *Physical Review Letters* **117** (25), 250502.
- [103] H. Paik, D. I. Schuster, L. S. Bishop, G. Kirchmair, G. Catelani, A. P. Sears, B. R. Johnson, M. J. Reagor, L. Frunzio, L. I. Glazman, S. M. Girvin, M. H. Devoret, and R. J. Schoelkopf (2011), “Observation of high coherence in Josephson junction qubits measured in a three-dimensional circuit QED architecture,” *Physical Review Letters* **107** (24), 240501.
- [104] A. Palacios-Laloy, F. Mallet, F. Nguyen, P. Bertet, D. Vion, D. Esteve, and A. N. Korotkov (2010), “Experimental violation of a Bell’s inequality in time with weak measurement,” *Nature Physics* **6** (6), 442–447.

- [105] M. Pechal, L. Huthmacher, C. Eichler, S. Zeytinoğlu, A. A. Abdumalikov, S. Berger, A. Wallraff, and S. Filipp (2014), “Microwave-controlled generation of shaped single photons in circuit quantum electrodynamics,” *Physical Review X* **4** (4), 041010.
- [106] W. Pfaff, C. J. Axline, L. D. Burkhardt, U. Vool, P. Reinhold, L. Frunzio, L. Jiang, M. H. Devoret, and R. J. Schoelkopf (2017), “Controlled release of multiphoton quantum states from a microwave cavity memory,” *Nature Physics* 10.1038/nphys4143.
- [107] M. Planck (1901), “On the Law of Distribution of Energy in the Normal Spectrum,” *Annalen der Physik* **4** (9), 553–.
- [108] F. Pobell (2007), *Matter and Methods at Low Temperatures*, 3rd ed. (Springer, New York).
- [109] D. M. Pozar (2012), *Microwave Engineering*, 4th ed. (John Wiley & Sons Inc.).
- [110] E. M. Purcell (1946), “Spontaneous emission probabilities at radio frequencies,” *Physical Review* **69** (681).
- [111] M. Reagor, W. Pfaff, C. Axline, R. W. Heeres, N. Ofek, K. Sliwa, E. Holland, C. Wang, J. Blumoff, K. Chou, M. J. Hatridge, L. Frunzio, M. H. Devoret, L. Jiang, and R. J. Schoelkopf (2016), “Quantum memory with millisecond coherence in circuit QED,” *Physical Review B* **94** (1), 014506.
- [112] M. D. Reed (2013), *Entanglement and Quantum Error Correction with Superconducting Qubits*, Ph.D. thesis (Yale University).
- [113] M. D. Reed, L. DiCarlo, S. E. Nigg, L. Sun, L. Frunzio, S. M. Girvin, and R. J. Schoelkopf (2011), “Realization of Three-Qubit Quantum Error Correction with Superconducting Circuits,” *Nature* **482** (7385), 382–385.
- [114] M. D. Reed, B. R. Johnson, A. A. Houck, L. DiCarlo, J. M. Chow, D. I. Schuster, L. Frunzio, and R. J. Schoelkopf (2010), “Fast reset and suppressing spontaneous emission of a superconducting qubit,” *Applied Physics Letters* **96** (20), 203110.
- [115] C. Rigetti, J. M. Gambetta, S. Poletto, B. L. T. Plourde, J. M. Chow, A. D. Córcoles, J. A. Smolin, S. T. Merkel, J. R. Rozen, G. A. Keefe, M. B. Rothwell, M. B. Ketchen, and M. Steffen (2012), “Superconducting qubit in a waveguide cavity with a coherence time approaching 0.1 ms,” *Physical Review B* **86** (10), 100506.
- [116] D. Ristè, C. C. Bultink, K. W. Lehnert, and L. DiCarlo (2012), “Feedback control of a solid-state qubit using high-fidelity projective measurement,” *Physical Review Letters* **109** (24), 240502.
- [117] D. Ristè, S. Poletto, M.-Z. Z. Huang, A. Bruno, V. Vesterinen, O.-P. P. Saira, and L. DiCarlo (2015), “Detecting bit-flip errors in a logical qubit using stabilizer measurements,” *Nature Communications* **6**, 6983.
- [118] D. Ristè, J. G. Van Leeuwen, H. S. Ku, K. W. Lehnert, and L. DiCarlo (2012), “Initialization by measurement of a superconducting quantum bit circuit,” *Physical Review Letters* **109** (5), 50507.

- [119] L. Robledo, L. Childress, H. Bernien, B. Hensen, P. F. A. Alkemade, and R. Hanson (2011), “High-fidelity projective read-out of a solid-state spin quantum register,” *Nature* **477** (7366), 574–578.
- [120] N. Roch, E. Flurin, F. Nguyen, P. Morfin, P. Campagne-Ibarcq, M. H. Devoret, and B. Huard (2012), “Widely tunable, nondegenerate three-wave mixing microwave device operating near the quantum limit,” *Physical Review Letters* **108** (14), 147701.
- [121] N. Roch, M. E. Schwartz, F. Motzoi, C. Macklin, R. Vijay, A. W. Eddins, A. N. Korotkov, K. B. Whaley, M. Sarovar, and I. Siddiqi (2014), “Observation of measurement-induced entanglement and quantum trajectories of remote superconducting qubits,” *Physical Review Letters* **112** (17), 170501.
- [122] A. Roy (2016), *Concurrent Remote Entanglement with Continuous Variables*, Ph.D. thesis (Yale University).
- [123] F. D. O. Schackert (2013), *Thesis*, Ph.D. thesis (Yale University).
- [124] D. I. Schuster, A. A. Houck, J. A. Schreier, A. Wallraff, J. M. Gambetta, A. Blais, L. Frunzio, J. Majer, B. Johnson, M. H. Devoret, S. M. Girvin, and R. J. Schoelkopf (2007), “Resolving photon number states in a superconducting circuit,” *Nature* **445** (7127), 515–518.
- [125] A. P. Sears, A. Petrenko, G. Catelani, L. Sun, H. Paik, G. Kirchmair, L. Frunzio, L. I. Glazman, S. M. Girvin, and R. J. Schoelkopf (2012), “Photon shot noise dephasing in the strong-dispersive limit of circuit QED,” *Physical Review B* **86** (18), 180504.
- [126] L. K. Shalm, E. Meyer-Scott, B. G. Christensen, P. Bierhorst, M. A. Wayne, M. J. Stevens, T. Gerrits, S. Glancy, D. R. Hamel, M. S. Allman, K. J. Coakley, S. D. Dyer, C. Hodge, A. E. Lita, V. B. Verma, C. Lambrocco, E. Tortorici, A. L. Migdall, Y. Zhang, D. R. Kumor, W. H. Farr, F. Marsili, M. D. Shaw, J. A. Stern, C. Abellán, W. Amaya, V. Pruneri, T. Jennewein, M. W. Mitchell, P. G. Kwiat, J. C. Bienfang, R. P. Mirin, E. Knill, and S. W. Nam (2015), “Strong Loophole-Free Test of Local Realism,” *Physical Review Letters* **115** (25), 250402.
- [127] P. W. Shor (1995), “Scheme for reducing decoherence in quantum computer memory,” *Physical Review A* **52** (4), R2493–R2496.
- [128] I. Siddiqi, R. Vijay, F. Pierre, C. M. Wilson, L. Frunzio, M. Metcalfe, C. Rigetti, R. J. Schoelkopf, M. H. Devoret, D. Vion, and D. Esteve (2005), “Direct Observation of Dynamical Bifurcation between Two Driven Oscillation States of a Josephson Junction,” *Physical Review Letters* **94** (2), 27005.
- [129] I. Siddiqi, R. Vijay, F. Pierre, C. M. Wilson, M. Metcalfe, C. Rigetti, L. Frunzio, and M. H. Devoret (2004), “RF-Driven {Josephson} Bifurcation Amplifier for Quantum Measurement,” *Physical Review Letters* **93** (20), 207002.
- [130] M. Silveri, E. Zaly-Geller, M. Hatridge, Z. Leghtas, M. H. Devoret, and S. M. Girvin (2016), “Theory of remote entanglement via quantum-limited phase-preserving amplification,” *Physical Review A* **93** (6), 062310.

- [131] K. M. Sliwa (2016), *Improving the Quality of Heisenberg Back-Action of Qubit Measurements made with Parametric Amplifiers*, Ph.D. thesis (Yale University).
- [132] K. M. Sliwa, M. Hatridge, A. Narla, S. Shankar, L. Frunzio, R. Schoelkopf, and M. Devoret (2015), “Reconfigurable Josephson Circulator/Directional Amplifier,” *Physical Review X* **5** (4), 041020.
- [133] L. Spietz, K. W. Lehnert, I. Siddiqi, and R. J. Schoelkopf (2003), “Primary Electronic Thermometry Using the Shot Noise of a Tunnel Junction,” *Science* **300** (5627).
- [134] A. Steane (1996), “Multiple Particle Interference and Quantum Error Correction,” *Proceedings of the Royal Society of London A: Mathematical, Physical and Engineering Sciences* **452** (1954), 10.1098/rspa.1996.0136.
- [135] R. Stockill, M. J. Stanley, L. Huthmacher, E. Clarke, M. Hugues, A. J. Miller, C. Matthiesen, C. L. Gall, and M. Atatüre (2017), “Phase-tuned entangled state generation between distant spin qubits,” arXiv:1702.03422 .
- [136] I.-M. Svensson, M. Pierre, M. Simoen, W. Wustmann, P. Krantz, A. Bengtsson, G. Johansson, J. Bylander, V. Shumeiko, and P. Delsing (2017), “Microwave photon generation in a doubly tunable superconducting resonator,” arXiv:1706.06821 .
- [137] T. R. Tan, J. P. Gaebler, Y. Lin, Y. Wan, R. Bowler, D. Leibfried, and D. J. Wineland (2015), “Multi-element logic gates for trapped-ion qubits,” *Nature* **528** (7582), 380–383.
- [138] R. Vijay (2008), *PhD thesis*, Ph.D. thesis (Yale University).
- [139] R. Vijay, C. Macklin, D. H. Slichter, S. J. Weber, K. W. Murch, R. Naik, A. N. Korotkov, and I. Siddiqi (2012), “Stabilizing Rabi oscillations in a superconducting qubit using quantum feedback,” *Nature* **490**, 77–80.
- [140] R. Vijay, D. H. Slichter, and I. Siddiqi (2011), “Observation of quantum jumps in a superconducting artificial atom,” *Physical Review Letters* **106** (11), 110502.
- [141] B. Vlastakis (2015), *Controlling Coherent State Superpositions with Superconducting Circuits*, Ph.D. thesis (Yale University).
- [142] A. Wallraff, D. I. Schuster, A. Blais, L. Frunzio, R. S. Huang, J. Majer, S. Kumar, S. M. Girvin, and R. J. Schoelkopf (2004), “Circuit Quantum Electrodynamics: Coherent Coupling of a Single Photon to a Cooper Pair Box,” *Nature* **431** (7005), 162–167.
- [143] T. Walter, P. Kurpiers, S. Gasparinetti, P. Magnard, A. Potočnik, Y. Salathé, M. Pechal, M. Mondal, M. Oppliger, C. Eichler, and A. Wallraff (2017), “Rapid High-Fidelity Single-Shot Dispersive Readout of Superconducting Qubits,” *Physical Review Applied* **7** (5), 054020.
- [144] C. Wang, C. Axline, Y. Y. Gao, T. Brecht, Y. Chu, L. Frunzio, M. H. Devoret, and R. J. Schoelkopf (2015), “Surface participation and dielectric loss in superconducting qubits,” *Applied Physics Letters* **107** (16), 162601.

- 
- [145] C. Wang, Y. Y. Gao, P. Reinhold, R. W. Heeres, N. Ofek, K. Chou, C. Axline, M. Reagor, J. Blumoff, K. M. Sliwa, L. Frunzio, S. M. Girvin, L. Jiang, M. Mirrahimi, M. H. Devoret, and R. J. Schoelkopf (2016), "A Schrödinger cat living in two boxes," *Science* **352** (6289).
- [146] W. K. Wootters (1998), "Entanglement of formation of an arbitrary state of two rebits," *Physical Review Letters* **80** (10), 2245.
- [147] T. Yamamoto, K. Inomata, M. Watanabe, K. Matsuba, T. Miyazaki, W. D. Oliver, Y. Nakamura, and J. S. Tsai (2008), "Flux-driven Josephson parametric amplifier," *Applied Physics Letters* **93** (4), 042510.